University of Alberta

Petrology and Geochronology from Basement Core of the Paleoproterozoic Red Earth Granulite Domain, North-Central Alberta

by

Ilona Maria Ranger 

A thesis submitted to the Faculty of Graduate Studies and Research in partial fulfillment of the

requirements for the degree of Master of Science

Department of Earth and Atmospheric Sciences

Edmonton, Alberta

Fall 2004

Your file Votre référence
ISBN: 0-612-95839-6
Our file Notre référence
ISBN: 0-612-95839-6

DEDICATION

For my mother,
Maria

ACKNOWLEDGEMENTS

Few words can express my gratitude for the mentorship I received during the course of this thesis. Sincerest thanks to R.A. Burwash, who kindly provided basement core samples and whose knowledge and enthusiasm provided much insight and invaluable discussion of Alberta basement geology, and to my thesis supervisor, T. Chacko, whose encouragement, wisdom and patient supervision provided a solid foundation on all aspects of this thesis project. Funding for this project was provided by an NSERC grant to T. Chacko. Many thanks to L. Heaman for much guidance and wisdom in laboratory training and interpretation of U-Pb radiogenic isotopes. A timely review of an earlier chapter draft is much appreciated. Many thanks to the Alberta Geological survey, particularly D. Pana and R. Olson for supporting this project and R. Eccles who helped initiate the undergraduate portion of this work. Analytical work was partly funded by the Alberta Geological Survey.

Several members of the Department of Earth and Atmospheric Sciences offered timely help in completion of this project. P. Cavell from the University of Alberta Collections offered much assistance in access to the Basement Rock Core Collection. Many thanks to S. Matveev for his wisdom and humor of the technicalities of the electron microprobe for the graduate portion of this work and L. Shi for the undergraduate portion of the reintegrated feldspar thermometry. D. Resultay and M. Labbe from the University of Alberta Thin Sectioning laboratory offered invaluable assistance during the course of this thesis. J. Schultz provided excellent and thorough training in the Rock crushing and Separation Facilities. Completion of the TIMS mass spectrometry portion of this work by S. Hagen is much appreciated. Many thanks to the Digital Imaging Facility, particularly R. Pakan for photographing the basement cores and M. Fisher for software support and poster presentations. G. Braybrook scanned several mineral separates by SEM on short notice. D. Caird provided XRD analysis for one sample. The De Beers Laboratory of Diamond Research helped solve a half-century mineral identification problem for one sample by use of their FTIR. Many thanks to fellow graduate students, old friends, and especially to Robert and his family for being there and understanding.

TABLE OF CONTENTS

Chapter 3

Chapter 4

LIST OF TABLES

LIST OF FIGURES

LIST OF SYMBOLS

Ab	Albite
Alm	Almandine
An	Anorthite
APT	Athabasca Polymetamorphic terrane
BH	Buffalo Head domain
B.R.P.	Basement Rock Project
BSE	Back-Scattered Electron image
Bt	Biotite
C	Coronation group
CH	Chinchaga domain
Chl	Chlorite
CL	Cathodoluminescence
Cpx	Clinopyroxene
Crd	Cordierite
DLS	Dominion Land Survey system
EDS	Energy Dispersive Spectrometer
EG	Elkins and Grove (1990)
EM	Electron microprobe
Epid	Epidote
ε_{Nd}	Epsilon Neodynium
FL	Fuhrman and Lindsley (1988)
GASP	Garnet-AluminoSilicate-Plagioclase
Gr	Grossular
Grt	Garnet
GSLsz	Great Slave Lake shear zone
H	Hottah arc
Hbl	Hornblende
IUGS	International Union of Geological Sciences
K_{eq}	Equilibrium constant
KFMASH	K_2O-FeO-MgO-Al_2O_3-SiO_2-H_2O
Kfs	K-feldspar
kV	KiloVolt
Ky	Kyanite
L	Liquid
Lat.	Latitude
Lg.	Large
Lk	Lake
LN	Lindsley and Nekvasil (1989)
Long.	Longitude
LREE	Light Rare Earth Elements
Mnz	Monazite
MSWD	Mean square of weighted deviates
Musc	Muscovite

Myr	Million years
nA	NanoAmp
NIH	National Institute of Health
NTS	National Topographic System
NWT	Northwest Territories
Opx	Orthopyroxene
Or	Orthoclase
Q	Queen Maud uplift
Qtz	Quartz
PbMα	M alpha line on Pb
Perth	Perthite
Pl	Plagioclase
P-T	Pressure-Temperature
Px	Pyroxene
Py	Pyrope
REE	Rare Earth Elements
RGD	Red Earth Granulite Domain
SEM	Scanning Electron Microscope
Serp	Serpentine
SHRIMP	Sensitive High Resolution Ion MicroProbe
Sil	Sillimanite
Smll.	Small
Sp	Spessartine
Spl	Spinel
STZ	Snowbird Tectonic Zone
TCPb	Total Common Pb
T_{DM}	Depleted Mantle age
TBC	Taltson Basement Complex
Th*	Sum of measured Th and fictive Th
ThMγ	M gamma line on Th
TIMS	Thermal Ionization Mass Spectrometry
TMA	Trout Mountain Anomaly
TMZ	Taltson Magmatic Zone
TTZ	Thelon Tectonic Zone
TWEEQU	Thermobarometry with Estimation of EQUilibration state (Berman, 1991)
UMβ	M beta line on U
vol%	Volume percent
wt.%	Weight percent
YLγ	L gamma line on Yttrium
%Disc.	Percent Discordance
%Prob. Of Fit	Percent Probability of Fit

CHAPTER 1
INTRODUCTION

Precambrian terranes record the evolution of Earth's early continental crust. A portion of this crust, Laurentia, forms the cratonic nucleus of North America and is composed of various crustal fragments formed and assembled during Archean and Paleoproterozoic time between 3.8 and 1.6 Ga (Figure 1). Rock outcrops of the Canadian Shield have shaped our understanding of the formation of this ancient craton; however, a significant portion of western Laurentia lies buried beneath younger Phanerozoic rocks of the Western Canadian Sedimentary Basin. Unlike the exposed shield, this buried Precambrian crust is only accessible through remote geophysical methods and sparse petroleum drill core intersections. Nevertheless, these buried rocks hold one of the keys to a more complete model of Laurentia's crustal evolution. The present study investigates petrological and geochronological data obtained on drill core samples for a portion of this buried Precambrian crust from the Peerless Lake map area of north-central Alberta. These data are used to evaluate proposed tectonic models for the formation of western Laurentia.

Existing tectonic models for this part of Laurentia fall into two broad categories. (1) A large portion of western Laurentia was assembled from formerly separate and possibly unrelated crustal blocks (e.g. Buffalo Head domain, Slave and Churchill cratons) that were brought together by ocean basin closure between ca. 2.0 to 1.9 Ga (Hoffman, 1987, 1988, 1989; Ross, 1990; Ross et al., 1991; Thériault and Ross, 1991; Thériault, 1992; Ross and Eaton, 2002). (2) A large portion of western Laurentia formed as a single, coherent entity in the Archean or was assembled from separate blocks prior to 2.0 Ga and then later reactivated at ca. 2.0 to 1.9 Ga during intraplate orogenesis (Bostock and van Breemen, 1994; Burwash et al., 2000a; De et al., 2000; Chacko et al., 2000).

According to the first group of models, east-directed subduction of oceanic crust beneath the western Churchill craton formed a magmatic arc along the continental margin. Himalayan-scale collision of the Slave and Churchill cratons resulted in extensive deformation of the Churchill margin and hinterland crust (Queen Maud uplift) and superimposed S-type magmatism on the earlier magmatic arc (Hoffman, 1987, 1988,

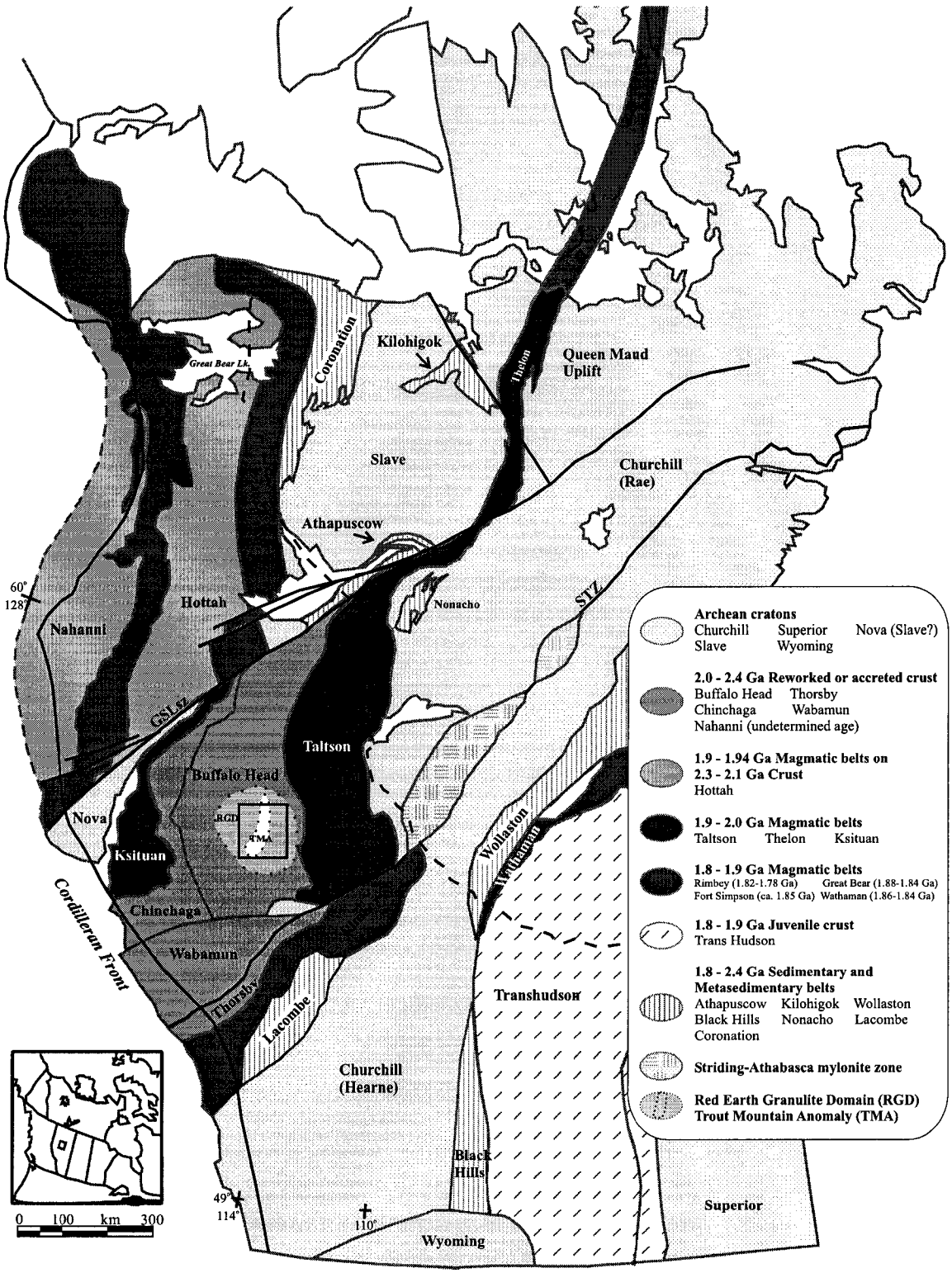

Figure 1. Tectonic framework of western Laurentia (modified after Burwash et al., 2000a; Chacko et al., 2000; Hanmer et al., 1994; McDonough et al., 1993; Ross et al., 1991; Burwash and Power, 1990; Hoffman, 1989; Bostock and van Breemen, 1984; van Breemen and Aspler, 1994). Precambrian rocks to the west and south of the dashed line are buried beneath Phanerozoic sedimentary rocks of the Western Canadian Sedimentary Basin. Black outlined square represents this study, Peerless Lake NTS 84B. GSLsz - Great Slave Lake shear zone, STZ - Snowbird Tectonic Zone, RGD - Red Earth Granulite Domain, TMA - Trout Mountain Anomaly.

1989). A similar subduction and collision model has also been applied to partially buried Precambrian crust to the south. In particular, east-dipping subduction of oceanic crust beneath the western Churchill craton is proposed again to have led to an initial phase of magmatism forming the Taltson magmatic zone (TMZ) along the Churchill continental margin (Figure 1) (Ross et al., 1991; Thériault and Ross, 1991; Ross and Eaton, 2002). In this case, closure of this ocean basin is proposed to have accreted the Buffalo Head domain (BH), a reworked Archean block, onto this western cratonic margin and superimposed a second collisional phase of magmatism on the earlier subduction-related magmatism. In this model, age, isotopic differences and a somewhat distinct geophysical signature primarily distinguishes the older (2.4-2.0 Ga) rocks of the BH domain from the younger (1.99-1.92 Ga) rocks of the TMZ (Ross et al., 1991; Thériault and Ross, 1991; Ross and Eaton, 2002). Critical to this group of models is the absence of younger (ca. <1.99 Ga) magmatic and high-grade metamorphic rocks within the BH domain.

The second group of models highlights age, petrologic, chemical, and isotopic similarities between the BH domain, the TMZ, and western Rae Province. Burwash et al. (2000a) proposed much of northern Alberta is composed of a large area of reworked Archean crust, termed the Athabasca Polymetamorphic terrane (APT) (2.4-1.9 Ga), and interpret this crust to represent the buried extension of Rae Province crust. On the basis of overlapping detrital zircon ages, Bostock and van Breemen (1994) propose crust along the western Rae margin passively rifted to form a Paleoproterozoic basin capturing sediment shed from both the western Rae Province and BH domain until ca. 2.13-2.09 Ga. U-Pb zircon and monazite ages indicate high-grade metamorphism and basin closure following deposition occurred between ca. 2.09 to 2.05 Ga (Bostock and van Breemen, 1994).

De et al. (2000) and Chacko et al. (2000) criticized the subduction-based models for ca. 2.0-1.9 Ga assembly of the BH domain and Rae Province. Their major element and Nd, Pb, and O isotope study of ca. 2.0-1.9 Ga TMZ granitoids showed that none of these granitoids resemble granitoids present in Phanerozoic and well-documented Paleoproterozoic subduction settings. Instead, these authors suggested that the TMZ granitoids formed in a plate interior setting akin to modern-day tectonics in the Tian Shan of central Asia, a mountain belt that is currently forming in the distant hinterland of the

Himalayan collision zone. Critical to this second group of models, there should be many parallels between both the pre- and post-2.0 Ga history of the BH domain, TMZ, and western Rae Province as all three blocks are inferred to have become a single, lithotectonic entity well before 2.0 Ga.

This thesis reports new petrological and geochronological data for drill core samples from the subsurface Red Earth granulite domain (RGD) (Burwash et al., 2000a), which is a local zone of high metamorphic grade located within Ross et al.'s (1991) Buffalo Head domain (Figure 1). This particular area was chosen because of the availability of an unusually large number of drill cores, and because it's high-grade character is generally reminiscent of rocks found in the adjacent TMZ. The data obtained in this study include temperatures and pressures from reintegrated feldspar thermometry and multi-equilibrium thermobarometry, and age dates from U-Th-total Pb chemical dating of monazite and U-Pb isotopic dating of monazite and zircon. These data show many similarities to comparable data from the TMZ and western Rae Province and suggest a strong connection between the pre- and post-2.0 Ga tectonothermal histories of the BH domain, TMZ, and western Rae Province.

REGIONAL GEOLOGY

Buffalo Head Domain

Encompassing ~30,000 km^2 of the north-central Alberta basement, the RGD is intersected by ~190 drill cores in the Peerless Lake map sheet (NTS 84B, Lat. 56°-57°, Long. 114°-116°) (Burwash et al., 2000a). The RGD is near the center of the buried Paleoproterozoic BH domain, which is bounded by the northeast-trending early Proterozoic Great Slave Lake shear zone (GSLsz; Hoffman, 1987, 1988; Hanmer, 1988; Hanmer et al., 1992) and the Snowbird tectonic zone (STZ; Hoffman, 1988; Hanmer et al., 1994, 1995a, b) to the north and south, respectively, and flanked by the Chinchaga domain (CH) and TMZ to the west and east, respectively. Because potential field data indicate both the BH domain and TMZ are broadly curved positive aeromagnetic signatures with scattered negative anomalies, a separation between these two domains is heavily based upon geochronological and lithological data (Appendix A). Petrographic studies reveal that BH domain rocks experienced widespread recrystallization, deformation and cataclasis notably within the RGD (Burwash, 1957; Burwash and Krupicka, 1969, 1970). Drill cores of the BH domain region were interpreted as either unmetamorphosed felsic and mafic plutonics and metamorphosed granulite-, amphibolite- and greenschist-facies rocks (Burwash et al., 2000a) or as older (2324-2014 Ma) metaplutonic and metavolcanic rocks intruded by younger (1998-1990 Ma) plutonic rocks (U-Pb zircon; Ross et al., 1991; Villeneuve et al., 1993). Ca. 1991-1915 Ma cooling (U-Pb titanite) followed with further ca. <1900 Ma cooling and retrogression (e.g. ^{40}Ar-^{39}Ar, 1882 Ma) (Plint and Ross, 1993; Burwash et al., 1962) (Appendix A).

Trout Mountain Anomaly

Within the RGD is an elliptically shaped region characterized by a negative Bouguer (residual -25 mgal) gravity anomaly (Sharpton, 1987; Walcott and Boyd, 1971). Low density ($\leq$2.65 g/cm^3), leucocratic, microcline-rich granitic gneisses are intersected by drill holes in the Red Earth and Utikuma oil fields. This anomaly, which is referred to as the Trout Mountain anomaly (TMA), has been modeled as a 25x25x160 km low density zone. It is proposed to represent a K-rich granitic pluton possibly formed by anatexis and/or by the influx of metamorphic fluids along a zone of late-stage

deformation (Burwash and Power, 1990). A preliminary Rb-Sr whole-rock isochron date of 1832±5 Ma from four Opx-bearing quartzofeldspathic rocks at the southern margin of the TMA (P. Cavell, pers comm.; Burwash and Muehlenbachs, 1997) is significantly younger than a single U-Pb age determination from the RGD area (1991 +225/-45 Ma, U-Pb zircon; Ross et al., 1991; Villeneuve et al., 1993).

Taltson Magmatic Zone and Western Rae Province

Studies in northeastern Alberta and the adjacent NWT (Baadsgaard and Godfrey, 1967; Godfrey and Langenberg, 1978; Nielsen et al., 1981; Langenberg and Nielsen, 1982; Langenberg, 1983; Goff et al., 1986), TMZ (Bostock, 1981, 1987), and western Rae Province (Lewry and Sibbald, 1977, 1980; Bostock et al., 1991; van Breemen et al., 1992; Crocker et al., 1993; Bickford et al., 1994) provide an analogue to the buried Shield (Appendix A). TMZ magmatism initiated at ca. 1.99-1.97 Ga with the intrusion of the early, metaluminous to weakly peraluminous Deskenatlata, Wylie and Colin Lake granitoids followed by the late (1.96-1.93 Ga), peraluminous Slave, Konth and Arch Lake granitoids (Bostock et al., 1987, 1991; Bostock and Loveridge, 1988; Ross et al., 1991; Villeneuve et al., 1993; McDonough et al., 1995b, 2000). These TMZ plutons intrude amphibolite, granodiorite, granitic to mylonitic gneiss, and paragneiss of the ca. 3.18-3.08 Ga and ca. 2.56-2.14 Ga Taltson Basement Complex (TBC) (Bostock and Loveridge, 1988; Bostock et al., 1991; van Breemen et al., 1992; McNicoll et al., 1994, 2000; McDonough et al., 1995a).

Dispersed throughout the TMZ granitoids (Slave and Konth) and TBC gneisses are bodies of granulite-grade metasedimentary rocks (Grt+Bt+Sil+Kfs±Crd) that are elongate approximately parallel to shear zones (Bostock et al., 1987; Thériault 1992; Grover et al., 1993, 1997; Bostock and van Breemen, 1994; Chacko et al., 1994). The sedimentary protoliths of these rocks are proposed to have been deposited in a 2.13-2.09 Ga sedimentary basin, termed the Rutledge River basin (Bostock and van Breemen, 1994).

Three major, high-grade (Grover et al., 1993, 1997), north-trending shear zones (Andrew, Leland and Charles Lake) record ductile shearing during and following TMZ plutonism (Hanmer et al., 1992; McDonough et al., 2000). Continued movement along

these shear zones formed localized areas of mylonite and deformed TMZ and TBC gneisses along with the high-grade metasedimentary cover (McDonough et al., 1993, 1995b, 2000; Bostock and van Breemen, 1994). The largest shear zone, the Charles Lake shear zone, divides the TBC blocks and acts as the eastern boundary for the major TMZ granitoids (McDonough et al., 2000). Several ca. 1.97-1.93 Ga Taltson plutons (Andrew, Charles, Arch, Wylie, Colin Lakes, southern Slave, Chipewyan) deformed by these shear zones record ca. 1.93-1.92 Ga granulite- to upper amphibolite-grade metamorphism and shear zone deformation (McDonough et al., 1995a, b, 2000). K-Ar and ^{40}Ar-^{39}Ar studies suggest widespread cooling and retrogression to greenschist-grade conditions between ca. 1900 to 1800 Ma followed magmatism, metamorphism and deformation (Burwash et al., 1962; Baadsgaard and Godfrey, 1967, 1972; Langenberg and Nielsen, 1982; Plint and McDonough, 1995).

East of the TMZ, numerous granitoids occur along the western Rae margin intruding TBC rocks. These include the ca. 1.81-1.96 Ga Benna Thy, Gagnon, Natael, Othikethe Falls and Thekulthili granitoids (Bostock et al., 1987; Bostock and Loveridge, 1988; Bostock et al., 1991; van Breemen et al., 1992; Bostock and van Breemen, 1994), ca. 1.96 Berrigan anorthosite (Bostock et al., 1991) and ca. 2.4-2.3 Ga hinterland monzogranites of the Berrigan and Andrew Lake blocks (Bostock and Loveridge, 1988; Bostock et al., 1991), ca. 2.27 Ga Yatsore Lake augen gneiss (Bostock et al., 1991), and ca. 2.3 Ga Thoa metagabbro (van Breemen and Bostock, 1994). Northwestern Saskatchewan, including the Tazin Lake, Nolan Lake and Beaverlodge region record >2.3 Ga U-Pb zircon ages with the exception of the ca. 1994 Ma Box Mine granite and ca. 1.82 Ga Junction granite (Van Schmus et al., 1986; Bickford et al., 1987). Basins along the western edge of the Rae Province include the Nonacho Group with detrital zircon $^{207}Pb/^{206}Pb$ model ages of ca. 2.13-2.06 Ga, ca. 2.5-2.3 Ga, and ca. 3.3-3.05 Ga (van Breemen et al., 1992; van Breemen and Aspler, 1994) and the Waugh Lake Group with detrital zircon ages of ca. 2.0-2.3 Ga and ca. 2.7 Ga (McNicoll et al., 1994; McDonough and McNicoll, 1997). The timing of basin deposition is constrained to be less than 1935 Ma for the Nonacho Group, inferred from the deformed 1934±2 Ma Natael granite, (van Breemen and Aspler, 1994; Bostock and van Breemen, 1994) and between 2.02-1.97 Ga for the Waugh Lake Group (McDonough and McNicoll, 1997).

Summary

- The RGD is located within ca. 2.4-2.0 Ga metaplutonic and metavolcanic or metamorphic granulite- to greenschist-grade rocks of the BH domain and encompasses an elliptical-shaped negative gravity anomaly, the TMA, which forms possibly either a zone of microcline-rich granitic rocks and/or deformation (Burwash and Power, 1990).
- Rocks of the BH domain also include ca. 1998-1990 Ma plutonic rocks and ca. 1991-1915 Ma cooling (U-Pb titanite) followed by ca. <1900 Ma retrogression.
- Rocks of the adjacent TMZ record a major period of magmatism between ca. 1.99-1.93 Ga intruding ca. 3.18-3.08 Ga and ca. 2.56-2.14 Ga TBC rocks, later deformed at ca. 1.93-1.92 Ga under granulite-grade conditions by major N-S trending shear zones.
- The western Rae Province is intruded by ca. 2.44-2.27 Ga magmatism characterized as part of the TBC and later ca. 1.96-1.81 Ga magmatism.
- High-grade paragneisses within TMZ granitoids and TBC gneisses record overlapping detrital zircon ages (Mama Moose and Tsu Lake; 2431-2251 Ma), with the BH domain as a possible sediment source, followed by metamorphism with basin closure at ca. 2.09-2.05 Ga under granulite-facies conditions (Grt+Bt+Sil+Kfs±Crd) followed by another high-grade metamorphism at ca. 1.93-1.92 Ga.

CHAPTER 2

METAMORPHISM OF THE RED EARTH GRANULITE DOMAIN

Previous Petrological Study

Over the past 5 decades, Burwash and co-workers, examined over 300 scattered petroleum drill cores or cuttings in order to characterize the metamorphic conditions of the buried Alberta basement (Shillibeer and Burwash, 1956; Burwash, 1957; 1978; Burwash et al., 1973; 2000a, b *and references therein*). Cores selected for this study are presented in Table 1 with corresponding University of Alberta Basement Core Collection numbers presented in Appendix E. Burwash and Krupicka (1969) classified into three broad groups based upon the degree of recrystallization and deformation; (a) deformed, for example with mortared or strained matrix surrounding feldspar or garnet porphyroblasts (e.g. mylonitic or cataclastic), (b) deformed then fully or partly recrystallized (e.g. blastomylonites) and (c) deformed and recrystallized with later further deformation. Groups (a) and (b) are representative of the polymetamorphic and dynamometamorphic textures common to these rocks, including fine to coarse grain size, poikiloblasts, abundant microcline and myrmekite. Due to a lack of outcrop data, differentiation between gneissic and granitic core was subjective (Burwash et al., 2000a). Therefore the terms gneiss and granite were used to discriminate sub-idioblastic to xenoblastic textures of unfoliated or weakly foliated plutonic granitic rocks from strongly foliated gneissic rocks (Burwash and Krupicka, 1969, 1970; Burwash et al., 2000a). Several rocks characterized as granites may in fact be polymetamorphic gneisses or some of the abundant gneisses may be the result of intense recrystallization or deformation of an igneous protolith (Burwash and Krupicka, 1969, 1970; Burwash et al., 2000a).

Gneissic rock types within the RGD (Peerless Lake map area) generally consist of pelitic to semi-pelitic metasediments (Sil-Kfs±Grt±Bt±Spl±Crd or Grt-Kfs±Sil±Bt±Crd), quartzofeldspathic Bt±Hbl gneiss to a single biotite amphibolite, and heavily altered Chl±Epid gneiss. Other rock types include quartzite (Bt or Grt-Sil), Bt- or Sil-Grt-bearing mylonite and scattered granite, granodiorite, diorite, and monzonite. Orthopyroxene±Cpx-bearing quartzofeldspathic rocks are also widespread.

Table 1. Cores examined in this study.

Well Name	B.R.P. #	Location	Rock Type	Grt	Sil	Crd	Spl	Opx	Cpx	Hbl	Bt	Pl	Kfs	Qtz	Musc	Serp	Chl
Granitoid			***Kfs + Pl ± Bt ± Grt ± Sil***														
	64 (M34)	05-32-088-08W4	Bt gneissic granite								x	x	x	x			
	100 (4035)	10-06-082-01W5	Bt-Sil-Grt gneissic granite	x	x						x	x	x	x			
PEX UTIKUMA	860140	13-08-081-09W5	Grt granite	x								x	x	x			
UNO-TEX ET AL SEAL	860550	08-02-083-14W5	Bt granite								x	x	x	x			
CDNRES EVI	860970	03-04-086-13W5	Bt granite								x	x	x	x			
	123 (4240)	02-19-087-08W5	Bt gneissic granite								x	x	x	x			
			Kfs + Pl + Bt + Hbl														
SOBC CALSTAN LAFOND CREEK	861810	10-16-092-09W5	Hbl-Bt granodiorite							x	x	x	x	x			
Pelitic Gneiss			***Crd + Kfs+ Bt ± Sil ± Grt ± Spl ± Pl***														
CANTERRA ONYX ET AL OTTER	861510	11-12-088-11W5	Spl-Crd-Sil-Grt migmatite	x	x	x	x				x	x	x	x			
TEXACO UNION REDFISH	861590	10-23-089-07W5	Sil-Bt-Crd paragneiss		x	x					x		x	x			
	110 (B54-9)	08-22-086-09W5	Grt-(Crd)-Bt gneiss	x		trace					x	x	x	x			
			Sil ± Grt + Bt + Pl ± Kfs														
	82 (4419)	06-06-075-05W5	Sil-Grt-Bt gneiss	x	x						x	x		x			
ASHLAND BTO TECK RED EARTH	861380	02-07-088-07W5	Sil-Grt-Bt gneiss	x	x						x	x	x	x			
UNION RED EARTH	861420	10-06-088-08W5	Grt-Sil-Bt gneiss	x	x						x	x	x	x			
	127 (3226)	04-20-088-07W5	Grt-Bt-Sil gneiss	x	x						x	x	x	x			
	128 (4239)	02-04-088-08W5	Sil-Bt gneiss		x						x	x	x	x			
UNION TEXACO RED EARTH	861100	04-03-087-08W5	Grt-Sil-Bt gneiss	x	x						x	x	x	x			
Gneiss			***Bt + Kfs + Pl ± Grt***														
	133 (4248)	02-17-089-07W5	Bt gneiss								x	x	x	x			
IOE BAT LAKE	860600	04-16-084-08W5	Bt-Grt gneiss	x							x	x	x	x			
UNION SLAVE	860670	06-23-084-14W5	Bt gneiss								x	x	x	x			
CHEVRON SUPTST DOME	860781	04-20-085-09W5	Bt gneiss								x	x	x	x			
DOME ET AL LOON	860790	07-26-085-09W5	Bt-Grt gneiss	x							x	x	x	x			
TEXACO IOE PEERLESS	860880	02-17-086-06W5	Bt-Grt gneiss	x							x	x	x	x			
UNION RED EARTH	861150	02-17-087-08W5	Bt-Grt gneiss	x							x	x	x	x			
UNION RED EARTH	861450	12-09-088-08W5	Bt-Grt gneiss	x							x	x	x	x			
TP ET AL OGSTON	861520	05-29-088-11W5	Bt gneiss								x	x	x	x			
SINCLAIR PEERLESS	861630	10-09-090-06W5	Bt-Grt gneiss	x							x	x	x	x			
ARCO ET AL HUNT	861740	06-35-091-07W5	Bt gneiss								x	x	x	x			
UNO TEX UNION VEGA	861750	04-08-091-08W5	Grt-Bt gneiss	x							x	x	x	x			
ULSTER ET AL OGSTON	861790	11-04-091-10W5	Bt gneiss								x	x	x	x			
			Kfs + Pl ± Bt ± Hbl ± Chl														
	108 (4007k)	11-03-085-12W5	Bt-Hbl gneiss							x	x	x	x	x			
ATLANTIC DOME LOON RIVER	861800	12-25-091-10W5	Chl gneiss									x	x	x			x
Mylonite																	
	126 (4245b)	14-17-088-06W5	Sil-Grt mylonite	x	x							x	x	x	x		
Charnockite			***Opx + Kfs +Pl ± Bt ± Cpx***														
ATLANTIC IOE UTIKUMA	860220	12-26-081-09W5	Bt-Cpx charnockite					x	x		x	x	x	x			
SHELL TROUT RIVER	860700	13-13-085-04W5	Serp charnockite					x				x	x	x		x	
CHEVRON SUPTST DOME LOON	860770	10-19-085-09W5	Bt charnockite					x			x		x	x			
TEXACO SOUTH PEERLESS	860870	06-10-086-05W5	Serp charnockite					x				x	x	x		x	
			Serp + Bt + Kfs+ Pl														
MOBIL NW NIPISI	860070	10-27-080-08W5	Bt-Serp charnockite								x	x	x	x		x	
PEX IOE UTIKUMA	860200	04-26-081-09W5	Bt-Serp charnockite								x	x	x	x		x	
AGIP ET AL NIPISI	860380	14-24-082-07W5	Serp-Bt charnockite								x	x	x	x		x	
PEX UTIKUMA	860530	01-28-082-10W5	Bt-Serp charnockite								x	x	x	x		x	
HOME PERMO UNION TROUT R.	860570	10-31-084-04W5	Bt-Serp charnockite								x	x	x	x		x	
IOE CHEVRON LUBICON	860640	02-27-084-10W5	Serp-Bt charnockite								x	x	x	x		x	
TRICENT ET AL LUBICON`	860930	06-11-086-10W5	Serp-Bt charnockite								x	x	x	x		x	
HUSKY ET AL EVI	861280	14-05-087-12W5	Serp-Bt charnockite								x	x	x	x		x	
CHEVRON TROUT	861360	01-31-088-03W5	Bt-Serp charnockite								x	x	x	x		x	
			Serp + Bt + Pl + Hbl														
CHEVRON GPD DOME LUBICON	860830	12-28-085-12W5	Serp-Bt-Hbl charnockite							x	x	x		x		x	

Including well name, sample number, DLS location, rock type (Burwash, 1957; Burwash, 1988 unpublished) and primary and secondary mineral phases.

Burwash and Power (1990) and Burwash et al. (2000a) tentatively referred to undeformed to moderately deformed quartzofeldspathic rocks, containing orthopyroxene or serpentine pseudomorphs after Opx, as granulite or retrograded granulite, respectively. The question then arises whether to call these Opx-bearing rocks granulites, which implies a high-grade metamorphic origin, or charnockites, which broadly implies an igneous origin. According to current IUGS classification (LeMaitre et al., 2002, p. 20);

> *"...the presence of orthopyroxene (or fayalite plus quartz) and, in many of the rocks, perthite, mesoperthite or antiperthite (Streckeisen, 1974, 1976)"*

defines and characterizes Opx-bearing granitoids or charnockites. Furthermore, the IUGS classification states;

> *"although many show signs of metamorphic overprinting, such as deformation and recrystallization, they conform to the group of "igneous and igneous-looking rocks"."*

Following the IUGS classification (LeMaitre et al., 2002, p. 20), these rocks will be referred to as charnockite on the basis of their broadly igneous appearance and the presence of Opx, perthite and/or antiperthite. Within the RGD, a total of 9 charnockite and 32 retrograded charnockite localities broadly flank, or are concentrated along the southern tip of, the TMA. This pattern was inferred by Burwash and Power (1990) to represent older Archean crust intruded or 'reactivated' by younger Proterozoic magmatism (TMA).

P-T Estimate Methods

The paucity of metamorphic mineral assemblages commonly used in geothermobarometry limits the ability to characterize the pressure and temperature conditions of Alberta basement samples. P-T conditions of the RGD were studied using reintegrated feldspar thermometry of exsolved ternary feldspars and Fe-Mg exchange and net-transfer equilibria of garnet-bearing samples.

Ternary feldspars ($NaAlSi_3O_8$ (Ab) - $CaAl_2Si_2O_8$ (An) - $KAlSi_3O_8$ (Or)) provide the opportunity to determine minimum metamorphic and perhaps magmatic temperatures using the technique of reintegrated feldspar thermometry. Textures of exsolved plagioclase lamellae in a K-feldspar host (perthite), K-feldspar lamellae in a plagioclase

host (antiperthite) or an equal balance of both feldspar phases (mesoperthite) have long been studied (e.g. Alling, 1938). These exsolution textures occur in several rock types, including amphibolite- to granulite-facies metamorphic rocks and magmatic rocks (e.g. Bohlen and Essene, 1977; Yund and Ackermand, 1979; Day and Brown, 1980; Yund et al., 1980; Voll et al., 1994).

Exsolution in ternary feldspars involves both *inter*grain exchange of CaAl-(Na, K)Si between distinct plagioclase and alkali feldspar crystals. This *inter*grain exchange ceases at a higher temperature than *intra*grain exsolution of perthite or antiperthite lamellae within a single feldspar grain (Kroll et al., 1993; Voll et al., 1994). The *intra*grain exsolution process involves the nucleation and growth of plagioclase lamellae in alkali feldspar or alkali feldspar lamellae in plagioclase feldspar. K-Ca exchange between host and lamellae (which also involves Al-Si exchange) closes at a higher temperature than Na-K exchange (Kroll et al., 1993). After An-rich lamellae are exsolved (Kroll et al., 1993), the latter process continues with further cooling until Na also becomes supersaturated and exsolves fine Ab-rich lamellae (films) within the host matrix or as rims surrounding coarse An lamellae (Yund and Ackermand, 1979; Kroll et al., 1993; Voll et al., 1994). Retrieving the composition of the original homogenous feldspar grain, before exsolution, is the objective of reintegrating host and lamellae feldspar compositions.

Ternary solution models for feldspars used in this study (Fuhrman and Lindsley (1988) (FL), Lindsley and Nekvasil (1989) (LN), and Elkins and Grove (1990) (EG)) permit calculation of the position of the feldspar solvus as a function of temperature. Reintegrated feldspar compositions plotted on a ternary feldspar solvus diagram provides a *minimum* estimate of peak temperature. More specifically, they provide an estimate of the temperature at which intergrain exchange of components between discrete plagioclase and alkali feldspar crystals ceased. The temperatures are regarded as minimum estimates because some samples only contain a single type of feldspar (alkali feldspar or plagioclase) and therefore may not be saturated in all feldspar components. Additionally, temperatures can be regarded as minima because of the possibility of lamellae loss from individual feldspar grains by deformation.

Relatively few Grt+Pl+Bt+Qtz±Sil±Crd-bearing assemblages from high-grade gneisses of the RGD are available to evaluate pressure and temperatures of peak metamorphism from net transfer or Fe-Mg exchange thermobarometry. Calculated pressures verify pressure estimates used to obtain minimum temperatures from reintegrated feldspar thermometry. Granulite-grade conditions can be inferred for at least part of the study area because of the presence of the garnet-cordierite-K-feldspar assemblage in a metapelite sample (861510). The presence of the K-feldspar-sillimanite assemblage and the absence of primary muscovite in several other samples indicate at least uppermost amphibolite- and possibly granulite-facies conditions (White et al., 2001).

P-T determinations were limited to twelve core samples containing garnet, with or without sillimanite. Six cores containing the garnet-sillimanite-plagioclase assemblage (GASP) and six garnet-plagioclase bearing cores lacking sillimanite enabled calculation of pressure and maximum pressure, respectively, using the GASP barometer [1]. One of these samples also contained cordierite, which permitted calculation of pressures using Grt-Crd-Sil-Qtz net-transfer reactions [2]. Temperatures were calculated using Fe-Mg exchange reactions between garnet and biotite [3] and garnet and cordierite [4].

[1] $3CaAl_2Si_2O_8 = Ca_3Al_2Si_3O_{12} + 2Al_2SiO_5 + SiO_2$
anorthite grossular sillimanite quartz

[2] $2Fe_3Al_2Si_3O_{12} + 4Al_2SiO_5 + 5SiO_2 = 3Fe_2Al_4Si_5O_{18}$
almandine sillimanite quartz Fe - cordierite

$2Mg_3Al_2Si_3O_{12} + 4Al_2SiO_5 + 5SiO_2 = 3Mg_2Al_4Si_5O_{18}$
pyrope sillimanite quartz Mg - cordierite

[3] $Fe_3Al_2Si_3O_{12} + KMg_3AlSi_3O_{10}(OH)_2 = Mg_3Al_2Si_3O_{12} + KFe_3AlSi_3O_{10}(OH)_2$
almandine phlogopite pyrope annite

[4] $2Mg_3Al_2Si_3O_{12} + 3Fe_2Al_4Si_5O_{18} = 2Fe_3Al_2Si_3O_{12} + 3Mg_2Al_4Si_5O_{18}$
pyrope Fe- cordierite almandine cordierite

In these high-grade samples, Fe-Mg exchange between garnet and biotite during cooling is of concern due to the low modal abundance of biotite in these samples. As such, biotite grains may experience large changes in Fe-Mg ratio through exchange with

garnet and other ferromagnesian phases (Spear and Florence, 1992). Therefore compositional maps of garnet and surrounding matrix minerals were made to determine if any Fe, Mg, Mn, or Ca compositional variation or zoning between core and rim of garnet developed since equilibration at peak temperature conditions. The GASP net-transfer reaction equilibrium assemblage commonly occurs in pelites but is based upon low grossular and anorthite contents in garnet and plagioclase, respectively. This leads to large uncertainties (±3 kbars, 1σ) in accuracy of the reported pressures (Kohn and Spear, 1991).

Mineral Petrography and Compositions

Reconnaissance of basement cores resulted in 46 samples selected for this study (Table 1), including those samples used for geochronology presented in the following chapter. Representative mineral phases and textures from selected core are shown in Figure 2 with representative mineral compositions found in Tables 2-4. Due to limitations in sampling density, systematic variation in mineral phase occurrences (Figure 3) or isograds cannot be accurately traced. Therefore mineralogy will be described as follows; phyllosilicates, garnet, sillimanite, cordierite, spinel, pyroxene, and feldspar.

Phyllosilicates

Mica is sparse throughout the study area. Red-brown biotite is fine-grained, <0.2-0.5 mm in size, ragged, and sparse (<5 to 15 vol%) with few coarse subhedral laths displaying bird's eye distinction from abundant zircon inclusions. Greenish-brown biotite laths are up to 1-2 mm in size. Gneissic fabric is dominantly defined by a mortar surrounding porphyroblasts of garnet or K-feldspar and only weakly defined by biotite. Some biotite may be retrograde, infilling fractures and rims around porphyroblastic minerals. Limited fine-grained laths of muscovite or sericite (<5 to 10 vol%) are found in the matrix of 4245b and 860890 (1-22-86-8W5). Muscovite is likely of retrograde origin, suggested by textures of intertwining laths with secondary chlorite, rimming and infilling fractures in garnet, surrounding relic sillimanite (4245b) or as radiating crystals within larger fractures throughout the rock. Retrograde chlorite ranges from abundant laths (e.g. 4240) to fine-grained, pale-green chlorite intergrown with biotite laths along garnet fractures or within the matrix.

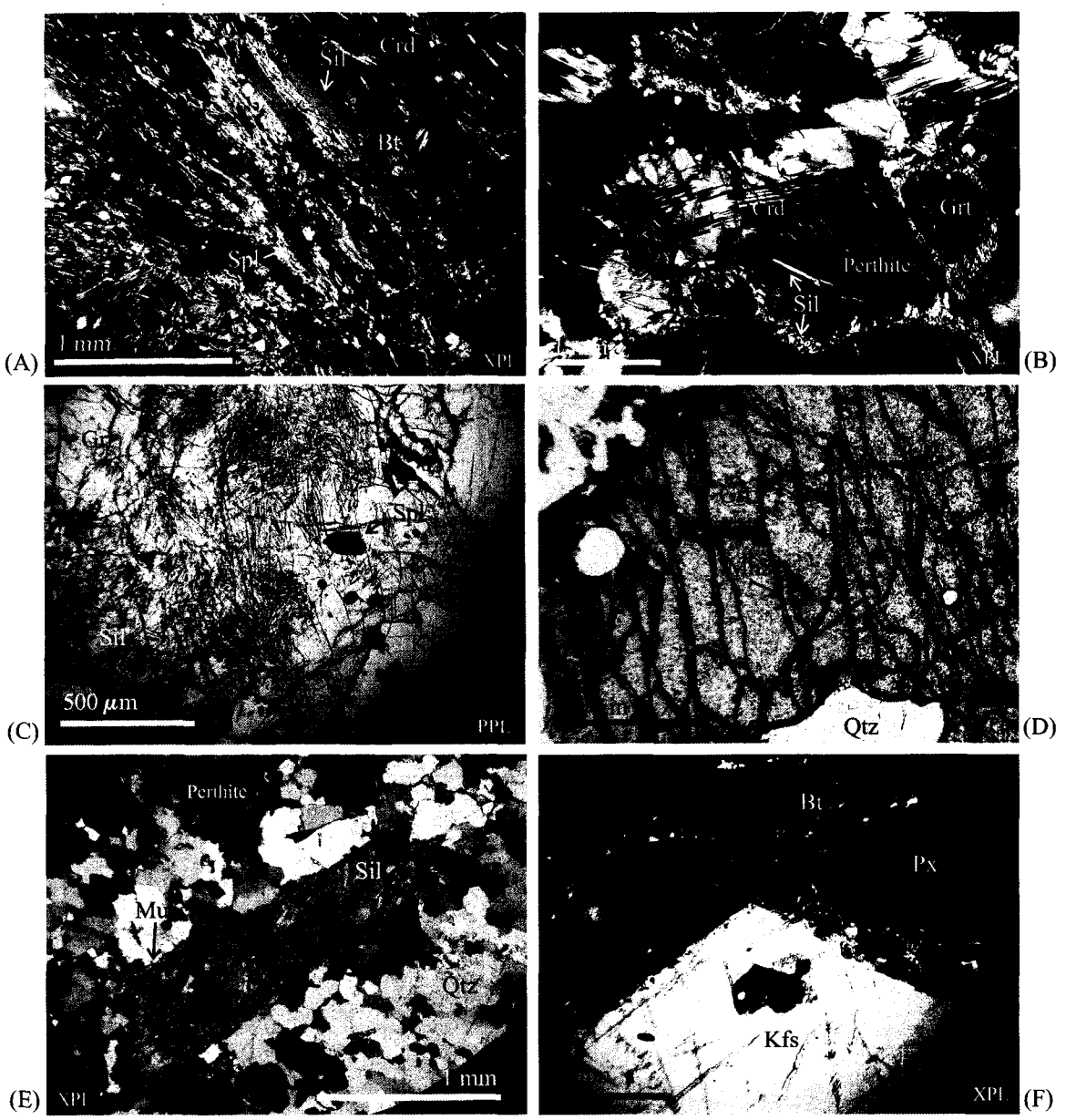

Figure 2. Representative microphotographs in plane (PPL) and cross-polarized light (XPL): melanosome of pelitic migmatite (861510) (A) metamorphic fabric defined by prismatic sillimanite, (B) garnet and twinned cordierite porphyroblasts encrusted with fine needles of sillimanite and enclosed within perthite, (C) large, fractured garnet with sillimanite needles and spinel inclusion. Pelitic mylonite (4245b) (D) euhedral monazite inclusion in large, fractured garnet, (E) relic sillimanite porphyroblast surrounded by retrograde muscovite/sericite. (F) Large K-feldspar and fractured pyroxene phenocrysts wrapped by biotite foliation in a weakly deformed charnockite (860770).

Table 2. Average chemical compositions of garnet, plagioclase and fine-grained biotite. Averages based upon 2-3 domains per sample.

Garnet	3226			4419			861100			861380		
	n=10	n=10	n=10	n=25	n=15	n=14	n=16	n=12	n=6	n=15	n=15	n=15
	core	rim near plagioclase	rim near biotite	core	rim near plagioclase	rim near biotite	core	rim near plagioclase	rim near biotite	core	rim near plagioclase	rim near biotite
SiO_2	37.12	37.08	37.00	37.29	37.02	36.78	36.85	37.07	36.89	36.88	36.81	36.76
TiO_2	0.01	0.02	0.02	0.00	0.01	0.01	0.01	0.00	0.01	0.01	0.01	0.01
Al_2O_3	21.60	21.55	21.34	21.51	21.37	21.22	21.91	21.89	21.80	21.21	21.13	21.03
FeO	35.60	35.96	36.29	35.04	35.53	36.11	36.32	36.22	36.61	35.30	35.02	35.15
MnO	1.62	1.71	1.85	1.47	1.60	1.72	1.73	1.69	1.70	4.64	4.84	5.16
MgO	3.38	3.16	2.64	3.74	3.15	2.73	3.76	3.74	3.38	1.69	1.57	1.31
CaO	0.57	0.57	0.58	1.09	1.08	1.08	0.62	0.52	0.56	0.59	0.66	0.64
Total	99.90	100.06	99.72	100.15	99.76	99.65	101.19	101.13	100.95	100.33	100.03	100.07
Si	2.985	2.983	2.996	2.985	2.986	2.983	2.937	2.952	2.950	2.993	2.996	2.998
Ti	0.001	0.001	0.001	0.000	0.000	0.001	0.001	0.000	0.001	0.001	0.001	0.001
Al	2.048	2.044	2.036	2.030	2.032	2.028	2.058	2.055	2.055	2.028	2.027	2.022
Fe	2.394	2.420	2.457	2.346	2.397	2.449	2.421	2.412	2.449	2.396	2.384	2.397
Mn	0.110	0.117	0.127	0.100	0.110	0.118	0.117	0.114	0.115	0.319	0.333	0.357
Mg	0.405	0.379	0.318	0.446	0.379	0.330	0.447	0.444	0.403	0.204	0.190	0.160
Ca	0.049	0.049	0.050	0.094	0.093	0.094	0.053	0.044	0.048	0.051	0.058	0.056
Total	7.991	7.994	7.985	8.000	7.997	8.003	8.033	8.021	8.021	7.992	7.989	7.990
Gr	0.0165	0.0167	0.0171	0.0314	0.0312	0.0313	0.0174	0.0147	0.0160	0.0173	0.0194	0.0187
Py	0.1369	0.1278	0.1077	0.1493	0.1272	0.1104	0.1470	0.1471	0.1337	0.0688	0.0641	0.0538
Alm	0.8094	0.8162	0.8324	0.7858	0.8047	0.8187	0.7972	0.8003	0.8121	0.8065	0.8040	0.8073
Sp	0.0372	0.0393	0.0429	0.0334	0.0368	0.0395	0.0385	0.0379	0.0383	0.1074	0.1125	0.1201

Plagioclase								
	n=8	n=20	n=10	n=13	n=11		n=10	n=15
	grain	core	inclusion in garnet	rim	grain		core	rim
SiO_2	63.83	61.53	60.88	61.25	63.92		62.98	63.16
Al_2O_3	22.86	24.19	24.85	24.53	23.02		23.82	23.28
FeO	0.15	0.15	0.35	0.23	0.28		0.23	0.41
CaO	3.26	4.87	5.72	4.94	3.12		3.76	3.71
Na_2O	9.78	8.80	8.53	8.70	9.72		9.33	9.48
K_2O	0.12	0.12	0.13	0.17	0.31		0.19	0.31
BaO	0.01	0.04	0.03	0.05	0.02		0.02	0.02
Total	100.02	99.69	100.50	99.87	100.38		100.34	100.37
Si	2.817	2.738	2.698	2.723	2.814		2.776	2.789
Al	1.189	1.269	1.299	1.286	1.194		1.238	1.212
Fe	0.006	0.005	0.013	0.009	0.010		0.008	0.015
Ca	0.154	0.233	0.272	0.236	0.147		0.178	0.176
Na	0.837	0.759	0.733	0.750	0.830		0.798	0.811
K	0.007	0.007	0.007	0.009	0.017		0.011	0.017
Ba	0.000	0.001	0.001	0.001	0.000		0.000	0.000
Total	5.010	5.011	5.023	5.014	5.013		5.009	5.020
An	0.1545	0.2331	0.2685	0.2367	0.1480		0.1803	0.1748
Ab	0.8386	0.7604	0.7243	0.7539	0.8345		0.8090	0.8079
Or	0.0069	0.0066	0.0071	0.0094	0.0175		0.0107	0.0173

Biotite					
	n=7	n=25		n=16	n=15
	grain	core	inclusion in garnet	grain	grain
SiO_2	34.20	34.95	35.80	36.06	34.44
TiO_2	0.10	2.00	0.47	0.49	1.11
Al_2O_3	20.69	19.28	19.67	17.88	19.45
FeO	18.00	17.33	15.07	16.06	22.31
MnO	0.04	0.03	0.01	0.02	0.12
MgO	9.94	10.63	13.68	14.18	6.96
CaO	0.01	0.01	0.01	0.01	0.02
Na_2O	0.03	0.14	0.20	0.04	0.02
K_2O	8.28	9.35	9.05	9.25	9.31
F	0.62	0.56	0.71	1.56	1.08
Cl	0.03	0.03	0.02	0.03	0.06
Total	91.68	94.07	94.40	94.93	94.43
Si	2.642	2.646	2.655	2.644	2.638
Ti	0.006	0.114	0.026	0.027	0.064
Al	1.885	1.720	1.719	1.545	1.756
Fe	1.163	1.097	0.935	0.985	1.430
Mn	0.003	0.002	0.001	0.002	0.008
Mg	1.145	1.199	1.512	1.550	0.795
Ca	0.001	0.001	0.001	0.001	0.002
Na	0.005	0.021	0.029	0.006	0.004
K	0.815	0.903	0.856	0.865	0.910
F	0.152	0.135	0.166	0.362	0.262
Cl	0.003	0.004	0.002	0.004	0.008
Total	7.820	7.842	7.902	7.992	7.877
TWQ 202					
XMg	0.4961	0.5222	0.6180	0.6113	0.3574
Xfe	0.5039	0.4778	0.3820	0.3887	0.6426
MgM1	0.2321	0.2713	0.3705	0.4788	0.1939
FeM1	0.2358	0.2483	0.2291	0.3045	0.3485
TiM1	0.0057	0.1142	0.0263	0.0271	0.0642
AlM1	0.5264	0.3662	0.3741	0.1896	0.3934
AlIV	0.3395	0.3385	0.3363	0.3389	0.3406
SiIV	0.6605	0.6615	0.6637	0.6611	0.6594
XK	0.9928	0.9766	0.9663	0.9919	0.9939
XOH	0.9221	0.9308	0.9160	0.8172	0.8648

Table 2. Average chemical compositions continued ....

Garnet	861420			860600			860790			860880	
	n=10	n=12	n=6	n=30	n=20	n=20	n=19	n=14	n=10	n=13	n=10
	core	rim near plagioclase	rim near biotite	core	rim near plagioclase	rim near biotite	core	rim near plagioclase	rim near biotite	core	rim near plagioclase
SiO_2	35.66	35.85	36.38	37.04	36.92	36.84	36.89	36.76	36.83	38.20	38.22
TiO_2	0.01	0.00	0.01	0.01	0.01	0.01	0.02	0.01	0.00	0.01	0.00
Al_2O_3	21.60	21.65	21.69	21.40	21.31	21.29	21.04	20.97	21.07	21.91	21.98
FeO	40.53	40.26	40.46	37.44	37.77	38.38	36.36	36.64	36.50	29.66	29.40
MnO	1.47	1.47	1.52	0.61	0.69	0.78	1.46	1.62	1.51	0.43	0.41
MgO	1.01	0.95	0.78	2.93	2.55	2.08	2.60	2.33	2.41	8.00	8.27
CaO	0.69	0.62	0.56	0.80	0.77	0.77	1.41	1.25	1.41	1.10	1.03
Total	100.96	100.81	101.39	100.23	100.00	100.15	99.79	99.57	99.74	99.31	99.31
Si	2.913	2.927	2.950	2.983	2.987	2.987	2.990	2.992	2.990	2.988	2.985
Ti	0.001	0.000	0.001	0.001	0.000	0.001	0.001	0.001	0.000	0.001	0.000
Al	2.080	2.083	2.073	2.031	2.032	2.034	2.010	2.012	2.016	2.020	2.023
Fe	2.769	2.749	2.744	2.522	2.556	2.602	2.464	2.494	2.478	1.940	1.920
Mn	0.102	0.101	0.105	0.042	0.047	0.054	0.100	0.112	0.104	0.028	0.027
Mg	0.123	0.115	0.094	0.352	0.307	0.251	0.315	0.283	0.291	0.932	0.963
Ca	0.060	0.055	0.048	0.069	0.066	0.067	0.123	0.109	0.123	0.092	0.086
Total	8.047	8.031	8.014	8.000	7.996	7.996	8.004	8.002	8.002	8.002	8.004
Gr	0.0198	0.0181	0.0162	0.0231	0.0223	0.0226	0.0409	0.0363	0.0409	0.0308	0.0287
Py	0.0403	0.0382	0.0315	0.1179	0.1031	0.0844	0.1048	0.0943	0.0973	0.3115	0.3213
Alm	0.9067	0.9102	0.9174	0.8450	0.8586	0.8750	0.8209	0.8321	0.8271	0.6483	0.6409
Sp	0.0333	0.0335	0.0349	0.0141	0.0159	0.0180	0.0334	0.0373	0.0347	0.0095	0.0091

Plagioclase								
	n=8	n=15	n=19	n=15		n=10	n=14	
	core	rim	grain	rim		core	rim along garnet	
SiO_2	63.56	63.74	63.11	62.97		59.13	58.86	
Al_2O_3	23.45	22.91	23.01	23.23		25.63	25.73	
FeO	0.10	0.35	0.33	0.19		0.02	0.26	
CaO	3.90	3.50	3.70	4.33		6.99	7.22	
Na_2O	9.37	9.52	9.56	8.68		7.43	7.34	
K_2O	0.17	0.15	0.22	0.24		0.30	0.21	
BaO	0.02	0.02	0.02	0.02		0.01	0.02	
Total	100.59	100.18	99.96	99.66		99.51	99.65	
Si	2.793	2.812	2.796	2.792		2.650	2.639	
Al	1.215	1.191	1.202	1.215		1.354	1.360	
Fe	0.004	0.013	0.012	0.007		0.001	0.010	
Ca	0.184	0.165	0.176	0.206		0.336	0.347	
Na	0.798	0.814	0.822	0.746		0.646	0.638	
K	0.010	0.009	0.012	0.014		0.017	0.012	
Ba	0.000	0.000	0.000	0.000		0.000	0.000	
Total	5.004	5.004	5.020	4.980		5.004	5.006	
An	0.1854	0.1673	0.1741	0.2133		0.3360	0.3478	
Ab	0.8049	0.8240	0.8136	0.7727		0.6469	0.6400	
Or	0.0097	0.0087	0.0122	0.0140		0.0171	0.0122	

Biotite				
	n=15	n=20	n=15	n=9
	grain	grain	core	rim
SiO_2	34.79	34.50	35.57	36.20
TiO_2	2.38	1.03	1.79	0.35
Al_2O_3	17.46	18.39	17.62	18.46
FeO	23.54	19.20	18.98	17.27
MnO	0.02	0.01	0.02	0.00
MgO	6.13	9.52	10.50	11.61
CaO	0.02	0.02	0.03	0.02
Na_2O	0.02	0.02	0.05	0.04
K_2O	9.55	9.39	9.48	9.62
F	2.23	1.56	1.46	1.73
Cl	0.04	0.08	0.07	0.05
Total	95.25	93.05	94.93	94.62
Si	2.618	2.627	2.655	2.671
Ti	0.135	0.059	0.101	0.019
Al	1.549	1.651	1.549	1.606
Fe	1.482	1.224	1.186	1.066
Mn	0.001	0.001	0.001	0.000
Mg	0.687	1.080	1.167	1.278
Ca	0.002	0.002	0.002	0.002
Na	0.003	0.004	0.008	0.006
K	0.917	0.913	0.903	0.906
F	0.531	0.376	0.345	0.404
Cl	0.005	0.011	0.009	0.006
Total	7.932	7.946	7.926	7.963
TWQ 202				
XMg	0.3168	0.4688	0.4960	0.5452
Xfe	0.6832	0.5312	0.5040	0.4548
MgM1	0.2210	0.3109	0.3450	0.3839
FeM1	0.4766	0.3522	0.3505	0.3203
TiM1	0.1348	0.0592	0.1006	0.0193
AlM1	0.1676	0.2777	0.2039	0.2765
AlIV	0.3454	0.3432	0.3363	0.3323
SiIV	0.6546	0.6568	0.6637	0.6677
XK	0.9946	0.9944	0.9890	0.9912
XOH	0.7316	0.8066	0.8233	0.7950

Table 2. Average chemical compositions continued ....

Garnet	861150			861450			861510 - leucosome			B54-9		
	n=22	n=14	n=6	n=15	n=15	n=15	n=13	n=10	n=10	n=20	n=18	n=19
	core	rim near plagioclase	rim near biotite	core	rim near plagioclase	rim near biotite	core	rim near plagioclase	rim near biotite	core	rim near plagioclase	rim near biotite
SiO_2	36.58	36.53	36.42	36.93	36.87	36.86	37.59	37.47	37.44	37.66	37.04	36.49
TiO_2	0.02	0.02	0.01	0.01	0.00	0.01	0.01	0.01	0.00	0.01	0.01	0.01
Al_2O_3	20.90	20.89	20.78	21.35	21.27	21.31	21.59	21.44	21.40	21.75	21.48	21.33
FeO	36.56	36.59	36.73	37.07	37.06	37.53	32.30	32.91	33.36	33.46	35.21	35.11
MnO	1.73	1.89	2.21	0.92	0.94	0.98	0.52	0.56	0.55	0.97	1.28	1.37
MgO	2.32	2.21	1.92	2.65	2.60	2.21	6.33	5.90	5.56	5.20	3.64	3.62
CaO	1.41	1.29	1.28	1.13	0.89	0.97	1.01	1.02	0.97	0.96	0.93	0.94
Total	99.52	99.43	99.35	100.06	99.63	99.86	99.34	99.31	99.28	100.02	99.59	98.87
Si	2.983	2.984	2.985	2.983	2.990	2.989	2.981	2.982	2.987	2.985	2.982	2.966
Ti	0.001	0.001	0.001	0.001	0.000	0.001	0.000	0.001	0.000	0.000	0.001	0.000
Al	2.009	2.012	2.007	2.032	2.033	2.037	2.018	2.012	2.012	2.032	2.039	2.044
Fe	2.494	2.499	2.518	2.504	2.514	2.546	2.142	2.191	2.226	2.219	2.371	2.387
Mn	0.120	0.131	0.154	0.063	0.065	0.067	0.035	0.038	0.037	0.065	0.087	0.094
Mg	0.282	0.269	0.234	0.320	0.314	0.267	0.749	0.700	0.661	0.615	0.437	0.439
Ca	0.124	0.113	0.112	0.097	0.078	0.084	0.085	0.087	0.083	0.082	0.080	0.082
Total	8.012	8.009	8.011	8.000	7.993	7.991	8.010	8.011	8.007	7.998	7.997	8.012
Gr	0.0409	0.0375	0.0371	0.0327	0.0261	0.0285	0.0284	0.0289	0.0277	0.0274	0.0269	0.0272
Py	0.0933	0.0892	0.0777	0.1071	0.1056	0.0899	0.2487	0.2322	0.2197	0.2063	0.1467	0.1463
Alm	0.8262	0.8297	0.8343	0.8391	0.8465	0.8589	0.7114	0.7263	0.7402	0.7444	0.7969	0.7951
Sp	0.0396	0.0435	0.0509	0.0212	0.0218	0.0227	0.0115	0.0125	0.0124	0.0219	0.0294	0.0314

Plagioclase												
	n=12			n=15			n=15	n=15		n=10	n=13	
	grain			grain			core	rim		core	rim	
SiO_2	61.82			63.32			59.63	60.70		60.24	59.81	
Al_2O_3	23.49			23.32			25.30	24.72		25.25	25.44	
FeO	0.23			0.23			0.02	0.05		0.03	0.17	
CaO	4.13			4.19			6.65	5.77		6.04	6.29	
Na_2O	8.85			9.21			7.90	8.45		8.21	8.13	
K_2O	0.62			0.10			0.23	0.12		0.19	0.14	
BaO	0.02			0.01			0.03	0.02		0.02	0.02	
Total	99.17			100.38			99.75	99.82		99.97	100.01	
Si	2.766			2.790			2.666	2.704		2.682	2.666	
Al	1.239			1.212			1.333	1.298		1.325	1.337	
Fe	0.009			0.008			0.001	0.002		0.001	0.006	
Ca	0.198			0.198			0.318	0.275		0.288	0.300	
Na	0.768			0.787			0.685	0.730		0.709	0.703	
K	0.036			0.006			0.013	0.007		0.011	0.008	
Ba	0.000			0.000			0.000	0.000		0.000	0.000	
Total	5.016			5.000			5.017	5.016		5.016	5.021	
An	0.1976			0.1998			0.3132	0.2722		0.2861	0.2971	
Ab	0.7665			0.7946			0.6738	0.7211		0.7035	0.6952	
Or	0.0360			0.0056			0.0129	0.0068		0.0105	0.0077	

Biotite												
	n=16			n=15			n=8	n=5		n=20	n=15	
	grain			grain			core	inclusion in garnet		core	rim	
SiO_2	37.33			34.64			35.87	35.80		34.29	34.89	
TiO_2	0.16			1.41			3.41	3.57		2.08	2.13	
Al_2O_3	20.92			18.27			17.87	16.83		17.28	17.45	
FeO	21.10			18.85			15.74	14.64		15.31	15.03	
MnO	0.03			0.02			0.00	0.01		0.03	0.03	
MgO	9.78			10.37			11.48	13.04		13.07	13.24	
CaO	0.03			0.03			0.00	0.03		0.00	0.02	
Na_2O	0.05			0.07			0.06	0.09		0.11	0.12	
K_2O	10.23			9.27			9.68	9.48		9.52	9.46	
F	1.40			1.55			0.48	0.48		1.50	1.53	
Cl	0.09			0.62			0.18	0.20		0.14	0.12	
Total	100.52			94.31			94.54	93.92		92.67	93.34	
Si	2.809			2.593			2.688	2.690		2.588	2.604	
Ti	0.009			0.081			0.192	0.202		0.118	0.120	
Al	1.855			1.612			1.578	1.490		1.537	1.535	
Fe	1.328			1.183			0.986	0.920		0.967	0.939	
Mn	0.002			0.001			0.000	0.001		0.002	0.002	
Mg	1.096			1.154			1.282	1.460		1.470	1.473	
Ca	0.003			0.003			0.000	0.002		0.000	0.001	
Na	0.008			0.010			0.009	0.014		0.016	0.018	
K	0.982			0.885			0.926	0.908		0.917	0.901	
F	0.334			0.367			0.113	0.113		0.358	0.362	
Cl	0.012			0.079			0.023	0.026		0.019	0.015	
Total	8.437			7.968			7.798	7.825		7.992	7.969	
TWQ 202												
XMg	0.4523			0.4938			0.5652	0.6135		0.6032	0.6107	
Xfe	0.5477			0.5062			0.4348	0.3865		0.3968	0.3893	
MgM1	0.1479			0.3526			0.3063	0.3796		0.4567	0.4532	
FeM1	0.1791			0.3615			0.2356	0.2391		0.3004	0.2889	
TiM1	0.0091			0.0807			0.1922	0.2017		0.1183	0.1195	
AlM1	0.6639			0.2052			0.2659	0.1796		0.1247	0.1384	
AlIV	0.2978			0.3517			0.3280	0.3276		0.3531	0.3491	
SiIV	0.7022			0.6483			0.6720	0.6724		0.6469	0.6509	
XK	0.9895			0.9860			0.9906	0.9826		0.9828	0.9792	
XOH	0.8271			0.7767			0.9316	0.9307		0.8116	0.8116	

Table 3. Average chemical compositions of garnet and cordierite. Averages based upon 2-3 domains per sample.

Garnet	861510-melanosome	
	n=15	n=15
	core	rim near cordierite
SiO_2	36.58	36.40
TiO_2	0.02	0.01
Al_2O_3	21.71	21.61
FeO	34.18	34.09
MnO	0.59	0.59
MgO	5.72	5.68
CaO	0.98	0.99
Total	99.79	99.37
Si	2.922	2.920
Ti	0.001	0.000
Al	2.044	2.045
Fe	2.283	2.288
Mn	0.040	0.040
Mg	0.682	0.679
Ca	0.084	0.085
Total	8.055	8.057
Gr	0.0272	0.0276
Py	0.2207	0.2197
Alm	0.7392	0.7397
Sp	0.0129	0.0130

Cordierite		
	n=15	n=15
	core	rim
SiO_2	48.18	48.13
Al_2O_3	33.49	33.73
FeO	7.50	7.37
MnO	0.03	0.03
MgO	8.41	8.47
CaO	0.01	0.00
Na_2O	0.05	0.06
K_2O	0.01	0.02
TiO_2	0.02	0.01
Total	97.70	97.83
Si	4.971	4.957
Al	4.072	4.093
Fe	0.647	0.635
Mn	0.003	0.003
Mg	1.293	1.301
Ca	0.001	0.001
Na	0.010	0.012
K	0.002	0.002
Ti	0.003	0.002
Total	10.986	10.989
XMg	0.6655	0.6711
XFe	0.3330	0.3275

Table 4. Averaged electron microprobe analyses of feldspar host and lamellae chemical compositions.

	4240		4035		M34		3226		4007K		8600070		8600550		8600670		8600880	
	host	lamellae	host	lamellae	host	lamellae	host	lamellae	host	lamellae	host	lamellae	host	lamellae	host	lamellae	host	lamellae
	Kfs	Pl	Kfs	Pl	Kfs	Pl	Kfs	Pl	Kfs	Pl	Kfs	Pl	Kfs	Pl	Kfs	Pl	Kfs	Pl
SiO_2	64.87	62.52	64.63	63.84	64.93	63.64	63.96	63.38	63.97	61.87	63.10	57.99	64.68	61.78	64.22	68.44	64.52	60.18
Al_2O_3	18.61	22.70	18.46	22.58	18.51	22.77	18.42	22.74	19.01	24.36	18.80	26.56	18.29	24.48	18.27	20.18	18.53	25.14
FeO	0.02	0.03	0.01	0.02	0.02	0.02	0.01	0.02	0.03	0.06	0.04	0.11	0.01	0.02	0.01	0.02	0.01	0.01
CaO	0.01	4.07	0.09	3.39	0.15	3.75	0.01	3.28	0.03	5.83	0.09	8.15	0.01	5.40	0.01	0.14	0.11	6.41
Na_2O	0.55	9.09	1.48	9.74	2.43	9.38	0.75	9.70	1.05	8.36	1.24	6.76	0.62	8.31	0.40	11.56	1.65	7.69
K_2O	15.91	0.35	14.82	0.13	13.32	0.16	15.56	0.28	14.68	0.19	14.13	0.25	15.79	0.35	16.14	0.22	14.12	0.44
BaO	0.17	0.02	0.10	-----	0.18	-----	0.04	0.01	1.18	0.04	1.53	0.03	0.23	0.02	0.35	-----	0.35	0.01
Total	100.14	98.79	99.60	99.71	99.55	99.73	98.76	99.40	99.94	100.72	98.93	99.84	99.63	100.35	99.40	100.56	99.30	99.88
Si	2.992	2.800	2.990	2.825	2.990	2.816	2.989	2.816	2.968	2.729	2.963	2.599	3.000	2.732	2.994	2.974	2.989	2.683
Al	1.012	1.199	1.006	1.178	1.005	1.187	1.015	1.191	1.040	1.267	1.040	1.403	1.000	1.276	1.004	1.034	1.012	1.321
Fe	0.001	0.001	0.000	0.001	0.001	0.001	0.000	0.001	0.001	0.002	0.002	0.004	0.000	0.001	0.001	0.001	0.000	0.000
Ca	0.000	0.196	0.005	0.161	0.008	0.178	0.001	0.156	0.001	0.276	0.004	0.391	0.001	0.256	0.000	0.006	0.006	0.306
Na	0.049	0.789	0.133	0.835	0.217	0.805	0.068	0.836	0.095	0.715	0.113	0.587	0.056	0.712	0.036	0.975	0.148	0.665
K	0.936	0.020	0.875	0.008	0.783	0.009	0.928	0.016	0.869	0.011	0.846	0.014	0.934	0.020	0.960	0.012	0.835	0.025
Ba	0.003	0.000	0.002	-----	0.003	-----	0.001	0.000	0.021	0.001	0.028	0.000	0.004	0.000	0.006	-----	0.006	0.000
Total	4.994	5.005	5.011	5.008	5.007	4.997	5.002	5.015	4.994	5.001	4.997	5.000	4.995	4.996	5.002	5.002	4.996	5.001
An	0.00	0.19	0.00	0.16	0.01	0.18	0.00	0.15	0.00	0.28	0.00	0.39	0.00	0.26	0.00	0.01	0.01	0.31
Ab	0.05	0.79	0.13	0.83	0.22	0.81	0.07	0.83	0.10	0.71	0.12	0.59	0.06	0.72	0.04	0.98	0.15	0.67
Or	0.95	0.02	0.86	0.01	0.78	0.01	0.93	0.02	0.90	0.01	0.88	0.01	0.94	0.02	0.96	0.01	0.84	0.03

	8600200		8600200		8600380		8600700		8601420		8601510		8601510		8601520		8601520	
	host	lamellae	host	lamellae	host	lamellae	host	lamellae	host	lamellae	host	lamellae	host	lamellae	host	lamellae	host	lamellae
	Kfs	Pl	Pl	Kfs	Kfs	Pl	Kfs	Pl	Kfs	Pl	Kfs	Pl	Kfs	Pl	Pl	Kfs	Kfs	Pl
SiO_2	64.47	59.88	60.02	63.97	64.34	59.66	64.35	55.43	64.72	64.71	64.16	61.20	64.81	62.95	60.20	64.24	64.34	60.36
Al_2O_3	18.87	25.22	25.24	18.79	18.66	26.15	19.28	28.64	18.60	22.21	18.73	24.23	18.79	21.98	24.91	18.46	18.55	24.86
FeO	0.03	0.08	0.07	0.02	0.02	0.08	0.02	0.08	0.01	0.02	0.01	0.01	0.03	0.02	0.03	0.02	0.01	0.05
CaO	0.11	6.50	6.64	0.06	0.04	7.14	0.17	10.25	0.03	2.84	0.07	5.19	0.02	3.03	6.14	0.04	0.04	6.06
Na_2O	2.01	7.88	7.66	1.33	0.90	7.21	1.16	5.46	1.36	10.06	1.65	8.68	0.89	9.31	7.97	0.95	1.40	7.98
K_2O	13.40	0.27	0.22	14.14	15.35	0.22	14.75	0.23	15.09	0.17	14.14	0.22	15.45	0.94	0.26	15.34	14.66	0.52
BaO	0.81	0.03	0.02	0.94	0.19	0.02	0.72	0.02	0.11	-----	0.39	0.03	0.12	0.03	0.02	0.38	0.42	0.02
Total	99.69	99.85	99.86	99.24	99.51	100.48	100.45	100.12	99.93	100.01	99.15	99.55	100.11	98.27	99.52	99.41	99.40	99.84
Si	2.977	2.673	2.676	2.977	2.984	2.646	2.962	2.491	2.987	2.850	2.979	2.730	2.986	2.834	2.691	2.988	2.986	2.693
Al	1.027	1.327	1.327	1.030	1.020	1.367	1.046	1.517	1.011	1.153	1.025	1.274	1.020	1.167	1.313	1.012	1.015	1.308
Fe	0.001	0.003	0.003	0.001	0.001	0.003	0.001	0.003	0.000	0.001	0.000	0.000	0.001	0.001	0.001	0.001	0.000	0.002
Ca	0.005	0.311	0.317	0.003	0.002	0.339	0.008	0.494	0.002	0.134	0.003	0.248	0.001	0.146	0.294	0.002	0.002	0.290
Na	0.180	0.682	0.662	0.120	0.081	0.620	0.104	0.476	0.121	0.860	0.149	0.750	0.079	0.813	0.691	0.086	0.126	0.690
K	0.790	0.015	0.012	0.839	0.909	0.012	0.866	0.013	0.889	0.009	0.838	0.013	0.908	0.054	0.015	0.910	0.868	0.029
Ba	0.015	0.000	0.000	0.017	0.003	0.000	0.013	0.000	0.002	-----	0.007	0.000	0.002	0.000	0.000	0.007	0.008	0.000
Total	4.994	5.012	4.998	4.987	5.000	4.987	5.000	4.995	5.013	5.008	5.001	5.015	4.998	5.016	5.005	5.004	5.004	5.013
An	0.01	0.31	0.32	0.00	0.00	0.35	0.01	0.50	0.00	0.13	0.00	0.25	0.00	0.14	0.29	0.00	0.00	0.29
Ab	0.18	0.68	0.67	0.12	0.08	0.64	0.11	0.48	0.12	0.86	0.15	0.74	0.08	0.80	0.69	0.09	0.13	0.68
Or	0.81	0.02	0.01	0.87	0.92	0.01	0.89	0.01	0.88	0.01	0.85	0.01	0.92	0.05	0.01	0.91	0.87	0.03

	8601810		8600530		8600570		8600640		8600930		8601280		8601360		8601630		8601740	
	host	lamellae	host	lamellae	host	lamellae	host	lamellae	host	lamellae	host	lamellae	host	lamellae	host	lamellae	host	lamellae
	Kfs	Pl	Kfs	Pl	Kfs	Pl	Pl	Kfs	Pl	Kfs	Kfs	Pl	Kfs	Pl	Kfs	Pl	Kfs	Pl
SiO_2	63.84	59.42	63.71	60.62	64.35	55.45	59.63	63.81	60.08	64.09	64.71	62.41	64.79	61.76	64.20	64.02	64.99	62.25
Al_2O_3	18.55	25.85	18.61	24.68	18.52	28.29	25.54	18.69	25.39	18.53	18.20	23.74	18.34	24.52	18.47	22.79	18.23	24.03
FeO	0.02	0.05	0.03	0.04	0.02	0.07	0.06	0.04	0.05	0.02	0.01	0.03	0.03	0.07	0.01	0.01	0.02	0.03
CaO	0.02	7.28	0.01	6.02	0.19	10.00	6.84	0.05	6.69	0.05	0.01	4.82	0.05	5.62	0.01	3.50	0.01	4.75
Na_2O	0.76	7.27	1.07	7.86	1.40	5.59	7.64	0.87	7.65	0.90	0.83	8.68	1.03	8.21	0.68	9.43	0.67	8.58
K_2O	15.47	0.30	14.75	0.25	14.20	0.30	0.22	15.09	0.25	15.07	15.42	0.30	15.18	0.22	15.96	0.41	15.89	0.21
BaO	0.78	-----	0.87	0.04	0.43	0.02	-----	1.22	-----	0.94	0.32	0.01	0.30	-----	0.16	-----	0.18	-----
Total	99.45	100.18	99.05	99.50	99.11	99.72	99.93	99.79	100.11	99.61	99.51	99.99	99.74	100.41	99.50	100.18	99.99	99.86
Si	2.979	2.646	2.978	2.707	2.989	2.502	2.660	2.973	2.673	2.983	3.003	2.765	2.998	2.729	2.986	2.821	3.004	2.758
Al	1.020	1.357	1.026	1.299	1.014	1.505	1.343	1.026	1.331	1.017	0.996	1.240	1.000	1.277	1.012	1.184	0.993	1.255
Fe	0.001	0.002	0.001	0.001	0.001	0.003	0.002	0.002	0.002	0.001	0.001	0.001	0.001	0.003	0.001	0.001	0.001	0.001
Ca	0.001	0.347	0.001	0.288	0.010	0.483	0.327	0.002	0.319	0.002	0.001	0.229	0.003	0.266	0.001	0.165	0.001	0.225
Na	0.068	0.628	0.097	0.681	0.126	0.489	0.661	0.078	0.660	0.082	0.075	0.745	0.092	0.703	0.062	0.806	0.060	0.737
K	0.921	0.017	0.880	0.014	0.841	0.017	0.012	0.897	0.014	0.895	0.913	0.017	0.896	0.012	0.947	0.023	0.937	0.012
Ba	0.014	-----	0.016	0.001	0.008	0.000	-----	0.022	-----	0.017	0.006	0.000	0.006	-----	0.003	-----	0.003	-----
Total	5.006	4.998	4.998	4.991	4.988	4.999	5.005	5.002	4.999	4.997	4.993	4.997	4.996	4.991	5.012	5.001	4.998	4.989
An	0.00	0.35	0.00	0.29	0.01	0.49	0.33	0.00	0.32	0.00	0.00	0.23	0.00	0.27	0.00	0.17	0.00	0.23
Ab	0.07	0.63	0.10	0.69	0.13	0.49	0.66	0.08	0.66	0.08	0.08	0.75	0.09	0.72	0.06	0.81	0.06	0.76
Or	0.93	0.02	0.90	0.01	0.86	0.02	0.01	0.92	0.01	0.91	0.92	0.02	0.90	0.01	0.94	0.02	0.94	0.01

Table 4. Continued ...

	8601100		8600970			.4248		
	host Kfs	lamellae Pl	host Kfs	lamellae Pl	lamellae PL-AB	host Kfs	lamellae Pl	lamellae PL-AB
SiO_2	64.50	64.22	64.25	61.14	68.46	64.09	62.56	68.24
Al_2O_3	18.49	22.37	18.35	24.32	20.02	18.35	23.53	19.88
FeO	0.03	0.01	0.02	0.03	0.01	0.01	0.02	0.04
CaO	0.04	3.10	0.02	5.36	0.18	0.03	4.49	0.30
Na_2O	1.31	9.96	0.52	8.70	11.64	0.69	8.99	11.33
K_2O	15.11	0.15	15.88	0.17	0.15	15.90	0.28	0.31
BaO	0.08	-----	0.34	-----	-----	0.19	-----	-----
Total	99.57	99.81	99.39	99.74	100.46	99.27	99.88	100.11
Si	2.988	2.837	2.993	2.723	2.978	2.989	2.774	2.980
Al	1.009	1.165	1.007	1.277	1.027	1.009	1.229	1.023
Fe	0.001	0.000	0.001	0.001	0.001	0.000	0.001	0.001
Ca	0.002	0.147	0.001	0.256	0.008	0.001	0.213	0.014
Na	0.118	0.853	0.047	0.752	0.982	0.062	0.772	0.960
K	0.893	0.008	0.944	0.010	0.008	0.946	0.016	0.017
Ba	0.002	-----	0.006	-----	-----	0.004	-----	-----
Total	5.013	5.011	4.999	5.019	5.004	5.011	5.006	4.997
An	0.00	0.15	0.00	0.25	0.01	0.00	0.21	0.01
Ab	0.12	0.85	0.05	0.74	0.98	0.06	0.77	0.97
Or	0.88	0.01	0.95	0.01	0.01	0.94	0.02	0.02

	8601590		8601790			8600870	
	host Kfs	lamellae Pl	host Kfs	lamellae Pl	lamellae PL-AB	host Kfs	lamellae Pl
SiO_2	64.66	65.72	64.78	62.78	68.49	64.53	56.18
Al_2O_3	18.38	22.01	18.22	23.49	20.33	18.33	27.75
FeO	0.02	0.02	0.02	0.02	0.02	0.03	0.09
CaO	0.01	2.17	0.01	4.36	0.14	0.10	9.78
Na_2O	0.61	10.36	0.57	8.97	11.42	0.73	5.74
K_2O	15.99	0.11	16.02	0.24	0.32	15.51	0.35
BaO	0.04	-----	0.16	-----	-----	0.33	0.03
Total	99.73	100.38	99.77	99.88	100.73	99.56	99.92
Si	2.996	2.876	3.002	2.780	2.972	2.995	2.528
Al	1.004	1.135	0.995	1.226	1.040	1.003	1.472
Fe	0.001	0.001	0.001	0.001	0.001	0.001	0.003
Ca	0.001	0.102	0.000	0.207	0.006	0.005	0.471
Na	0.054	0.879	0.051	0.770	0.961	0.066	0.501
K	0.945	0.006	0.947	0.014	0.018	0.918	0.020
Ba	0.001	-----	0.003	-----	-----	0.006	0.001
Total	5.002	4.999	5.000	4.999	4.998	4.995	4.997
An	0.00	0.10	0.00	0.21	0.01	0.00	0.48
Ab	0.05	0.89	0.05	0.78	0.98	0.07	0.50
Or	0.95	0.01	0.95	0.01	0.02	0.93	0.02

	8601800		8601750			8600830	
	host Kfs	lamellae Pl	host Kfs	lamellae Pl	lamellae Pl-AB	host Kfs	lamellae Pl
SiO_2	64.26	59.83	64.72	61.75	68.48	63.91	60.12
Al_2O_3	18.26	25.52	18.46	23.88	19.76	18.47	25.03
FeO	0.02	0.04	0.03	0.04	0.01	0.02	0.05
CaO	0.01	6.92	0.06	5.30	0.09	0.03	6.40
Na_2O	0.56	7.52	1.41	8.55	11.66	0.92	7.76
K_2O	15.62	0.19	14.77	0.17	0.15	15.32	0.33
BaO	0.67	0.02	0.22	-----	-----	0.53	0.03
Total	99.39	100.04	99.68	99.70	100.15	99.21	99.71
Si	2.996	2.664	2.992	2.747	2.987	2.983	2.685
Al	1.003	1.340	1.006	1.252	1.016	1.016	1.318
Fe	0.001	0.001	0.001	0.001	0.000	0.001	0.002
Ca	0.001	0.330	0.003	0.253	0.004	0.002	0.306
Na	0.051	0.650	0.127	0.738	0.986	0.084	0.672
K	0.929	0.011	0.871	0.009	0.008	0.912	0.019
Ba	0.012	0.000	0.004	-----	-----	0.010	0.000
Total	4.992	4.996	5.004	5.001	5.003	5.007	5.002
An	0.00	0.33	0.00	0.25	0.00	0.00	0.31
Ab	0.05	0.66	0.13	0.74	0.99	0.08	0.67
Or	0.95	0.01	0.87	0.01	0.01	0.91	0.02

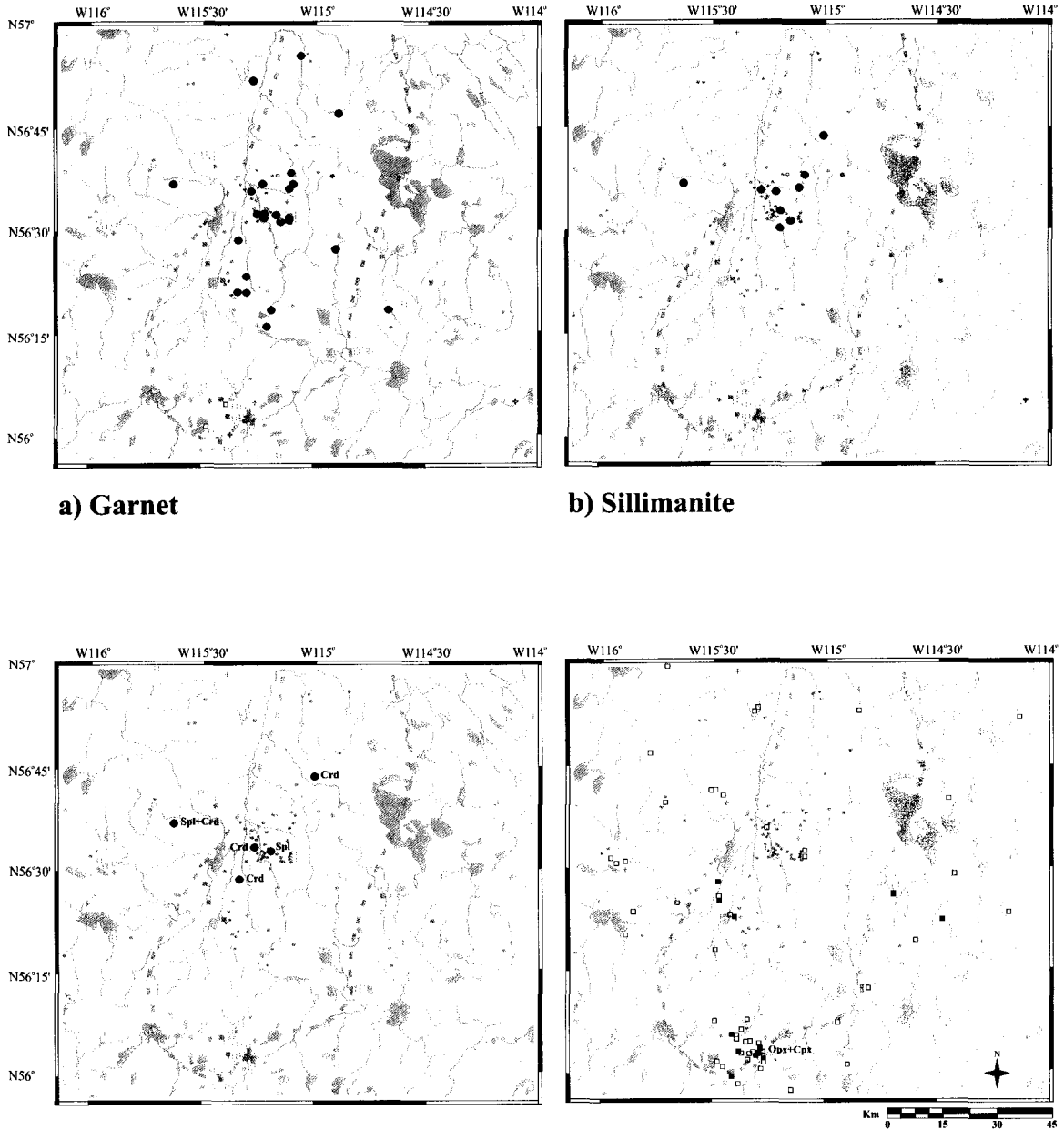

Figure 3. Distribution of garnet, sillimanite, spinel, cordierite, orthopyroxene, and clinopyroxene from available core throughout the Peerless Lake map area (NTS 84B). TMA represented by dashed elliptical outline (Burwash and Power, 1990). Basemap from Alberta Provincial Basemap (1997).

Garnet

Most garnet porphyroblasts are heavily fractured with fine-grained sericite, chlorite or muscovite infilling. Porphyroblasts are subhedral to anhedral, embayed or flattened, 0.2 to 2 mm poikiloblasts with randomly oriented sillimanite needles, anhedral quartz and rarely biotite and K-feldspar, spinel and few cordierite inclusions (Figure 4). Complex inclusion trails in large, embayed garnets are defined by swarms of sillimanite needles in one pelitic migmatite (861510) (Figure 2c, 4). A matrix of fine-grained, anhedral quartz and feldspar mortar, sparse biotite, sillimanite needles, and/or myrmekite often surrounds garnet as well as K-feldspar and cordierite porphyroblasts. In a pelitic migmatite (861510), fine sillimanite needles encrust both garnet and twinned cordierite porphyroblasts present within a matrix of perthite (Figure 2b). Some small (<0.3 mm), subhedral to euhedral garnet with little (sillimanite) to no inclusions and very little sillimanite crust, if present, occurs in the melanosome of pelitic migmatite. Garnet abundance varies from <5 to 20 vol% and is in some samples completely pseudomorphed by retrograde chlorite with biotite (B54-9, 4245b). A representative BSE image and composition map of garnet for Mg, Fe, Mn and Ca are found in Figure 5. Garnet porphyroblasts appear to be homogenous and unzoned except along fractures, but microprobe analyses indicate a slight variability between core and rim compositions (Table 2). Garnet core compositions range from $Gr_{1.6-4}$, Py_{3-25}, Alm_{65-92}, and Sp_{1-5} and confirm low grossular content. Garnet commonly occurs within the center of the TMA, as indicated by Figure 3a.

Sillimanite

Prismatic sillimanite ranges from <5 to ~20 vol % with <0.2–0.3 mm wide needles or fragments defining fabric, such as the matrix foliation in the melanosome of a pelitic migmatite (861510). Thin needles randomly swarm through large and embayed garnet porphyroblasts as inclusion trails (e.g. 861420, 861510) (Figure 4) or rim garnet or K-feldspar porphyroblasts (861510). Sillimanite is also found as inclusions in cordierite or appears retrograde, randomly oriented and surrounded by patchy red-brown biotite (861510). Sillimanite is present generally within the center of the TMA (Figure 3b).

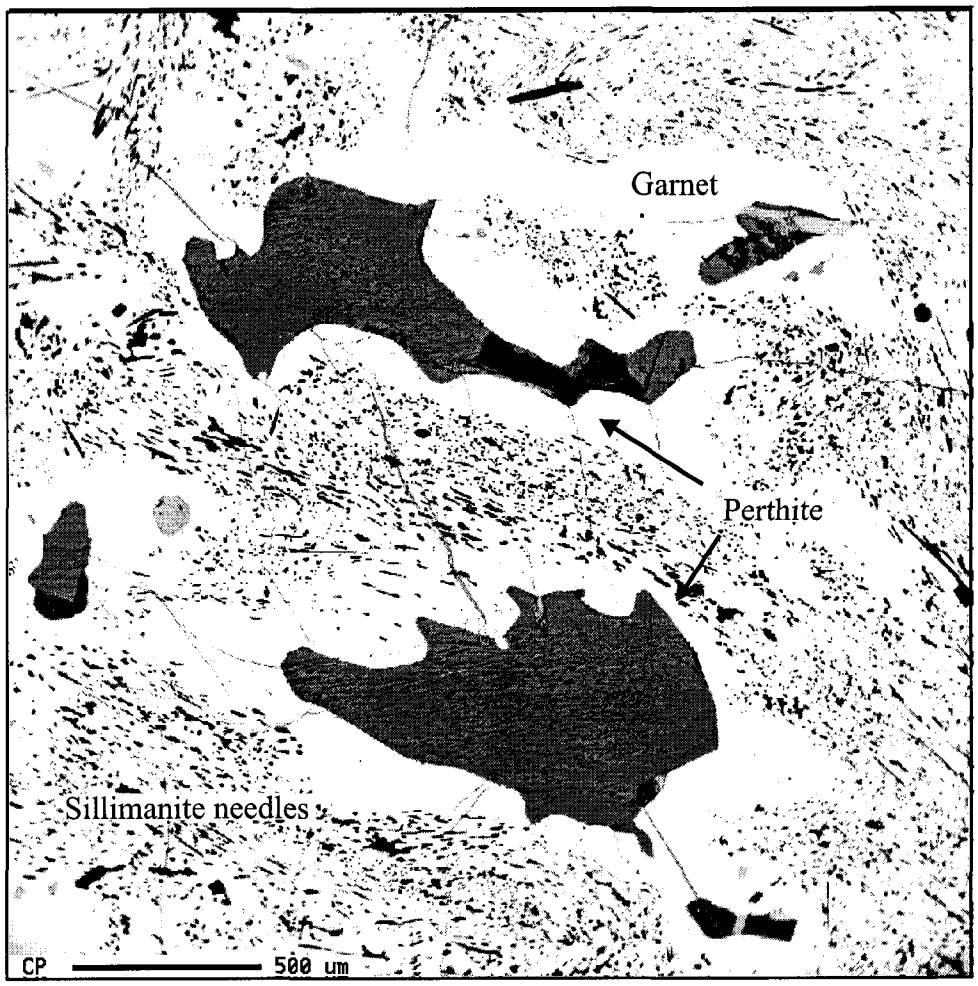

Figure 4. BSE image of perthite included within garnet porphyroblast from a pelitic migmatite (861510).

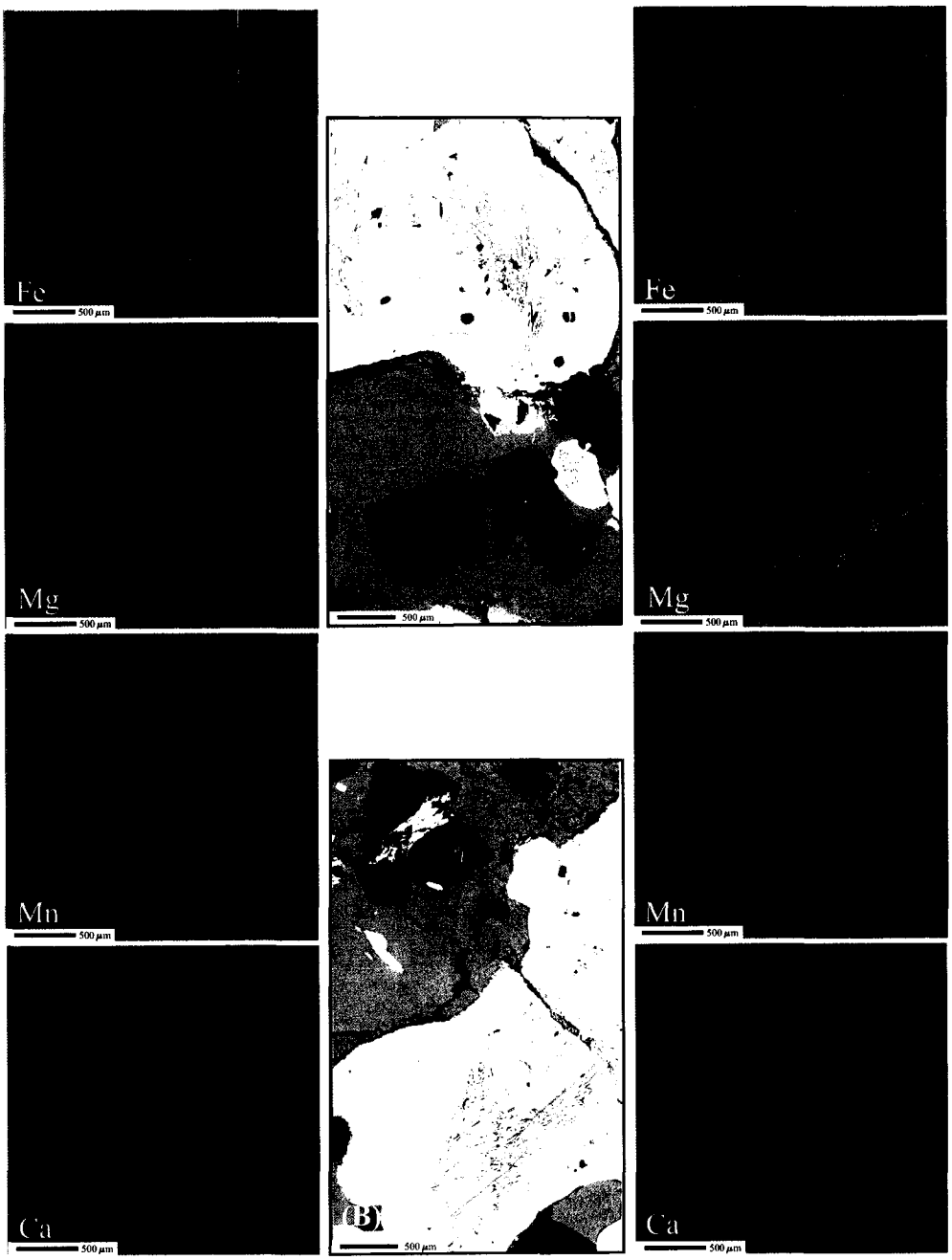

Figure 5. BSE and composition maps of two separate garnet-cordierite domains (A) and (B) from the melanosome of pelitic migmatite (861510).

Cordierite

Few cordierite-bearing cores are present dominantly within the center or along the western flank of the TMA (Figure 3c). The melanocratic band of a pelitic migmatite (861510) contains abundant dark blue cordierite in hand specimen and twinned porphyroblasts in thin section. Cordierite is absent in the leucosome of the same sample. Large (up to ~2 mm), subhedral to anhedral, cordierite porphyroblasts display excellent polysynthetic twinning (Figure 2b). Cordierite porphyroblasts are sometimes encrusted or rimmed by fine sillimanite needles or retrograde chlorite, poikiloblastic with sillimanite, biotite and spinel inclusions, infill garnet embayments or are included within garnet porphyroblasts. Another sample (4246) not used in this study due to a lack of garnet and sillimanite, contains sparse (<10 to 15 vol%) anhedral cordierite grains rimming or infilling embayments within K-feldspar porphyroblasts. Only slight pinnite alteration along grain boundaries or fractures is visible, except for unaltered cordierite in pelitic migmatite (861510). Biotite grain-size and abundance appears to decrease with the presence of cordierite. Dehydration melting may have produced cordierite and K-feldspar, as seen by cordierite included in or in contact with perthitic K-feldspar porphyroblasts (861510, 4246) and cordierite present in the matrix, likely formed along the prograde path by the KFMASH reactions:

$$Bt+Sil+Qtz = Crd+Kfs+L$$

$$Bt+Sil+Qtz = Grt+Crd+Kfs+L$$

(White et al., 2001; e.g. Mezger et al., 2001). In some places, cordierite is found in contact with embayed and resorbed garnets suggesting formation during decompression or heating by the reaction:

$$Grt+Sil+Qtz = Crd$$

(White et al., 2001; e.g. Mezger et al., 2001). Furthermore, randomly oriented fine-grained sillimanite (861510) in association with retrograded biotite growth could form as part of the retrograde reaction:

$$Grt+Kfs+Crd+melt = Bt+Sil$$

(White et al., 2001). The presence of retrograde biotite could imply temperature estimates derived from Grt-Bt thermometry represent disequilibrium temperatures (Spear and Florence, 1992).

Spinel

Dark green spinel (hercynite) of <10 vol% abundance and <0.5 mm in grain-size is only found in the melanocratic portion of a pelitic migmatite (861510) and in trace amounts in Spl-Sil-Bt gneiss (861190; 4-22-87-8W5) occurring with opaques in irregular or lobate forms. Spinel occurs as inclusions or in contact with K-feldspar, sillimanite, cordierite or garnet (Figure 2c). The presence of resorbed garnet grains in cordierite and garnet in contact with spinel (top of Figure 6) suggest the prograde spinel-forming reaction by decompression (or heating):

$$(Bt+)Grt+Sil+Qtz = Crd+Kfs+Spl+L$$

(White et al., 2001). Closer electron microprobe examination reveals sillimanite rims spinel (861510). The occurrence of sillimanite rims on some spinel grains, particularly spinel in contact with garnet (Figure 6), suggests the retrograde reaction by cooling (or compression):

$$Crd+Spl = Grt+Sil$$

(White et al., 2001; e.g. Mezger et al., 2001). Trace, anhedral dark green spinel occurs without garnet or cordierite in sample 861190, but near and in contact with sillimanite fragments and some biotite present in the matrix or as inclusions in garnet or K-feldspar. Otherwise coronas, retrograde reaction rims, or intergrowths of quartz or cordierite with spinel are not observed (e.g. Waters, 1991).

Orthopyroxene

Orthopyroxene (~10 to 15 vol%) is partially altered and fractured, subhedral to anhedral with <1 mm grains generally occurring in clusters. A sub-equigranular texture predominates where there is little to no (<5 to 15 vol%) fine-grained (<0.5 mm) biotite (860870, 860700) present. If present, very large (<6 mm) K-feldspar and heavily fractured, deformed, smaller (0.5-2 mm) orthopyroxene phenocrysts are wrapped by abundant coarse-grained biotite in the matrix suggestive of later deformation and formation of biotite possibly on the retrograde path (Kilpatrick and Ellis, 1992) (Figure 2f, 860770). Sample 860220 contain anhedral and slightly altered (<0.1-3 mm) clinopyroxene and orthopyroxene phenocrysts. Exsolution lamellae are not present in pyroxene. Retrograded charnockites contain approximately 5 to 20 vol% anhedral (<1

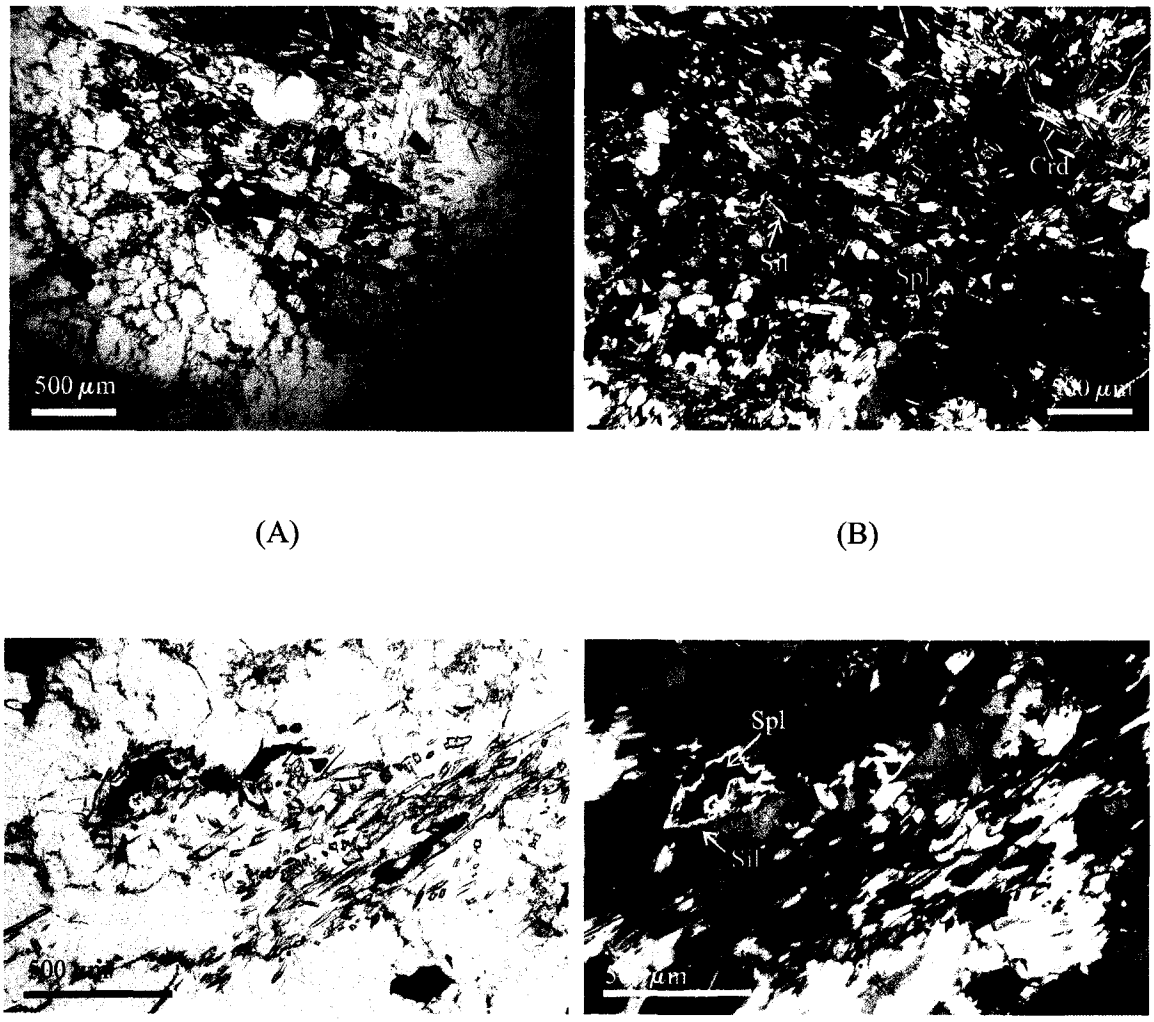

(A) (B)

Figure 6. Spinel rimmed by sillimanite from the melanosome of pelitic migmatite (861510). (A) plane polarized light (B) crossed polarized light.

mm) and heavily fractured, patchy or web-like serpentine. Blocky antiperthite (860640) and syntectonically recrystallized quartz is commonly observed with the latter suggestive of later deformation or overprinting.

Feldspar

Microcline porphyroblasts (up to 1.5cm), commonly poikilitic with inclusions of matrix minerals such as quartz or biotite, are widespread across the study area regardless of lithology. Burwash and Krupicka (1969) attributed this occurrence to younger metasomatism and recrystallization forming microcline porphyroblasts compared to older, 'relict', and deformed plagioclase found 'granulated' or 'crushed' as mortar in the matrix. K-feldspar porphyroblasts are commonly perthitic with few mesoperthite and antiperthite and are described following the classification scheme of Alling (1938). A third feldspar phase of albite lamellae was found in four samples (860970, 861790, 4248, 861750) and is characterized by plagioclase beads or strings wrapped by thin dark albite string tails, either oriented with or opposite to bead perthite (Figure 7a). Albite appears to curve around and not cut through plagioclase beads suggesting plagioclase lamellae exsolved before albite (Figure 7b). Extremely fine (<1 μm) strings or films exsolved between plagioclase bead and rod perthite are found oriented either in the opposite or a similar crystallographic direction to the larger lamellae throughout the grain (Figure 7c, d). Remaining perthitic samples indicate a range of lamellae textures including string, rod, and bead perthite up to 20 μm in width (Figure 7a-e, h). Deformed K-feldspar lamellae in some samples (Figure 7e) suggest some loss of K-feldspar from the bulk of the feldspar grains. Feldspar from a Sil-Bt-Crd-bearing gneiss (861590) consist of nearly equal amounts of plagioclase lamellae and potassium feldspar host, forming a mesoperthitic, ~15 μm thick texture of alternating bands throughout the grain (Figure 7f). Two samples of retrograded charnockite (860640, 860930) along the western flank of the TMA dominantly yield antiperthite with large (up to 50 μm), irregularly to blocky K-feldspar lamellae surrounded by a plagioclase-rich, lamellae-free area (Figure 7g).

The highest-grade mineral assemblage in the field area is from a pelitic migmatite (861510), which contains the assemblage Grt+Crd+Kfs(+Sil+Spl). This assemblage is diagnostic of granulite-facies conditions in pelitic bulk compositions. Evidence

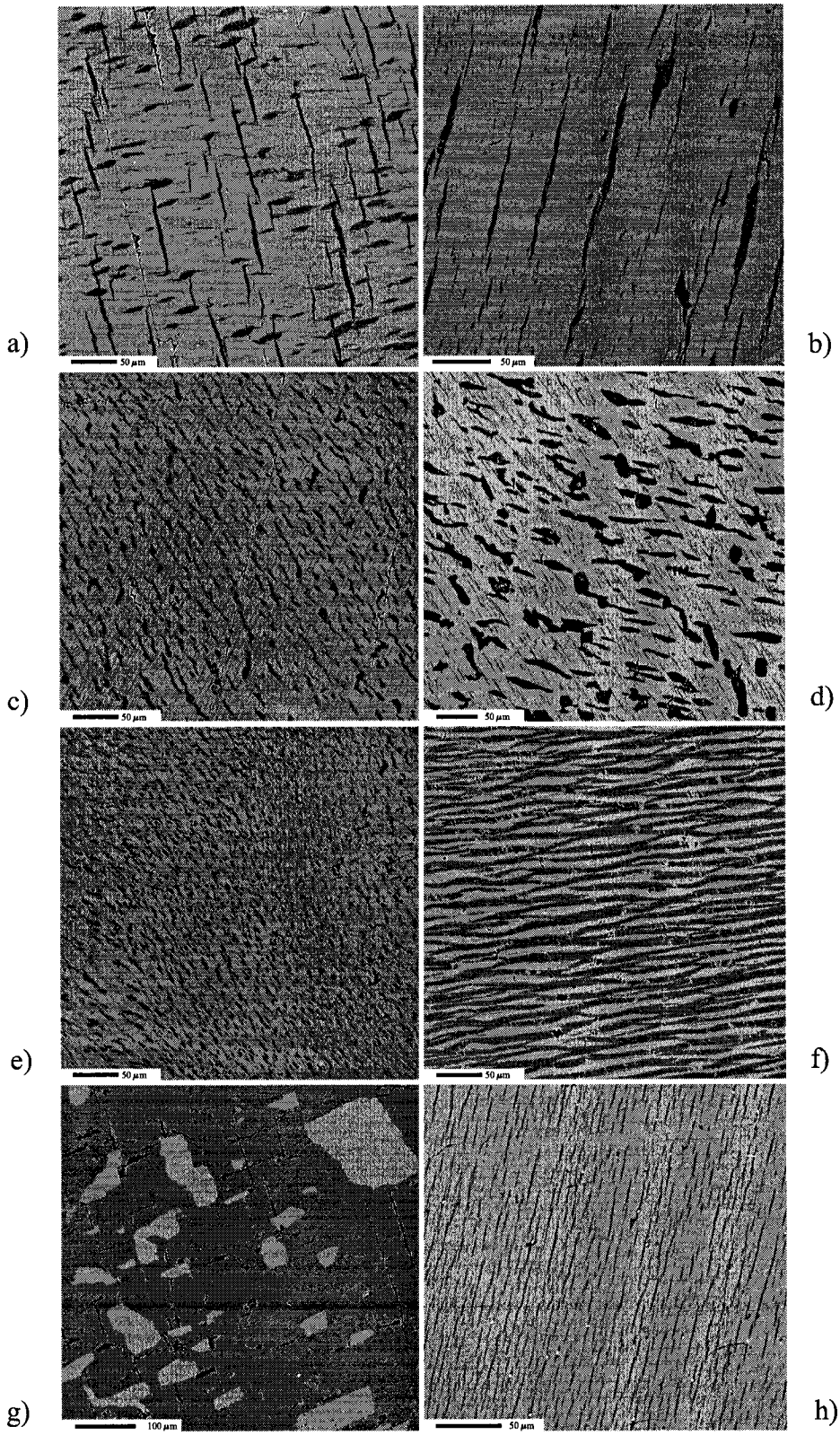

Figure 7. Representative BSE images of (a) 860970 string and rod perthite, (b) 861790 string perthite, (c) M34 rod perthite with few bead perthite, (d) 4035 bead and interlocking rod perthite, (e) 861740 bead, rod, and string perthite, (f) 861590 mesoperthite, (g) 860930 antiperthite, and (h) 4007k string perthite.

indicative of retrograde metamorphism comes from retrograde chlorite, muscovite, biotite, and chlorite pseudomorphs after garnet. Rimming of mineral phases such as spinel-quartz or spinel-cordierite is not observed, only rimming of spinel-sillimanite. The presence of the Grt-Crd-Kfs assemblage, combined with the absence of Ky and Opx-Sil assemblages constrains pressure-temperature conditions above ~750°C and below 10 kbars (White et al., 2001).

Analytical Procedure

Reintegrated Feldspar Thermometry

Available samples containing large and coarse perthite, mesoperthite or antiperthite were chosen for reintegrated feldspar thermometry. Samples with large grains bearing clear and distinct exsolution phases were selected from areas of dense drill core concentration, such as from the center of the map sheet near the Red Earth oil field, to optimize coverage across the TMA. Alteration, fractures, inclusions, and disequilibrium textures by way of mineral overgrowths or resorption along the rims within or surrounding the grains were avoided (Fuhrman and Lindsley, 1988). Feldspar grains with widely spaced fractures and deformed lamellae were used with caution. Although myrmekite is ubiquitous, this texture was avoided in all BSE images and feldspar compositions in such samples were carefully examined for consistency. Two feldspar grains meeting these requirements were petrographically chosen per sample. More feldspar grains were chosen if exsolution was heterogeneous across the grain. The compositions of host and lamellae feldspar were analyzed using the JEOL 8900 electron microprobe at the University of Alberta. Plagioclase and K-feldspar were measured with an accelerating voltage of 15 kV and beam current of 15 nA, with element standards presented in Table 5. A 3 to 4 μm focused beam measured host compositions whereas a 1 to <1 μm focused beam measured lamellae compositions. A minimum of two clear BSE images were acquired per grain, avoiding the grain boundary, pits or other imperfections, and a minimum of two host and lamellae compositions were analyzed per BSE image, dependent upon lamellae heterogeneity. Multiple quantitative analyses were checked for compositional consistency in order to determine an accurate reintegrated minimum temperature (Burwash et al., 2000a).

Table 5. Standard conditions for garnet, biotite, cordierite, plagioclase and K-feldspar for multiequilibria calculations and reintegrated feldspar thermometry.

Element	Garnet	Biotite	Cordierite	Plagioclase	K-Feldspar
Si	Kaersuitite Rvgar1	Kaersuitite Biotite	Osumilite	Plagioclase (Albite)	Sanidine
Al	Rvgar1	Rvgar1 Biotite	Plagioclase	Plagioclase	Orthoclase
Mg	Rvgar1 Pyrope	Biotite Hypersthene	Rvgar1	---------- (Osumilite)	Osumilite
Fe	Fayalite Osumilite Rvgar1	Fayalite Biotite	Rvgar1	Osumilite	Osumilite
Mn	Willemite	Willemite	Willemite	---------- (Willemite)	Willemite
Ca	Rvgar1 Kaersuitite	Kaersuitite	Rvgar1	Plagioclase	Plagioclase
Ti	Kaersuitite	Biotite Kaersuitite	Kaersuitite	----------	----------
Na	----------	Kaersuitite	Scapolite	Albite	Albite
K	----------	Calbiotite Biotite	Osumilite	Orthoclase (Sanidine)	Orthoclase
Ba	----------	----------	----------	Sanidine	----------
Cl	----------	Tugtupite	----------	----------	----------
F	----------	Caalbiotite Phlogopite	----------	----------	----------

( ) represents separate composition used for reintegrated feldspar thermometry

Two unique limitations between host and lamellae compositions were encountered. Firstly, film perthite (<1 μm), such as found by Kroll et al. (1993) and Raase (1998), are dispersed throughout the host of some samples (e.g. Figure 7c and d). To retain an average host composition, ten analyses were collected using a 10 μm beam for each BSE image to incorporate these dense films into the host rather than lamellae composition. Secondly, Ab-rich lamellae intertwine, rim and/or are oppositely oriented to the An-rich lamellae, such as documented by Kroll et al. (1993) (e.g. Figure 7a and b). Tracing by NIH *Image* (v. 1.0) estimated modal proportions of Ab-rich lamellae. The public domain NIH *Image* program was developed at the U.S. National Institute of Health and is available on the Internet at http://rsb.info.nih.gov/nih-image/. Although very fine film lamellae could not be accurately traced, large Ab-rich lamellae were traced if a separate BSE volume peak could not be distinguished. The minimal proportion of this third phase contributed only a slight change (<10°C) to reintegrated minimum temperatures.

Multiple analyses of lamellae and host were averaged per grain per sample to examine a detailed range in minimum temperatures. Modal proportions of host and lamellae were determined from BSE images. Using the level modify function within the area analysis component of the electron microprobe software, two to three distinct volume peaks of feldspar phases could be estimated. Volume percentage and normalized cation composition of feldspar phases were converted to reintegrated cation compositions by multiplication with a density ratio and the proportion of each feldspar component. Densities of feldspar phases were determined by interpolation between feldspar end-member densities given in Klein and Hurlbut, Jr. (1993). In addition to these determinations, calculation for a second, Ab-rich, lamellae were incorporated for four samples (860970, 861790, 4248, 861750) as follows: a) compositions of the host and Ca-rich lamellae were combined into a single host composition, then b) Ab-rich lamellae compositions were substituted for Ca-rich lamellae composition. If host and lamellae compositions did not define two or more distinguishable volume peaks then the graduated area analysis scale within the electron microprobe software was reduced and feldspar proportions were then visually estimated.

Minimum temperatures were primarily obtained using the solution model of Fuhrman and Lindsley (1988). This model utilizes Margules parameters derived from the

experimental database of Seck (1971), experimentally determined from activities of dehydrated ternary gels as starting materials at 650, 750, 825, and 900°C and 0.5, 1, and 2 kbars. Elkins and Grove (1990) based their calibration on experiments carried out using crystalline starting materials over a range of 600-900°C at 1-3 kbars. Reintegrated temperatures (Ab, An, Or) were graphically determined using the SOLVCALC 2.0 program (Wen and Nekvasil, 1994). Fuhrman and Lindsley (1988) assume an accuracy of ±2 mol% feldspar composition and account for complete ternary solid solution between Ab-Or and Ab-An joins but limited solid solution along the An-Or join. This generally results in a temperature error range of ±50°C (Wen and Nekvasil, 1994; Fuhrman and Lindsley, 1988). Temperature estimates are compared with those given by the Lindsley and Nekvasil (1989) (LN) and Elkins and Grove (1990) (EG) solution models. The EG calibration typically gives temperatures that are 50-90°C higher than the FL calibration whereas the LN calibration gives temperatures that are similar to or slightly lower (5-45°C) than the FL calibration.

Net Transfer and Fe-Mg Exchange Thermobarometry

Reconnaissance for suitable assemblages included criteria such as lack of alteration, large and inclusion-free garnet, and a broad geographic distribution across the study area. Several samples met these criteria but fine-grained plagioclase mortared in the matrix was difficult to identify optically. The high-grade, deformed nature and variable grain size of these rocks were difficult to assess in terms of mineral assemblage equilibration. Up to four garnets were chosen per section and compositional maps of Mg, Ca, Fe, and Mn were made of each grain to check for compositional zonation (e.g. Figure 5). Five analyses of garnet, plagioclase, biotite, and cordierite cores and rims were obtained, avoiding fractures and pits. Although the largest grains were chosen, several plagioclase and biotite grains were still too fine-grained to acquire more than five analyses each. Operating conditions include a focused beam width of 5 μm, accelerating voltage of 15 kV and beam current of 20 nA (15 nA for some biotite compositions). Garnet, plagioclase, biotite, and cordierite domain compositions were averaged for each sample (Table 2 and 3). Garnet rim compositions vary slightly from core compositions likely reflecting compositional re-equilibration of garnet rims on cooling. Therefore core

compositions were used for pressure-temperature determinations. Element standards used for analysis of garnet, plagioclase, biotite, and cordierite are given in Table 5.

Pressure-temperature determinations were obtained by using the internally consistent thermodynamic data set TWEEQU v. 2.02 (Thermobarometry With Estimation of EQUilibration state; Berman, 1991). These temperature estimates are compared to minimum temperatures derived from reintegrated feldspar thermometry. Non-ideal interactions of garnet (Mg-Fe-Ca-Mn) and cordierite (Mg-Fe), and biotite non-ideal mixing corrections (Mg-Fe-Ti-Al) are from Berman and Aranovich (1996) whereas plagioclase (Ca-Na-K) is taken from Fuhrman and Lindsley (1988). P-T paths were not constrained due to a lack of poikiloblastic biotite or plagioclase inclusion trails and a lack of growth zoning of garnet porphyroblasts (e.g. Spear and Selverstone, 1983).

Results

A summary of reintegrated feldspar compositions and temperatures is given in Table 6. Minimum temperature estimates of individual feldspar grains from a given sample were within 50°C. Therefore Figure 8 plots the average minimum reintegrated temperature per sample, with the exception of the large minimum temperature range of Bt-Grt gneiss (861630) (Figure 8d). Reintegrated feldspar temperatures were calculated at a pressure of 7.0 kbars using the solution models of Fuhrman and Lindsley (1988), Lindsley and Nekvasil (1989) and Elkins and Grove (1990). Variation in pressure had a minimal effect in calculation of the reintegrated feldspar temperatures. The celsian (Ba-rich) component was minimal and averaged <0.03 mol% therefore was not included in reintegrated temperatures estimates. Feldspar temperatures are reported for a total of 35 core samples and includes data from Ranger (2000). The P-T positions mineral equilibria calculated with TWEEQU (Berman, 1991) are given in Table 7 and Figure 9 for pelitic migmatite (861510). Figure 10 presents reintegrated feldspar temperature and pressure estimates within the Peerless Lake map sheet (NTS 84B).

Table 6. Results of reintegrated feldspar thermometry with exsolution texture and reintegrated compositions of lamellae and host.

Sample #		K-feldspar			Plagioclase			Mode-Vol. %		Mode-Wt. %		Reintegrated Composition			FL (°C)	FL Avg	EG (°C)	LN (°C)
		X_{Ca}	X_{Na}	X_K	X_{Ca}	X_{Na}	X_K	Kfs	Pl	Kfs	Pl	An	Ab	Or				
Granitoid			***Kfs + Pl ± Bt ± Grt***															
M34-b	P	0.0083	0.2209	0.7707	0.1804	0.8101	0.0094	87.10	12.90	0.8480	0.1520	0.0345	0.3105	0.6550	840	835	880	820
M34-c	P	0.0066	0.2105	0.7829	0.1778	0.8134	0.0088	87.55	12.45	0.8522	0.1478	0.0319	0.2996	0.6685	830		870	800
4035-a	P	0.0062	0.1625	0.8313	0.1690	0.8232	0.0078	81.65	18.35	0.7942	0.2058	0.0397	0.2985	0.6618	860	840	900	840
4035-b	P	0.0030	0.0998	0.8972	0.1516	0.8412	0.0071	81.55	18.45	0.7926	0.2074	0.0338	0.2536	0.7126	825		880	800
860550-b	P	0.0007	0.0564	0.9429	0.2590	0.7211	0.0199	95.10	4.90	0.9182	0.0818	0.0218	0.1107	0.8674	730	730	800	725
860970-a	P	0.0010	0.0455	0.9536	0.2550	0.7350	0.0100	92.40	7.60	0.8919	0.1081	0.0284	0.1200	0.8516	780		875	775
w Ab		0.0284	0.1200	0.8516	0.0076	0.9839	0.0085	95.40	4.60	0.9366	0.0634	0.0271	0.1747	0.7982	770	770	840	775
860970-b	P	0.0006	0.0500	0.9495	0.2483	0.7429	0.0088	92.90	7.10	0.8971	0.1029	0.0261	0.1213	0.8527	760		850	760
w Ab		0.0261	0.1213	0.8527	0.0100	0.9819	0.0082	96.90	3.10	0.9511	0.0489	0.0253	0.1634	0.8114	770		840	750
4240-a	P	0.0005	0.0592	0.9403	0.1870	0.7824	0.0306	91.50	8.50	0.8871	0.1129	0.0216	0.1408	0.8376	730	750	800	730
4240-b	P	0.0002	0.0409	0.9589	0.1926	0.7945	0.0130	88.60	11.40	0.8580	0.1420	0.0275	0.1479	0.8245	780		850	710
			Kfs + Pl + Bt + Hbl															
861810-a	P	0.0010	0.0691	0.9299	0.3501	0.6326	0.0173	96.40	3.60	0.9266	0.0734	0.0266	0.1104	0.8629	775	775	870	770
Pelitic Gneiss			***Crd + Kfs + Bt ± Sil ± Grt ± Spl ± Pl***															
**861510-a	P	0.0012	0.0776	0.9212	0.1668	0.8018	0.0314	84.40	15.60	0.8195	0.1805	0.0311	0.2083	0.7606	805	790	870	790
**861510-b	P	0.0009	0.0828	0.9163	0.1220	0.8023	0.0756	82.10	17.90	0.8000	0.2000	0.0251	0.2267	0.7482	785		820	760
*861510-a	P	0.0039	0.1552	0.8409	0.2333	0.7525	0.0142	96.95	3.05	0.9396	0.0604	0.0177	0.1913	0.7910	730	725	770	700
*861510-b	P	0.0025	0.1370	0.8605	0.2573	0.7319	0.0108	96.30	3.70	0.9316	0.0684	0.0199	0.1777	0.8024	725		780	700
861590-a	M	0.0002	0.0503	0.9495	0.1064	0.8882	0.0054	44.70	55.30	0.4349	0.5651	0.0602	0.5238	0.4160	915	905	920	880
861590-b	M	0.0008	0.0584	0.9409	0.0994	0.8939	0.0067	59.00	41.00	0.5743	0.4257	0.0428	0.4140	0.5432	890		900	860
			Sil ± Grt + Bt + Pl + Kfs															
861420-a	P	0.0015	0.1043	0.8942	0.1275	0.8629	0.0096	86.75	13.25	0.8442	0.1558	0.0211	0.2225	0.7564	750	750	800	730
861420-c	P	0.0021	0.1265	0.8713	0.1395	0.8513	0.0093	88.80	11.20	0.8641	0.1359	0.0208	0.2250	0.7542	750		800	730
3226-a	P	0.0007	0.0680	0.9312	0.1559	0.8270	0.0171	91.50	8.50	0.8885	0.1115	0.0180	0.1527	0.8293	700	700	775	700
3226-b	P	0.0009	0.0713	0.9279	0.1533	0.8335	0.0132	91.10	8.90	0.8847	0.1153	0.0184	0.1592	0.8224	700		775	700
4239-c	P	0.0007	0.0663	0.9329	0.1185	0.8443	0.0371	89.65	10.35	0.8726	0.1274	0.0157	0.1655	0.8188	700	710	740	680
4239-a	P	0.0008	0.0602	0.9390	0.1468	0.8387	0.0145	88.85	11.15	0.8629	0.1371	0.0208	0.1669	0.8123	730		800	720
86110-a-	P	0.0021	0.1327	0.8652	0.1524	0.8388	0.0089	89.60	10.40	0.8714	0.1286	0.0215	0.2235	0.7551	760	750	800	740
86110-b-	P	0.0019	0.1077	0.8904	0.1432	0.8486	0.0083	89.55	10.45	0.8708	0.1292	0.0201	0.2034	0.7765	750		800	725
Gneiss			***Bt + Kfs + Pl ± Grt***															
860670-a	P	0.0005	0.0367	0.9628	0.0078	0.9778	0.0143	94.75	5.25	0.9265	0.0735	0.0010	0.1058	0.8931	<700	<700	<700	<700
860670-b	P	0.0003	0.0355	0.9642	0.0050	0.9847	0.0103	95.70	4.40	0.9359	0.0641	0.0006	0.0964	0.9030	<700		<700	<700
860880-d	P	0.0058	0.1499	0.8443	0.3011	0.6609	0.0381	95.05	4.95	0.9184	0.0816	0.0299	0.1916	0.7785	800	790	860	780
860880-c	P	0.0054	0.1501	0.8445	0.3040	0.6751	0.0209	95.60	4.40	0.9232	0.0768	0.0283	0.1904	0.7812	790		850	780
861520-e	A	0.0017	0.0858	0.9125	0.2942	0.6912	0.0146	9.75	90.25	0.0940	0.9060	0.2667	0.6343	0.0990	820	730	780	810
861520-a	P	0.0021	0.1269	0.8710	0.2413	0.7216	0.0372	95.60	4.40	0.9259	0.0741	0.0199	0.1709	0.8092	725		800	710
861520-b	P	0.0014	0.1260	0.8726	0.3032	0.6785	0.0183	97.05	2.95	0.9364	0.0636	0.0206	0.1611	0.8183	730		800	720
861630-a	P	0.0009	0.0612	0.9379	0.1687	0.8120	0.0193	86.60	13.40	0.8402	0.1598	0.0277	0.1812	0.7911	780		850	770
861630-b	P	0.0008	0.0627	0.9365	0.1625	0.8138	0.0238	91.10	8.90	0.8843	0.1157	0.0195	0.1496	0.8309	710		780	700
861630-c	P	0.0001	0.0598	0.9401	0.1677	0.8067	0.0256	88.40	11.60	0.8578	0.1422	0.0240	0.1660	0.8100	760		825	750
861740-a	P	0.0011	0.0558	0.9432	0.2256	0.7570	0.0174	91.65	8.35	0.8864	0.1136	0.0266	0.1354	0.8380	770	785	850	770
861740-c	P	0.0003	0.0643	0.9354	0.2346	0.7562	0.0092	89.50	10.50	0.8652	0.1348	0.0319	0.1576	0.8105	800		900	800
861750-b	P	0.0040	0.1477	0.8483	0.2608	0.7291	0.0101	95.70	4.30	0.9259	0.0741	0.0230	0.1908	0.7862	750	740	800	740
w Ab	P	0.0230	0.1908	0.7862	0.0043	0.9872	0.0084	98.95	1.05	0.9729	0.0271	0.0225	0.2124	0.7651	750		800	740
861750-d	P	0.0019	0.1056	0.8925	0.2448	0.7466	0.0087	95.65	4.35	0.9251	0.0749	0.0201	0.1536	0.8263	725		800	720
w Ab	P	0.0201	0.1536	0.8263	0.0039	0.9878	0.0083	99.25	0.75	0.9748	0.0252	0.0197	0.1747	0.8057	725		780	700
861790-a	P	0.0003	0.0485	0.9512	0.2157	0.7682	0.0161	94.40	5.60	0.9133	0.0867	0.0189	0.1110	0.8701	710	700	800	700
w Ab	P	0.0189	0.1110	0.8701	0.0108	0.9777	0.0115	98.30	1.70	0.9641	0.0359	0.0186	0.1421	0.8393	700		780	700
861790-b	P	0.0003	0.0534	0.9463	0.1873	0.8016	0.0111	96.00	4.00	0.9301	0.0699	0.0133	0.1057	0.8810	670		700	<700
w Ab	P	0.0133	0.1057	0.8810	0.0015	0.9681	0.0304	98.85	1.15	0.9699	0.0301	0.0130	0.1317	0.8553	670		700	<700
4248-a	P	0.0016	0.0599	0.9385	0.2013	0.7806	0.0181	90.60	9.40	0.8775	0.1225	0.0261	0.1481	0.8258	760	750	840	750
w Ab		0.0261	0.1481	0.8258	0.0140	0.9610	0.0250	99.60	0.40	0.9784	0.0216	0.0258	0.1657	0.8085	760		830	750
4248-b	P	0.0012	0.0631	0.9357	0.2246	0.7615	0.0139	93.95	6.05	0.9088	0.0912	0.0215	0.1268	0.8517	740		800	725
w Ab		0.0215	0.1268	0.8517	0.0152	0.9761	0.0086	99.00	1.00	0.9712	0.0288	0.0214	0.1512	0.8274	740		800	725
			Kfs + Pl ± Bt ± Hbl ± Chl															
4007k-d	P	0.0020	0.1206	0.8773	0.3213	0.6690	0.0097	93.40	6.60	0.9001	0.0999	0.0340	0.1754	0.7906	810	800	900	800
4007k-c	P	0.0007	0.0755	0.9239	0.2603	0.7284	0.0113	92.90	7.10	0.8971	0.1029	0.0274	0.1426	0.8300	770		850	770
861800-a	P	0.0000	0.0516	0.9484	0.3297	0.6588	0.0115	95.80	4.20	0.9212	0.0788	0.0260	0.0994	0.8746	775	795	860	760
861800-b	P	0.0010	0.0516	0.9474	0.3350	0.6546	0.0105	94.50	5.50	0.9085	0.0915	0.0316	0.1067	0.8617	810		900	800
Charnockite			***Opx + Kfs + Pl***															
860700-a	P	0.0086	0.1060	0.8853	0.4981	0.4889	0.0130	98.40	1.60	0.9398	0.0602	0.0381	0.1291	0.8328	830	830	950	825
860870-d	P	0.0056	0.0651	0.9292	0.4708	0.5122	0.0170	94.80	5.20	0.9057	0.0943	0.0495	0.1073	0.8432	900	890	1040	900
860870-b	P	0.0043	0.0680	0.9277	0.4878	0.4818	0.0304	97.00	3.00	0.9261	0.0739	0.0400	0.0986	0.8614	870		980	850
			Bt +Kfs + Pl															
860070-a	P	0.0050	0.1201	0.8749	0.3942	0.5915	0.0143	97.80	2.20	0.9392	0.0608	0.0286	0.1488	0.8226	780	780	860	775
860200-c	A	0.0030	0.1245	0.8725	0.3198	0.6676	0.0126	19.30	80.70	0.1860	0.8140	0.2609	0.5666	0.1725	950		1000	955
860200-b	P	0.0057	0.1920	0.8023	0.3059	0.6846	0.0095	96.05	3.95	0.9282	0.0718	0.0272	0.2274	0.7453	790	790	840	770
860200-d	P	0.0051	0.1766	0.8183	0.3114	0.6676	0.0210	95.95	4.05	0.9268	0.0732	0.0275	0.2125	0.7599	790		850	770
860380-a	P	0.0023	0.1072	0.8904	0.3449	0.6408	0.0143	96.50	3.50	0.9286	0.0714	0.0268	0.1453	0.8279	770	760	850	760
860380-b	P	0.0024	0.0810	0.9166	0.3508	0.6373	0.0119	97.50	2.50	0.9372	0.0628	0.0243	0.1159	0.8598	750		840	750
860530-b	P	0.0010	0.1117	0.8874	0.2975	0.6871	0.0154	96.40	3.60	0.9300	0.0700	0.0217	0.1519	0.8263	740	740	800	725
860530-a	P	0.0006	0.0720	0.9274	0.3034	0.6853	0.0113	96.40	3.60	0.9287	0.0713	0.0222	0.1157	0.8621	740		800	725
860570-a	P	0.0120	0.1600	0.8280	0.4928	0.4940	0.0132	96.95	3.05	0.9276	0.0724	0.0469	0.1842	0.7690	870	860	975	870
860570-c	P	0.0125	0.1434	0.8441	0.4929	0.4825	0.0246	97.30	2.70	0.9308	0.0692	0.0457	0.1669	0.7875	860		960	860
860570-d	P	0.0055	0.1004	0.8941	0.4824	0.5001	0.0175	97.30	2.70	0.9298	0.0702	0.0390	0.1285	0.8325	840		960	840
860640-a	A	0.0024	0.0817	0.9159	0.3296	0.6561	0.0143	15.25	84.75	0.1468	0.8532	0.2816	0.5718	0.1467	920	925	970	900
860640-c	A	0.0023	0.0787	0.9189	0.3241	0.6656	0.0103	16.20	83.80	0.1559	0.8441	0.2740	0.5740	0.1520	930		970	920
860930-a	A	0.0019	0.0840	0.9141	0.3179	0.6684	0.0137	28.40	71.60	0.2735	0.7265	0.2315	0.5085	0.2600	1035	1015	1105	1025/1040
860930-c	A	0.0030	0.0827	0.9144	0.3243	0.6609	0.0148	21.50	78.50	0.2070	0.7930	0.2578	0.5412	0.2010	990		1045	975/990
861280-a	P	0.0005	0.0754	0.9242	0.2216	0.7534	0.0250	94.95	5.05	0.9191	0.0809	0.0184	0.1302	0.8514	700	740	775	700
861280-b	P	0.0006	0.0736	0.9257	0.2349	0.7515	0.0136	93.10	6.90	0.9003	0.0997	0.0240	0.1412	0.8348	750		825	750
861280-c	P	0.0009	0.0774	0.9217	0.2303	0.7532	0.0165	92.75	7.25	0.8973	0.1027	0.0245	0.1468	0.8287	750		825	750
861360-b	P	0.0031	0.0936	0.9033	0.2818	0.7074	0.0108	92.60	7.40	0.8938	0.1062	0.0327	0.1588	0.8085	800	800	900	800
861360-d	P	0.0024	0.0928	0.9048	0.2602	0.7252	0.0146	92.30	7.70	0.8919	0.1081	0.0302	0.1612	0.8086	800		875	780
			Bt +Pl + Hbl															
860830-b	P	0.0010	0.0769	0.9220	0.3009	0.6809	0.0182	95.20	4.80	0.9176	0.0824	0.0257	0.1267	0.8476	760	780	850	760
860830-c	P	0.0021	0.0904	0.9075	0.3253	0.6530	0.0217	95.30	4.70	0.9178	0.0822	0.0287	0.1367	0.8346	780		870	775

*Calculated at pressure = 7 kbars for the following ternary solution models: FL = Fuhrman and Lindsley (1988), EG = Elkins and Grove (1990), LN = Lindsley and Nekvasil (1988). Exsolution textures are A = antiperthite, M = mesoperthite, P = perthite. * from leucosome, ** from perthite inclusion in garnet porphyroblast from melanosome, w Ab = calculated with Ab-rich lamellae component*

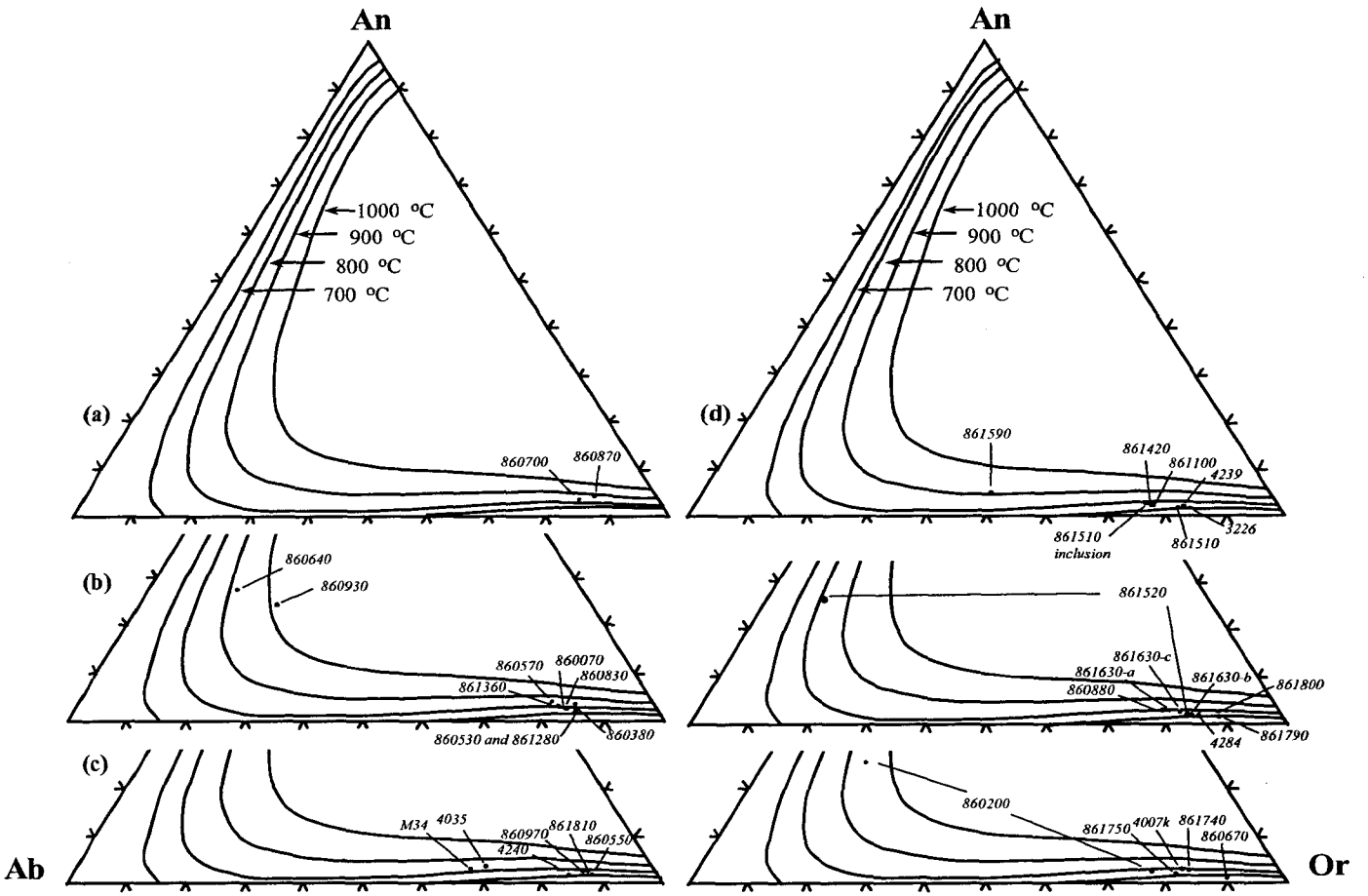

Figure 8. Average minimum temperatures from reintegrated feldspar thermometry plotted upon isotherms calculated from the Fuhrman and Lindsley (1988) solution model for (a) charnockite, (b) retrograded charnockite, (c) granite, and (d) gneissic cores. Average minimum temperatures calculated at a pressure of 7.0 kbars.

Table 7. P-T estimates for Fe-Mg exchange (Grt-Crd) and net transfer (GASP and Grt-Crd) thermobarometry.

	GASP	Grt-Crd	
	P	**P**	**T**
Sample #	(kbars)	(kbars)	(°C)
Grt + Bt + Pl + Qtz (Sil absent)			
B54-9	6.3*	*calculated to Reint. Fspar T of 800° C*	
861150	9.7*		
860790	9.4*		
860600	8.1*		
861450	8.9*		
860880	6.9*		
Grt + Bt + Pl + Sil + Qtz			
861380	5.4		
3226	7.2		
861100	7.8		
861420	5.9		
4419	7.9		
[1] 4419	6.9		
861510 (leucosome)	6.4		
Grt + Crd + Sil + Qtz			
861510 (melanosome)		6.2	740
		6.2 - 7.0	*at 800° C*

[1] *plagioclase and biotite inclusions in garnet*

* *represents maximum pressures*

GASP ± 3 kbar
Grt + Crd + Sil + Qtz ± 1 kbar

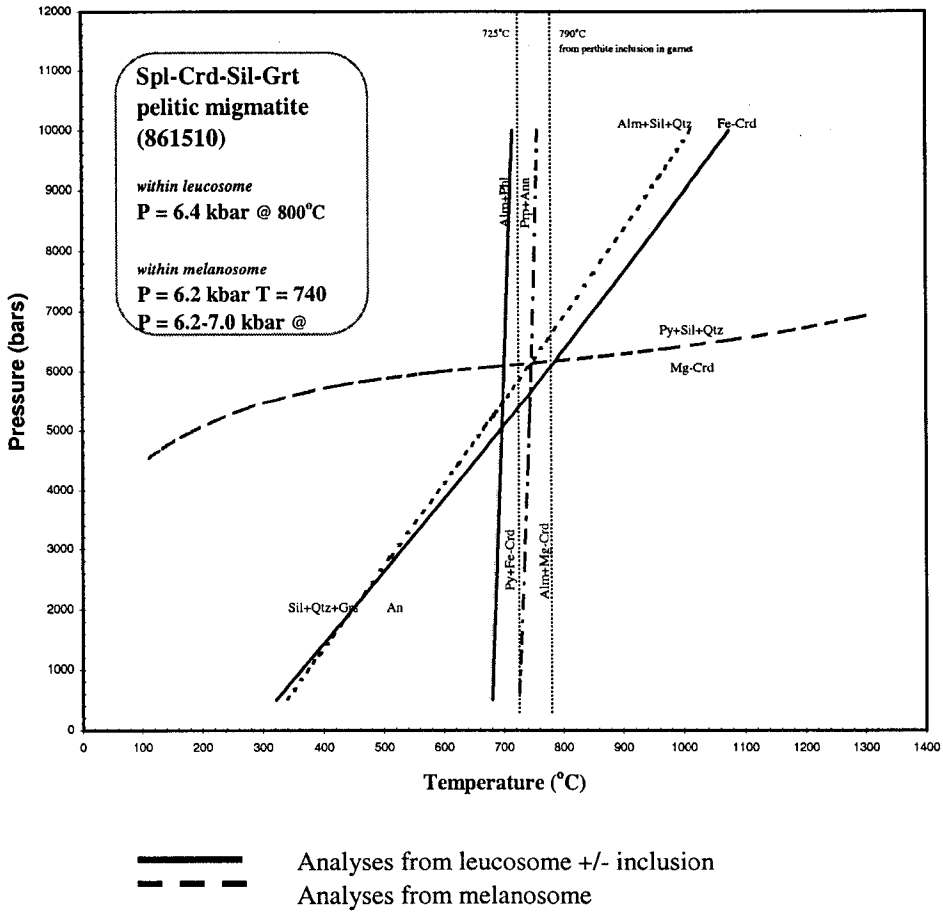

Figure 9. P-T estimates for pelitic migmatite (861510) from Grt-Bt, GASP and Grt-Crd equilibria calculated simultaneously by TWEEQU (Berman, 1991) to produce lines of K_{eq} using average chemical compositions. Dashed vertical lines indicate available minimum feldspar temperatures. Legend indicates results from leucosome and melanosome portion.

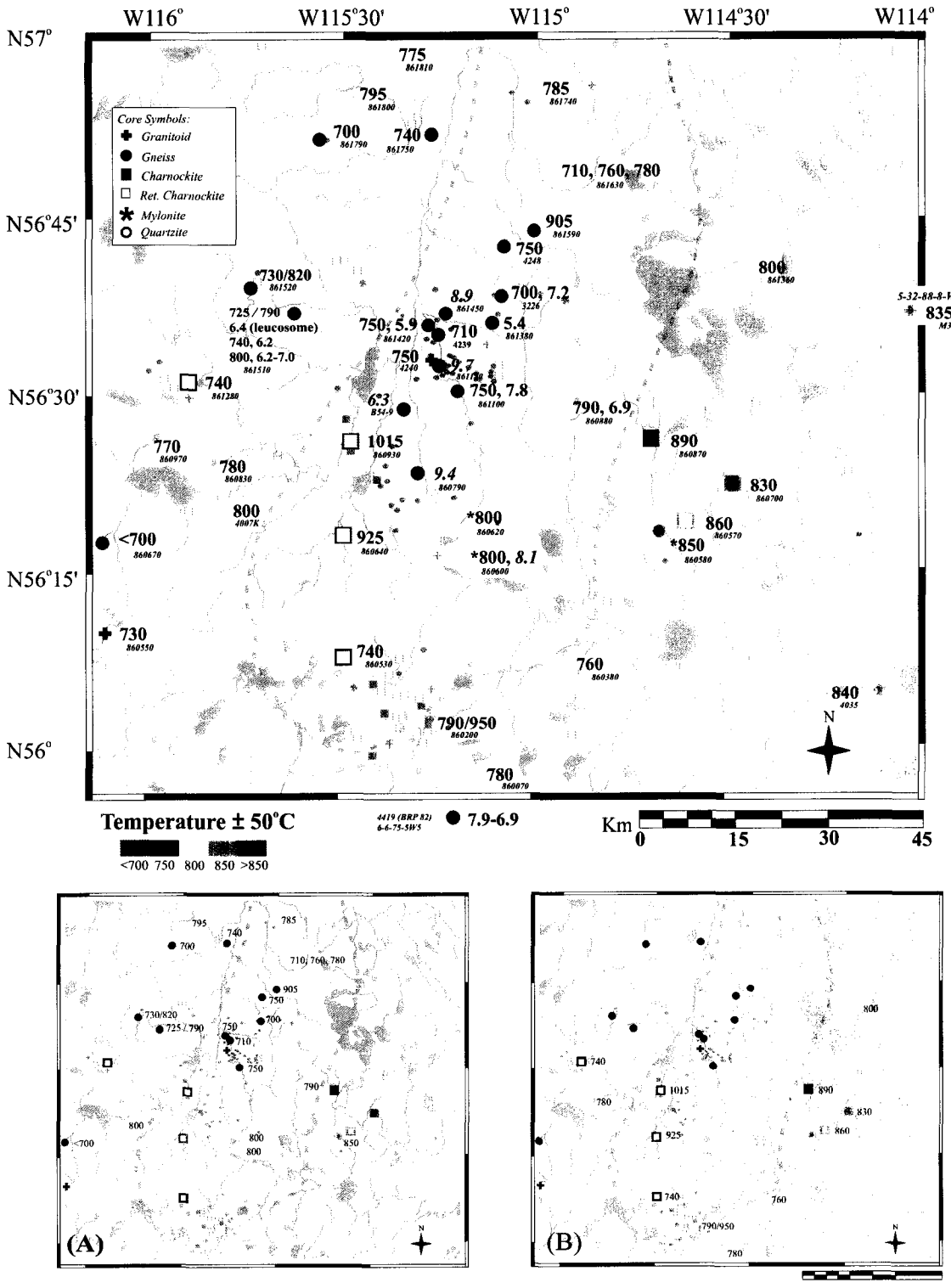

Figure 10. Pressure and temperature distribution in Peerless lake map sheet (NTS 84B). Minimum reintegrated feldspar temperatures are colored <800°C blue and >800°C yellow to red. Minimum temperatures as shown for (A) gneiss and (B) charnockite. * from Burwash et al. (2000a). Pressure estimates (including *maximum pressures*) are recalculated to an average of 800°C. Dashed outline is the TMA (Burwash and Power, 1990). Sample numbers are beneath each temperature and pressure determination. Basemap from Alberta Provincial Basemap (1997).

Garnet-Biotite Fe-Mg Exchange Thermometry

Compared to the predicted range of P-T conditions indicated by mineral assemblages (>750°C and <10 kbars; White et al., 2001), Grt-Bt temperatures suggest extensive re-equilibration of mineral phases (biotite and garnet) upon slow cooling. Temperatures derived by Grt-Bt Fe-Mg exchange thermometry are below 700°C with most temperatures below 600°C. These estimates are up to and/or greater than 100°C lower than the lowest minimum ternary feldspar estimates and are too low to be consistent with the stability of the Kfs-Sil assemblage or the garnet-Crd-K-feldspar assemblage (White et al., 2001). The low Grt-Bt temperatures suggest that either the biotite is of retrograde origin or the primary biotite has undergone extensive Fe-Mg exchange with other ferromagnesian phases upon cooling. A more accurate representation of temperature conditions of the RGD are likely reflected by an estimated 800°C, or possibly up to 900°C, metamorphic temperature from reintegrated feldspar thermometry presented below.

Garnet-Aluminosilicate-Plagioclase (GASP) Net Transfer Barometry

The GASP equilibrium indicates pressure of 5.4 to 7.8 kbar (calculated at 800°C) in sillimanite-bearing samples and 6.3 to 9.7 kbar in sillimanite-absent samples; the latter must be taken as maximum estimates of pressure (Table 7). Because the degree of equilibration between garnet core and matrix plagioclase compositions cannot be clearly determined, these pressure estimates may not be an accurate reflection of conditions experienced by these rocks (e.g. Spear, 1995). Therefore these pressure estimates should only be used for comparison with estimates determined by garnet-cordierite net-transfer equilibria in the pelitic migmatite (861510). Spatially, pressures are clustered within the TMA according to mineralogy and prevent a detailed broad scale characterization of pressure variations. Due to a lack of mineral assemblages for thermobarometry, a Sil-Grt-Bt gneiss (4419) southeast of the Peerless Lake map sheet (6-6-75-5w5) was examined because of the presence of a single occurrence of plagioclase and biotite inclusions within a garnet porphyroblast (Table 7). Pressure estimates recorded from this sample range from 6.9 to 7.9 kbars

Spl-Crd-Sil-Grt-bearing Pelitic Migmatite (861510)

Two minimum reintegrated feldspar temperatures were calculated from a Spl-Crd-Sil-Grt-bearing pelitic migmatite (861510) west of the TMA. Perthite textures for this sample ranged from small (2-10 μm) bead lamellae from the Grt-bearing leucosome to coarse rod lamellae from perthite inclusions within a garnet porphyroblast from the Spl-Crd-Sil-Grt-bearing melanosome (Figure 4). Average FL minimum temperatures ranged from 725°C in the leucosome to 790°C in the melanosome.

Only sample 861510 allowed for the calculation of more than two linearly independent equilibria. P-T conditions were constrained from this sample by analysis of Fe-Mg and net transfer equilibria involving Grt, Crd, Bt, Sil, Pl and Qtz. Very little biotite was present in section but biotite included within a garnet porphyroblast from the leucosome portion was analyzed (Table 2) and yielded a low temperature. The best temperature constraint was provided by garnet and cordierite of the melanosome portion at 740°C, which agrees well within the range of reintegrated feldspar temperatures obtained for this sample (725 to 790°C) (Figure 9). Grt-Crd equilibria indicate a pressure of 6.2 kbars. Intersection of an average reintegrated feldspar temperature estimate of 800°C with GASP equilibria from the leucosome and Mg-Crd-Grt and Fe-Crd–Grt equilibria from the melanosome yields a well-constrained pressure range of 6.2 to 7.0 kbars, which suggests this mineral assemblage is near equilibrium. Therefore P-T conditions yielded from pelitic migmatite range from 6.2 to 7.0 ± 1 kbars and a minimum of 740 to 800 ± 50°C (e.g. Kohn and Spear, 1991).

Sil±Bt±Crd±Grt-bearing Pelitic Gneiss (861590, 4239, 3226, 86110, 861420)

Mesoperthite occurs in a Sil-Bt-Crd-bearing gneiss (861590) from the north-central portion of the TMA. Host and lamellae compositions formed distinct modal peak proportions and yielded an average FL temperature of 905°C. Sil±Bt±Grt-bearing gneissic samples (4239, 3226, 86110, 861420(+Grt)) are located centrally within the TMA. Perthite textures range from small (2 μm), coarse (10-15 μm) and dense beads, coarse rods and coarse beads with film lamellae, respectively. Average FL temperatures range from 710 to 750°C. Only two samples (861100, 861420) recorded distinct modal peak proportions from BSE images.

Gneiss (860880, 861630, 861750, 861800, 860670, 861740, 861790, 4248, 861520, 4007k)

Gneisses (Bt+Grt) (860880, 861630, 861750) within and along the northwestern flank of the TMA yield perthite ranging from poor rod lamellae with films, small even bead lamellae, and blocky to bead lamellae with even films, respectively. Sample 861800 (with Chl) yields moderate (<10 by 25 μm) bead to rod lamellae and flanks the TMA along its northwestern end. Remaining Bt gneisses (860670, 861740, 861790, 4248, 861520) are characterized by very fine strings, tiny (3 μm) deformed beads, coarse yet heterogeneous beads with very thick Ab-rich lamellae, string to tiny beads to long thin (>100 by 5 μm) rod lamellae, respectively. The latter samples (4248, 861740) are located within and flanking the TMA along its western edge. Average FL minimum temperatures range from <700 to 795°C. Sample 861520 yields both blocky antiperthite and small bead perthite in the same section with FL minimum temperatures of 730 to 820°C (perthite-antiperthite). Only two samples (861750, 861790) produced distinct modal peak proportions recorded by BSE image. A Hbl-bearing gneiss (4007k) flanks the southwestern edge of the TMA. Perthite from 4007k was not well developed and slightly heterogeneous, containing only fine string to large bead lamellae and gives an average FL minimum temperature of 800°C.

Charnockite (860700, 860870, 860070, 860200, 860380, 860530, 860570, 861280, 861360, 860830)

Two Opx-bearing rocks flanking the eastern edge of the TMA yielded perthite (860700 and 860870). Blocky antiperthite was also found in sample 860700 but was fine-grained and heterogeneous. BSE images of perthite showed fine rod to string lamellae (860870) with several areas of heterogeneous and poorly developed coarse bead perthite. Only one grain from 860700 was examined due to a lack of perthite, which yielded distinct modal peak proportions from BSE image. FL minimum temperatures average 830 and 890°C, respectively.

Both perthite and antiperthite were found from retrograded charnockitic rocks concentrated along the southern end and flanking the TMA (860070, 860200, 860380, 860530, 860570, 861280, 861360, 860830). Sparse blocky antiperthite with abundant fractures and inclusions were found in samples 860070 and 860830. Perthite textures ranged from broadly heterogeneous, very small (3 μm) and fine bead or string lamellae,

to grains with or without films (860070, 860380, 860570). Only one feldspar grain was examined from sample 860070 due to a lack of perthite. Clear rod perthite with fine, evenly spaced (~5 μm) films were found in samples 861280 and 861360, flanking the TMA with only sample 861280 recording distinct peak modal proportions in BSE image. Sample 860200 yielded both blocky rod to beads with films and blocky antiperthite. A Hbl-bearing retrograded charnockite (860830) along the western edge of the TMA yielded tiny (3 μm) bead perthite with films. Average FL temperatures range from 740 to 860°C and 790-950°C (perthite-antiperthite). The highest temperature of 860°C (860570) was obtained on a sample located outside of the eastern edge of the TMA. Hbl-bearing retrograded charnockite yielded temperatures similar to those retrograded charnockites without hornblende. Rocks containing antiperthite (860640, 960930) along the western edge of the TMA record the highest temperatures in the study area from clear and distinct peak modal proportions in BSE image. Blocky and coarse antiperthitic lamellae were present in section and record an average FL temperatures of 925 and 1015°C respectively.

Granitoid (860550, 860970, M34, 4240, 4035, 861810)

Biotite granite (860550, 860970, M34, 4240), Bt-Sil-Grt-bearing granite (4035) and Hbl-Bt-bearing granodiorite (861810) flank or are within the centre of the TMA (Figure 10). Perthite ranged from string to bead, coarse beads with thick (<10 μm) Ab-rich lamellae or with films, small bead, rod and strings, and string lamellae, respectively. Only one grain was examined from samples 861810 and 860550 due to lack of perthite. Exsolved feldspar grains from sample M34 indicate some lamellae deformation. Perthite from sample 860970 yields abundant Ab-rich lamellae at similar and opposing crystallographic orientation (nearly 90°) to the majority of coarse (90 by 20 μm) bead lamellae (Figure 7a). Average FL temperatures obtained range from 730 to 840°C. Two samples (4035, M34) with high minimum temperatures of 840 and 835°C, respectively, were calculated from exsolution lamellae forming distinct peak modal proportions.

Discussion

Previous temperature constraints within the BH domain were reintegrated feldspar temperatures determined by Burwash et al. (2000a). These minimum temperatures of 800 to 850°C from Bt-Grt gneisses within the center of the current study area aided in

initial characterization of granulite-grade conditions of the RGD. Reintegrated feldspar temperatures obtained from metasedimentary samples provide some evidence of a regional temperature gradient with slightly increasing temperatures from west to east (Figure 10a). Ideally, inclusions, zoning and/or multiple equilibrium assemblages in one sample would provide the best measure of internal consistency and degree of equilibration between mineral phases for pressure and temperature constraints or path histories. Garnet composition maps appear generally homogenous with slight compositional zoning near fractures or slight retrogression along the rim. Due to the often fine-grained nature of matrix plagioclase, it cannot be confirmed if garnet and plagioclase compositions recrystallized and equilibrated together under the same conditions. As is commonly the case in polymetamorphic terranes, it is difficult to constrain the timing of growth or degree of equilibration between various mineral phases, which introduces a measure of uncertainty in interpretation. Nevertheless, the similarity of pressures obtained in this study between less deformed and more deformed samples suggests a reasonable approach to equilibrium and likely reflect pressure conditions within the RGD.

Reintegrated feldspar temperatures provide the most realistic record of the minimum temperatures experienced by rocks of the RGD. Comparison of feldspar temperatures to those derived by garnet-cordierite net transfer and Fe-Mg exchange equilibria of pelitic migmatite provides a measure of the degree of mineral equilibration. Reintegrated feldspar thermometry of pelitic and semi-pelitic gneisses, indicative of a sedimentary protolith, record minimum metamorphic temperatures ranging from <700 to 850°C and up to 905°C (this study; Burwash et al., 2000). Either a lack of cores or well-developed perthite limited spatial coverage of reintegrated feldspar temperatures in each of the four quadrants of the map sheet. P-T estimates from multiequilibrium calculation of pelitic migmatite records metamorphic conditions at 6.2 to 7.0 kbars and 740 to 800°C. Temperature estimates based on Fe-Mg exchange reactions (determined by TWEEQU) are more susceptible to reequilibration than are the reintegrated feldspar temperatures. Therefore, the highest reintegrated feldspar temperatures obtained on metasedimentary samples (800°C or even up to 900°C) provide the best estimate of regional metamorphic temperatures. These two techniques combined place granulite-grade conditions within

the middle crust (up to ~25km depth) (Thompson, 1988). Garnet-biotite temperatures are much lower than indicated by the high-grade mineral assemblage of pelitic migmatite. This supports both retrograde Fe-Mg exchange of primary biotite and the petrographic observation that fine-grained biotite is not part of the primary mineral assemblage but rather formed by retrograde growth after dehydration at high temperature.

Felsic magmatic rocks record widely variable minimum reintegrated feldspar temperatures. Few perthite-bearing felsic granites record either magmatic or overprinted metamorphic minimum temperatures of 730-840°C. Only one Bt granite (4240) within the TMA yielded a minimum magmatic or overprinted metamorphic temperature of 750°C from well-defined perthite lamellae. Reintegrated feldspar temperatures from charnockite record some of the highest metamorphic or magmatic temperatures in the study area from perthite (740-890°C) and antiperthite (925-1015°C). Minimum temperatures greater than 900°C recorded by antiperthite from charnockite agree with temperature estimates for charnockite by Kilpatrick and Ellis (1992). These high temperatures create an abrupt high temperature break throughout the centre of the study area in association with the western flank of the TMA.

The presence of antiperthite in granulite-grade pelites and charnockites has been suggested to form by exsolution during slow cooling (Raase, 2000; Carstens, 1967; Hubbard, 1965), replacement involving fluids (Griffin, 1969), or both (Sen, 1959). If antiperthite were a product of replacement, one would expect anhedral, ragged and unevenly distributed lamellae closely associated with sources permeable to fluid influx (i.e. fractures or flaws). On the basis of clearly defined, unaltered and common blocky textures of K-feldspar lamellae in plagioclase (Figure 7g), antiperthite is likely exsolution rather than replacement derived. Sen (1959) noted high-temperature conditions are required to overcome the high energy constraints required for Al-Si reorganization to form antiperthite exsolution lamellae. Sen (1959) suggested such high temperatures may be obtained by shear, thermal or hydrothermal activity, which is possible for charnockitic magma. In this study, Bt gneiss (861520) and retrograded charnockite (860200) containing both perthite and antiperthite were found to yield minimum reintegrated feldspar temperatures of 820 and 950°C, respectively. These estimates are 90 to 160°C higher than minimum temperatures obtained from well-defined and unaltered perthite

from the same rocks (Table 6, Figure 8). In this case, reintegrated feldspar temperatures were derived from less abundant antiperthite which could be recording slightly greater minimum temperatures. However, perthite-bearing retrograded and unretrograded charnockite flanking both sides of the TMA range in minimum feldspar temperatures of 740 to 800°C with a high temperature up to 890°C east of the TMA. This latter temperature derived from perthite supports the idea that antiperthite could be recording temperatures >900°C, possibly reached during magmatic intrusion into the middle crust.

A single occurrence of mesoperthite from Sil-Bt-Crd-bearing pelitic gneiss (861590) records a minimum reintegrated feldspar temperature of 905°C calculated from distinct mesoperthite lamellae, which do not indicate any lamellae loss by deformation (Figure 10). Mesoperthite is common in granulite-grade metamorphic rocks or "...large deep-seated intrusions..." (Smith and Brown, 1988, p.577) therefore in this study, the presence of mesoperthite in a pelitic bulk composition could support high temperatures were reached in metamorphism of a sedimentary protolith, whether part of the same metamorphism as recorded by pelitic migmatite (861510) or overprinting of previous regional temperature values possibly associated with the TMA. Alternatively, the aluminous mineralogy of this sample could be an example of, or similar to, some of the peraluminous granitoids common in the TMZ derived by partial melting at ultra-high temperatures of a metapelitic source (e.g. Pelican Rapids; Chacko et al., 1994; Creaser and Chacko, 1995; Chacko, 1997). In hand sample, this medium-red and slightly foliated rock lacks banding or mineral segregation by partial melting, such as observed from pelitic migmatite (861510). Mesoperthite-bearing pelitic gneiss also lacks both spinel and garnet otherwise present in pelitic migmatite. Nevertheless, high intracrustal temperatures are implied to have been reached by this mesoperthite-bearing sample as recorded by >900°C reintegrated feldspar temperatures, regardless of an igneous or sedimentary protolith.

Conclusions

Solvus, Fe-Mg exchange and net transfer thermobarometry record the following pressure-temperature conditions for rocks of the RGD;

- Grt-Crd multiequilibria calculations from a pelitic migmatite (861510) records granulite-facies conditions at 6.2 to 7.0 kbars and minimum temperatures of 740 to 800°C.
- Charnockite records reintegrated feldspar temperatures up to 890°C from perthite and 925-1015°C from antiperthite.
- A felsic biotite granite (4240) within the TMA records a (likely magmatic) minimum reintegrated feldspar temperature of 750°C.
- Mesoperthite-bearing pelitic gneiss records a minimum reintegrated feldspar metamorphic temperature of 905°C.

CHAPTER 3

U-Th-Total Pb EM AND U-Pb TIMS DATING OF MONAZITE AND ZIRCON

Introduction

Monazite (Th, Ce, REE)PO_4 and zircon ($ZrSiO_4$) occur as accessory minerals in a variety of rock types. Both minerals have been widely used for dating igneous, metamorphic, and less commonly diagenetic events (Parrish, 1990). A geochronological study of monazite and zircon in fourteen samples from the Peerless Lake (NTS 84B) study area was undertaken using two complementary techniques – chemical dating of monazite by electron microprobe (EM dating), and isotopic dating of monazite and zircon by thermal ionization mass spectrometry (TIMS). Dating of monazite and zircon was carried out to shed light on the following questions:

- The age(s) of high-grade metamorphism in the RGD.
- The relationship of Opx-bearing rocks, of either igneous (charnockite) or metamorphic (granulite) origin, to granulite-facies metamorphism.
- The igneous crystallization and metamorphic ages of granitoids within the study area.
- Age(s) of late-stage deformation and retrogression in the study area.

The chemical EM dating technique is well suited to this study because it is fast, non-destructive and connects ages within either chemically zoned domains in individual grains and/or a grain's textural position in thin section (Montel et al., 1996). Small grains, otherwise not captured during conventional methods of mineral separation, may be quantitatively measured by the electron microprobe's excellent spatial resolution (<2 μm) (Montel et al., 1996). The EM method also only requires the preparation of a thin section from a small amount of rock, which is advantageous given the limited size and availability of basement drill core samples from the study area. As well, multiple age populations from complexly zoned grains may be differentiated and compared to higher precision ages obtained with conventional isotopic methods (e.g. Cocherie et al., 1998). This is especially valuable in cases such as the BH domain, where there is a distinct possibility of polymetamorphism. Lower precision and accuracy (e.g. ±30-20 Ma; Montel et al., 1996, Cocherie et al., 1998) arising from errors associated with

standardizing and counting statistics of the electron microprobe, low Pb concentration of monazite (Cocherie and Albarede, 2001), and the inability of the technique to ascertain concordance within the U-Th-Pb system are the major limitations of the EM method.

The TIMS method offers the advantage of measuring both unstable uranium nuclides, ^{238}U and ^{235}U, and their decay daughter products, ^{206}Pb and ^{207}Pb, which provide an internal measure of closed-system behavior by recording the concordance between two apparent ages (Heaman and Parrish, 1991). Additionally, the method provides much higher analytical accuracy and precision than is possible with EM techniques. Disadvantages of the TIMS technique include the loss of spatial resolution and information of the textural context of the grains being dated. The EM and TIMS methods, when used in combination, offer more powerful geochronological insight than either method by itself.

Zircon and monazite are well suited to dating metamorphic events in part because of their relatively high closure temperatures for Pb diffusion (e.g. Asami et al., 2002; Copeland et al., 1988; Parrish, 1990; Suzuki et al., 1994; Heaman and Parrish, 1991; Lee et al., 1997). Nevertheless, when approaching granulite-grade conditions, closure temperature and lead diffusion remain a primary concern in understanding the reliability of ages produced from both monazite and sometimes even very robust zircon. Closure temperature is dependent upon several factors including diffusion coefficient, grain size and shape, and cooling rate (Dodson, 1973; Parrish, 1990). Experimental diffusion studies yield a wide array of closure temperatures for Pb diffusion in monazite; estimates range from 600 to >900°C for typical grain sizes and geologically reasonable cooling rates (Smith and Giletti, 1997; Cherniak et al., 2000). Recently, Cherniak et al. (2004) confirm closure temperature estimates for monazite reach 900°C or possibly greater. Closure temperature estimates for zircon are generally greater than for monazite, ranging from >900 to >1000°C (Cherniak and Watson, 2000; Mezger and Krogstad, 1997; Lee et al., 1997). In addition to the diffusion of Pb through the monazite crystal lattice, hydrothermal fluid-rock activity below closure temperature (Dahl et al., 2001; Asami et al., 2002), recrystallization, dissolution or reprecipitation along fractures in monazite could facilitate lead loss and result in discordance in U-Th-Pb systematics (Hawkins and Bowring, 1997; Harrison et al., 2002; Dobmeier and Simmat, 2002). In this regard,

monazite inclusions shielded within garnet have received recent attention in that several studies record slightly older monazite inclusion ages compared to matrix monazites along grain boundaries. This suggests that garnet may armor the inclusion from recrystallization, alteration, and resetting at high-grade conditions (Montel et al., 2000; Zhu and O'Nions, 1999; Catlos et al., 2002). Alternatively, age differences between inclusion and matrix monazites may reflect multiple episodes of monazite growth occurring before and after garnet growth.

Accessory Mineral Petrography

Available thin sections were scouted for the presence of monazite using BSE imaging on the electron microprobe. Samples for which P-T data had been obtained were specifically targeted in an effort to connect metamorphic age determinations with P-T conditions. As well, different rock types were targeted to broadly cover the entire study area to determine if a geographic age variation exists. Representative BSE images of monazite are presented in Figure 11. A complete inventory of monazite images is given in Appendix C. Photomicrographs of isotopically analyzed monazite and zircon crystals are given in Appendix D.

Spl-Crd-Sil-Grt-bearing Pelitic Migmatite (861510)

In strongly aluminous rocks, such as the high-grade pelitic migmatite (861510), pale yellow, round grains of monazite and zircon are abundant. This migmatitic core sample contains both a leucocratic and a more melanocratic portion. Monazites analyzed by electron microprobe from the leucocratic portion include large and round matrix grains in contact with a smaller spherical zoned zircon (Figure 11a), round inclusions within garnet with little to no alteration (Figure 11b), perthite, quartz, retrograde biotite, and plagioclase or elongate grains aligned with lamellae in perthite and approximately with the overall fabric of the rock (Figure 11c). Some elongate monazite grains from the melanocratic portion of the rock are aligned with metamorphic fabric defined by sillimanite. In places, both sillimanite and monazite are included within cordierite. Round monazite grains occurs as inclusions in minerals, such as cordierite, garnet or K-feldspar (perthite), which are diagnostic of granulite-facies metamorphism.

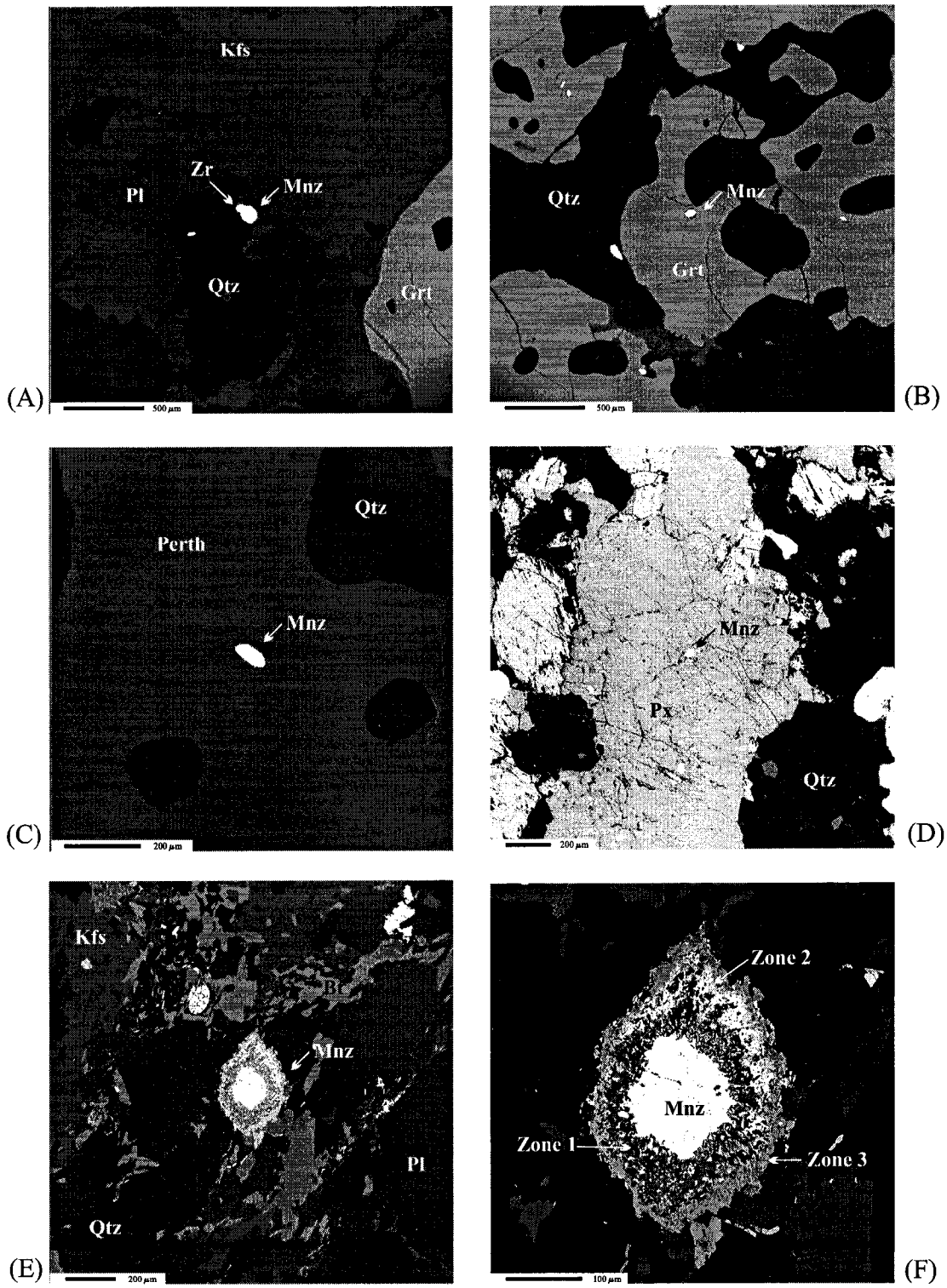

Figure 11. BSE images of representative monazite (center) within thin section: pelitic migmatite (A) 861510-mon4, (B) 861510-mon8, and (C) 861510-mon12 approximately aligned with overall fabric of the rock, (D) Bt-Cpx charnockite 860220-mon13, and Bt gneiss (E) and (F) 860781-mon1 with surrounding alteration.

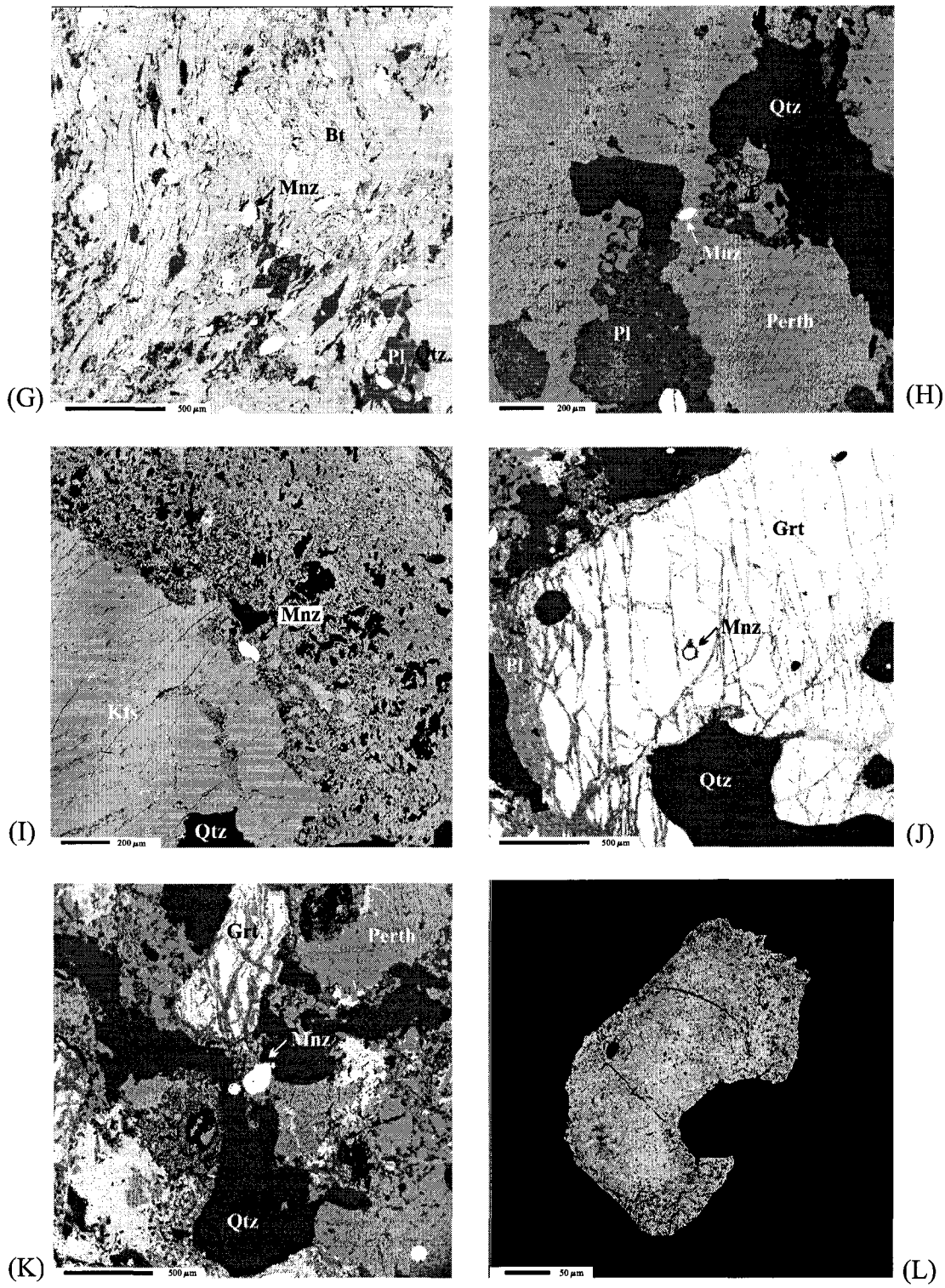

Figure 11. Continued ... BSE images of representative monazite (center) within thin section: (G) Bt charnockite 860770-mon3, (H) Bt granite 4240-mon5, (I) Grt granite 860140-mon1, pelitic mylonite (J) 4245b-mon1 and (K) 4245b-mon5, and (L) charnockite 861710 thorite/huttonite.

Sil-Grt-Bt-bearing Pelitic Gneiss (861380, 861420)

One large monazite from Sil-Bt-Grt gneiss (861380) occurs along the grain boundary between K-feldspar and plagioclase, and has a pitted or resorbed ~<10 μm rim. Monazites examined in Grt-Sil-Bt gneiss (861420) are included in K-feldspar or sometimes patchy perthite, biotite, and along grain boundaries between quartz, K-feldspar and biotite. This sample yielded abundant large (~<100 μm), irregular, elongate and round monazites within the matrix or as inclusions (e.g. in perthite) with variable pitting, fractures and little chemical zoning. Some elongate monazites appear aligned with metamorphic fabric defined by biotite laths and fine-grained mortar of quartz and plagioclase.

Bt±Grt-bearing Gneiss (860781, 860880, 861740, 861790)

In thin section, large anhedral monazite grains are surrounded by pale yellow to brown complex halos speckled with spongy-textured Th-silicate from biotite gneiss (860781). Grains analyzed by electron microprobe occur along grain boundaries, as either large and anhedral grains or small and spherical grains, between plagioclase, quartz, K-feldspar or are included within plagioclase (Figure 11e and f). Detailed examination of the grain shown in Figure 11f reveals approximately three concentric alteration zones (1, 2, and 3) surrounding a resorbed monazite core. Zone 1 (dark) contains apatite with patches of an Fe-Al±Mg silicate mineral (garnet?); Zone 2 (bright) contains a Ca-La-Ce silicate mineral; and Zone 3 (moderately bright) contains an Al-Ca-La-Ce (±Fe) silicate mineral (allanite?) with patches of a Th-rich silicate mineral. In thin section, monazites from Bt-Grt-bearing gneiss (860880) range from round and tiny to elongate and are in places included within garnet, quartz or along grain boundaries. BSE imaging revealed a few small (10-20 μm) and fewer large (~100 μm) monazite grains. Biotite gneiss (861740 and 861790) yielded moderate-sized (~50 μm) to sparse round monazite commonly as inclusions within perthite. Elongate monazite in 860781 and 860880 are roughly aligned with a biotite and/or mortar metamorphic fabric while monazite in 861740 and 861790 are generally tiny and spherical crystals.

Charnockite (860220, 860770, 860380)

Although several monazite and zircon grains were found by EDS in Bt-Cpx charnockite (860220), in thin section monazite is difficult to distinguish from abundant zircon. Elongate and tiny anhedral monazites analyzed by electron microprobe were situated within quartz and large fractured pyroxene, respectively (e.g. Figure 11d). In the mineral separation process, monazite was not found in any magnetic fractions from 0.5-0.8A. One potential monazite grain was revealed by SEM but appeared to be intergrown with a Ca-rich mineral (apatite?). Halos surround anhedral to round, small (<60 μm) monazite included in biotite from a charnockite (860770). One elongate grain (Figure 11g) is roughly aligned with foliation defined by biotite. A retrograded charnockite (860380) yielded a tiny round monazite included within blocky lamellae in antiperthite. Tan zircon is very abundant in sample 860220 and occurs as elliptical, spherical and fewer subhedral columnar shapes in the matrix and sometimes in pyroxene.

Granitoid (4240, 860970, 860140)

Because few monazites were found in granitic rocks, only three granitoids were targeted for monazite chemical EM dating (4240, 860970, 860140). Weakly foliated, biotite granite (4240) yielded a few pale yellow-brown, elongate to round monazite grains commonly found along grain boundaries or included within feldspar with elongate grains approximately oriented parallel to the weak foliation. Analyzed monazite occurs within patchy plagioclase, perthite or along the grain boundaries between quartz and perthite (Figure 11h). The few remaining monazite grains are generally <20 μm and fractured with little chemical zoning. Elongate and round zircon is present in the matrix and some prismatic crystals included within K-feldspar. Another biotite granite with K-feldspar megacrysts (860970) contains elongate, round and irregularly shaped, clear to pale yellow monazite grains with most crystals smaller than 5 μm. Elongate monazites present within the matrix are aligned parallel to the weak fabric defined by biotite. Similarly, elongate zircons are weakly aligned with fabric suggesting some crystallization might have occurred at a similar time to monazite. Analyzed monazites were located along perthite and plagioclase/myrmekite grain boundaries or are slightly altered within plagioclase. Garnet-bearing granite (860140) yielded few large monazite grains located

along the grain boundary between K-feldspar and myrmekite (Figure 11i) whereas smaller (<30 μm) monazite grains are within perthite, myrmekite or matrix.

Sil-Grt-bearing Pelitic Mylonite (4245b)

Monazites from a Sil-Grt-bearing mylonite (4245b) occur as round or euhedral inclusions within large fractured garnets (Figure 11j) or as round matrix grains (Figure 11k) along grain boundaries between quartz and K-feldspar. Elongate monazites are aligned parallel to the metamorphic fabric defined by fine-grained mortar of quartz and plagioclase and few remaining relic sillimanite grains partially pseudomorphed by fine-grained muscovite/sericite. Separated monazites from this sample were not readily visible. Therefore a total of 21 subhedral to fragmented grains were picked and identified as monazite by SEM. Carbon from the SEM mount was removed by a carbon tetrachloride wash, prior to chemical processing for isotopic analyses.

Thorium-Silicate-bearing Cores

Rare thorite and/or the monazite silicate-end-member, huttonite, which share the same chemical composition ((Th, U)SiO_4), sometimes occur in association with monazite (Watt, 1995; Deer, Howie and Zussman, 1992). Several grains, intergrowths or inclusions of thorite/huttonite with representative compositions of 45-62 wt% ThO_2, 14-18.5 wt% SiO_2 and 1.2-11 wt% UO_2 and analytical totals between 95-98 wt% were found during search for monazite (860830, 861280, 4249, 861750, 4245b, 861710). A charnockite sample (861710), same as that dated by U-Pb zircon by Villeneuve et al. (1993), in the northeast quadrant of the map sheet yielded a large, subhedral matrix thorite/huttonite of very porous and uneven spongy texture (Figure 11l) suggestive of severe radiation damage from high Th concentrations (Heaman and Parrish, 1991). Similar thorite/huttonite grains were described by Hecht and Cuney (2000) in their study of monazite hydrothermal alteration in Precambrian basement rock of the Athabasca Basin in northwestern Saskatchewan. These authors observed a porous Th-silicate mineral to be a hydrothermal alteration product of monazite, possibly by fluid activity of 'diagenetic brines' through fractured basement rock.

Analytical Procedure

U-Th-Total Pb EM Age Dating of Monazite

Monazite chemical analyses were performed using the University of Alberta JEOL 8900 electron microprobe. Depending upon the abundance of monazite, one to three large and minimally fractured grains were targeted for analysis in each sample. A large number of monazite analyses were obtained in order to produce a statistically robust age determination. In particular, detailed analysis of monazite grains revealed if age and chemical zoning exists within chemical domains. BSE images were prepared for each grain before setting a series of line traverses with 5 to 25 μm spacing between individual analytical points depending upon grain size. Analytical spots were checked before quantitative analysis for overlap with pits, fractures, cracks, imperfections, and chemical domains. A secondary electron image was collected after quantitative analysis to verify the location of each analytical spot.

The analyses were obtained with an accelerating voltage of 20 kV, a beam current of 100 nA and a spot size of 1 μm. Table 8 provides details of x-ray peak positions, counting times and standards chosen for REE, Si, Ca, and P analysis. Peak overlap corrections were performed for YLγ on PbMα and ThMγ on UMβ (Scott and Love, 1983; Suzuki and Adachi, 1991; Scherrer et al., 2000). A few analyses from small grains (e.g. 860380) yielded anomalously high or low analytical totals (<98 wt% or >102 wt%). These were not accepted unless compositions and ages were comparable to neighboring analyses. Poor stoichiometric totals generally correlated with increased concentration of SiO_2 along the grain edge or fractures, suggesting that the X-ray excitation volume incorporated surrounding silicate minerals. Chemical ages were periodically cross-checked with isotopic ages obtained from a suite of in-house monazite standards. Average deviation between TIMS and chemical ages on six standard monazite crystals ranging in age from Jurassic to Archean was 15 million years (Chacko and Heaman, unpublished). Representative analyses of monazite from samples investigated in this study are given in Table 9.

Chemical ages are calculated iteratively following the equations of Suzuki and Adachi (1991) and Suzuki et al. (1991). Decay constants for ^{232}Th, ^{238}U, and ^{235}U taken from Jaffey et al. (1971) were used in the age calculation.

Table 8. X-ray lines, standards, and counting times used for electron microprobe operating conditions during analysis of monazite.

Element	Standard	Emission Line	Spectrometer Crystal	Channel	Counting Time (peak/background) (s)
La	$LaPO_4$	Lα	PET	CH1	20/2*10
Ca	Apatite/diopside	Kα	PET	CH1	20/2*10
Th	THO_2	Mα	PET	CH1	40/2*20 - 60/2*30
P	$CePO_4$/ YPO_4	Kα	PET	CH1	20/2*10
U	UO2	Mβ	PET	CH4	120/2*60
Y	YPO_4	Lα	PET	CH4	20/2*10
Si	Diopside	Kα	PET	CH4	15/2*7.5
Pb	NBS-K-456	Mα	PETH	CH5	180/2*90
Ce	$CePO_4$	Lα	LiF	CH2	20/2*10
Nd	$NdPO_4$	Lα	LiF	CH2	20/2*10
Pr	$PrPO_4$	Lβ	LiF	CH2	20/2*10
Sm	$SmPO_4$	Lα	LiF	CH2	20/2*10
Gd	$GdPO_4$	Lβ	LiF	CH2	20/2*10

Y concentration corrected for YL γ peak overlap with PbM α

Th concentration corrected for ThM γ peak overlap with UM β

Table 9. Representative monazite compositions from one quantitative EM analysis for each sample, including calculated age (Ma) for that spot location.

	Pelitic Gneiss			Gneiss				Charnockite					Granitoid		Mylonite
Sample #	**861510**	**861380**	**861420**	**860781**	**860880**	**861740**	**861790**	**860220**	***Th-rich 860220***	**860770**	***Th-rich 860770***	**860380**	**4240**	**860970**	**860140**	**4245b**
SiO_2	0.516	4.272	0.457	0.902	1.499	4.266	1.448	1.255	*16.472*	1.457	*20.407*	3.860	3.639	2.872	0.171	0.637
CaO	1.404	2.545	2.560	1.386	1.507	0.768	1.076	0.399	*2.361*	0.981	*0.847*	0.408	0.820	0.990	0.245	1.420
La_2O_3	13.566	5.833	10.745	15.400	11.750	12.176	15.611	21.366	*3.329*	17.248	*0.463*	11.989	12.302	14.406	16.777	13.593
Ce_2O_3	28.968	17.719	25.755	28.952	27.552	28.633	29.271	33.156	*8.593*	32.926	*3.496*	26.150	26.382	28.383	33.743	29.579
Pr_2O_3	3.172	3.005	4.177	2.793	4.502	4.529	4.810	2.395	*0.932*	5.117	*1.112*	2.734	4.181	4.506	3.261	2.868
Nd_2O_3	12.160	9.721	9.145	10.005	12.243	10.350	9.423	8.249	*3.060*	9.409	*6.604*	10.347	9.158	8.786	11.898	11.333
Sm_2O_3	2.490	2.656	2.099	1.542	2.219	1.649	1.682	1.172	*0.548*	1.132	*1.489*	1.628	1.608	1.383	2.155	2.318
Gd_2O_3	1.169	1.779	1.249	0.645	0.819	0.556	0.696	0.233	*0.134*	0.349	*0.777*	0.849	0.647	0.604	0.670	1.212
Y_2O_3	0.265	0.758	1.734	0.566	0.153	0.421	0.431	0.212	*0.624*	0.227	*0.989*	1.318	0.699	0.580	0.434	0.311
ThO_2	6.944	23.646	8.929	8.917	11.028	10.761	8.946	4.461	*54.776*	5.112	*58.331*	14.715	15.778	12.018	0.785	7.502
UO_2	0.535	1.492	1.944	0.193	0.216	0.976	0.298	0.047	*0.341*	0.248	*1.165*	0.719	0.582	0.691	0.571	0.664
PbO	0.788	2.561	1.401	0.844	1.052	1.259	0.883	0.385	*0.141*	0.511	*1.233*	1.458	1.528	1.293	0.244	0.835
P_2O_5	28.680	22.961	29.517	28.092	27.427	25.443	27.847	28.217	*7.010*	27.383	*1.105*	23.946	24.367	25.508	29.684	29.306
Total	100.657	98.948	99.712	100.237	101.967	101.787	102.422	101.547	*98.321*	102.100	*98.018*	100.121	101.691	102.020	100.638	101.578
Calculated Age (Ma)	1992	1983	1957	1984	2012	1977	1988	1887		1921		1903	1931	2003	1899	1900

Errors on individual chemical ages were determined with a Monte Carlo method (e.g. Scott and Love, 1983). Errors on Th* vs. Pb plots were calculated with standard error propagation methods using the program Isoplot v. 2.49 (Ludwig, 2001). The *minimum* error on any single age arises from the statistics of counting Th, U and Pb X-ray photons, which in turn is related to net X-ray peak intensities (peak – background) and counting times for each element. The 1σ precision of net X-ray counts is given by (Scott and Love, 1983):

$$\text{Relative precision } (\%) = [n_P / t^2_P + n_B / t^2_B]^{0.5} / (n_P / t_P - n_B / t_B) \times 100$$

Where n_P and n_B are the total counts measured at the peak and background positions, and t_P and t_B are the corresponding counting times at each position. To determine errors on the chemical age, the concentration errors on each element were propagated through the age calculation using a Monte Carlo approach. More specifically, using a representative monazite analysis of a sample as a seed, 1000 normally distributed random numbers were generated with an EXCEL spreadsheet for each oxide involved in the age calculation (ThO_2, UO_2 and PbO). The mean of each oxide distribution corresponded to the seed analysis, and the standard deviation to that given by the equation above. The randomly generated oxide concentrations were then each processed through the age calculation with the standard deviation of all of these ages used to arrive at the Monte Carlo error reported in Table 10 (at the 2σ level). For the samples examined in this study, the minimum 2σ uncertainty on the reported age of any *single* analytical point ranges from 16 to 77 Ma, with uncertainties for most samples between 10 and 20 Ma. It should be emphasized that these are the age uncertainties on an individual analytical point arising solely from X-ray counting statistics. Actual analytical uncertainties can be 2-3 times larger than this as other factors such as instrument drift, polishing imperfections, sample contamination, etc can also contribute to variation in measured elemental concentrations (e.g. Kohn and Spear, 1991).

Cumulative probability plots, using a representative minimum 1σ Monte Carlo error calculated for each sample were generated with Isoplot v. 2.49 (Ludwig, 2001). Most samples reflect only a single major age population, but a few contain two or more age populations of monazite (Figure 12). The best estimate of the age and uncertainty of each age population was determined with a plot of Th* vs. Pb concentrations, where Th*

Table 10. U-Th- total Pb monazite chemical ages including compositional range of Th, U and Pb oxides.

Sample #	# of grains	# of analyses	# of analyses used	[1]ThO_2 wt%	UO_2 wt%	PbO wt%	Histogram Average or Range (Ma)	Cumulative Probability Peak(s) (Ma)	Monte Carlo ± 2σ		[2]Th* vs Pb (Ma)	Th* vs Pb ± 2σ (Ma)	MSWD
Granitoid		***Kfs + Pl ± Bt ± Grt***											
4240	4	94	88	20.231-2.777	0.992-0.108	1.918-0.449	1925	1927	21		1923	6	10
								2020			2017	10	2
										4240-mon5			
										core	2007	23	5
										middle	1928	12	13
										rim	1880	17	5
860140	4	98	80	2.532-0.000	1.047-0.068	0.390-0.019	1910-1980	-----	77		-----	-----	-----
860970	2	67	62	15.043-6.540	0.778-0.257	1.566-0.742	2000	2004	25		1999	7	7
Pelitic Gneiss		***Spl + Crd + Sil + Grt + Pl + Kfs***											
861510	3	261	250	11.316-4.590	1.336-0.000	1.145-0.623	1990	1992	37		1989	5	7
		Sil + Grt + Bt + Kfs + Pl											
861380	1	31	28	25.316-15.874	1.531-1.215	2.647-1.795	1980	1986	16		1979	8	10
861420	4	134	133	13.935-6.843	2.318-0.586	1.541-1.036	1950	1953	22		1950	4	9
Gneiss		***Bt + Kfs + Pl ± Grt***											
860781	3	126	117	30.817-2.052	1.018-0.000	2.743-0.142	1980-1990	1988	38	*all grains*	1966	9	15
										anhedral (mon1)	1980	12	10
										spherical (mon3)	1956	23	12
860880	2	95	88	20.165-5.206	1.315-0.084	1.856-0.611	2020	2021	29		2011	7	6
								1917			1921	8	2
								1867			1865	12	1
861740	1	25	22	11.121-5.563	0.947-0.490	1.256-0.661	2000	-------	25	*core*	1988	21	8
										rim	1910	26	14
861790	3	79	79	13.375-7.453	0.897-0.019	1.370-0.621	2010	2005	33		2001	7	7
											1906	12	9
										861790-mon5			
										core	1967	41	45
										rim	1908	18	10
Mylonite		***Sil + Grt + Pl + Kfs***											
4245b	2	293	285	1.140-18.042	1.207-0.104	1.629-0.121	1900	1902	33	*inclusions*	1913	4	4
										matrix	1875	4	4
Charnockite		***Opx + Kfs ± Bt ± Pl ± Cpx***											
860220	3	101	87	15.154-0.047	0.141-0.000	1.411-0.008	~1900	1887	61		1897	13	5
860770	1	18	18	13.446-1.032	0.464-0.141	1.283-0.134	~1900	-------	45		1921	26	10
		Serp + Bt + Kfs + Pl											
860380	1	21	16	15.388-14.345	0.755-0.654	1.505-1.387	~1900	1905	24		1893	9	4

Ages and errors are reported in Ma

[1] *Th concentrations exclude Th-rich areas*

[2] *Th* vs. Pb method calculated as outlined by Suzuki and Adachi (1991)*

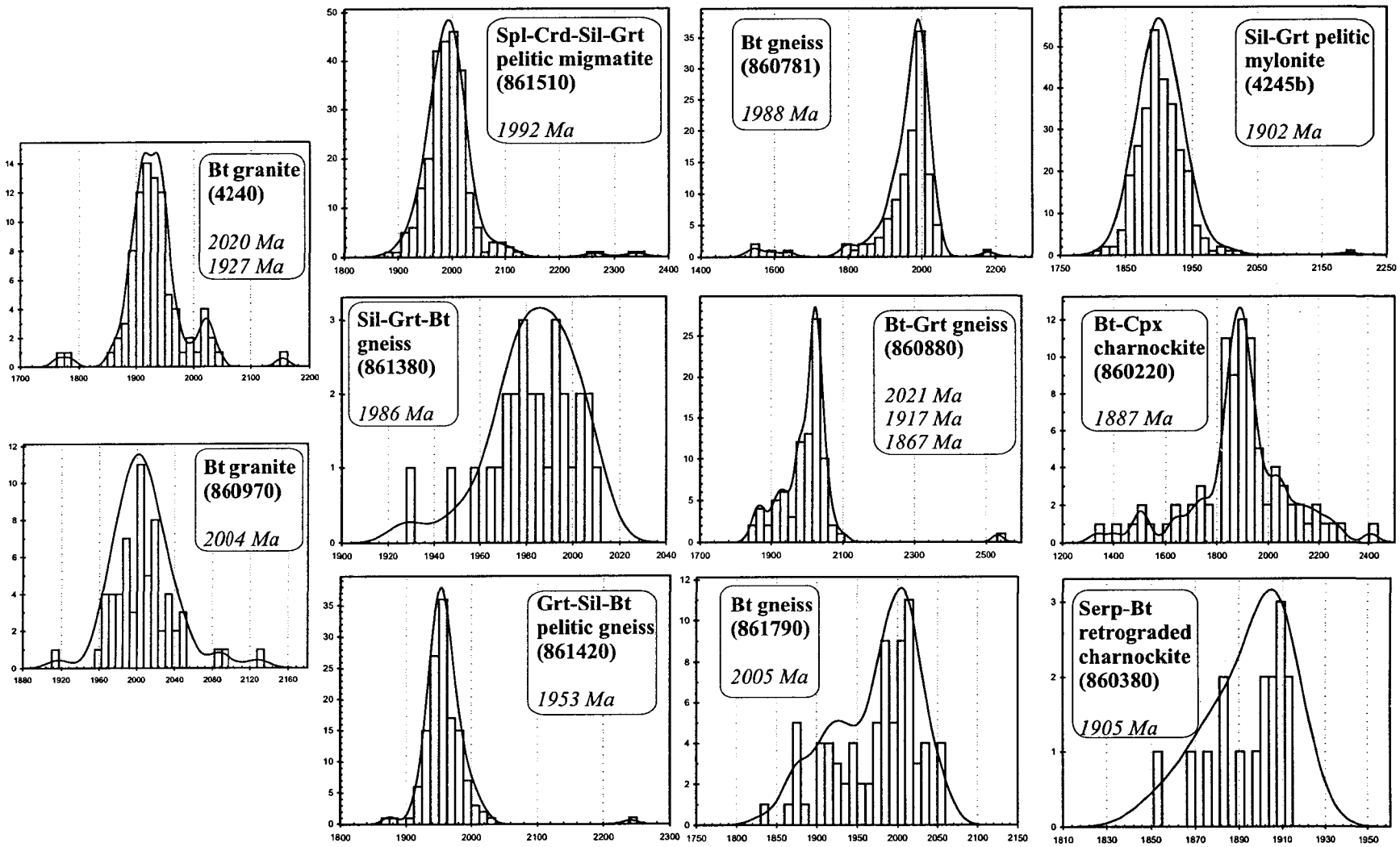

Figure 12. Cumulative probability plots and histograms, including major cumulative probability peaks, generated by Isoplot v. 2.49 (Ludwig, 2001) for select samples.

is the sum of measured Th concentration plus the amount of fictive Th needed to account for the amount of radiogenic Pb produced by U decay in monazite (Suzuki and Adachi, 1991). Following Cocherie et al. (1998), the regression line was forced through the origin on the Th* vs. Pb plot, which is consistent with the observation that monazites contain virtually no common Pb upon crystallization (Parrish, 1990). In samples with more than one age population of monazite, separate regression lines were fitted to each population. A few analyses, which represent older ages not used in Th* vs. Pb plot fitting, are represented by open squares on the plots. Slope (m) and error from Th* vs. Pb plots were generated by Isoplot v. 2.49 (Ludwig, 2001) and were used to calculate an age using the following equation (Suzuki and Adachi, 1991):

$$T = 1 / \lambda_{232} \ln (1 + m (W_{Th} / W_{Pb})$$

where W are the atomic weights of Th and Pb. Uncertainties on these chemical ages are reported at the 2σ level and are generally in the 4 to 41 Ma range. If the 2σ error was increased by a factor of 2 to account for measured error (e.g. Kohn and Spear, 1991), the chemical age and error remained the same but the mean square of weighted deviates (MSWD) decreased significantly. If the regression was not forced through the origin, the chemical age and error changed with the greatest variation from samples with few and clustered analyses.

Conventional Isotopic Geochronology of Monazite and Zircon (TIMS)

Separation of monazite and zircon from five basement cores followed laboratory procedures at the University of Alberta Rock Crushing Facility (Heaman et al., 2002a). Each core was photographed (Figure 13) and a slice kept as reference. Thorough and careful cleaning procedures were followed at all times to prevent any contamination of this small amount of sample. Liberation of monazite and zircon began with crushing and mineral separation as outlined by Heaman et al. (2002a). The amount of core crushed ranged from approximately half to a full hand-size sample, free of labels, tape or whiteout. Each core was initially broken-up by rock press, then further fragmented by jaw crusher to ~1 cm pieces. Fragments were ground in a Shatterbox to approximately sand- to silt-size. Powdered core was slowly passed over a Wilfley^{TM} table, in small amounts, to acquire a heavy mineral concentrate. The dried heavy mineral concentrate

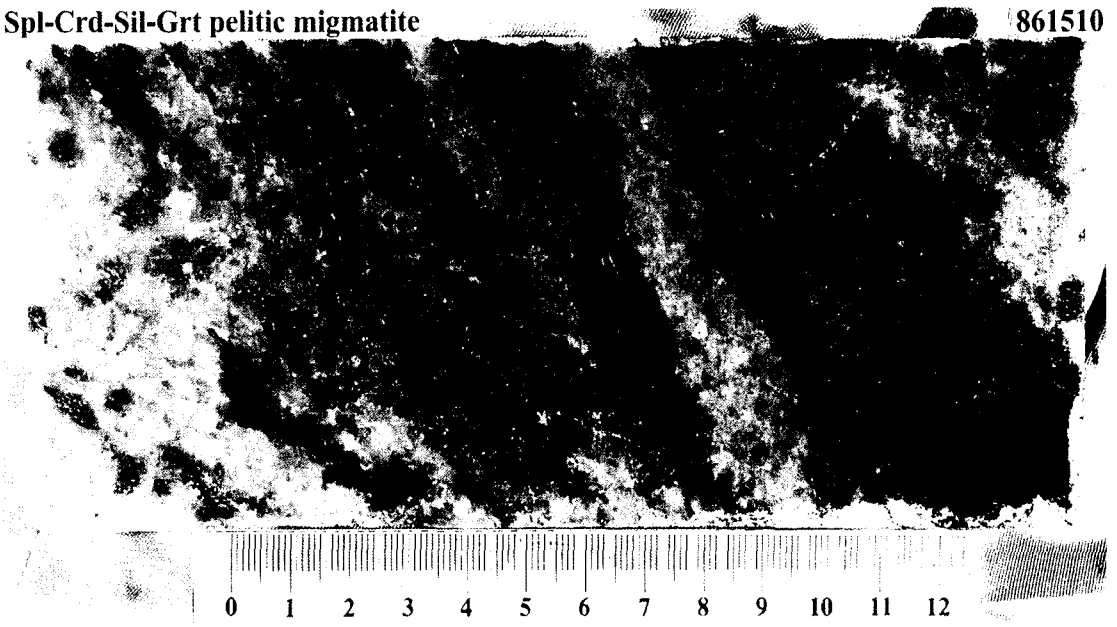

(A)

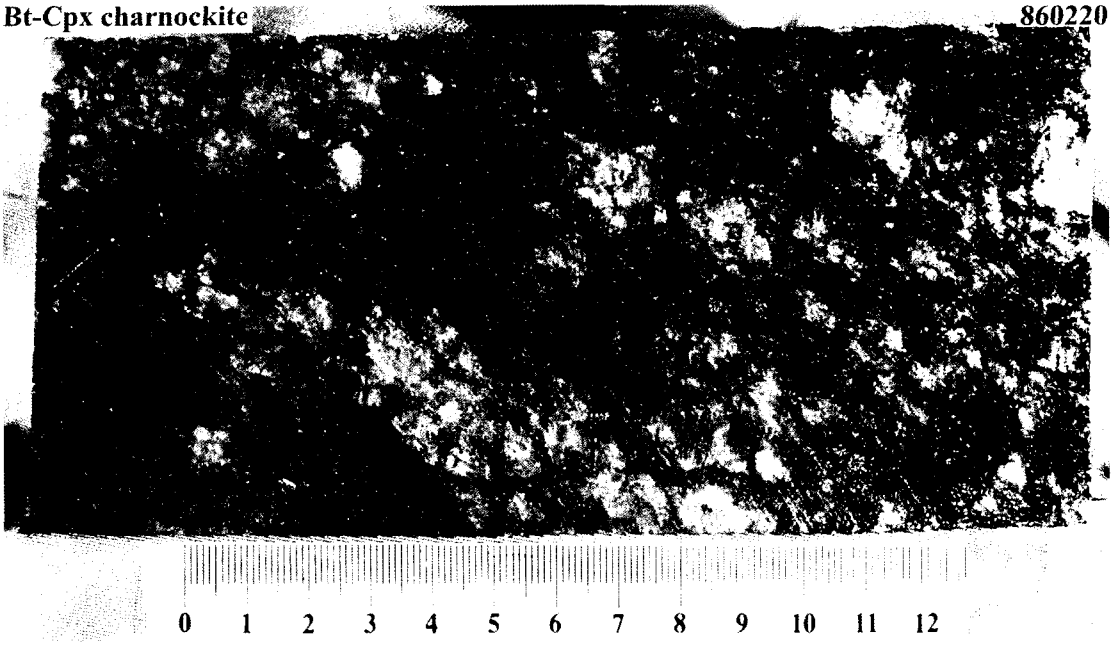

(B)

Figure 13. Photographs of select Alberta basement cores; (A) Spl-Crd-Sil-Grt pelitic migmatite (861510), (B) Bt-Cpx charnockite (860220), (C) Bt granite within the TMA (4240), (D) Bt granite west of the TMA (860970), (E) Grt-Sil-Bt pelitic gneiss (861420), and (F) Sil-Grt pelitic mylonite (4245b). Scale bar in centimetres.

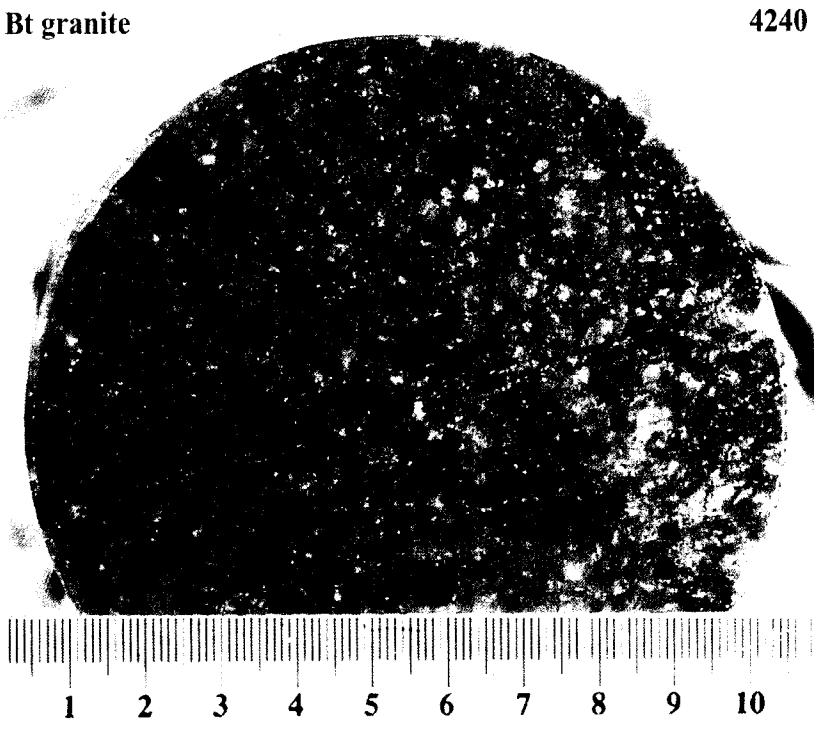

(C)

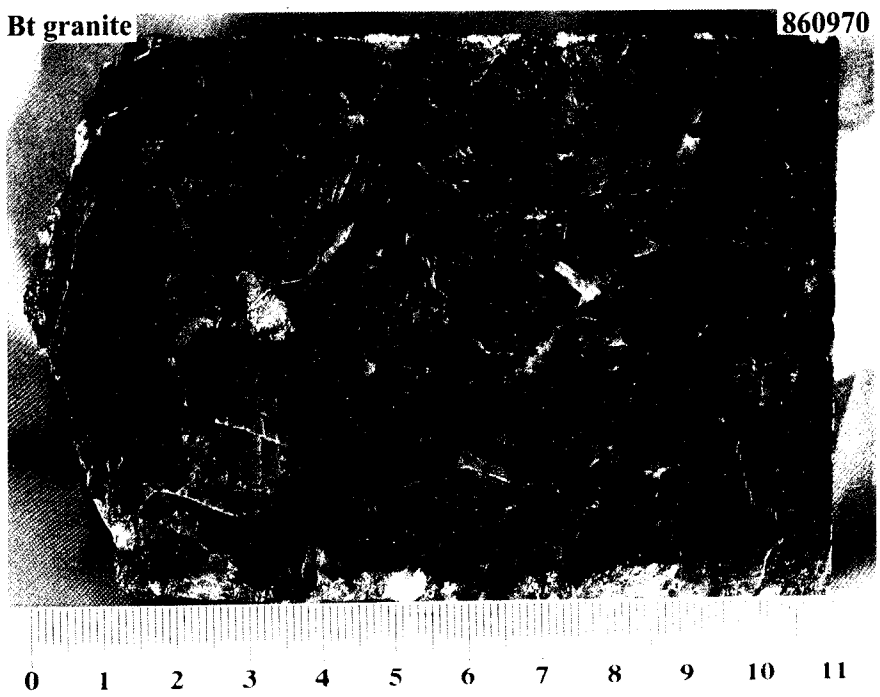

(D)

Figure 13. Continued .....

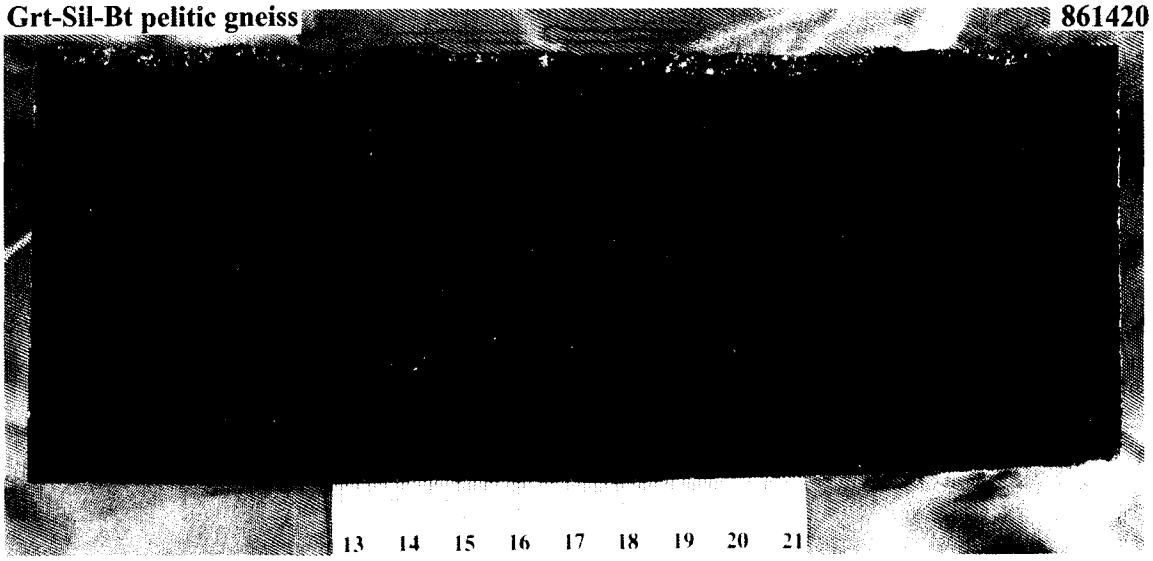

(E)

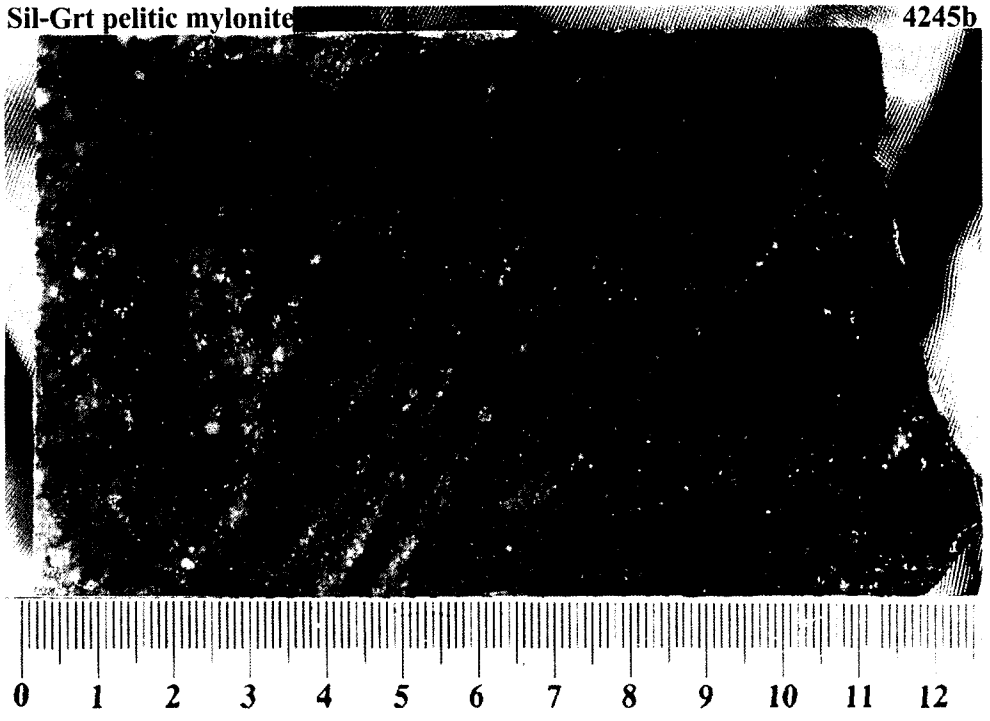

(F)

Figure 13. Continued .....

was passed over +70 mesh nylon disposable sieve to remove very coarse particles. Heavy minerals (–70 mesh) were passed in front of a vertical Frantz™ isodynamic separator to remove strongly magnetic minerals, then initially passed through a Frantz™ isodynamic separator at a current of 0.3 and 0.4 A with a 15° side tilt and 10° forward tilt. A mafic heavy fraction from the remaining non-magnetic portion was concentrated by heavy liquid separation (methylene iodide). A final Frantz magnetic separation of the heavy mineral concentrate was passed at currents of 0.5, 0.6, 0.7, 0.8, 0.9, 1.0 and 1.2 A until zircon was collected at 1.8A with a 15° side tilt and further refined with side tilts of 10°, 5° to 2°, dependent upon the amount of material present, to produce a cleaner zircon fraction. Monazite was handpicked in ethanol from the 0.5A fraction and zircon from 1.8A at side tilts of 5° or 2°. After monazite and zircon were initially sorted by shape, size, colour and clarity (clear transparent grains without inner turbidity, inclusions, fractures, or alteration) and photographed, selected zircon fractions were abraded (e.g. Krogh, 1982) with pyrite for 2 to 6 hours at 4 psi and 2 hours at 2 psi for a final polish or lightly abraded for 2 to 6 hours at 2 to 2.5 psi to remove fractured edges or overgrowths. Abraded zircons were separated from remaining pyrite by a 4N HNO_3 wash (Heaman and Parrish, 1991).

Single grains or groups of monazite and zircon were initially cleaned to remove outside contaminants. Monazite and zircon were washed in ethanol once, followed by distilled acetone then filled with millipore and 2N HNO_3 for monazite or 4N HNO_3 for zircon and placed on a hot plate, uncovered, for ~1 hour. Grains were then immersed in millipore, beakers briefly held in a mini-ultrasonic cleaner, and rinsed three times with distilled acetone. Monazite and zircon fractions were then weighed with a Mettler UTM-2 ultra-microbalance and ~30 drops of 6.2N HCl were added to cleaned Savillex screw top capsules containing monazite and ~20 drops of HF and ~3 drops of 7N HNO_3 were added to cleaned Teflon TFE digestion vessels containing zircon followed by addition of $^{235}U/^{205}Pb$ spike. Capsules containing monazite were placed, covered, on a hot plate for a minimum of 1-2 days whereas bombs containing zircon were placed in an oven for a minimum of 3 days at ~220°C to ensure complete dissolution and spike equilibration. Column chemistry was not completed for zircons with a sample weight of <5 μg. In this case, the HF and HNO_3 solution containing dissolved zircon were poured into a pre-

cleaned PMP beaker and evaporated to dryness, followed by addition of 6N HCl and ~2 drops of 0.125N H_3PO_4 and dried. For samples >5 μg, anion exchange resin columns were initially rinsed with Millipore (H_2O) and acetone followed by addition of AG-1X8 anion exchange resin. Columns were cleaned by alternating Millipore (H_2O) and 6N HCl approximately 2-3 times each followed by addition of ~15 drops of 3.1N HCl to equilibrate resin. Three drops of 3.1N HCl were added to each capsule or bomb prior to loading of the sample into columns. REE impurities were removed by addition of ~5-6 drops of 3.1N HCl, which was repeated twice more with a last pass of 10-12 drops. Lastly, 6.2N HCl then Millipore (H_2O) were added to columns for Pb and U elution, respectively, followed by ~2 drops of 0.125N H_3PO_4 and evaporated to dryness. Uranium and lead were analyzed together on a rhenium filament by a VG354 thermal ionization mass spectrometer (TIMS) by single Faraday and/or Daly collector. For some monazite fractions noted throughout the text, very high ^{208}Pb from high Th concentrations of monazite and low ^{205}Pb spike presented difficulty in TIMS measurement and, in some cases, recorded less precise data with larger error ellipses. Measured atomic ratios of $^{207}Pb/^{205}Pb$ were carefully examined for effects of ^{205}Tl (thallium) isobaric interference. Atomic ratio results were corrected for addition of spike, blank (2 pg Pb, 0.5 pg U), fractionation and initial common Pb. The initial Pb isotopic composition was determined using the lead evolution model of Stacey and Kramers (1975) with age estimates from EM dating. Concordia plots with regression lines were plotted by Isoplot v. 2.49 (Ludwig, 2001). U-Pb intercept ages and errors were calculated according to U-Pb linear regression model of Davis (1982), unless otherwise noted. Decay constants for ^{238}U (1.55125×10^{-10} y^{-1}) and ^{235}U (9.8485×10^{-10} y^{-1}) and the isotopic composition of uranium ($^{238}U/^{235}U = 137.88$) are the values recommended by Jaffey et al. (1971).

Results

ThO_2, UO_2 and PbO concentrations and calculated EM monazite ages are presented in Figure 14 and Table 10. The TIMS analytical results are given in Table 11.

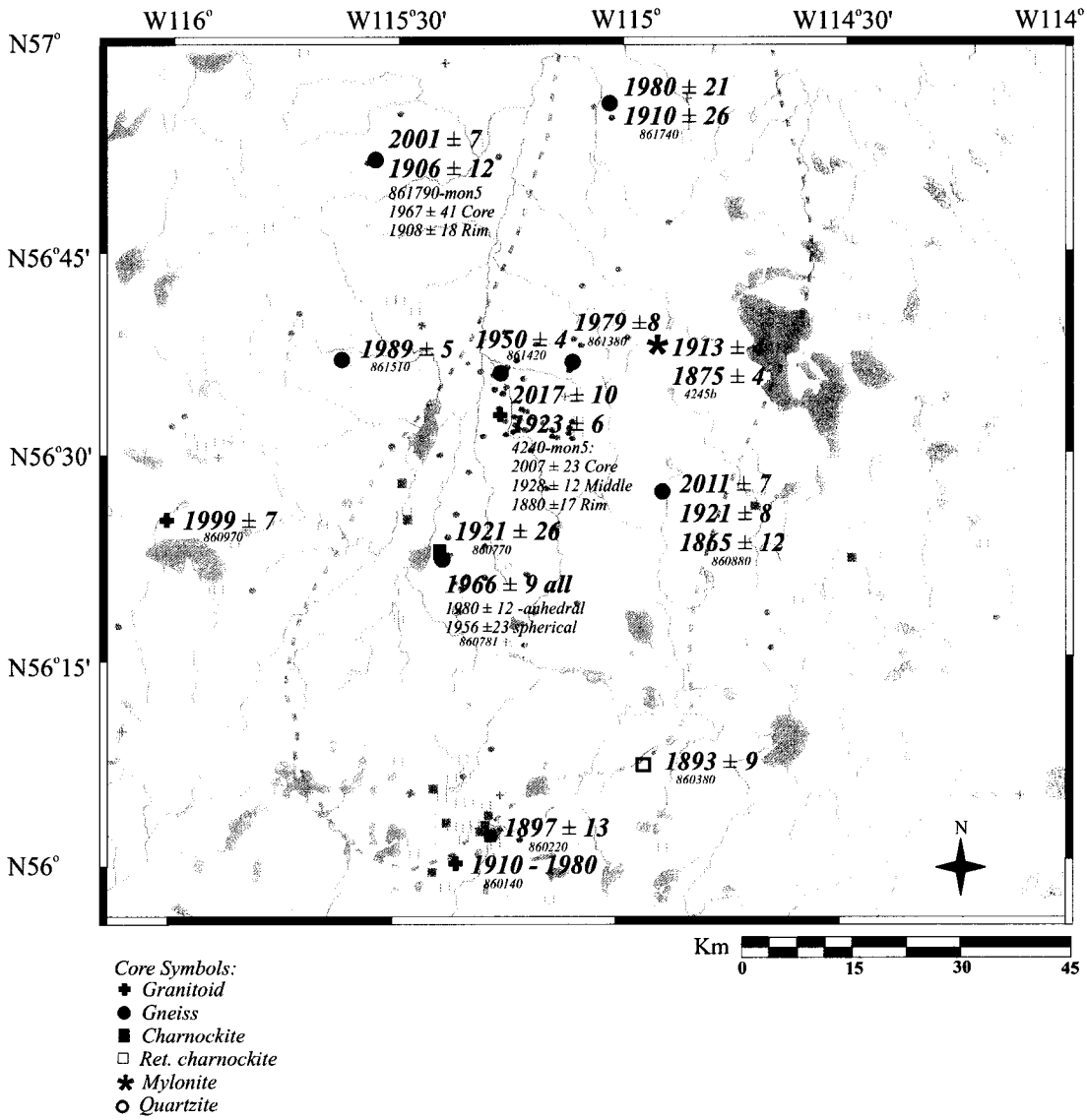

Figure 14. Monazite chemical ages within Peerless Lake map sheet (NTS 84B). Dashed outline is the TMA (Burwash and Power, 1990). Ages (in Ma) reported are from Th* vs. Pb plots with 2 σ error. Basemap from Alberta Provincial Basemap (1997).

Table 11. TIMS U-Pb Results for Monazite (M) and Zircon (Z)

Description	Weight (g)	U (ppm)	Th (ppm)	Pb (ppm)	Th/U	TCPb (pg)	$^{206}Pb/^{204}Pb$	$^{206}Pb/^{238}U$	$^{207}Pb/^{235}U$	$^{207}Pb/^{206}Pb$	Model Ages (Ma) $^{206}Pb/^{238}U$	Model Ages (Ma) $^{207}Pb/^{235}U$	Model Ages (Ma) $^{207}Pb/^{206}Pb$	%Disc
861510 (Spl-Crd-Sil-Grt pelitic migmatite)														
1M. Tiny, clear, round (34)	27	2701	60838	6707	22.53	31	53822	0.36915±53	6.4370±93	0.12647±2	2025.4±2.5	2037.3±1.3	2049.5±0.3	1.4
2M. Lg irregular (1)	11	1647	57670	5997	35.02	18	23627	0.3669±23	6.2660±392	0.12387±6	2014.7±10.8	2013.7±5.5	2012.7±0.8	-0.1
3M. Mod, yellow, spherical (1)	2	1782	79712	8055	44.73	5	16633	0.3640±12	6.2680±192	0.12489±12	2001.1±5.5	2014.0±2.7	2027.2±1.6	1.5
4M. Smll, pale yellow, spherical (1)	2	2144	59071	6503	27.55	38	2679	0.37940±44	6.6777±78	0.12765±6	2073.5±2.1	2069.7±1.1	2065.9±0.8	-0.4
5M. Lg, yellow, irregular/round (1)	4	3131	33520	4334	10.71	16	20317	0.38338±43	6.6040±75	0.12493±3	2092.1±2.0	2059.9±1.0	2027.8±0.4	-3.7
860220 (Bt-Cpx charnockite)														
1Z. Lg, elliptical, tan, abraded (1)	6	688	382	282	0.56	6	15574	0.36869±46	6.3224±79	0.12437±3	2023.2±2.2	2021.6±1.1	2019.9±0.4	-0.2
2Z. Spherical, abraded (1)	3	310	112	122	0.36	5	3846	0.37013±50	6.3320±89	0.12408±5	2030.0±2.4	2022.9±1.3	2015.6±0.8	-0.8
3Z. Spherical, abraded (1)	5	415	206	175	0.50	4	13319	0.38595±56	6.6405±94	0.12479±5	2104.0±2.6	2064.7±1.3	2025.8±0.7	-4.5
5Z. Smll, elliptical, tan, abraded (1)	4	545	250	234	0.46	26	1807	0.38730±48	6.6556±87	0.12463±6	2110.3±2.2	2066.7±1.2	2023.6±0.9	-5.0
4240 (Bt granite)														
1M. Lg, composite (1)	9	5096	130832	13248	25.67	124	7800	0.34306±68	5.5648±110	0.11765±2	1901.4±3.3	1910.7±1.7	1920.8±0.3	1.2
2M. Yellow spherical (1)	1	6229	231967	22558	37.24	10	17572	0.34355±50	5.8339±81	0.12316±6	1903.7±2.4	1951.5±1.2	2002.5±0.8	5.7
3M. Light yellow, spherical (1)	1	3420	91744	9466	26.83	8	9138	0.35061±55	5.7648±81	0.11925±9	1937.5±2.6	1941.1±1.2	1945.0±1.3	0.5
1Z. Spherical, tan (1)	3	1643	150	551	0.09	38	2750	0.33284±38	5.5696±64	0.12136±4	1852.1±1.8	1911.4±1.0	1976.4±0.6	7.2
2Z. Tan fragments (4)	10	1502	165	518	0.11	50	6688	0.34449±36	5.7921±62	0.12194±3	1908.2±1.7	1945.2±0.9	1984.8±0.4	4.5
3Z. Prismatic, abraded (1)	3	1854	217	671	0.12	12	9993	0.36197±43	6.1596±70	0.12342±5	1991.5±2.0	1998.7±1.0	2006.2±0.8	0.9
860970 (Bt granite)														
2M. Smll, irregular yellow (1)	2	5127	100084	10976	19.52	7	26154	0.35848±62	6.0527±104	0.12246±4	1975.0±3.0	1983.5±1.5	1992.3±0.6	1.0
3M. Smll, yellow (1)	1	5832	108903	12049	18.67	9	19872	0.35899±41	6.0601±67	0.12243±5	1977.4±2.0	1984.5±1.0	1992.0±0.7	0.9
1Z. Smll, structure (0.5A) (1)	2	384	78	24	0.20	7	307	0.04415±12	0.5968±57	0.09803±84	278.5±0.7	475.2±3.7	1589.0±16.0	84.2
2Z. Short, prismatic, abraded (1)	5	852	255	312	0.30	5	15684	0.35059±38	5.9369±65	0.12282±3	1937.4±1.8	1966.7±1.0	1997.6±0.4	3.5
3Z. Long, prismatic, abraded (1)	5	493	204	180	0.41	16	3609	0.33576±38	5.6840±66	0.12278±4	1866.2±1.8	1928.9±1.0	1997.0±0.6	7.5
4Z. Lg, prismatic, fragment abraded (1)	2	499	188	187	0.38	5	5568	0.35137±37	5.9644±65	0.12311±5	1941.1±1.8	1970.7±1.0	2001.8±0.7	3.5
5Z. Smll, prismatic, fragment abraded (1)	2	249	64	97	0.26	6	2194	0.37341±49	6.3315±90	0.12298±9	2045.4±2.3	2022.8±1.3	1999.8±1.3	-2.7
4245b (Sil-Grt pelitic mylonite)														
1M. Lg, round, yellow (1)	7	3027	102724	10210	33.93	9	49908	0.35193±44	5.7130±71	0.11773±3	1943.8±2.1	1933.3±1.1	1922.1±0.5	-1.3
2M. Pale light yellow fragment (1)	2	3454	71886	7592	20.81	9	14515	0.34883±45	5.6647±65	0.11778±8	1929.0±2.2	1926.0±1.0	1922.7±1.2	-0.4
3M. Lg, subrounded, yellow (1)	5	2353	54955	5722	23.35	6	40279	0.36048±43	5.8418±66	0.11754±6	1984.4±2.1	1952.6±1.0	1919.1±0.9	-4.0
2Z. Tiny, round, clear (26)	10	475	100	178	0.21	8	13138	0.36361±39	6.5078±71	0.12981±2	1999.3±1.9	2047.0±1.0	2095.4±0.3	5.3

All errors reported at the 1 sigma level.

Errors in the isotopic ratios reflect variations in the last two significant figures (e.g. 0.36862 ± 40 refers to 62 ± 40).

Spl - spinel, Crd - cordierite, Sil - sillimanite, Grt - garnet, Bt - biotite, Cpx - clinopyroxene

Spl-Crd-Sil-Grt-bearing Pelitic Migmatite (861510)

The leucosome of a pelitic migmatite (861510) west of the TMA yielded a single dominant monazite chemical age population (Figure 16). Ages ranged from 1876 to 2117 Ma with four older points (>2260 Ma) within the core of a complexly zoned matrix monazite (Figure 15c). Although each monazite varied in shape, zoning and textural location, individual chemical age histograms (Figure 15) suggest little variability between grains that occur as inclusions within garnet or feldspar. These data correspond to an EM age of 1989±5 Ma from 246 out of 250 analyses of three large (up to 150 μm), round to elongate monazites (Figure 15, 16a).

Five monazite fractions were selected for U-Pb TIMS ages (Table 11). A few of these fractions consisted of single crystals that weighed between 2-11 μg with U and Th concentrations between 1647 to 3131 ppm and 33520 to 79712 ppm, respectively. The U-Pb monazite data are shown in Figure 16b and yielded two groups of single analyses, one group with a $^{207}Pb/^{235}U$ weighted average of 2013.9±4.8 Ma (2M and 3M) and a second group (4M and 5M) best represented by a near concordant fraction (4M) with a $^{207}Pb/^{206}Pb$ model age of 2065.9±1.6 Ma. A single, large, subhedral grain with irregular internal fractures (861510-2M) plotted on concordia with a $^{207}Pb/^{206}Pb$ age of 2012.7±1.6 Ma. The large error ellipse for this analysis is due to large measurement errors in the $^{207}Pb/^{205}Pb$ and $^{238}U/^{235}U$ ratios. Larger than normal measurement errors in $^{207}Pb/^{205}Pb$, $^{207}Pb/^{206}Pb$ and $^{207}Pb/^{208}Pb$ ratios accounts for the larger error ellipse for fraction 3M. Fraction 1M contains a higher total common Pb of 31 pg likely due to analysis of a group (34) of small, clear, spherical crystals. A single, yellow, subhedral crystal (861510-5M) yielded the most reversely discordant analysis.

The U-Pb monazite data may be presented in two different ways. Because analyses 2M and 3M are somewhat less precise, the isotopic ratios may in fact plot below concordia. Regression of fractions 1M, 3M, and 4M defines a line with an upper intercept age of 2063.3 +3.9/-2.9 Ma with a low % probability of fit (Figure 16b). According to the error expansion routine from the U-Pb age calculation program of Davis (1982), the upper intercept age lowers slightly to 2060.6 +9.1/-36.1 Ma. Alternatively, fractions 4M and 5M could be recording a separate ca. 2065 Ma event from a less well constrained ca. 2014 Ma event recorded by fractions 2M and 3M. In this case, the group

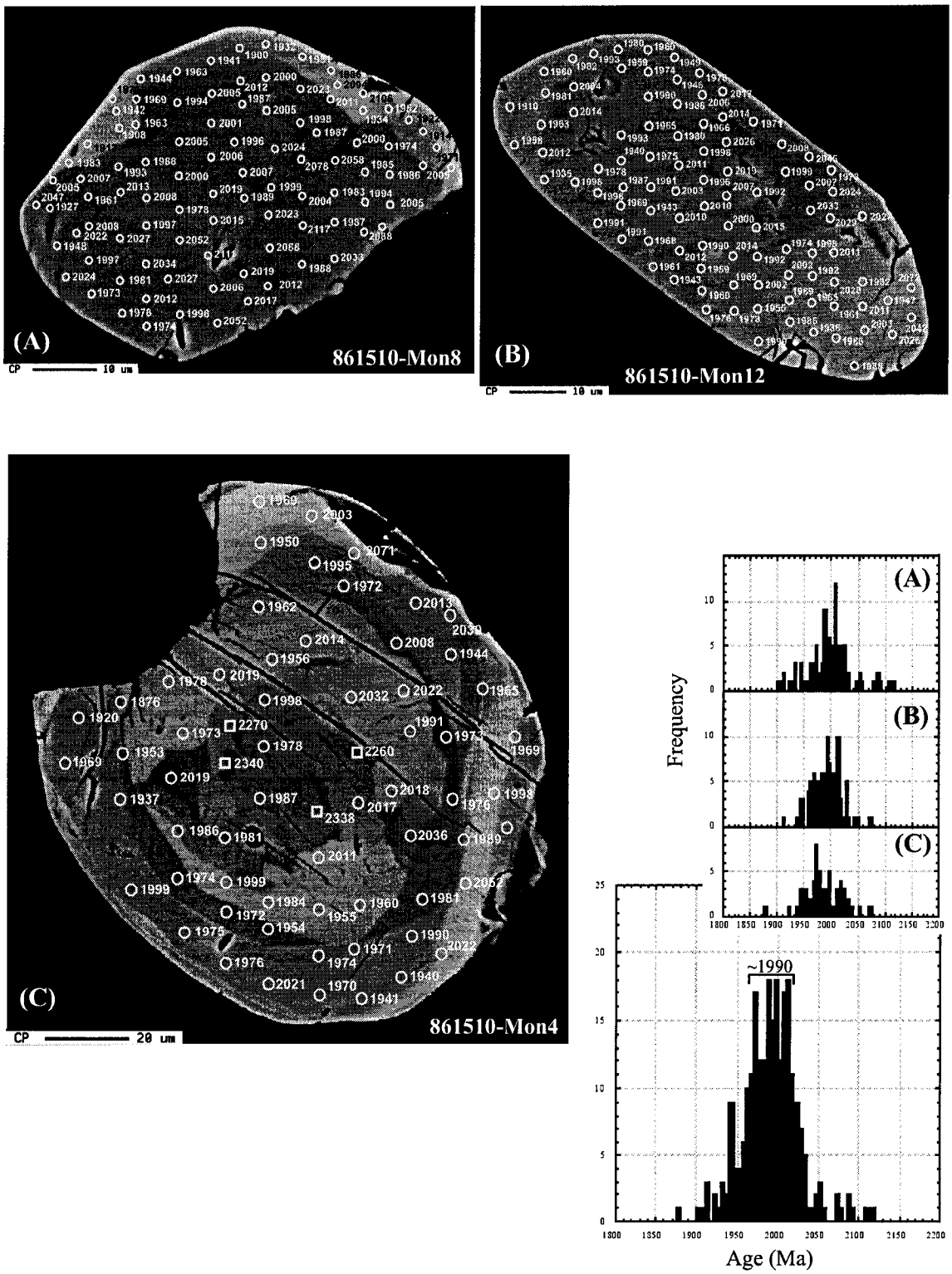

Figure 15. BSE images of monazite with chemical ages and histograms for a Spl-Crd-Sil-Grt pelitic migmatite (861510); (A) Mon8 as inclusion in garnet, (B) Mon12 aligned within perthite and approximately with the overall fabric of the rock and (C) Mon4 along grain boundaries in the matrix. Square symbols represent older ages not used in Th* vs. Pb plot fitting.

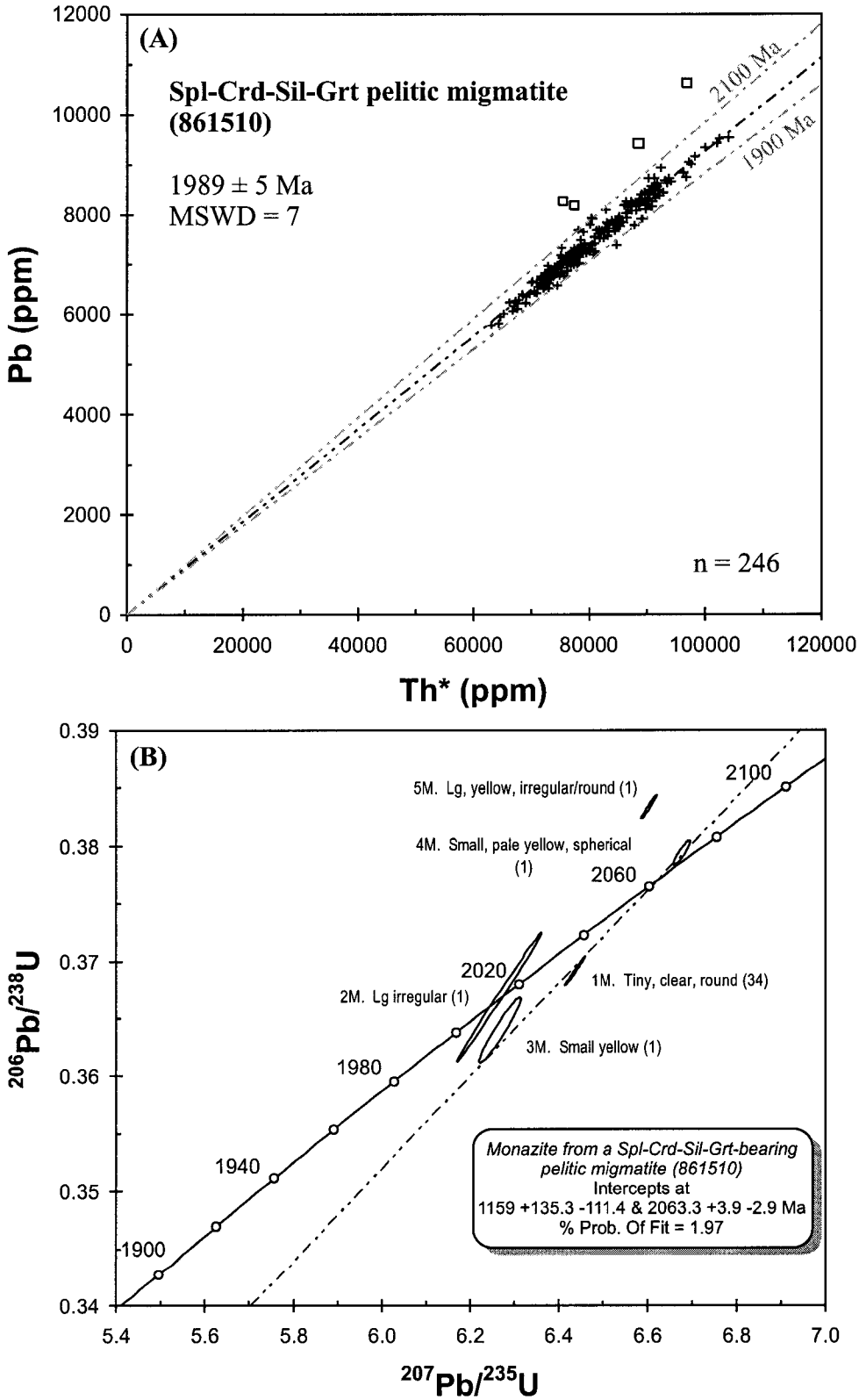

Figure 16. (A) Th* vs. Pb concentrations (ppm) for monazite chemical ages and (B) concordia diagram for TIMS isotopic analyses of monazite for pelitic migmatite (861510). Crosses and ellipses are at 2σ error. Squares are older ages not used in Th* vs. Pb plot fitting.

of monazite grains from fraction 1M could record mixing of two separate age populations or discordant older grains. Both scenarios imply ages that are older and more complex than the single, ca. 1989 Ma age population recorded by monazite chemical ages from the leucocratic portion of the migmatite.

Sil-Grt-Bt-bearing Pelitic Gneiss (861380, 861420)

Sil-Grt-Bt pelitic gneisses (861380 and 861420) yielded single monazite chemical age populations of 1979±8 and 1950±4 Ma, respectively (Figures 17, 18). Four monazite grains investigated from 861420 reveal little age variation between grains (Figure 17). Of 134 analyses, only one was rejected. Monazites from both samples were very Th-rich yielding ample Pb concentrations for electron microprobe measurement.

Bt±Grt-bearing Gneiss (860781, 860880, 861740, 861790)

Large, irregular matrix monazites in gneissic sample 860781 within the TMA yielded chemical ages ranging from 1786 to 2041 Ma with a cumulative age population of 1966±9 Ma (Figure 19, 20a) calculated excluding only 5 of 112 analyses from Th-rich patches (~30% ThO_2), near fractures or along the grain rim. Separate Th* vs. Pb plots of a large, anhedral monazite and a small, spherical monazite grain (Figure 20b) yielded chemical ages of 1980±12 Ma and 1956±23 Ma, respectively (Figure 20b), suggesting anhedral monazites may reflect some breakdown prior to another episode of monazite growth.

A Bt-Grt gneiss (860880) along the eastern border of the TMA reveals up to three age populations of 2011±7 Ma, 1921±8 Ma and 1865±12 Ma from two large, oval, moderate to elongate monazites weakly aligned with fabric and variable ThO_2 wt% compositions (5 to 20 wt%) (Figure 21). Only one analysis (2533 Ma) was excluded from calculation. EM age populations appear to correspond with chemical zoning in monazite grains with the oldest population generally occurring within the center of the grain and the youngest population along the margins matching lighter colored areas in BSE image.

Biotite gneisses (861740 and 861790) from the northern tip and northwest of the TMA yielded multiple age populations. A single grain from 861740 yielded a core age of 1988±21 Ma and rim age of 1910±26 Ma, from 22 analyses (Figure 22). Sample 861790

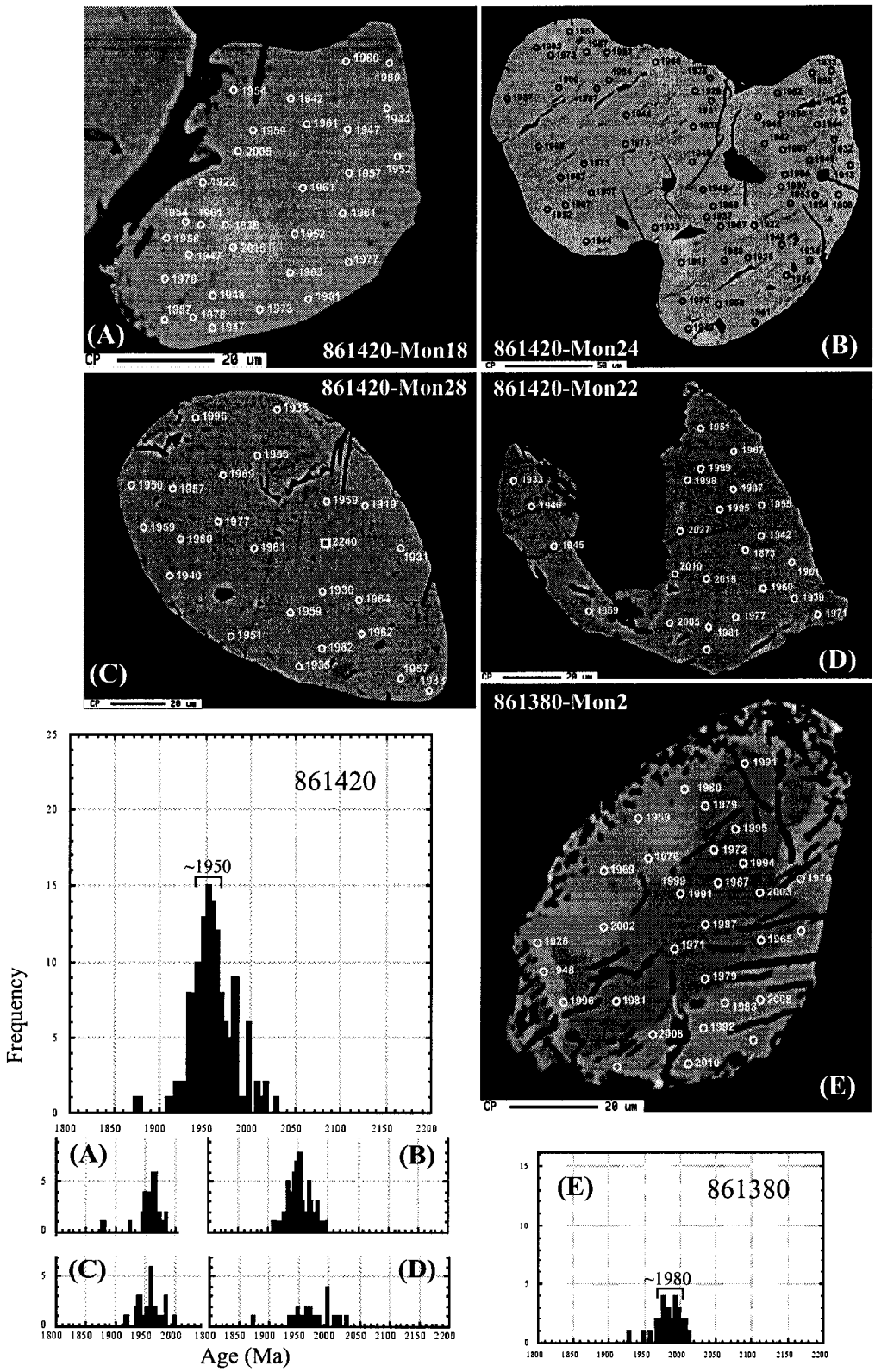

Figure 17. BSE images of monazite with chemical ages and histograms for Grt-Sil-Bt gneiss (861420); (A) Mon18 included in perthite, (B) Mon24 along grain boundary, (C) Mon28 in matrix quartz, and (D) Mon22 included in biotite/perthite. Age histograms for each grain indicate minimal variability except for (D). Sil-Grt-Bt gneiss (861380-Mon2) (E) is weakly aligned with matrix fabric. Square symbols represent older ages not used in Th* vs. Pb plot fitting.

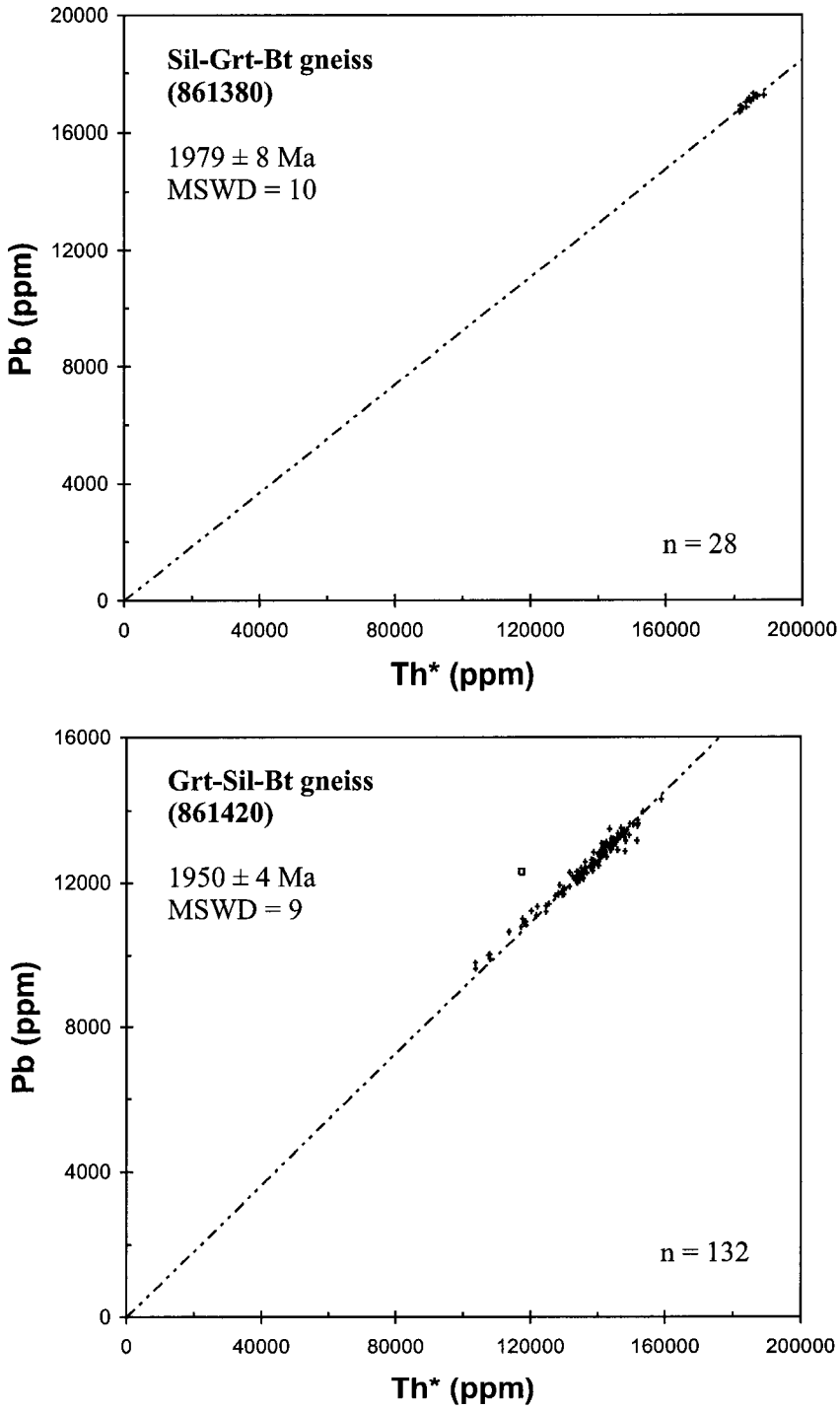

Figure 18. Th* vs. Pb concentrations (ppm) for monazite chemical ages for Sil-Grt-Bt gneiss (861380) and Grt-Sil-Bt gneiss (861420). Crosses are at 2σ error. Squares represent older ages not used in Th* vs. Pb plot fitting.

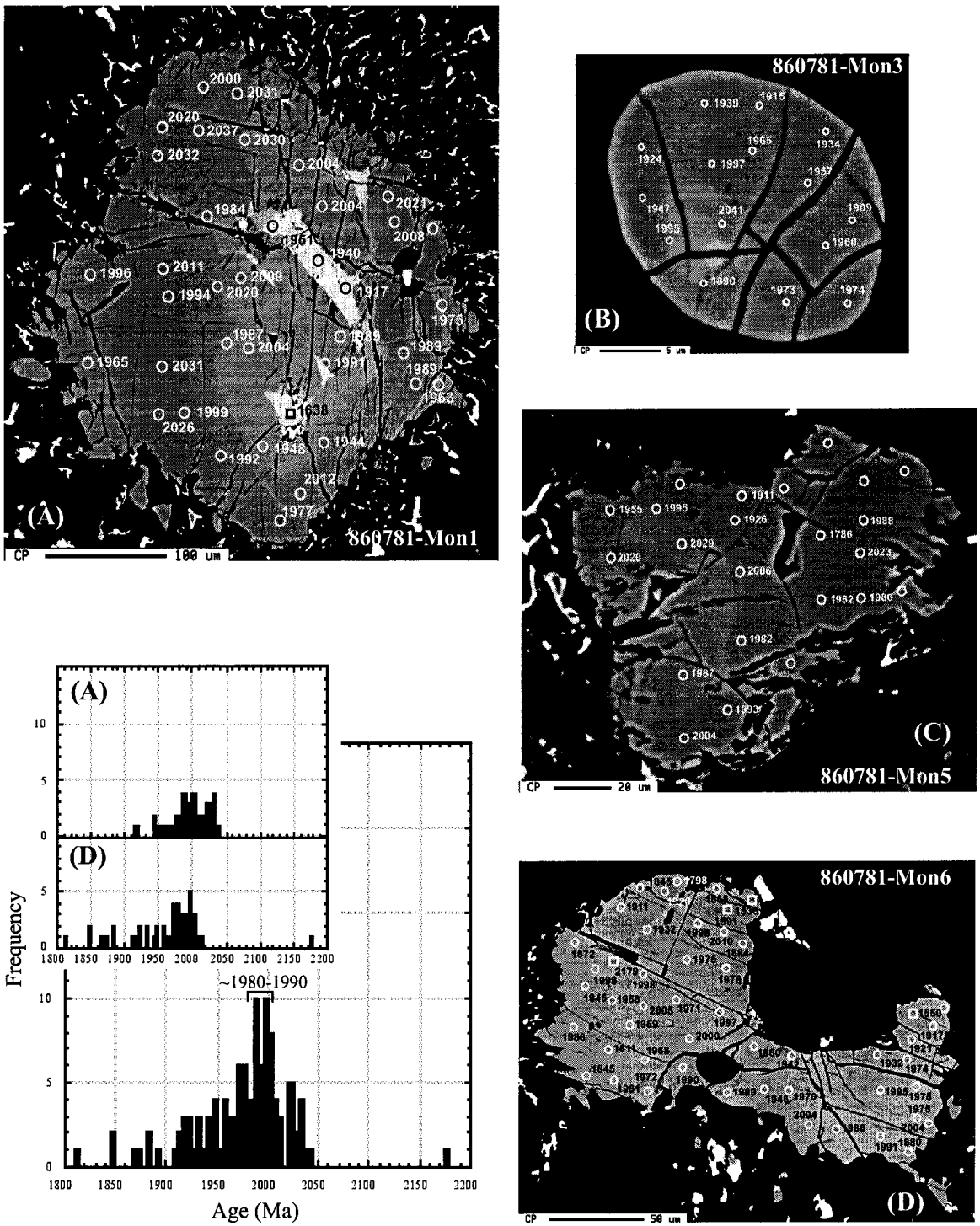

Figure 19. BSE images of monazites with chemical ages and histograms for Bt gneiss (860781); (A) Mon1, (B) Mon3 and (C) Mon5 within matrix quartz whereas (D) Mon6 within matrix quartz and plagioclase. (A) and (C) appear weakly aligned with fabric defined by fine-grained mortar. Individual age histograms for (A) and (D) suggest minimal age variation between larger monazite grains. Square symbols represent older ages not used in Th* vs. Pb plot fitting..

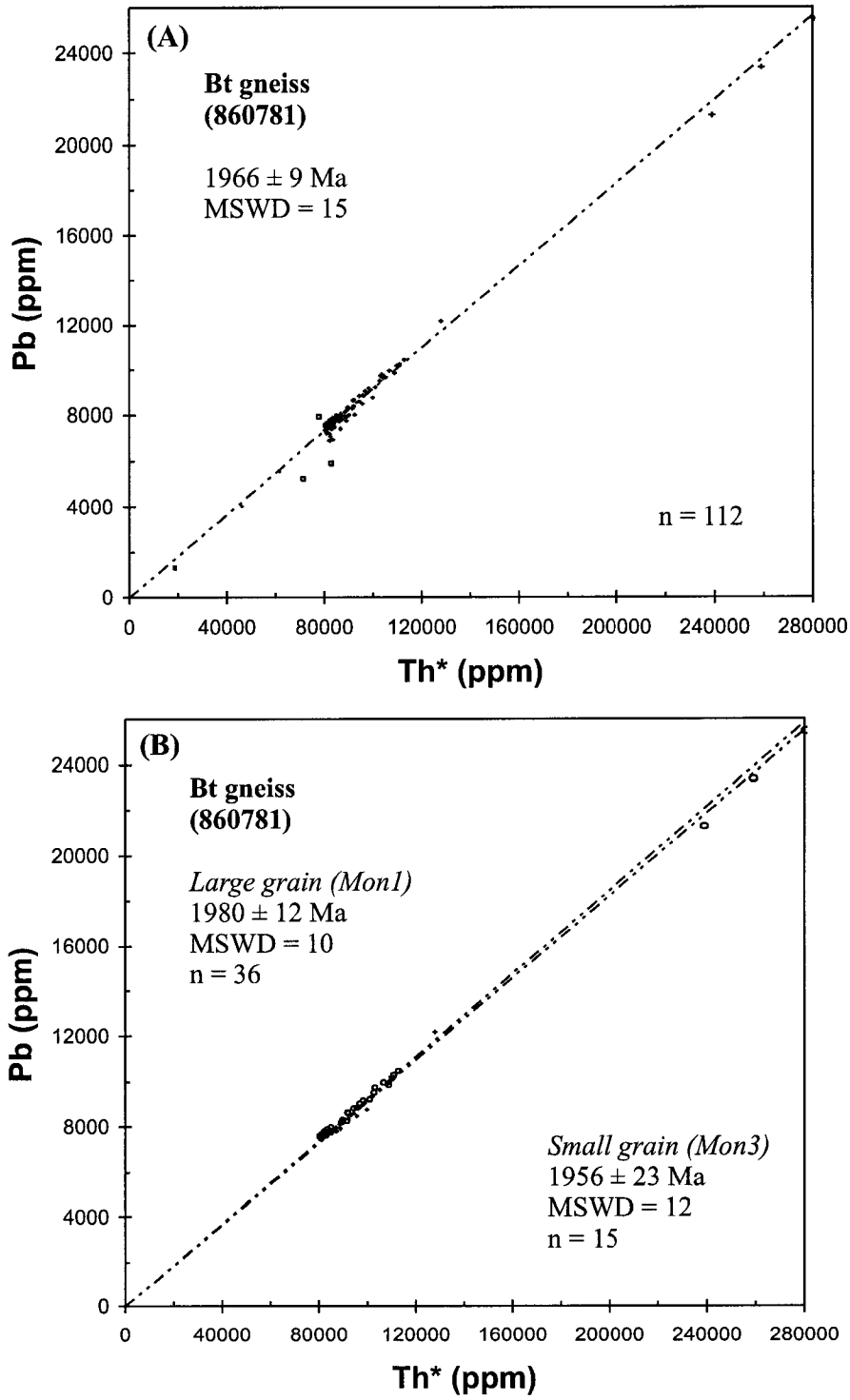

Figure 20. Th* vs. Pb concentrations (ppm) for monazite chemical ages for Bt gneiss (860781) including individual large and small grains. Crosses and ellipses are at 2σ error. Squares represent older ages not used in Th* vs. Pb plot fitting.

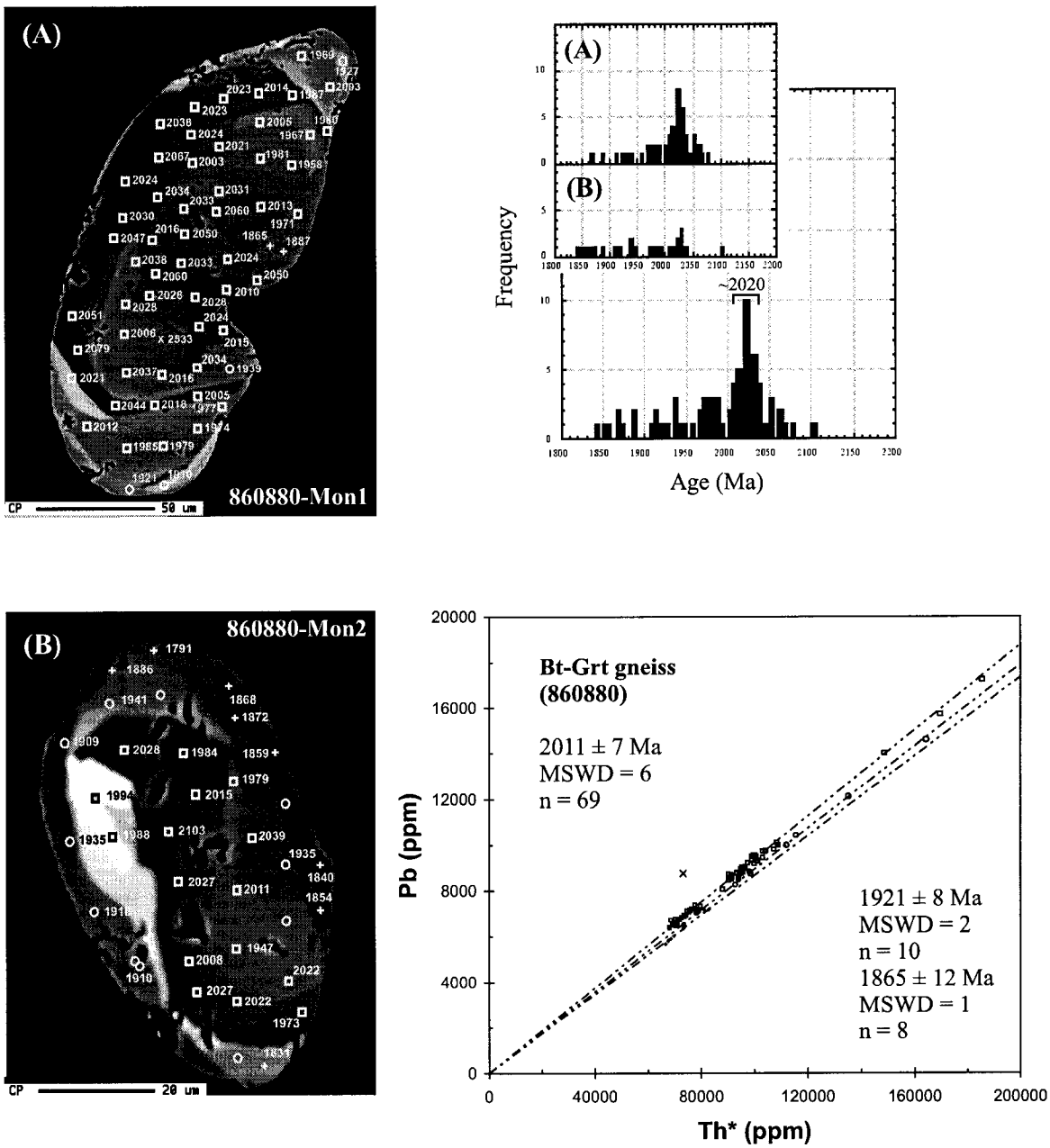

Figure 21. BSE images of monazites with chemical ages and histograms for Bt-Grt gneiss (860880); (A) Mon1 within matrix quartz and (B) Mon2 within K-feldspar. Both grains appear weakly aligned with gneissic fabric. Individual age histograms suggest a similar spread in chemical ages between grains. Th* vs. Pb concentrations (ppm) plotted at 2σ error. Symbols match Th* vs. Pb plot with a single older age not used in Th* vs. Pb plot fitting represented by a cross.

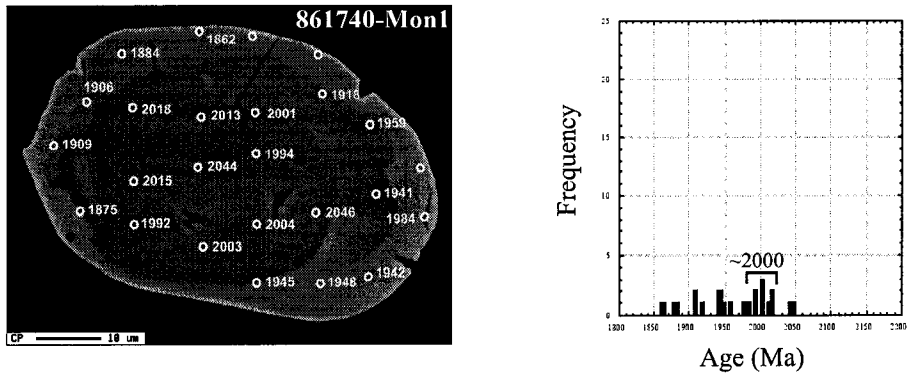

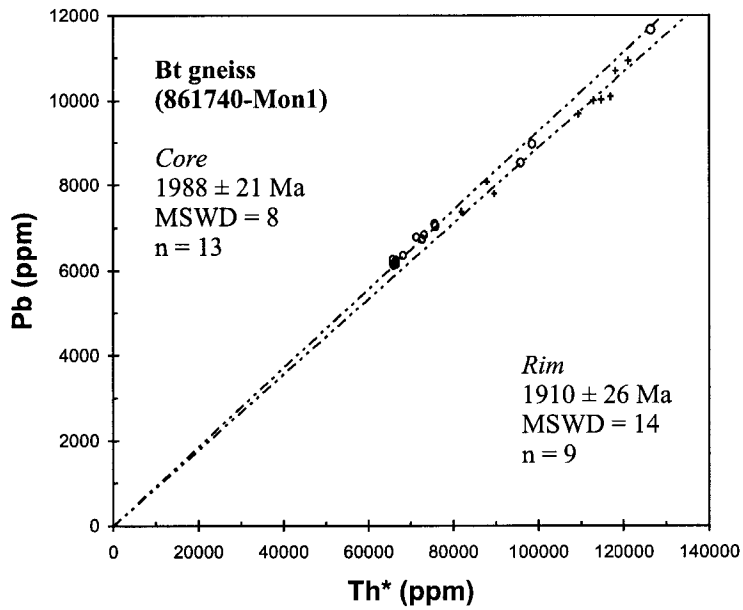

Figure 22. BSE images of monazites with chemical ages and histogram for Bt gneiss (861740-Mon1) with monazite inclusion in perthite. Th* vs. Pb concentrations (ppm) plotted at 2σ error.

was plotted two different ways. A multiple age population of all analyses yields ages of 2007±7 and 1906±12 Ma (Figure 23d) whereas a single grain (861790-mon5) yields a core age of 1967±41 Ma and rim age of 1908±18 Ma (Figure 23e).

Charnockite (860220, 860770, 860380)

Opx-bearing rocks yielded less well-defined chemical ages from very small and irregularly shaped monazite. A large, elongate, fractured monazite from a Bt-Cpx charnockite (860220) has a thorite/huttonite region present along one side of the grain (Figure 24a). Histograms indicate broadly scattered ages, even from small irregular inclusions in pyroxene, with an approximate age of 1897±13 Ma from 32 of 87 analyses (Figure 25a). Charnockite (860770) contained one large grain weakly aligned in the foliation with a similar thorite/huttonite centre (Figure 24b) and yielded an age of 1921±26 Ma (Figure 24d). Th, U and Pb concentrations of monazite from both samples indicate thorite/huttonite has not affected the composition of the surrounding monazite grain (Table 9). Only one small, subhedral monazite was found in thin section of a retrograded charnockite (860380) (Figure 24c) and records an age of 1893±9 Ma (Figure 24e).

TIMS analysis of Bt-Cpx Charnockite (860220)

Single zircon crystals with the greatest clarity and free of fractures were strongly to lightly abraded for analysis for Bt-Cpx charnockite (860220). Zircons record moderate U and Th contents of 310 to 688 ppm and 112 to 382 ppm, respectively (Table 11). Th/U ratio ranges from 0.36 to 0.56, similarly to Th/U ratios of zircon recorded from igneous rocks (Ahrens et al., 1967). Despite differing shapes, two single, large, abraded, elliptical (~3:1) (860220-1Z) and spherical (860220-2Z) zircons recorded similar and nearly concordant data with $^{207}Pb/^{206}Pb$ model ages of 2019.9±0.8 Ma and 2015.6±1.6 Ma, respectively, clustering on and slightly above concordia with no indication of inheritance from an older protolith (Figure 25b). Another single, spherical abraded zircon (860220-3Z) from the same abraded fraction and a smaller and lightly abraded elliptical grain (860220-5Z) were selected to see if any age variation exists. These fractions yielded reversely discordant ages, which will be discussed further below. Abraded, spherical fractions (2Z, 3Z) yielded differing $^{207}Pb/^{206}Pb$ model ages of 2015.6±1.6 Ma and

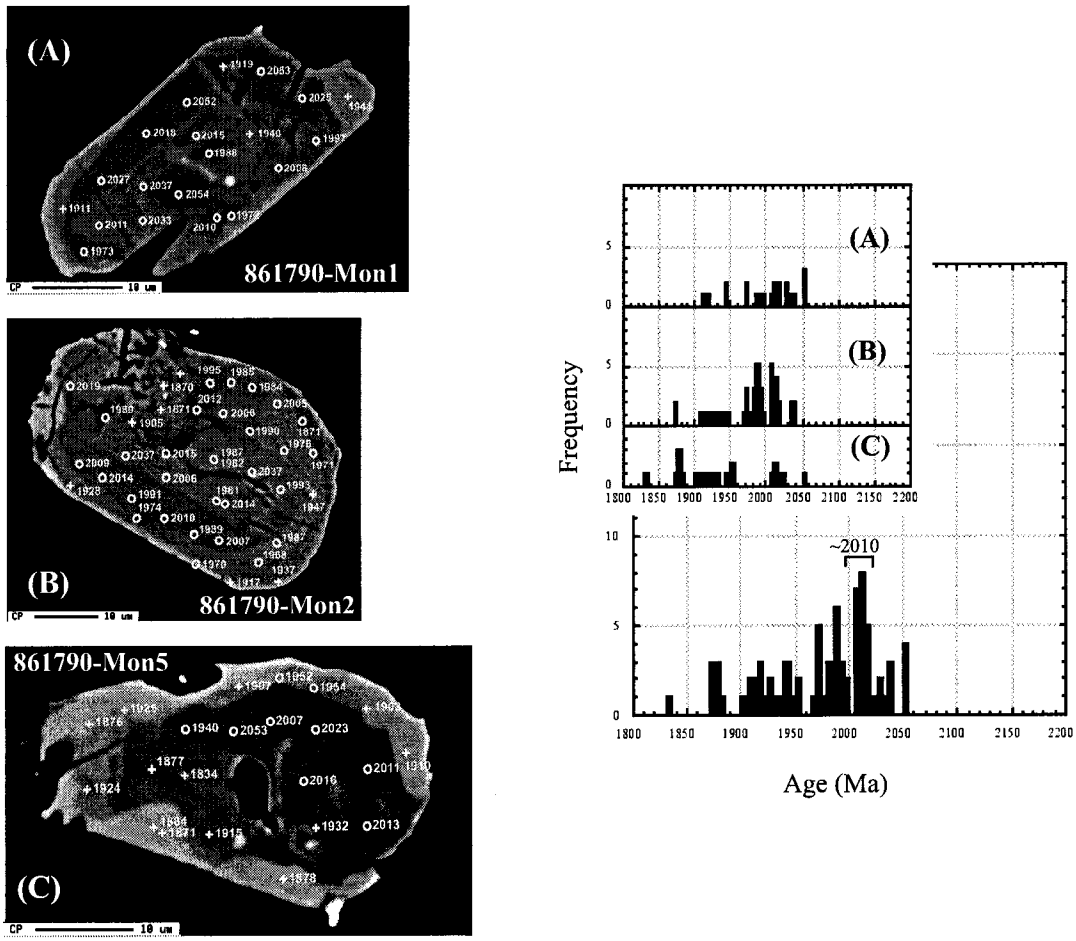

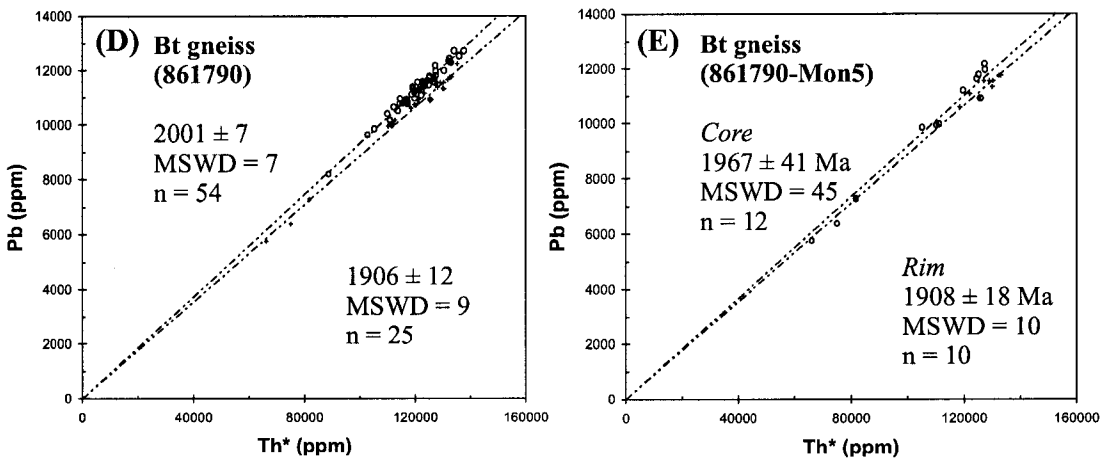

Figure 23. BSE images of monazites with chemical ages and histograms for Bt gneiss (861790); (A) Mon1, (B) Mon2, and (C) Mon5. All monazite grains occur as inclusions in perthite. Individual age histograms suggest a similar spread in chemical ages between grains. Th* vs. Pb concentrations (ppm) for monazite chemical ages (D), including individual grain Mon5 (E), with ages plotted at 2σ error. Symbols match Th* vs. Pb plot with the exception of (C) 861790-mon5 where symbols match core-rim zoning of Th* vs. Pb plot.

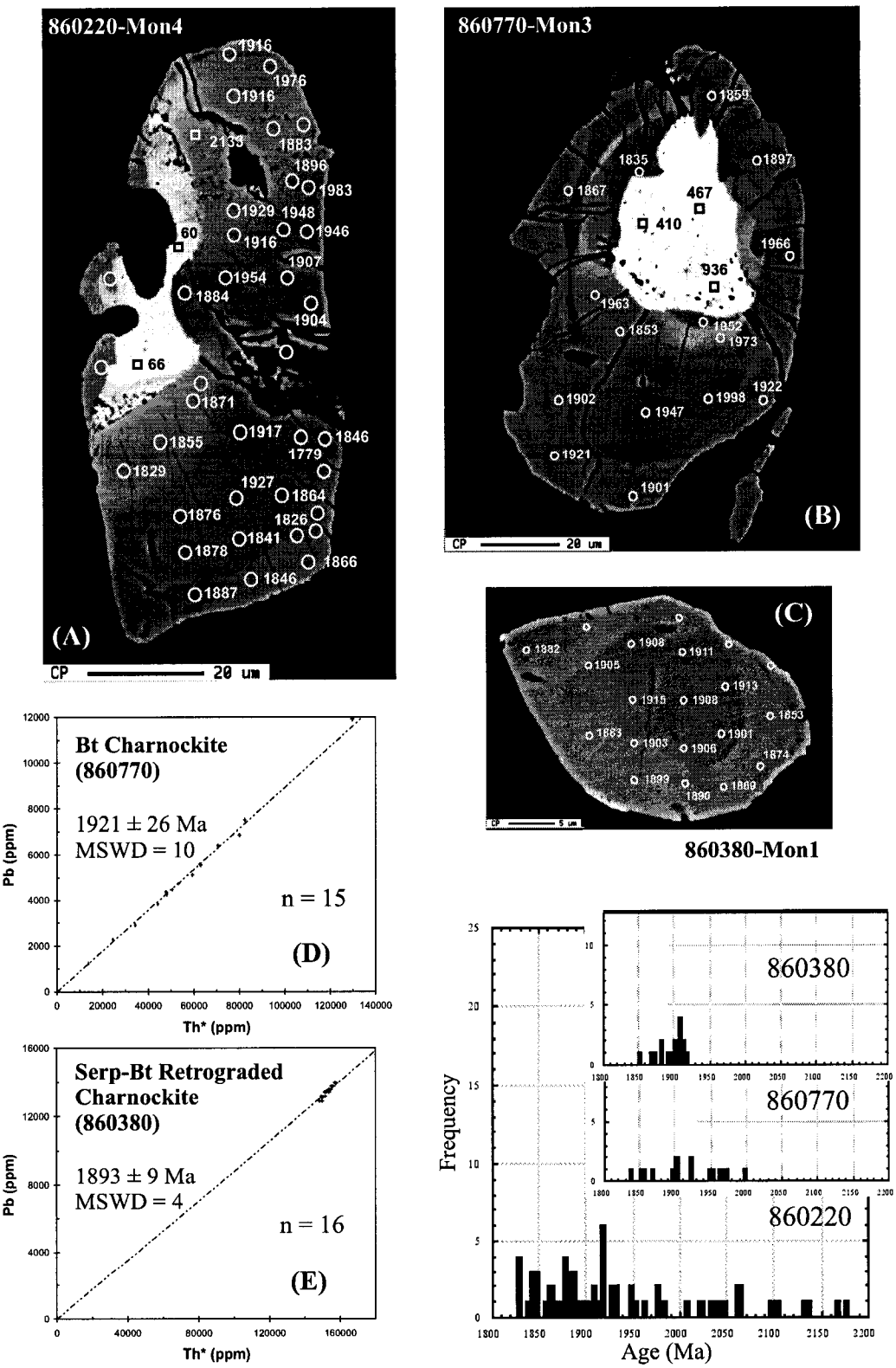

Figure 24. BSE images of monazites with chemical ages and histograms for (A) Bt-Cpx charnockite (860220-Mon4) within matrix quartz, (B and D) Bt charnockite (860770-Mon3) aligned with biotite fabric, and (C and E) Serp-Bt retrograded charnockite (860380-Mon)1 within blocky K-feldspar antiperthite lamellae. Th* vs. Pb concentrations (ppm) plotted at 2σ error. Square symbols represent older ages not used in Th* vs. Pb plot fitting.

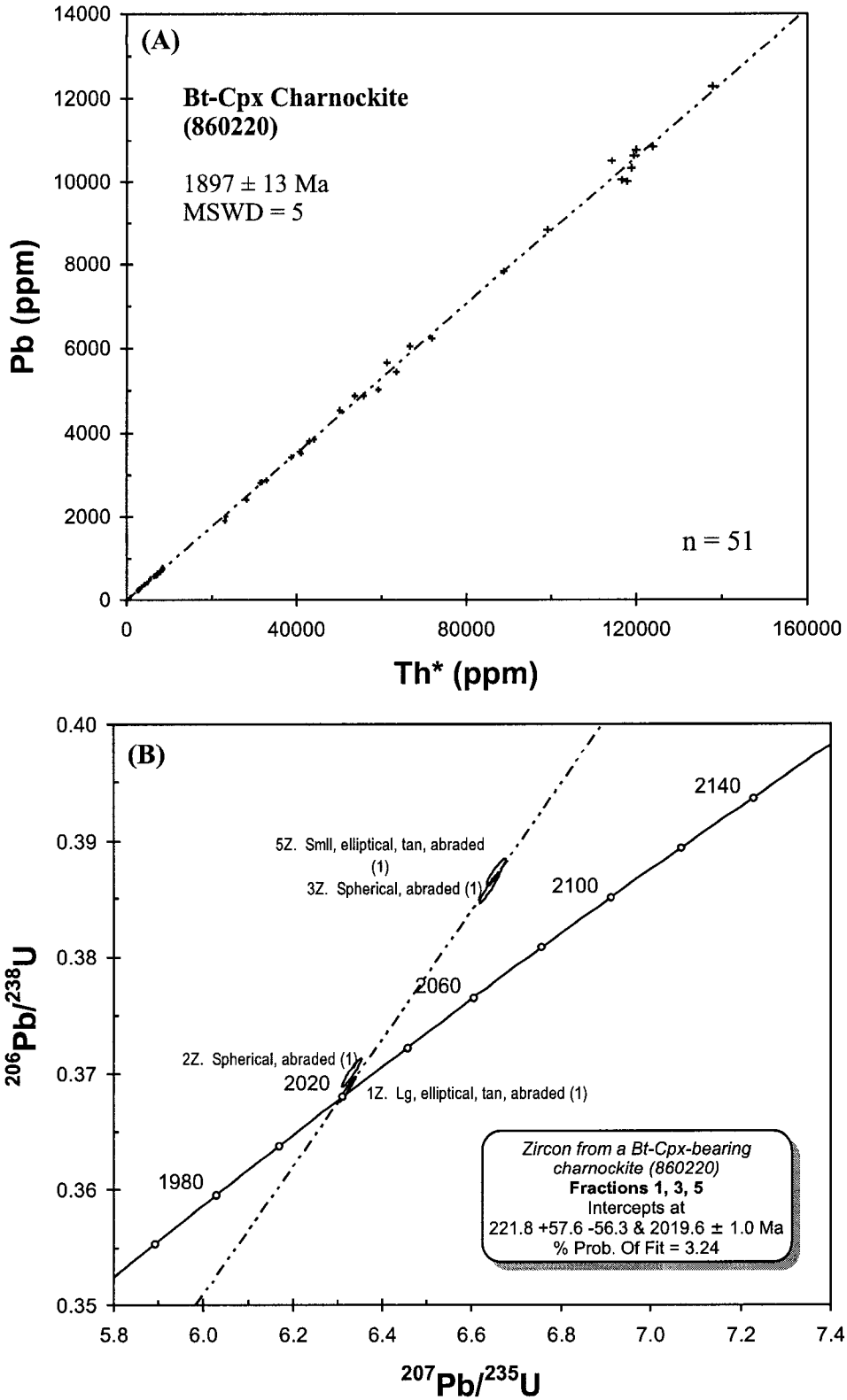

Figure 25. (A) Th* vs. Pb concentrations (ppm) for monazite chemical ages and (B) concordia diagram for TIMS isotopic analyses of zircon for Bt-Cpx charnockite (860220). Crosses and ellipses are at 2σ error.

2025.8±1.4 Ma, respectively. A weighted average of $^{207}Pb/^{206}Pb$ model ages of 2025±14 Ma for 3Z and 5Z gave the lowest MSWD of 3.7 (fractions 1Z and 2Z yielded 2019 ± 22 Ma, MSWD = 23). Age calculation of fractions 1Z, 3Z and 5Z yields an intercept age of 2019.6±1.0 Ma (% probability of fit = 3.24) coinciding with nearly concordant fractions 1Z and 2Z. As discussed further below, this age could be interpreted as either a metamorphic or an igneous crystallization age. An igneous origin is supported by Th/U ratios from zircon.

Granitoid (4240, 860970, 860140)

Four elongate or oval, slightly fractured and/or pitted monazite grains from biotite granite within the TMA (4240) yielded heterogeneously distributed monazite chemical ages ranging from 1865 to 2042 Ma. One grain (4240-mon5, Figure 26b) suggests a core-rim age zonation corresponding to compositional zonation with chemical ages of 2007±23 Ma, 1928±12 Ma and 1880±17 Ma (Figure 27a). Approximately two major cumulative probability peaks (Figure 12) indicate an older age of 2017±10 Ma and a dominant population of ages at 1923±6 Ma, which approximates age zoning reflected by this single monazite crystal. Three of 88 analyses were rejected from the rim of a fractured or very small grain.

Two small, irregular or elongate monazite grains were investigated from biotite granite (860970) west of the TMA (Figure 28e, f) and reveal no consistent spatial or chemical pattern to ages within each grain. A single age population of 1999±7 Ma (62 analyses with 3 points >2083 Ma not used in the age calculation from a small irregular grain) reflects an age distribution more comparable to ca. 2000 Ma gneisses than biotite granite (4240) (Figure 29a).

Ages obtained from four monazite grains from Grt-bearing granite at the southern tip of the TMA (860140) vary considerably from ca. 1910 to 1980 Ma (Figure 28a-d). Small grains (<15 μm) indicate some susceptibility to Pb loss or resetting therefore mainly the largest grain was used to approximate an age from histogram. Calculation of a Th* vs. Pb age was not completed due to the low Th concentration in the monazite (Table 10).

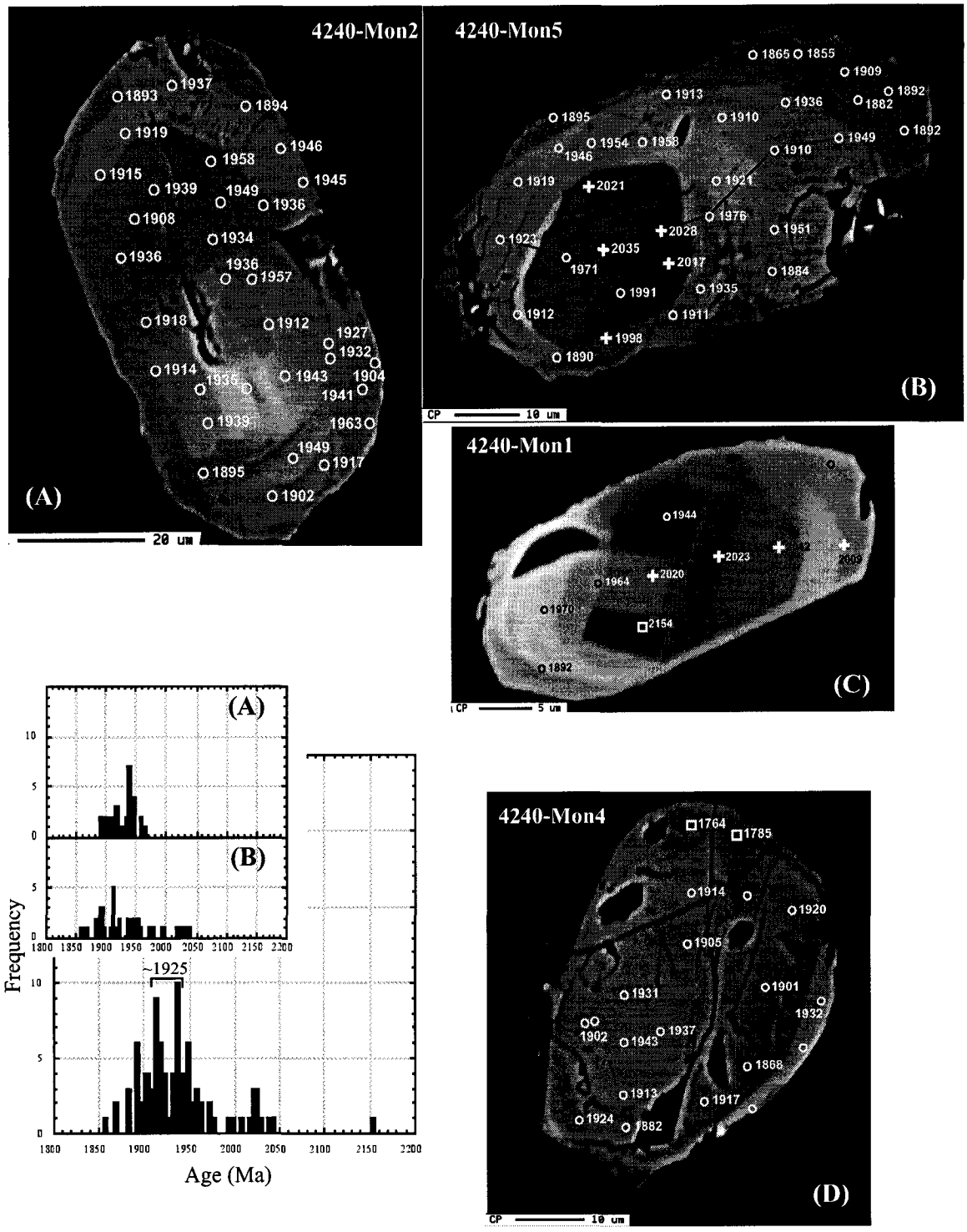

Figure 26. BSE images of monazites with chemical ages and histogram for Bt granite (4240); (A) Mon2 and (B) Mon5 within K-feldspar, (C) Mon1 within plagioclase,and (D) Mon4 within matrix. Individual age histograms for (B) and (D) indicate slight age variability. Black line across length of grain (D) represents chemical profile. Symbols match Th* vs. Pb plot with older ages not used in plot fitting represented by squares.

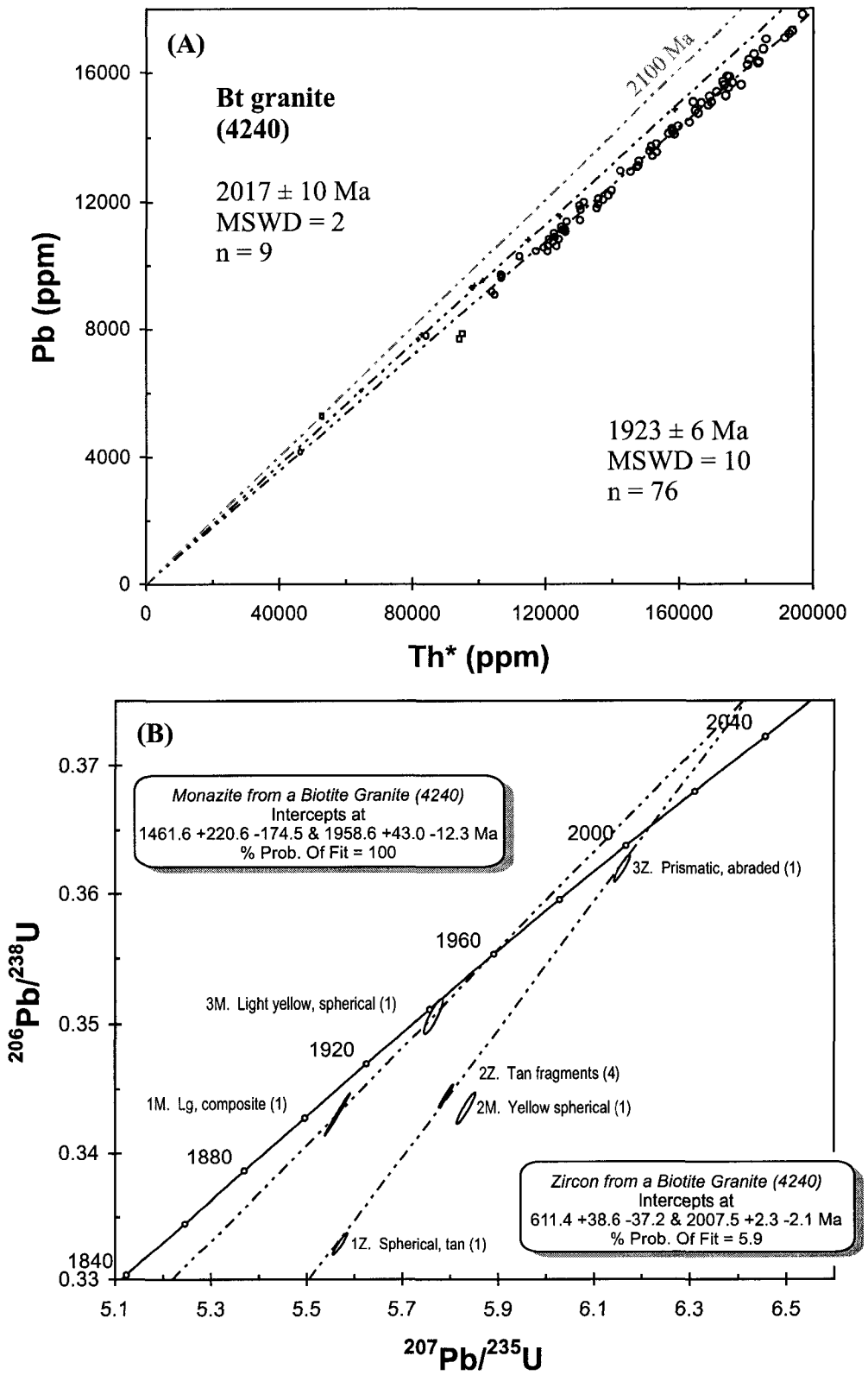

Figure 27. Th* vs. Pb concentrations (ppm) for monazite chemical ages and concordia diagram for TIMS isotopic analyses of monazite and zircon for Bt granite (4240). Crosses and ellipses are at 2σ error. Squares represent older ages not used in Th* vs. Pb plot fitting.

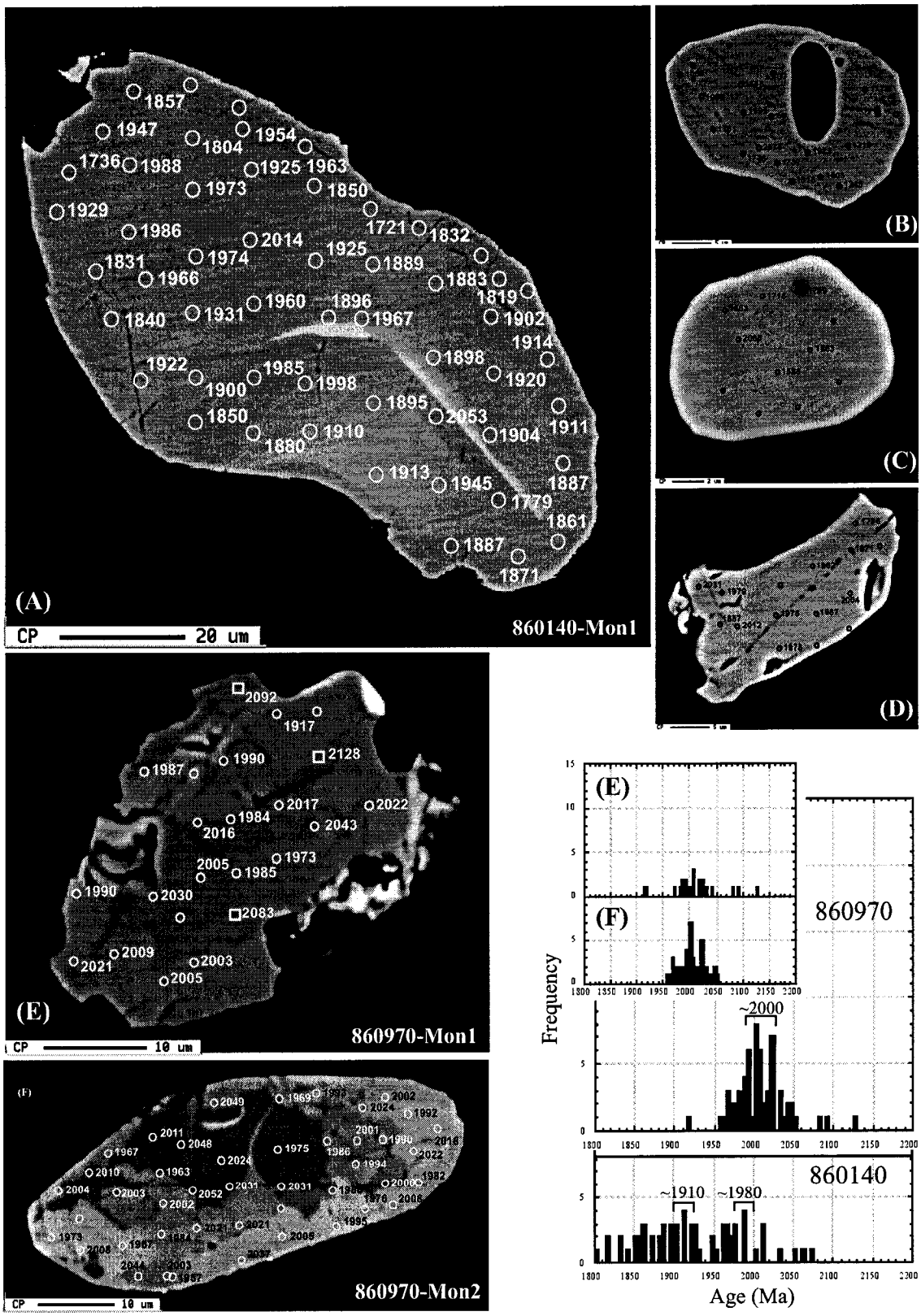

Figure 28. BSE images of monazites with chemical ages and histograms for Grt granite (860140); (A) Mon1 and (B to D) small grains. Bt granite (860970) (E) Mon1 included in garnet and (F) Mon2 within matrix plagioclase. Individual histograms (E and F) indicate little variation. Squares represent older ages not used in Th* vs. Pb plot fitting.

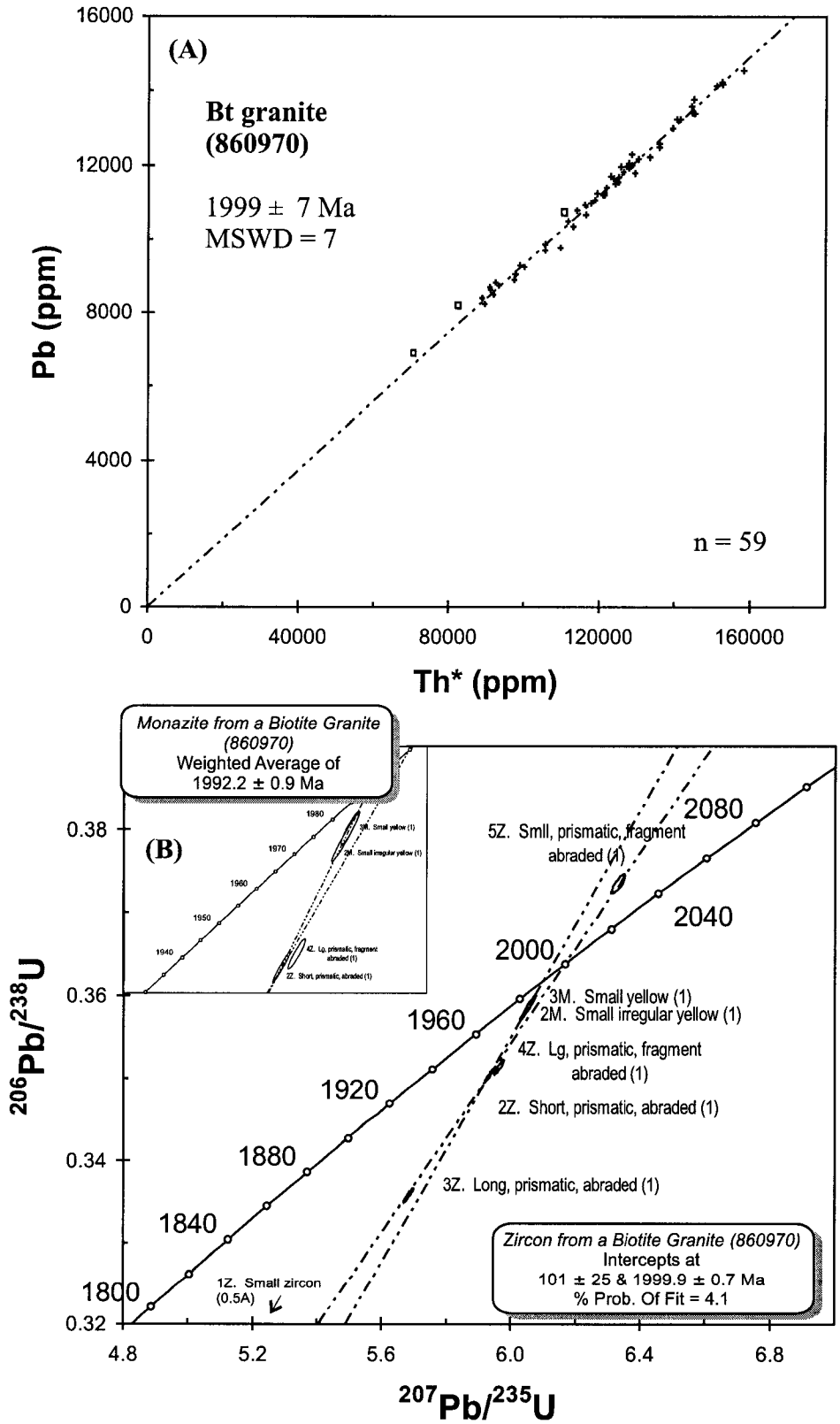

Figure 29. (A) Th* vs. Pb concentrations (ppm) for monazite chemical ages and (B) concordia diagram for TIMS isotopic analyses of monazite and zircon for Bt granite (860970). Crosses and ellipses are at 2σ error. Squares represent older ages not used in Th* vs. Pb plot fitting.

TIMS analysis of Bt Granite (4240) within the TMA

Three zircon fractions from this sample showed varying degrees of discordance. The most concordant analysis was obtained from an abraded, single, pale yellow-tan, subhedral to euhedral, bypyramidal (2-3:1) crystal (4240-3Z), which yielded a $^{207}Pb/^{206}Pb$ age of 2006.2±0.8 Ma, with larger than normal measurement error on the $^{207}Pb/^{205}Pb$ and $^{238}U/^{235}U$ atomic ratios. Zircon records a high U content ranging between 1502 to 1643 ppm, moderate Th content ranging between 150 to 217 ppm and a low Th/U ratio of 0.09-0.12. A regression line of all three zircon analyses through this abraded crystal yields an upper intercept age of 2007.5 +2.3/-2.1 Ma with a low % probability of fit. The error expansion routine of Davis (1982) improves the probability of fit with minimal change in the age of the upper intercept (2010.2 +12.8/-10.4 Ma). This upper intercept age could reflect either a magmatic age with subsequent lead loss or a metamorphic age, as suggested by the low Th/U ratios of all three grains (e.g. Hoskin and Black, 2000).

Three monazite fractions reveal differing $^{207}Pb/^{206}Pb$ model ages and Th concentrations, with larger measurement errors on $^{207}Pb/^{206}Pb$ (for 3M) and $^{207}Pb/^{205}Pb$ atomic ratios. A line between two of the three single monazite fractions defines an upper intercept age of 1958.6 +43.0/-12.3 Ma (Figure 27). A small, light yellow, spherical grain (4240-3M) recorded the most concordant result with a $^{207}Pb/^{206}Pb$ model age of 1945±2.6 Ma. A large composite monazite (4240-1M) yielded a $^{207}Pb/^{206}Pb$ model age of 1920.8±0.6 Ma, similar to the younger 1923±6 Ma chemical age peak. However, this analysis recorded the highest amount of common Pb (124 pg) of all grains analyzed in this study, likely due to the composite nature of the grain. The most discordant monazite was a spherical yellow grain (4240-2M) with very high Th and U concentrations. The large degree of discordance may reflect mixing of two age components, an older component with a ca. 2017 Ma age similar to that recorded in some of the chemical dates for this sample and a much younger Th-rich, thorite/huttonite, component such as seen in Figure 35. Compared to zircon results, the younger monazite upper intercept likely records metamorphic or cooling ages.

TIMS analysis of Bt Granite (860970) west of the TMA

Two single fractions of irregular pale-yellow colored (860970-2M, 3M) monazite yielded nearly concordant $^{207}Pb/^{206}Pb$ ages of 1992.3±1.2 Ma and 1992.0±1.4 Ma, respectively. The $^{207}Pb/^{206}Pb$ weighted average of 2M and 3M yielded 1992.2 ± 0.9 Ma (Figure 29b).

Abraded columnar zircons were also analyzed in attempt to determine if monazite analyses reflect granite emplacement or a metamorphic age. Two abraded single grains and two fragments of abraded single grain fractions were chosen from grains with the least amount of internal turbidity. Regressing various combinations of these 5 fractions to better the % probability of fit yields a narrow age range from ca. 1998.5 to 2000.7 Ma, therefore choosing the age with the most fractions (four of five) records an upper intercept of 1999.9±0.7 Ma, not including 4Z but including a highly discordant zircon from the 0.5A separation. Not including this latter highly discordant grain decreases the upper intercept age to 1998.5±1.2 Ma (% probability of fit = 42.04). A ca. 1997 Ma $^{207}Pb/^{206}Pb$ model age is recorded by both abraded prisms (2Z and 3Z) whereas abraded prism fragments yield slightly older ca. 2000 Ma $^{207}Pb/^{206}Pb$ model ages. All four abraded prism and abraded prism fragments have U concentrations less than 852 ppm, in contrast to high U concentrations of biotite granite within the TMA. The smallest abraded prism fragment (5Z) recorded a reversely discordant analysis, the lowest U, Th and Pb concentrations and some variability in $^{207}Pb/^{205}Pb$ and $^{207}Pb/^{204}Pb$ atomic ratios. Excluding this fraction yields no change in upper intercept age and error. Th/U ratios range between 0.26-0.41, similar to that typically reported for zircons in felsic igneous rocks (Ahrens et al., 1967). $^{207}Pb/^{206}Pb$ model ages between monazite and zircon differ up to ~10 Myr, suggesting zircon and monazite could be recording a separate episode of monazite growth ~10 Myr after granite emplacement or zircon and monazite could be recording similar magmatic ages but monazite experienced lead diffusion and cooling from this event.

Sil-Grt-bearing Pelitic Mylonite (4245b)

Analysis of three monazite crystals from a Sil-Grt-bearing mylonite (4245b) reveals two distinct age populations depending if monazite grains occur as inclusions in

garnet or in the rock matrix (Figure 30). Regression of data from the two grains included in garnet yielded a monazite chemical age of 1913±4 Ma (Figure 31a) whereas regression of data from the matrix grain yielded a younger age of 1875±4 Ma (Figure 31b).

Three single grain monazite fractions yielded reversely discordant isotopic analyses (Figure 32), which will be discussed below. These analyses fall on a regression line intersecting concordia at 1923.5±1.3 Ma (Figure 32). A light pale yellow fragment (4245b-2M) yielded the most concordant result with a $^{207}Pb/^{206}Pb$ model age of 1922.7±2.4 Ma, similar in age to 1M. A discordant, large, subrounded, patchy yellow grain (4245b-3M) yielded a $^{207}Pb/^{206}Pb$ model age of 1919.1±1.8 Ma. $^{207}Pb/^{204}Pb$ atomic ratios were high and total common lead blank was acceptable for these grains indicating the presence of little common lead. A group of 26 tiny, clear, colorless and round zircons (4245b-2) were selected for correlation with monazite ages but recorded a discordant $^{207}Pb/^{206}Pb$ model age of 2095.4±0.6 Ma. BSE imaging of larger zircon crystals revealed multicomponent grains consisting of metamorphic overgrowth surrounding a detrital igneous core.

Summary

EM and TIMS dating revealed three main clusters of ages:

- Ca. 2020 Ma to 1980 Ma ages generally represent the oldest cluster of ages, except for one older TIMS monazite age at ca. 2065 Ma from pelitic migmatite. Ages recorded in this range include TIMS zircon ages from charnockite and granite. Also, TIMS and EM monazite ages from monazite core from a granite, Bt gneisses, and pelitic migmatite and gneiss.
- Ca. 1960 Ma to 1910 Ma ages generally represent an intermediate cluster of ages defined by EM monazite ages from pelitic gneiss, Bt gneiss, and EM and TIMS monazite ages from pelitic mylonite (inclusions) and granite.
- Ca. 1910 Ma to 1865 Ma ages generally represent the youngest cluster of ages defined exclusively by EM monazite ages from pelitic mylonite, Bt gneiss, monazite rims from granite and Bt gneiss, and charnockite.

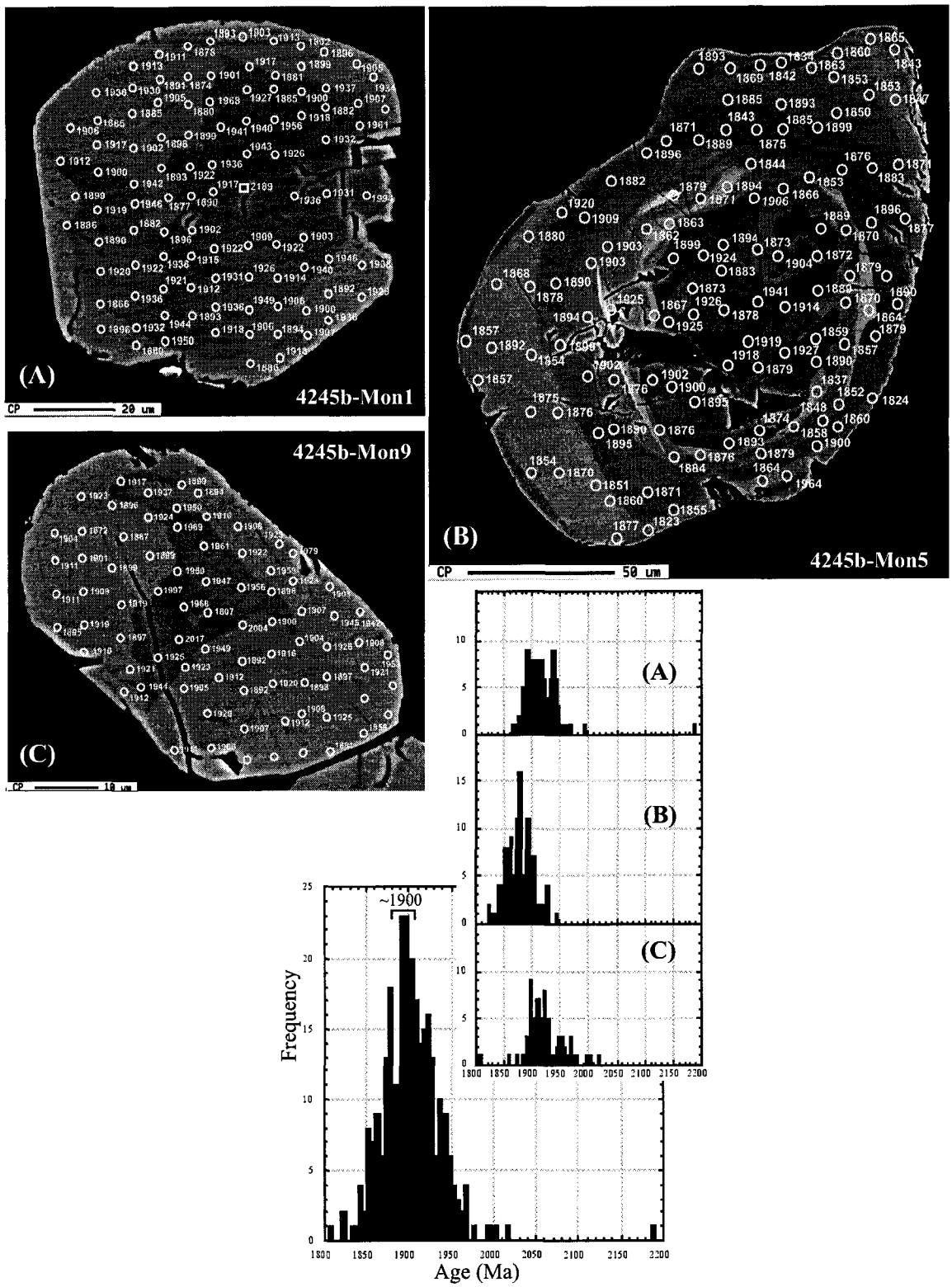

Figure 30. BSE images of monazites with chemical ages and histogram for Sil-Grt pelitic mylonite (4245b); (A) Mon1 and (C) Mon9 included in garnet, and (B) Mon5 within matrix quartz. Individual age histograms indicate monazite inclusions in garnet retain slightly older ages than matrix monazite. Black line across length of grain (A) represents chemical profile. Square symbols represent older ages not used in Th* vs. Pb plot fitting.

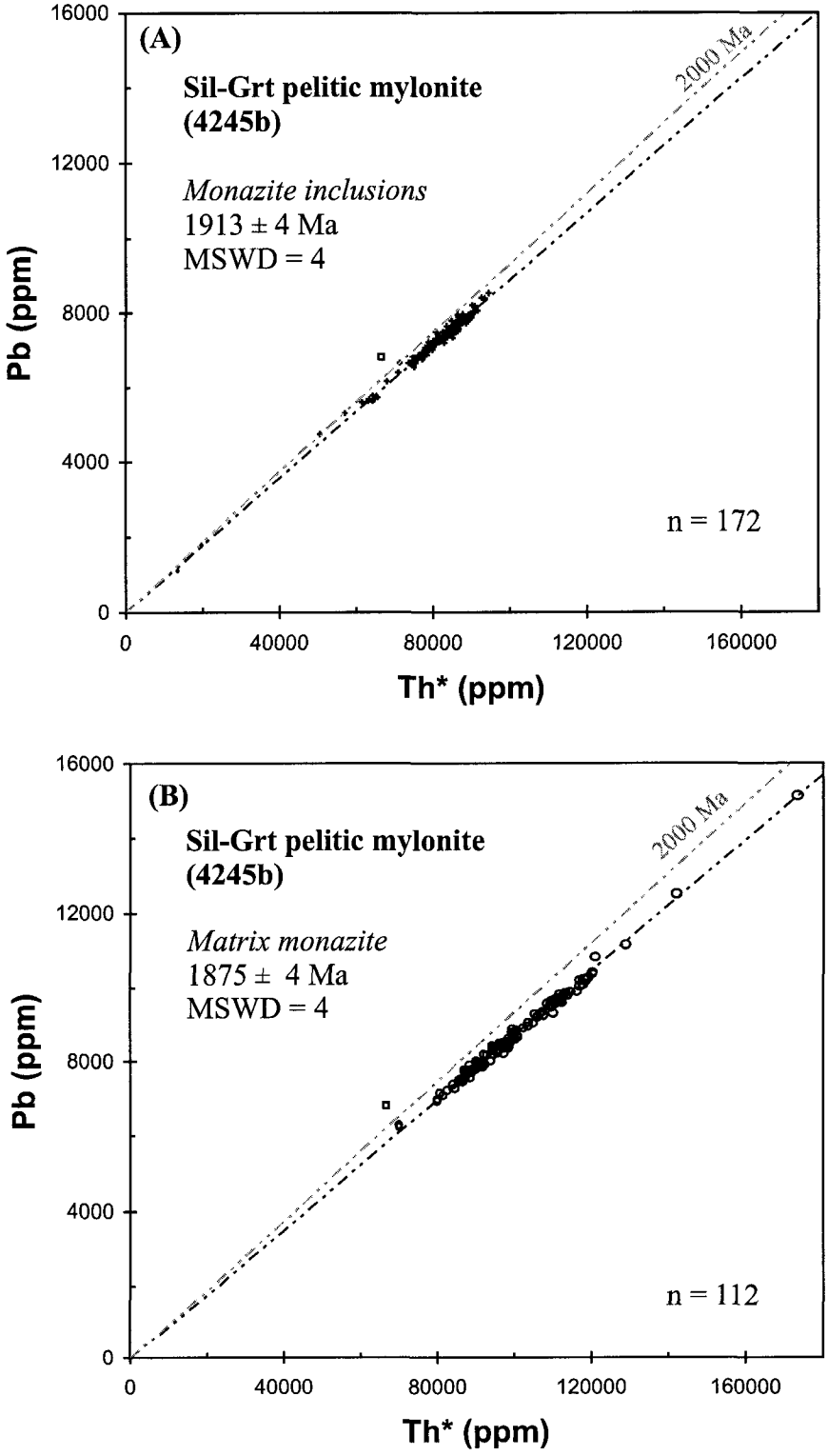

Figure 31. Th* vs. Pb concentrations (ppm) for monazite chemical ages for Sil-Grt pelitic mylonite (4245b). Crosses are at 2σ error. Squares represent older ages not used in Th* vs. Pb plot fitting.

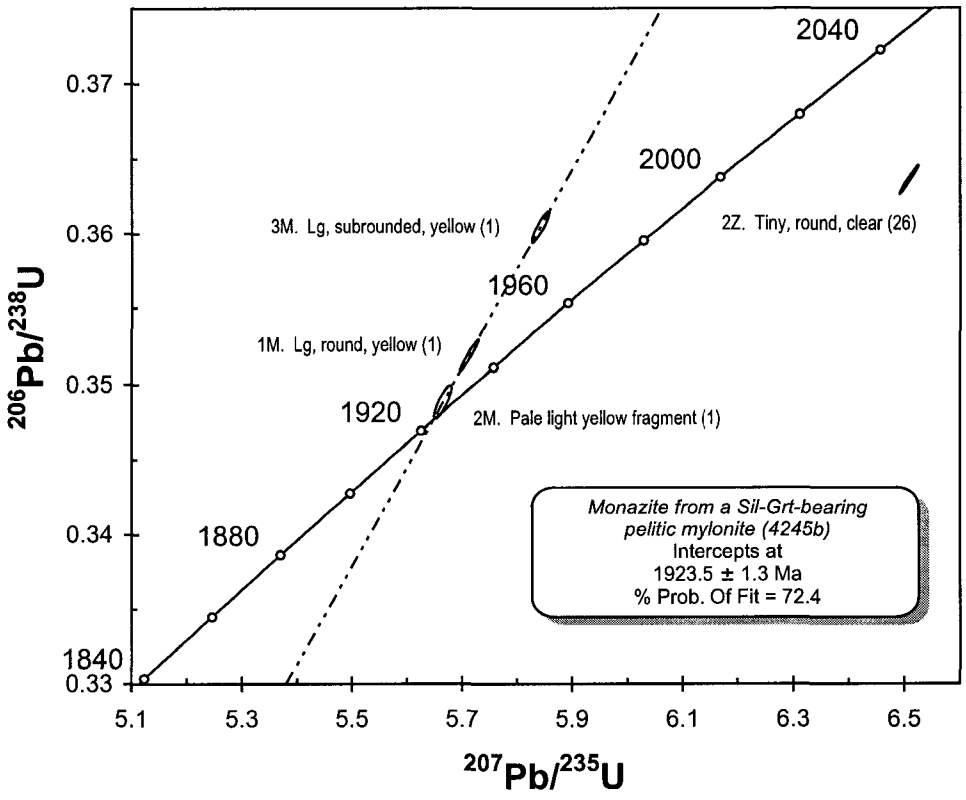

Figure 32. Concordia diagram for TIMS isotopic analyses of monazite for Sil-Grt pelitic mylonite (4245b). Ellipses are at 2σ error.

Discussion

Comparison of EM and TIMS Ages

Monazite ages obtained for the same sample with chemical and isotopic methods are generally in good agreement. For example, there is excellent correspondence of ages for Bt granite (860970) and Sil-Grt-bearing mylonite (4245b). In sample 860970, U-Pb zircon ages record the same age (ca. 1999 Ma) as monazite using the EM method whereas isotopic monazite ages are about 10 Myr younger. EM ages from monazite inclusions and TIMS age determinations for 4245b agree within 7 Myr.

A more complex history is recorded by Bt granite (4240), pelitic migmatite (861510) and charnockite (860220). The EM monazite data for sample 4240 indicate a major age population at ca. 1920 Ma and secondary age population at ca. 2020 Ma. The TIMS monazite data for this sample more closely reflect the younger chemical age peak (ca. 1960 Ma) whereas TIMS zircon data for this sample coincide more closely with the older chemical age peak (ca. 2010 Ma). The TIMS monazite ages derived from sample 861510 could be recording up to two groups of ages 25 and 70 Myr older than the major chemical age population for the sample. Possible reasons for these discrepancies are discussed below. Charnockite recorded the least well-defined and scattered chemical age population. Generally, monazite EM ages are much younger (>100 Myr) than U-Pb zircon ages and must record an entirely different event. The overall conclusion that can be drawn from this comparison of EM and TIMS results is that the EM technique provides reconnaissance age information that is very useful in selecting samples for more precise (and time consuming) TIMS analysis.

Reverse Discordance in Monazite and Zircon

More than 30% of the monazite and zircon analyses performed in this study show the unusual characteristic of reverse discordancy, which has not previously been reported in BH domain rocks (Villeneuve et al., 1993). Samples 4245b and 860220 both record monazite and zircon analyses, respectively, which plot in a linear pattern above concordia and yield a narrow range of $^{207}Pb/^{206}Pb$ model ages. The common explanation given for reverse discordance is that of Schärer (1984) who noted that incorporation of one of the short-lived ^{238}U daughter products, ^{230}Th, produces unsupported ^{206}Pb in monazites,

which can lead to their reverse discordance. However, rocks older than 200 Ma generally do not need correction for unsupported ^{206}Pb because the great majority of ^{206}Pb in these older samples is the result of ^{238}U decay (Schärer, 1984; Heaman and Parrish, 1991; Parrish, 1990). Therefore, reverse discordance in Precambrian monazite is not common as the amount of radiogenic Pb accumulated over time is far greater than the minor amount of unsupported lead incorporated initially upon crystallization (e.g. Heaman and LeCheminant, 2000). Below, several other analytical and natural possibilities are examined for potential causes of reverse discordance in monazite and zircon U-Pb data.

Possible explanations for the reversely discordant data include; a) thallium isobaric interference skewing $^{207}Pb/^{205}Pb$ atomic ratios, b) poor measurement of U and Pb atomic ratios, c) incomplete dissolution of the grain in bomb, or d) a natural occurrence of uranium loss or lead gain. Only two analyses (3Z and 5Z from sample 860220) show any evidence for thallium interference in the analytical routine. Although analyses of fractions 3Z and 5Z suggest the presence of thallium in the first few blocks of atomic ratios measured by the mass spectrometer, the constancy of atomic ratios in the remaining 15 blocks of data, which cover at least two temperature intervals, indicates that thallium was burned off early in the analytical routine and did not significantly affect the reported atomic ratios. Of all the reversely discordant analyses reported in Table 11, only analyses from sample 860220 had larger than normal errors in measurement of uranium isotopic ratios. Thus, poor analytical precision cannot provide a general explanation for the reverse discordancy observed in this study. Incomplete dissolution of zircon or monazite grains in the digestion vessel with preferential lead dissolution is possible but it is unlikely that such small (2 to 7 μg) grains would not dissolve after 3 days, even if stuck to the side of the vessel.

Reverse discordance in zircon is even less common and implies preferential loss of U relative to Pb from the zircon grain. This is contrary to the results of diffusion experiments (e.g. Pidgeon et al., 1966; Lee et al., 1997), which indicate Pb mobility is far greater than U or Th mobility in the zircon structure. Mattinson et al. (1996) outline 'internal' and 'external' mechanisms for producing reverse discordance in zircon. Internal mechanisms involve redistribution of Pb within parts of the zircon grain by spatial decoupling of radiogenic Pb from the U or Th parent atom. Therefore, ion

microprobe analysis of individual spots on a zircon grain could yield local reversely discordant results due to redistribution of radiogenic Pb into otherwise U-poor areas. This explanation cannot be applied to results in the present study because TIMS analyses involve dissolution of the whole grain rather than localized spot analyses. External mechanisms are more likely to be the cause of reverse discordance in whole zircon populations. This mechanism involves selective removal of U from more susceptible radiation damaged U-rich portions of a zircon crystal by fluids leaving behind U-poor areas. Preferential loss of U relative to Pb from zircon by oxidizing fluids would be particularly effective in this regard. In the zircon structure, U in its oxidized form (6+) is much more soluble than in reduced form (4+) because the reduced form substitutes readily for Zr^{4+}. Therefore, U^{6+} is more easily mobilized from the zircon crystal. Importantly, removal of uranium will not have a major impact on $^{207}Pb/^{206}Pb$ ages provided that it is a relatively recent phenomenon (e.g. U removal occurs post 100 Ma). Although theoretically possible, reverse discordance by addition of radiogenic lead is unlikely because Pb^{2+} does not easily substitute into either Zr^{4+} or Si^{4+} cation sites in the zircon structure. As well, the addition of lead to zircon would increase the concentration of common lead in these analyses, which is not indicated by the $^{206}Pb/^{204}Pb$ ratio.

Several observations made in this study are relevant to possible natural causes for reverse discordance. These include: 1) colorless or nearly colorless monazite in sample 4245b, 2) the presence of thorite/huttonite associated with both monazite and zircon, and 3) the use of drill core samples buried beneath a sedimentary basin. In experiments involving the hydrothermal alteration of monazite, Teufel and Heinrich, 1997, observed their bright yellowish-green monazite starting material became colorless after interaction with ultrapure H_2O fluid. Interestingly, monazite crystals from sample 4245b could not be identified optically because of their very pale yellow coloration or a lack of color altogether, which is uncharacteristic of the commonly yellow color of monazite (Overstreet, 1967). Teufel and Heinrich (1997) did not observe Pb or U loss in monazite fractions in their hydrothermal experiment, but the lack of coloration of monazite crystals in this study suggests the possibility of interaction with a fluid.

The presence of a thorite/huttonite mineral texturally associated with monazite and zircon was observed in several samples of the study. Thorite/huttonite has recently

been suggested to represent a product of hydrothermal alteration of monazite (e.g. Poitrasson et al., 1996; Hecht and Cuney, 2000; Mathieu et al., 2001). The occurrence of thorite/huttonite as inclusions in monazite (e.g. Figure 35e), zircon (e.g. Figure 33) and as single grains (e.g. Figure 11l) could point to recent fluid-rock interaction. The EM ages obtained from select thorite/huttonite grains record a wide span of ages from ca. 900 Ma to ca. 60 Ma. Monazite alteration to Th-silicate in the adjacent Athabasca basin unconformity-related uranium deposit (Hecht and Cuney, 2000) is remarkably similar to the textural relationships observed between these minerals in the present study. Unique to this study is the use of drill core samples from the buried basement beneath ~1.5 km of sedimentary rocks of the Western Canadian Sedimentary Basin. These samples were taken from the base of oil wells from the Red Earth and Utikuma oilfields (TMA) near the Precambrian - Phanerozoic unconformity. Drill core at this boundary is likely more susceptible to low-temperature fluid interaction through large-scale fracture conduits and crystal micro-fractures. For example, altered monazite within hydrothermally overprinted areas has been recorded up to ~200 m in depth below the basement unconformity of the Athabasca basin (Hecht and Cuney, 2000). Also, Burwash and Cumming (1976) point out that unaltered drill core from Alberta and southern Saskatchewan contain an average twice as much U and Th as exposed shield rocks with anomalies coinciding with the Snowbird tectonic zone (Kasba Lake-Edmonton gravity low) and a high U anomaly nearly coinciding with this study area. If oxidizing fluids were introduced in recent geological time, perhaps uranium loss or mobilization resulting in reverse discordance could be expected from both zircon and monazite crystals in buried basement rocks.

Age(s) of High-Grade Metamorphism

A Spl-Crd-Sil-Grt-bearing pelitic migmatite (861510) records a complex array of EM and TIMS monazite ages. Although a few older EM ages are retained, monazite grains from the leucocratic portion of the migmatite record a single, major EM age population at ca. 1989 Ma irrespective of whether these grains occur as simply zoned inclusions in garnet and perthite or as complexly zoned matrix grains (Figure 15). TIMS data, on the other hand, do not record this younger age population but rather two older

populations at ca. 2014 Ma and at ca. 2065 Ma. The ca. 2014 Ma age is the weighted average of fractions 2M and 3M. The ca. 2065 Ma age is the $^{207}Pb/^{206}Pb$ model age of fraction 4M which coincides with an upper intercept age of a 2063 +3.9/–2.9 Ma discordia broadly defined by three monazite fractions (1M, 3M, 4M). The low probability of fit of this discordia is possibly due to the complexity of the TIMS data.

The wide range of monazite ages could be explained in several possible ways. One possibility is that the three ages (ca. 2065, 2014, 1989 Ma) represent three separate episodes of monazite growth, perhaps corresponding to three episodes of metamorphism. The occurrence of the youngest monazite age population at ca. 1989 Ma in the migmatitic leucosome suggests that the putative third episode of metamorphism was high enough grade to induce partial melting.

A second possibility is that one or both of the older ages represent the ages of detrital monazite grains in the sedimentary protolith of the migmatite. This protolith then experienced either one (at ca. 1989 Ma) or two (at ca. 2014 and ca. 1989 Ma) episodes of metamorphism. Some support for a metamorphic event at ca. 2014 Ma is provided by the study of Villeneuve et al. (1993). They report U-Pb data on three dark brown monazite fractions from a Crd-Sil-Bt-Grt paragneiss (Imperial Pelican Hills, 06-10-077-25W4, #42). These discordant monazites were interpreted as partially reset from an older age because they define a discordia between a ca. 2017 Ma U-Pb lower intercept age and a possible ca. 2395 Ma upper intercept age. The lower intercept monazite age corresponds to the U-Pb age (2017 +2/-1 Ma) obtained on round zircons from the same metasedimentary sample, which have been interpreted to record a time of upper amphibolite- to granulite-facies metamorphism (Villeneuve et al. 1993). Thus, the lower intercept monazite age may correspond to the age of high-grade metamorphism and the upper intercept to the age of detrital monazite in the sample. The age of a ca. 2017 Ma high-grade metamorphic event recorded in the Imperial Pelican Hills sample coincides with a ca. 2014 Ma TIMS monazite age recorded in sample 861510. This suggests that the ca. 2014 Ma monazite in this sample is of metamorphic rather than detrital origin.

A third possibility is that the age indicated by the EM technique is erroneously low, and that the monazites analyzed by this technique are in fact one and the same as the younger age recorded by TIMS (ca. 2014 Ma). The accuracy of EM monazite ages is

strongly dependent on the standards chosen for Th, U and particularly Pb analyses, and on the choice of background positions for Pb analysis. A discrepancy of ~25 Myr between EM and TIMS ages is not impossible although it is somewhat larger than the average deviation in ages (~15 Myr) obtained with the two techniques on six in-house monazite standards (see above). Because some samples (e.g. 4245b) analyzed during the same electron microprobe session record EM ages within this average deviation, inaccuracy in standard compositions or background positions is not particularly indicated.

Although a ca. 1989 Ma age peak dominates the EM data for sample 861510, some older EM ages are also recorded in these monazites (Figure 13). In particular, a significant number of EM ages between 2010 and 2020 Ma and smaller number of ages between 2050 and 2070 Ma are recorded from each analyzed monazite grain. Therefore a broad correlation between the EM and TIMS data is present in this sample although each age population is represented in significantly different proportions within these two analytical methods. EM data from sample 861510 also records a scattering of old ages between 2250 to 2350 Ma, which is not recorded by the TIMS data for this sample but reminiscent of the 'detrital' monazite age from Imperial Pelican Hills (Villeneuve et al., 1993).

A clearly defined choice between the three scenarios presented above is precluded by the existing data for sample 861510, except that EM and TIMS data do indicate multiple age populations are present in this sample. An older age population (ca. 2250 to 2350 Ma), which is likely of detrital origin, is weakly recorded by the EM data. A ca. 2065 Ma detrital age or initial period of metamorphism of unknown metamorphic grade is recorded by the TIMS data and to some degree by the EM data. The ca. 2014 Ma TIMS age probably represents a metamorphic age analogous to data from Imperial Pelican Hills paragneiss reported by Villeneuve et al. (1993). The ca. 1989 Ma EM age may be one and the same as a ca. 2014 Ma metamorphic age or indicate a separate episode of metamorphism and melting.

Younger ca. 1960-1910 Ma EM monazite ages are recorded in samples generally local to the TMA, including granite, pelitic and semi-pelitic gneiss, migmatite and mylonite, and a few in charnockite. In particular, a well-defined EM age of ca. 1950 Ma is recorded in a Sil-Grt-bearing gneiss (861420). The high Th and Pb concentration of

the four monazite grains analyzed in this sample result in a relatively precise EM age, which varies little between matrix monazite and monazite included within perthite. Reintegrated perthite compositions from this sample indicate a minimum temperature of 750°C. Thus, this sample must have experienced at least upper amphibolite-grade metamorphic conditions during or after 1950 Ma. Small, spherical monazite from Bt gneiss (860781-mon3) records an EM age of 1956±23 Ma in addition to a ca. 1980 Ma age from large and anhedral monazite (860781-mon1) (Figure 11f). There is also a record of limited ca. 1950 Ma monazite growth in pelitic migmatite (861510, Figure 15). As well, monazite growth may have begun as early as ca. 1950 Ma in pelitic mylonite (4245b) with the main period of growth towards ca. 1920 Ma, as recorded by EM and TIMS data (Figure 15). Collectively, these age data suggest that the TMA, and some of the RGD, experienced a post-2000 Ma high-grade (upper amphibolite- or granulite-facies) metamorphic event. Metamorphism of this age has not previously been recognized in the BH domain, but is widespread in the adjacent Taltson magmatic zone.

Opx-Bearing Rocks – Igneous Charnockite or Metamorphic Granulite Origin?

Burwash and Power (1990) interpreted Opx-bearing rocks of the RGD to be of Archean age overprinted by a Paleoproterozoic metamorphic event. A single Opx-bearing core examined by Villeneuve et al. (1993) from within this study area yielded a poorly constrained U-Pb zircon age of 1991 +225/-41 Ma (Chevron Hunt Creek, 02-17-091-6W5, #47). The complex nature of these rocks is highlighted by their varied interpretation as a granodiorite, granitic gneiss, metamorphic or retrograded granulite and, more recently, as a magmatic charnockite (Ross et al., 1991; Villeneuve et al., 1993; Burwash et al., 1988; Ross et al., 2000). U-Pb zircon ages of ca. 2020 Ma obtained for charnockite 860220 can be interpreted in two fundamentally different ways; 1) This age represents the time at which charnockitic magma crystallized or 2) the sample is of metamorphic rather than magmatic origin and the zircon U-Pb age represents the time of high-grade metamorphism. Opx-bearing metamorphic granulite would have formed from metamorphism of quartzofeldspathic rocks as a consequence of high temperatures attained during granulite-facies metamorphism and simultaneously with pelites that experienced partial melting.

Data obtained in this study provide some support for both of these possibilities. Evidence in support of a magmatic origin includes the fact that antiperthite in some of the charnockitic samples of the TMA record ternary feldspar temperatures of 925-1015°C, which is similar to temperatures reported for charnockite of known magmatic origin (Kilpatrick and Ellis, 1992). Zircon Th/U ratios (0.36-0.56) in 860220 are typical of zircons from felsic magmas and are more in line with a magmatic than a metamorphic origin for the charnockite (Ahrens et al., 1967). The overall morphology of the zircons is also more consistent with a magmatic origin. Metamorphic crystals generally form equant, multi-faceted grains (e.g. van Breemen et al., 1987) unlike the somewhat resorbed or externally altered appearance to these crystals (Appendix D). These zircons define an intercept age of 2019.6±1.0 Ma with no indication of lead loss or inheritance from an older protolith but rather an atypical reverse discordance. Aside from this latter feature, these characteristics suggest a magmatic origin.

On the other hand, except for one zircon grain in thin section (Figure 33), BSE and CL imaging of unabraded zircon separates (Figure 34) do not reveal distinct oscillatory zoning commonly seen in zircons crystallized from granitic magmas (e.g. van Breemen et al., 1987). Rather, the zircons have an unusual internal structure regardless of size or shape. Internally, crystals appear smeared or blurred (in BSE) often with a faint suggestion of remnant oscillatory zoning parallel to crystal faces (e.g. Figure 34e), repetitive fine-scale sector zoning throughout portions of the crystal (e.g. Figure 34d) or weak truncated zoning (e.g. Figure 34g) most clearly seen in CL images. Some crystals show evidence of a thin and fractured overgrowth, although this is not always present. Although these crystals are not structureless, this unique internal structure is unlike either typical oscillatory-zoned magmatic zircon with metamorphic overgrowths or structureless metamorphic zircon. This could imply a metamorphic origin for the charnockite with metamorphic zircon growth occurring during high-grade metamorphism.

Zircons with an elliptical morphology are the most common zircon type in this rock. $^{207}Pb/^{206}Pb$ model ages from large and small elliptical and spherical fractions vary little implying that the zircon crystals formed at nearly the same time. If this rock represents a metamorphic granulite from a quartzofeldspathic protolith, it would be likely that some inherited zircon from this older protolith would be present. Because evidence

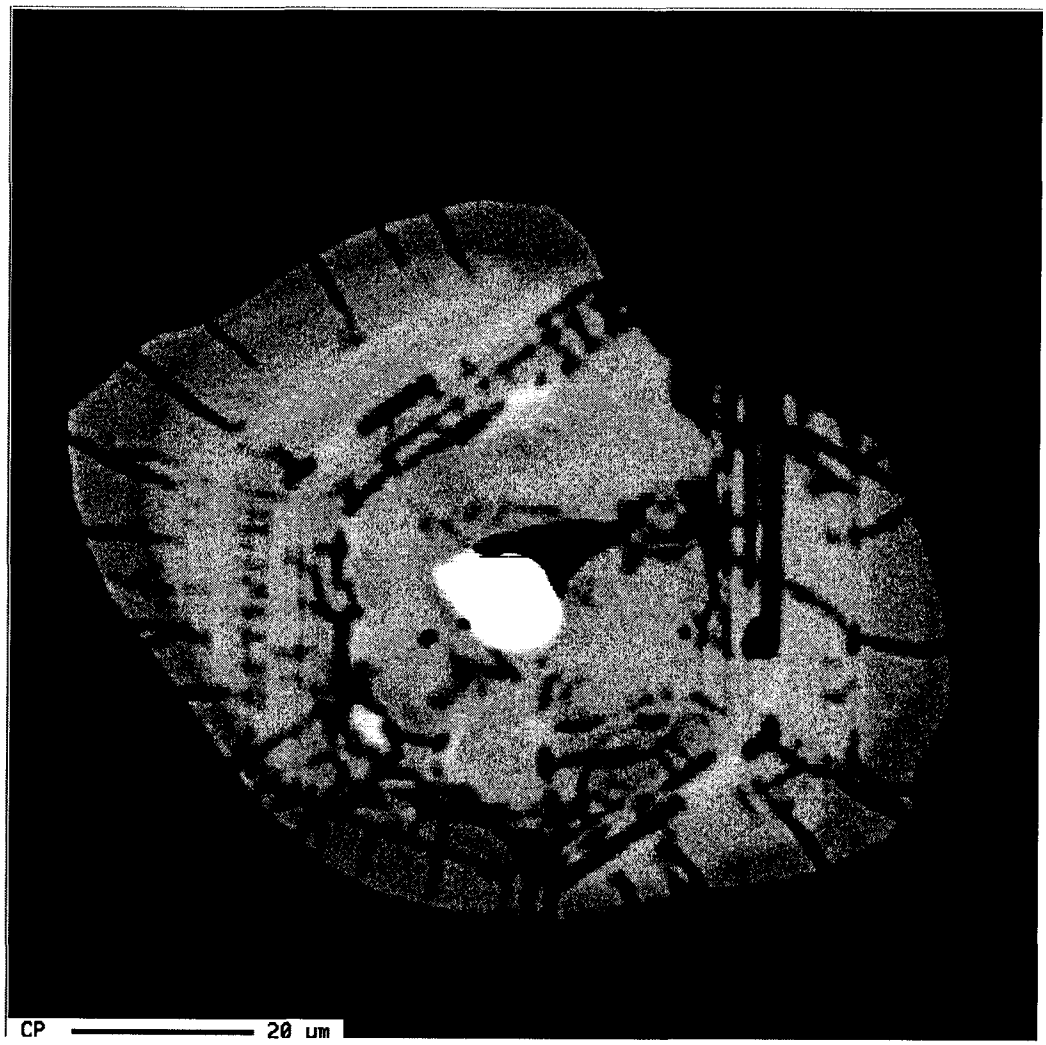

Figure 33. BSE image of zircon in thin section of Bt-Cpx charnockite (860220). Zircon crystal reveals some fractured overgrowth surrounding oscillatory zoning and a Th-Si rich inclusion within the core.

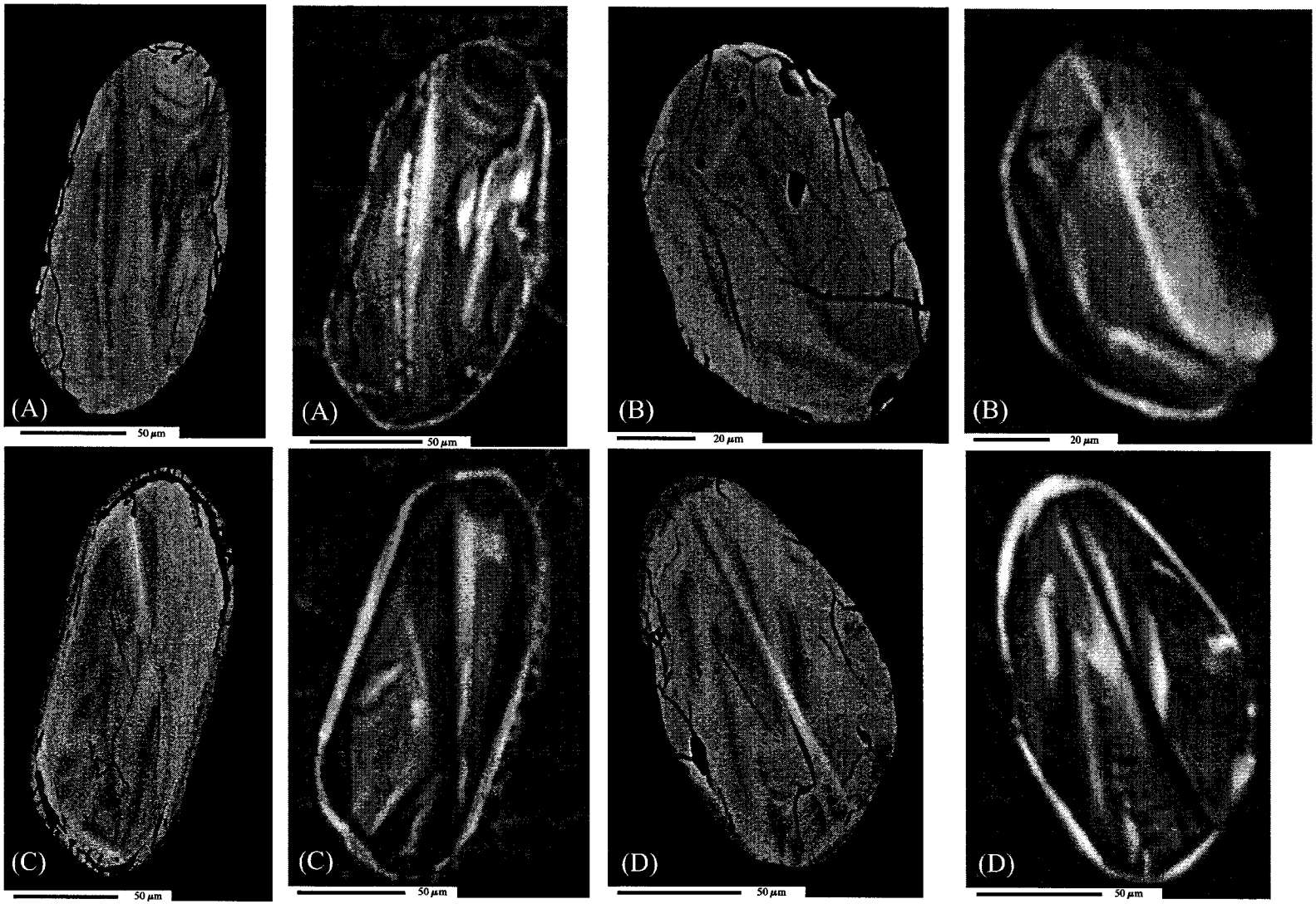

Figure 34. BSE composition and CL images of representative zircon from Bt-Cpx charnockite (860220). CL images are right of BSE images.

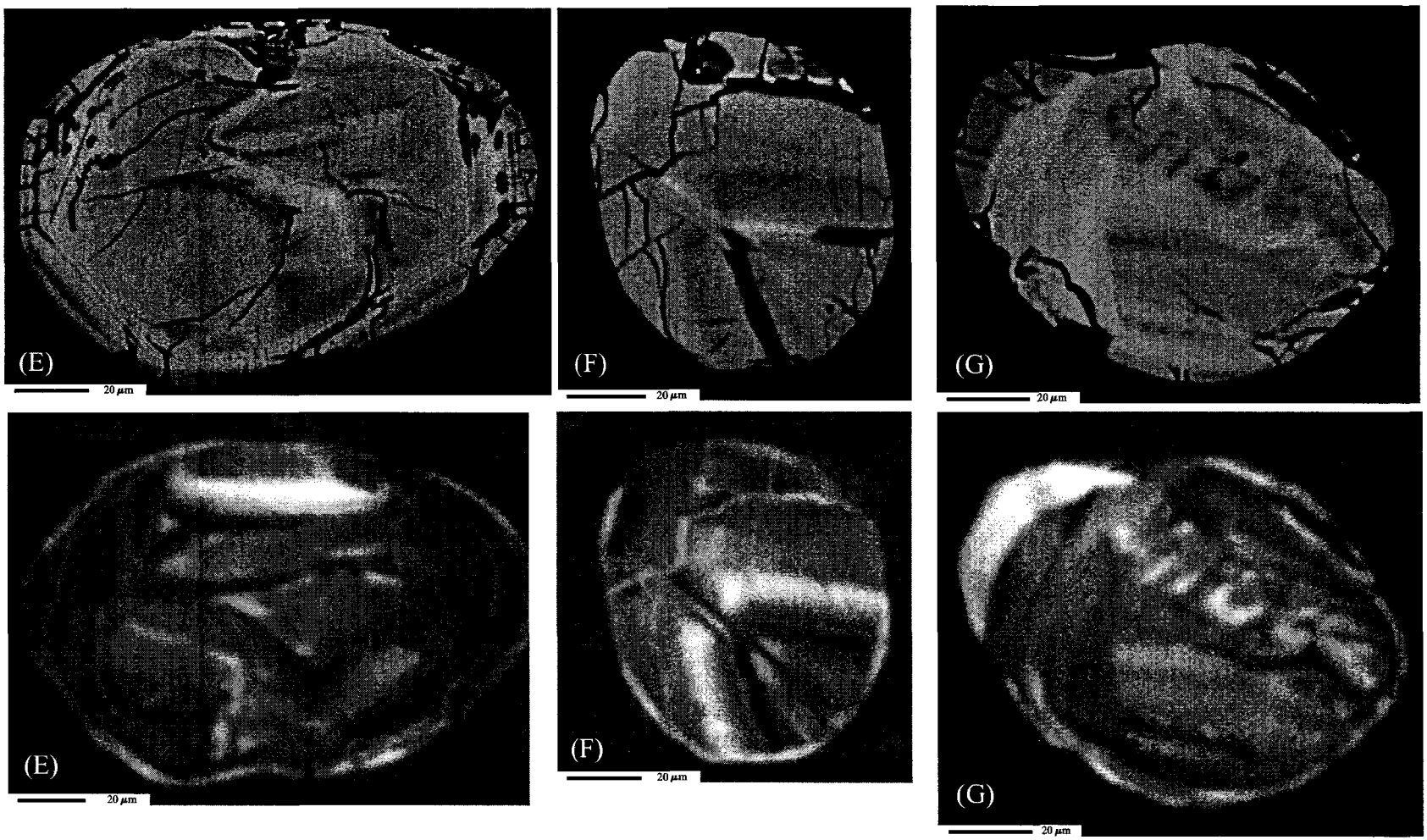

Figure 34. Continued ....

of an older history is not apparent, traces of this history would have had to been erased, presumably by ultra-high metamorphic temperatures (>1000°C) required to reset U-Pb systematics in zircon by diffusional processes. Although the bulk composition of charnockite cannot define if such extreme metamorphic temperatures were reached, the lack of ultra-high metamorphic mineral assemblages, such as spinel-quartz or sapphirine-quartz, from metasedimentary rocks in this study suggest metamorphism at such high grade did not occur in the RGD.

A few examples of similar zircon internal morphology are documented. Zircon from eclogite xenoliths of the Jericho kimberlite, NWT, reveal a somewhat similar chemical structure but $^{207}Pb/^{206}Pb$ model ages scatter broadly and record inheritance from a minimum eclogite protolith age and later growth or 'Mesoproterozoic thermal disturbance' (Heaman et al., 2002b). Cherniak and Watson (2000) estimated zoning in zircon at the 1 μm scale would become "blurred" or lost at 800°C after approximately 5.5 or 10 m.y. or 'blurred' at the 10 μm scale after 550 Myr (Pb diffusion). Average pressure estimates of ~7 kbars from metasediments places charnockitic intrusion or granulite-forming metamorphism within the middle crust. High temperatures (>900°C) reached during either scenario likely resulted in slow cooling (e.g. 10°C/Myr). Therefore, according to Cherniak and Watson's calculations, oscillatory zoning in zircon, even if originally present, would become blurred on at least the 1 μm scale. This would imply the internal morphology of zircon might not be a reliable measure of a magmatic or metamorphic origin for these mid-crustal rocks.

In an ion microprobe study of zircon recrystallization from an igneous protolith, Hoskin and Black (2000) found that zircons yielded a 1000 Myr range of ages. Some parts of zircon crystals preserved a 'memory' of protolith chemistry, producing an array of ages between the igneous protolith age and the age of the recrystallization event. Importantly, Th/U ratios also reflected this age array with more fully recrystallized zircons having Th/U ratios <0.1 whereas the least recrystallized zircons, or zircons recording the protolith age, having typical magmatic Th/U ratios from 0.4 to 0.7. Similar to the abundant elliptical zircons from sample 860220, these authors note common ovoid zircon shapes and suggest this resorbed morphology could be due to a Zr-undersaturated partial melt present during recrystallization.

Although the external morphology and internal structure of the zircon grains in sample 860220 bear some resemblance to the recrystallized zircon grains described by Hoskin and Black, the relatively high Th/U ratio, and the absence of older protolith ages in the grains of 860220 are better interpreted in terms of a magmatic rather than a metamorphic origin. This interpretation is consistent with the high antiperthite temperatures obtained for these samples, and implies that the sample 860220 is an igneous charnockite that intruded at ca. 2020 Ma.

Granitoids within and adjacent to the Trout Mountain Anomaly

Monazite and zircon from two granitic samples (4240 and 860970) occur as elongate or round crystals in the rock matrix or as inclusions in K-feldspar (4240). A linear array through three zircon analyses for Bt granite within the TMA (4240) yields an upper intercept of 2007.5 +2.3/-2.1 Ma (low % probability of fit) defined by a nearly concordant abraded prism (3Z). Four abraded zircon prisms and prism fragments from Bt granite west of the TMA (860970), yield a well-defined upper intercept age of 1999.9±0.7 Ma, which closely correlates with abraded prism fragments (likely core material). Zircon intercept ages could be interpreted as either metamorphic or magmatic with subsequent lead loss.

Zircons are compositionally and structurally distinct between these two Bt granites. Bt granite (4240) within the TMA has exceptionally high U concentrations (>1500 ppm) and high common Pb likely due to radiation damage caused by the high uranium. Bt granite (860970) west of the TMA has more typical U concentrations (<852 ppm). Th/U ratios differ significantly with low Th/U ratios (<0.12) reminiscent of metamorphic zircons from 4240 and typical magmatic Th/U ratios (0.20-0.41) from 860970 (Ahrens et al., 1967). Hoskin and Black (2000) report low Th/U ratios for recrystallized zircon are characterized by a low Th concentration with no correlation to U concentration. They attribute this observation to the incompatibility of Th in the zircon structure and its mobility along with Pb upon recrystallization. Because Th concentrations of zircon from sample 4240 are comparable to those of sample 860970, one could infer that zircon was not affected by Th loss during a metamorphic recrystallization event. Rather, the low Th/U ratio of zircon from sample 4240 could

reflect a higher U concentration than zircon from 860970, potentially due to zircon crystallization from a U-rich magma rather than to metamorphic recrystallization of a previously formed igneous zircon.

Structurally, BSE and CL images of representative abraded and unabraded prismatic zircon grains and fragments from 4240 revealed a faint oscillatory zoning suggesting some form of melt involved in crystal growth (Figure 35b), a synneusis twin suggestive of 'igneous clustering' (Hanchar and Miller, 1993; van Breemen and Hanmer, 1986; van Breemen et al., 1987) with a subhedral bypyramidal core separated from a large metamorphic overgrowth by a metamict ring (Figure 35c), and faint oscillatory zoning especially along the outer rim of a fragment (Figure 35d). Unabraded representative zircons from 860970 were imaged in BSE and CL and suggest a multicomponent history to these cloudy, iron-stained, and inclusion-rich crystals. Figure 35a shows an unabraded columnar zircon crystal composed of a subhedral, prismatic and fractured core with at least one end of the crystal preserving a pyramidal termination. Some oscillatory zoning is preserved within the core, which is surrounded by a thick (metamorphic) overgrowth, and suggests a magmatic origin for the crystal core.

On the basis of imaging and Th/U ratio, zircons from 860970 likely indicate an emplacement age for this granite at ca. 2000 Ma whereas zircons from 4240 are much more complex. Zircons from sample 4240 lack memory of an older protolith, indicate the presence of a thick overgrowth surrounding a synneusis twin, and reveal weak zoning from an abraded prism implying a magmatic origin to the rock. Although these zircons have a low Th/U ratio and nondefinitive oscillatory zoning compared to zircons in 860970, the evidence on balance suggests that anatexis was widespread between ca. 2010 and 2000 Ma with partial melting of different source rocks to form compositionally distinct magmas with variable U concentrations.

Monazite ages obtained for samples 4240 and 860970 are younger than zircon ages for the same samples. Two fractions from 4240 plot along an array with an upper intercept of 1958.6 +43.0/-12.3 Ma whereas two monazite fractions from 860970 with a weighted average of 1992.2±0.9 Ma closely coincides with the zircon upper intercept. Both Bt granites record minimum ternary feldspar temperatures between 750 to 770°C, which fall within the range of earlier 600 to >900°C closure temperature estimates for

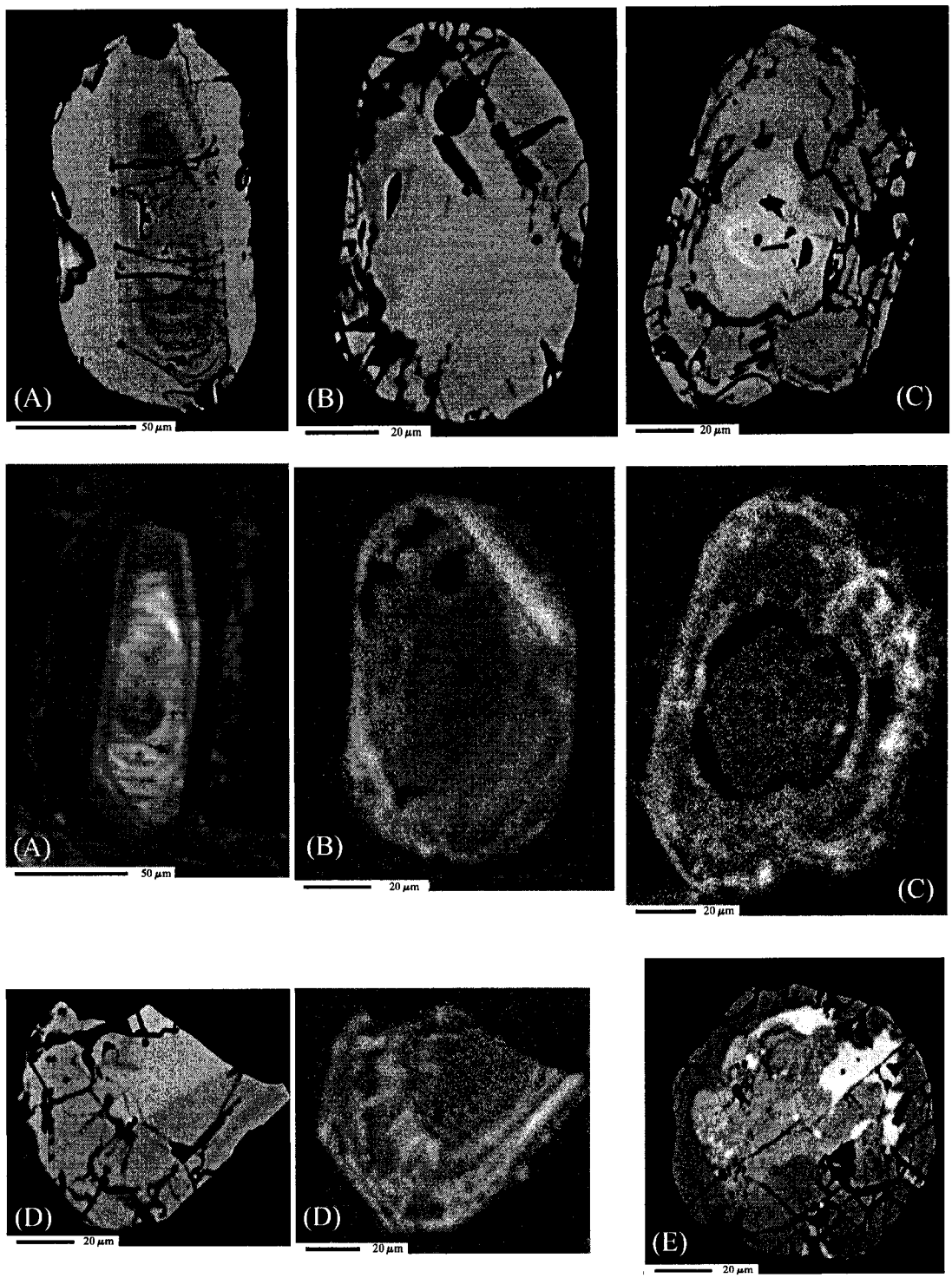

Figure 35. Representative BSE and CL composition images of zircon for (A) Bt granite (860970), (B to D) Bt granite (4240) and (E) monazite from Bt granite (4240). CL images are below or to the right of BSE image.

monazite (Smith and Giletti, 1997) but below more recent closure temperature estimates of 900°C (Cherniak et al., 2000, 2004). $^{207}Pb/^{206}Pb$ model ages between monazite and zircon from 860970 differ by up to ~10 Myr. Zircon and monazite could be recording either a separate episode of monazite growth ~10 Myr after granite emplacement or zircon and monazite could be recording similar magmatic ages but monazite experienced some open-system behavior and lead loss by diffusion after ca. 2000 Ma granite emplacement. Because a gradual decrease in ages from core to rim due to lead diffusion and cooling from this event is not observed, the 1992 Ma age more likely reflects monazite growth at that time resulting from the influx of fluids from other granites also emplaced at ca. 1990 Ma. Also, ca. 1992 Ma U-Pb monazite ages from Bt granite (860970) coincide in time with ca. 1989 Ma EM ages from the leucosome of a pelitic migmatite. Although TIMS monazite data from Bt granite 860970 could be recording cooling ages, a metamorphic origin is supported by detailed EM analyses, EM ages of metamorphic monazite from the pelitic migmatite sample, and recent closure temperature estimates for monazite.

A discordant monazite outlier (4240-2M) ($^{207}Pb/^{206}Pb$ age 2002.5 Ma) reflects some mixing with an older inherited magmatic or metamorphic component. Inherited radiogenic Pb in monazite was found to preserve an analogous inherited memory as that of zircon (Copeland et al., 1988). Copeland et al. found that a linear array through monazite analyses from granite recorded an older upper intercept age from previous metamorphism of a metasedimentary protolith. Monazite analyses do not indicate much older protolith ages but a close examination of the BSE image of a single, strongly zoned monazite crystal analyzed for chemical ages (4240-mon5; Figure 26b) reveals a dark older core surrounded by a light younger rim. Th* vs. Pb plots of core and rim regions, correlated with chemical zoning, of this single crystal (Figure 36) yield a chemical age of 2007±27 Ma for the dark core, 1928±12 Ma for the rim which progressives to an even younger light rim of 1880±17 Ma. The chemical core age of this single grain correlates exactly with the zircon isotopic age and part of the rim correlates within 31 Myr of the monazite isotopic age. A chemical profile across this crystal supports the idea that an age zonation has survived in monazite (Figure 36). Following a traverse spacing of 5 μm across monazite grain 4240-mon5, a sharp compositional (Th, U, Si, Pb, Y) and age

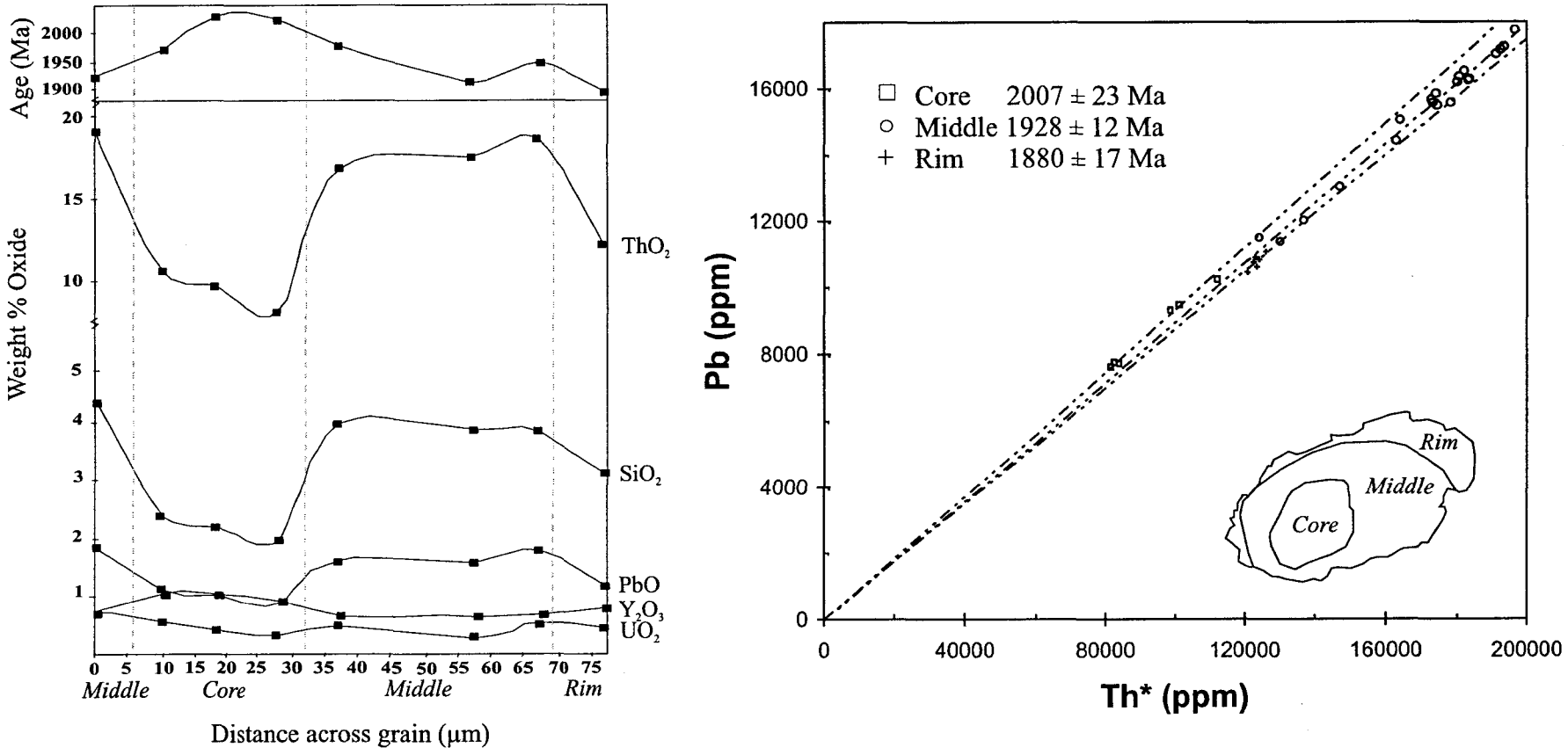

Figure 36. Chemical profile and Th* vs. Pb plot of monazite grain from Bt granite (4240-mon5). Dashed grey lines correspond with chemical zoning in monazite. Traverse as outlined in Figure 26.

affected by diffusional homogenization at high temperatures or, at least, diffusion cannot be measured at less than ~5 μm from the electron microprobe (e.g. Spear and Pyle, 2002; Crowley and Ghent, 1999). If this grain had experienced lead diffusion and/or cooling during a prolonged thermal event, one would expect to find a more gradual transition in age zoning decreasing from core to rim (Suzuki et al., 1994). Preserved contrasts in age and chemical zoning at this scale support a lack of lead diffusion homogenizing isotopic ratios for these grains at high-grade conditions (Schmitz and Bowring, 2003). Therefore monazite from 4240 appears to record the presence of an older component (either magmatic or metamorphic), which may have been derived from the metasedimentary source rock that produced the granite.

Monazite chemical ages even in granitic samples could reflect magmatic or metamorphic ages. If magmatic, one would expect monazite to be recording ages similar to (magmatic) zircon, as it would be unlikely that monazite and zircon record two separate magmatic events. If metamorphic, reflected by the spherical nature of the crystals, monazite could be reflecting multiple metamorphic growth events at ca. 1992 and ca. 1960 Ma preserved in Bt granite west of or within the TMA, respectively. Because of the similarity in timing of metamorphism recorded by pelitic rocks, monazite from Bt granites may be reflecting metamorphism and deformation in the RGD after 1992 Ma.

A ca. 1923 Ma Sil-Grt-bearing Pelitic Mylonite

A mylonitized Sil-Grt-bearing rock (4245b) within the TMA records the youngest major group of chemical and isotopic monazite ages. TIMS analysis of three monazite fractions from this sample yield an intercept age of 1923.5±1.3 Ma and all three monazite crystals record varying extents of reverse discordance. Euhedral and elongate monazite inclusions in garnet record an EM age of 1913±4 Ma in close agreement with TIMS monazite data. Older ca. 1950 Ma EM spot ages from these inclusions suggest some monazite formed prior to the bulk of monazite growth at ca. 1913 Ma. A large matrix monazite (4245b-mon5) with an EM age of 1875±4 Ma also records few similar EM spot ages up to ca. 1925-1940 Ma. A chemical profile across this large matrix monazite indicates this ca. 1940 Ma EM age coincides with a Y-rich core. As well, EM ages

appear to progressively decrease along with yttrium concentration towards the rim until yttrium finally plateaus at ca. 1870 Ma (Figure 37). Because garnet has a strong affinity for yttrium, yttrium zoning in monazite has been linked to garnet growth and breakdown. Y-poor monazite is observed to form after garnet growth whereas Y-rich monazite likely forms prior to garnet growth or upon garnet breakdown (e.g. along the monazite crystal rim) (Foster et al., 2002, Zhu and O'Nions, 1999; Finger and Helmy, 1998; Spear and Pyle, 2002). A decreasing yttrium supply, as demonstrated from core to rim by this grain, could correspond with the initiation of garnet growth during a post-2000 Ma metamorphism possibly constrained prior to or during ca. 1940-1925 Ma. Garnet growth at this time would deplete yttrium otherwise available for incorporation into monazite. Furthermore, crystallization of a ca. 1913 Ma euhedral, undeformed and unaltered monazite inclusion constrains the growth of its garnet porphyroblast host to a post-2000 Ma metamorphism (Figure 11j, 30a). Alternatively, if garnet breakdown, as indicated by the presence of fractures, retrograde biotite, chlorite and muscovite growth in some garnet relics, was widespread at approximately ca. 1940 Ma some other mineral (e.g. xenotime) would be necessary to deplete the supply of yttrium in the system. BSE imaging indicates a distinct chemical contrast, between the core and rim of this large matrix monazite, is absent along the rim of monazite inclusions in sample 4245b. This observation supports continued monazite growth along the rim of only the matrix monazite during ca. 1875 Ma retrogression whereas monazite inclusions remained armored from monazite-forming fluids.

This deformed metasedimentary rock records not only some of the youngest ages in the study area but also a group of discordant, tiny spherical zircons likely of detrital origin ($^{207}Pb/^{206}Pb$ model age of 2095.4±0.6 Ma). Elongate monazites aligned with the overall metamorphic fabric of this rock support ca. 1923 Ma growth during metamorphism and deformation potentially within the TMA. A few young (<1860 Ma) EM monazite ages recorded by this sample and some granite, Bt gneiss, and charnockite within the TMA (Figure 12) would be consistent with further monazite growth by fluids during retrogression and reactivation. This suggests the negative Bouguer anomaly defining the TMA represents a zone of weakness in the crust subjected to late-stage fluid

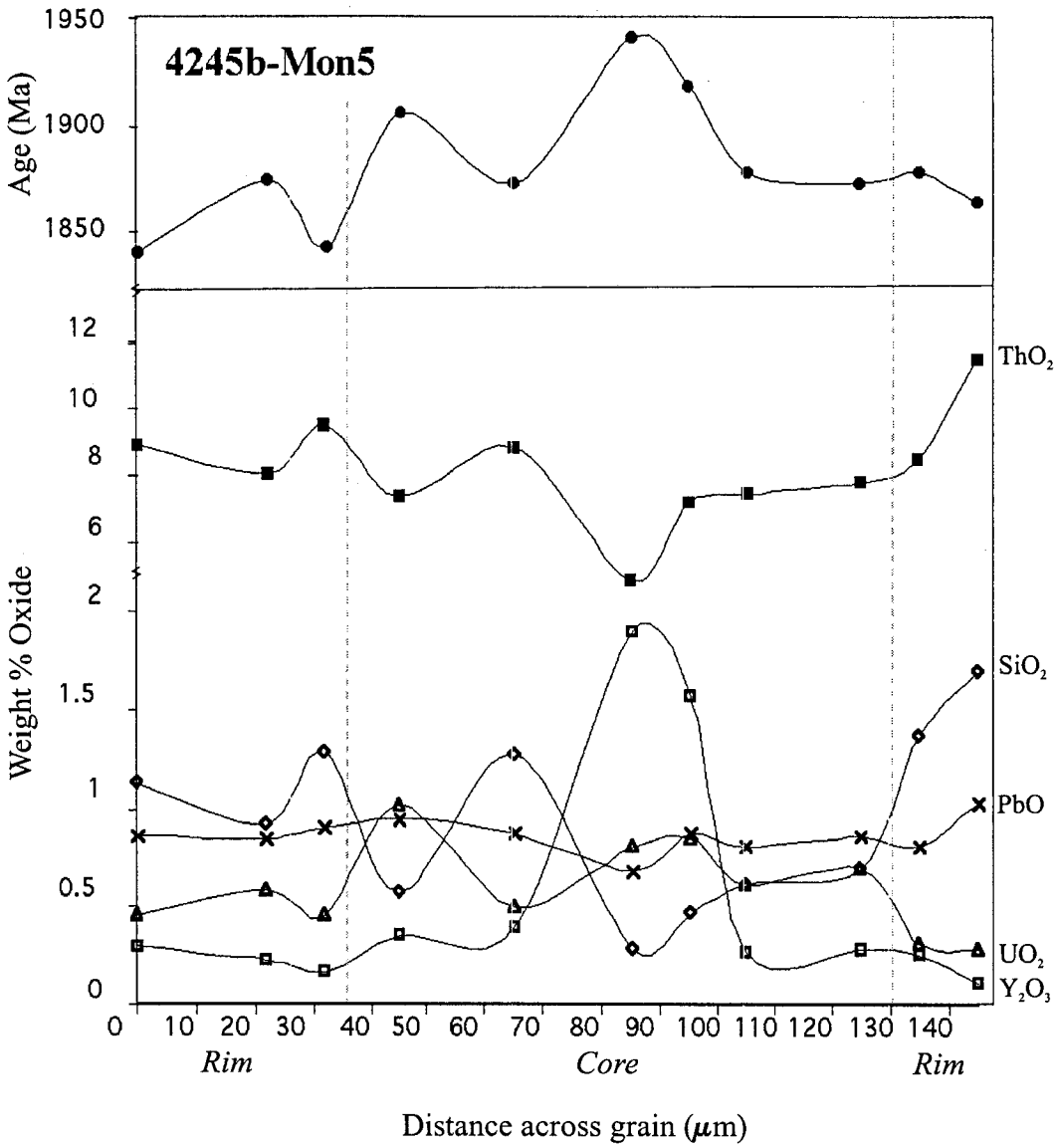

Figure 37. Chemical profile of matrix monazite from Sil-Grt pelitic mylonite (4245b-mon5). Dashed grey lines correspond with chemical zoning in monazite. Traverse as outlined in Figure 30.

influx with subsequent alteration possibly lowering the average density of the TMA rocks.

Conclusions

The geochronologic data reported in this chapter lead to the following conclusions, which corresponds to the lettering on Figure 38:

(A) A ca. 2065 Ma TIMS monazite age represents either the age of a detrital grain or the age of an initial phase of metamorphism.

(B) A period of mid-crustal felsic magmatism from ca. 2020 to 2000 Ma is recorded in TIMS zircon data from charnockitic and granitic rocks of the RGD.

(C) TIMS monazite data on a pelitic migmatite records a high-grade metamorphic event at ca. 2014 Ma. EM monazite data obtained from a different part of the same sample indicate a younger age (ca. 1989 Ma). The younger age estimate may reflect inaccuracy in the EM technique or, more likely, a separate episode of high-grade metamorphism.

(D) A ca. 1960-1910 Ma upper amphibolite-facies metamorphism with garnet growth is recorded by EM monazite ages from pelitic gneiss and EM and TIMS monazite ages from a mylonitic pelite.

(E) EM data from a few samples indicate late-stage monazite growth (at ca. 1910-1865 Ma) associated with deformation and the influx of retrogressing fluids.

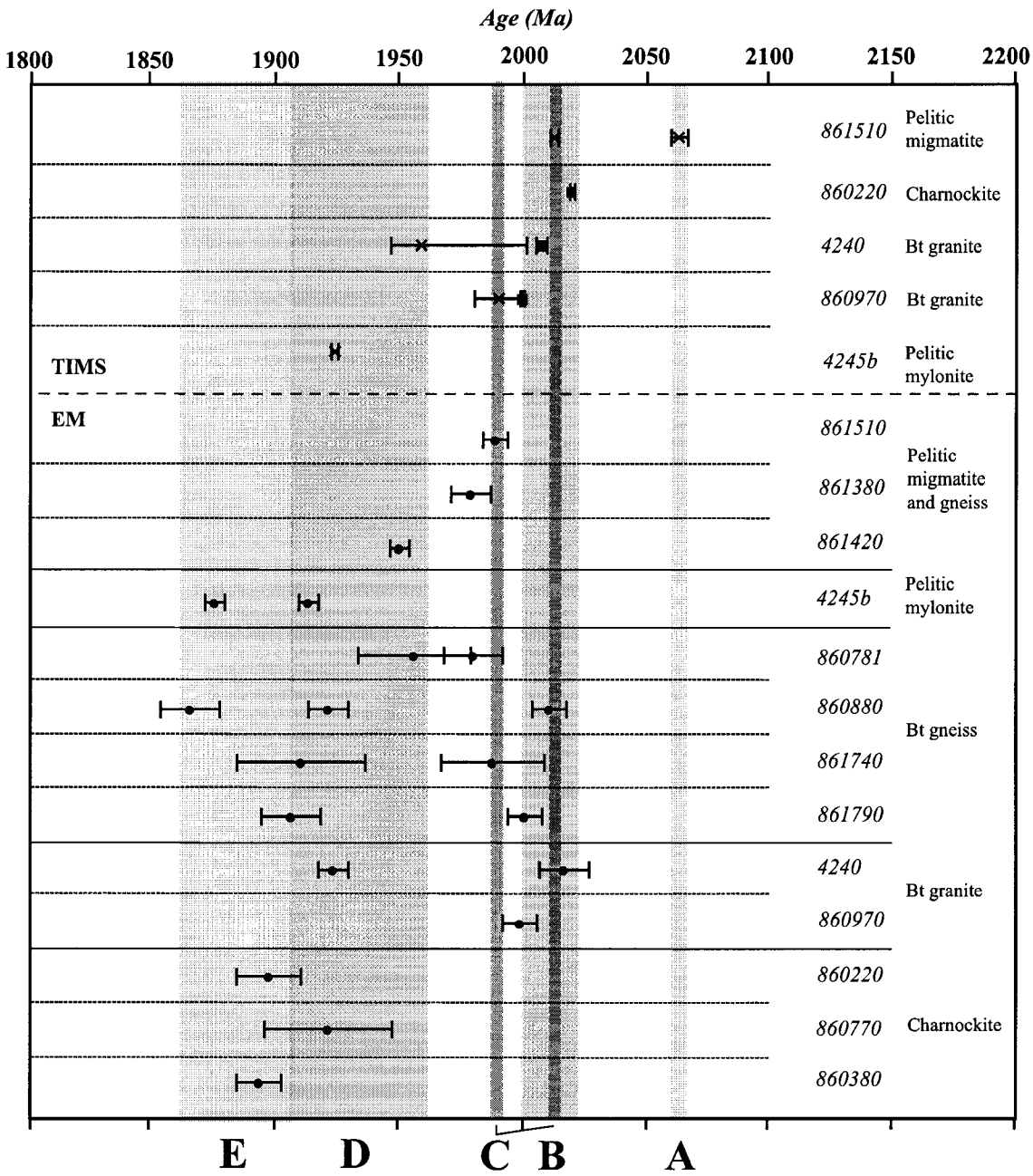

Figure 38. Summary of EM monazite and TIMS monazite and zircon geochronology from the Red Earth granulite domain. TIMS zircon data represented by filled square and TIMS monazite data represented by cross. Errors reported at the 2 sigma level. Shaded areas correspond with summary of ages (A, B, etc...) in conclusion.

CHAPTER 4

COMPARISON OF THE RGD WITH ADJACENT DOMAINS OF WESTERN LAURENTIA

One of the most significant finds of this study is a pelitic migmatite (861510) containing the high-grade mineral assemblage Spl (hercynite)-Crd-Grt-Sil-Perthite. Not only does this aluminous mineral assemblage confirm granulite-grade conditions by multiequilibria estimates of ca. 6.5 kbar and 800°C, but this high-grade assemblage also provides a critical mineralogical starting point for comparison to adjacent domains. Granulite-grade metapelitic gneiss found in the TMZ contains similar mineral assemblages and yield comparable P-T estimates of 5.8-7.2 kbar and 730-880°C (Grover et al., 1997). Still higher-temperature granulite-grade assemblages of spinel + quartz (Chacko et al., 1994; Creaser and Chacko, 1995) are recognized to the east of the present study area. Such assemblages occur widely throughout northeastern Alberta (Langenberg and Nielsen, 1982) as elongate bodies of high-grade paragneiss in the TBC and TMZ plutons (Grover et al., 1993, 1997; Bostock and van Breemen, 1994), migmatitic metasedimentary enclaves and granite at Pelican Rapids (Chacko et al., 1994; Creaser and Chacko, 1995; Chacko, 1997), and late, peraluminous Slave and Konth batholiths (Berman and Bostock, 1997; Bostock, 1981, 1987). The narrow 200 Myr window of EM and TIMS ages of zircon and monazite from rocks of the RGD are also reminiscent of ages reported for the TMZ, Thelon Tectonic Zone and western Rae Province. Below, published U-Pb monazite and zircon data from these adjacent domains are compared to data collected in this study (Figure 39, 40).

A ca. 2065 Ma TIMS monazite date obtained on a pelitic migmatite (861510) from the RGD could represent either the age of a detrital grain in this metasedimentary rock or the age of an early phase of metamorphism in the RGD. These two possible origins for this monazite grain are evaluated in light of available age data from adjacent basement domains. Because ca. 2065 Ma source rocks have not been reported from the BH domain, potential source rocks from other domains must also be considered. Metamorphic monazite and brown zircons from the Tsu and Rutledge Lake paragneisses provide the nearest age comparison. Bostock and van Breemen (1994) proposed that

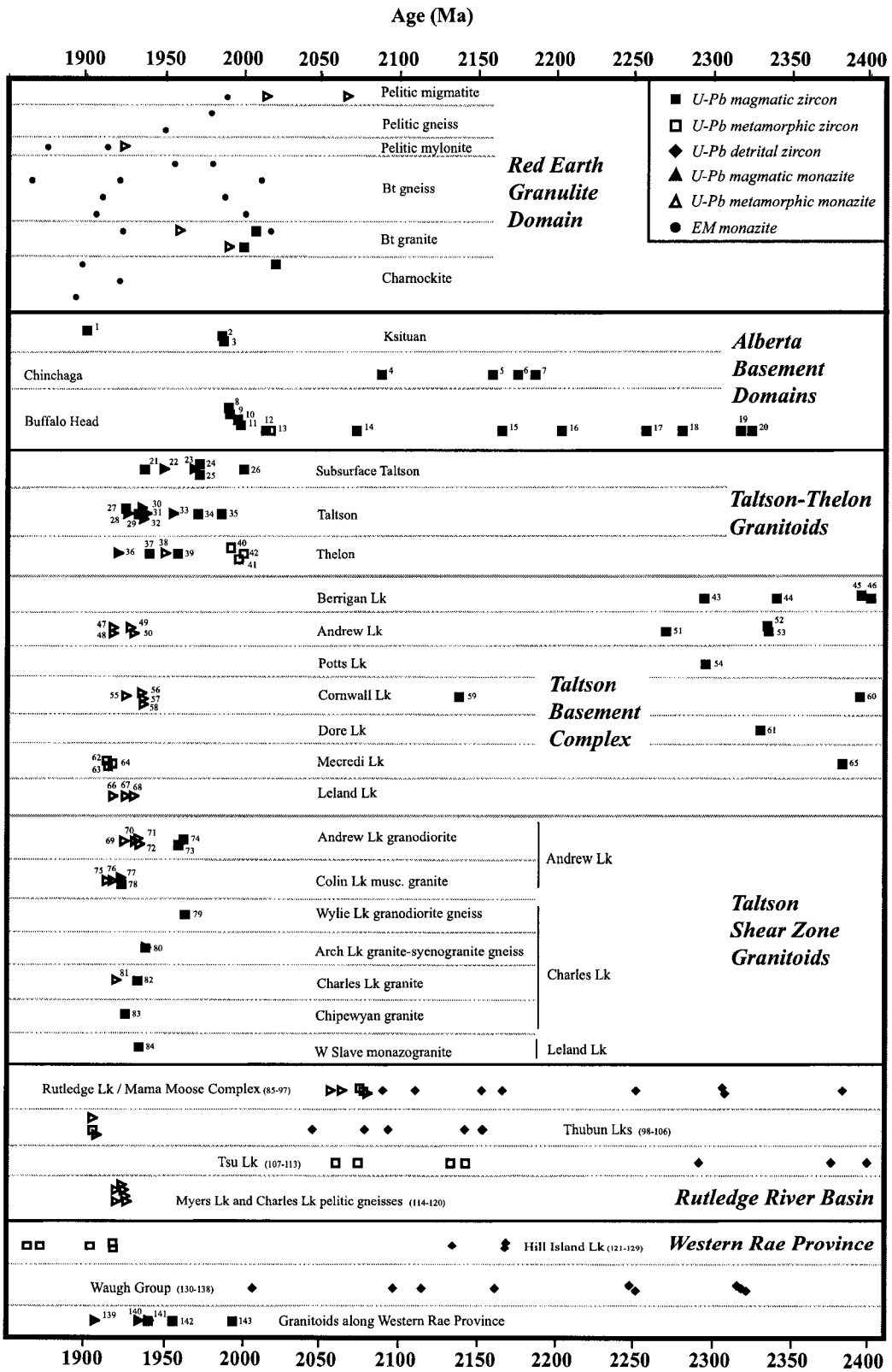

Figure 39. Comparison of U-Pb zircon and monazite data for western Laurentia (see also Appendix A). Numbers correspond to reference numbers listed in Appendix A.

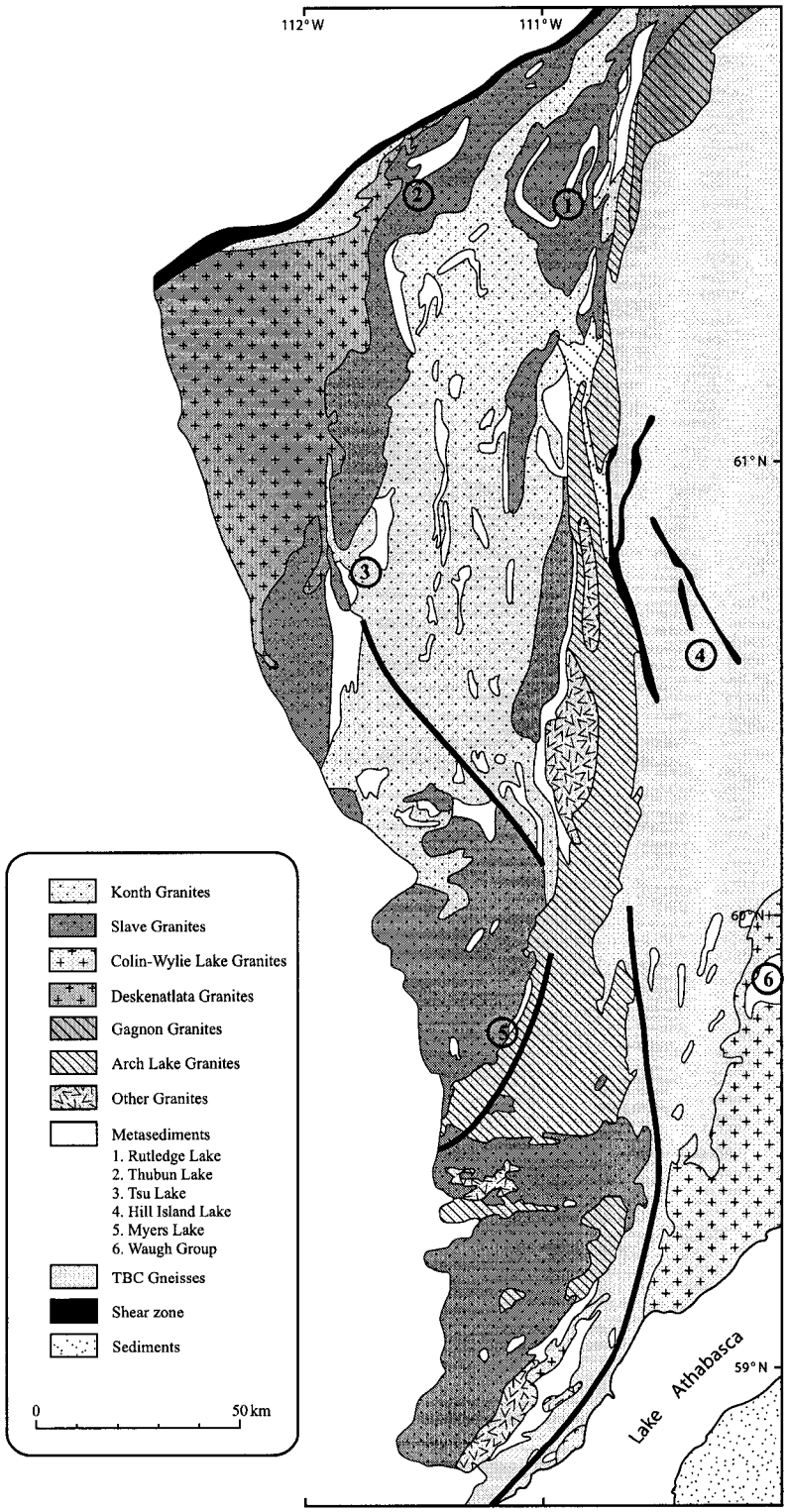

Figure 40. General geology of the Taltson magmatic zone and part of the western Rae Province. Modified from Chacko et al. (2000). Locations of metasedimentary rocks from Bostock and van Breemen (1994), McDonough and McNicoll (1997), and McDonough et al. (2000).

deposition of sediments in the Rutledge River basin ended by ca. 2.13-2.09 Ga and was followed by ca. 2.09-2.05 Ga basin closure and granulite-grade metamorphism. These metamorphic source rocks may have provided some of the detritus for the protolith of the RGD metasediments and implies the presence of a sedimentary basin in the RGD to capture the ca. 2065 Ma detrital material prior to high-grade metamorphism. If the monazite in the RGD pelitic migmatite sample is of metamorphic rather than of detrital origin, then the BH domain may contain a basin analogous to the Rutledge River basin of the TMZ. Specifically, the sediments in this basin must have been deposited prior to 2065 Ma and then metamorphosed during the same general time period as the first high-grade metamorphic event in the Rutledge River basin (2.09-2.05 Ga). If this is the case, then ages of detrital zircon grains in the RGD pelitic migmatite could be similar to the detrital zircon grains in the Rutledge basin paragneisses, which range in age from ca. 2.4 to 2.09 Ga (Figure 39).

The RGD experienced an episode of felsic magmatism between ca. 2020-2000 Ma. Bt-Cpx charnockite (860220) records a magmatic age of ca. 2020 Ma. Reintegrated feldspar thermometry of perthite and antiperthite in charnockite suggest such charnockitic intrusions into the middle crust may have reached temperatures in excess of 1000°C, consistent with temperatures suggested by Kilpatrick and Ellis (1992) for magmatic charnockites. Charnockite 'remnants' of unknown age reported from the TMZ peraluminous granitoids have not been described in detail (Bostock, 1981; Berman and Bostock, 1997). A ca. 1950 Ma charnockitic gneiss has been reported from the Thelon tectonic zone (van Breemen et al., 1987).

Following shortly after charnockitic magmatism, TIMS zircon ages from Bt granites (860970, 4240) in this study and from three other granitoids within the BH domain (Villeneuve et al., 1993) record an episode of granitic magmatism between 2010-1990 Ma. Magmatism in this age range overlaps U-Pb zircon and monazite ages of subsurface TMZ rocks (Villeneuve et al., 1993) and the ca. 1994 Ma Box Mine granite from the Beaverlodge area, northwestern Saskatchewan (Van Schmus et al., 1986). The age of RGD magmatism does not overlap with the main phase of TMZ magmatism, which began at ca. 1986 Ma (Deskenatlata batholith) (Bostock et al., 1987).

The timing of high-grade metamorphism in the RGD broadly coincides with the timing of felsic magmatism suggesting an association between attainment of high-grade conditions and the intrusion of mid-crustal felsic magmas. In particular, ca. 2020 Ma charnockitic magmatism occurs just prior to ca. 2014-2017 Ma high-grade metamorphism (Villeneuve et al., 1993; this study). High temperature (>900°C) intrusions could have provided a primary or secondary heat source for high-grade metamorphism. Granitic magmatism between ca. 2010-1990 Ma suggests crustal anatexis was widespread during that time and seems to culminate with possible ca. 1989 Ma high-grade metamorphism accompanied by partial melting. Metamorphism at ca. 2014 Ma or ca. 1989 Ma is not recorded in rocks of the TMZ but is similar to ages reported from the Thelon Tectonic Zone. Henderson and van Breemen (1992) report metamorphic growth at 2000±10 Ma from zircon tips and metamorphic zircon with $^{207}Pb/^{206}Pb$ model ages ranging from ca. 1994 to 2009 Ma from the Mary Francis migmatitic metasedimentary gneiss. Van Breemen et al. (1987) report ~ca. 2000 Ma U-Pb metamorphic zircon ages from mylonitic and possibly tonalitic granulite gneisses.

EM and TIMS monazite data from RGD pelitic migmatite, gneiss and mylonite indicate a later, ca. 1960-1910 Ma, upper amphibolite- or even higher-grade metamorphic event that was accompanied by garnet growth. Metamorphism during this interval has not been previously described in the BH domain but does coincide with a major period of magmatism and/or high-grade metamorphism recorded by adjacent terranes, such as the ca. 1987-1900 Ma Ksituan arc, ca. 2000-1937 Ma subsurface TMZ rocks (Villeneuve et al., 1993), ca. 1986-1937 Ma exposed TMZ (Bostock and Loveridge, 1988, Bostock et al., 1987), and ca. 2.0-1.9 Ga Thelon tectonic zone (van Breemen et al., 1987). In the present study, a mesoperthite-bearing pelitic gneiss (861590) within the TMA records a minimum reintegrated feldspar temperature of 905°C reminiscent of ultra-high temperature conditions in the TMZ reported from granite and metasedimentary enclaves at Pelican Rapids (920-1000°C, Farquhar et al., 1996; 975-1000°C and 6-8 kbars, Chacko, 1997) and mesoperthite-bearing peraluminous batholiths (930°C, 6.7 kbars, Pattison et al., 2003; Berman and Bostock, 1997). These mineralogical and pressure-temperature similarities suggest a connection between RGD and TMZ rocks. Age data

have not yet been obtained for sample 861590 with which to further evaluate this connection.

Three large-scale north-south trending shear zones east of the RGD deform TBC gneisses (McDonough et al., 1995b; McNicoll et al., 2000), TMZ batholiths (McNicoll et al., 2000; McDonough et al., 2000) and high-grade paragneisses (Bostock and van Breemen, 1994; McDonough et al., 2000). This deformation occurred at upper amphibolite to granulite-grade conditions following the main period of TMZ magmatism (Grover et al., 1997; McDonough et al., 2000). Granitoids intruded along these shear zones record the timing of ductile shear zone deformation and metamorphism by U-Pb zircon and monazite geochronology to a maximum of ca. 1938 Ma granulite-grade to ca. 1919 Ma amphibolite-grade metamorphism (McDonough and McNicoll 1997, McDonough et al., 2000; Grover et al., 1997). Concordant to nearly concordant $^{207}Pb/^{206}Pb$ model ages of monazite from TBC gneisses record similar ages of metamorphism and deformation between ca. 1936 and ca. 1917 Ma (McNicoll et al., 2000). The Myers Lake pelitic gneisses near the Leland and Charles Lake shear zones record U-Pb monazite ages between ca. 1926-1923 Ma (McDonough et al., 2000). Nearly concordant ca. 1918 Ma $^{207}Pb/^{206}Pb$ ages from zircons from a Hill Island Lake quartzite within the western Rae Province parallels reactivation in the TMZ (Bostock and van Breemen, 1994). Mylonitic granitic granulite gneiss from the Thelon Tectonic Zone records a minimum 1950±4 Ma monazite age of granulite-facies metamorphism (van Breemen et al., 1987). Widespread ca. 1.95-1.92 Ga metamorphism and deformation in the TMZ, western Rae Province and Thelon Tectonic Zone resemble ca. 1960-1910 Ma ages from metasedimentary rocks in the RGD. The correspondence is particularly close for RGD pelitic mylonite sample (4245b), which yielded a TIMS monazite age of ca. 1923 Ma and minimum upper amphibolite facies mineral assemblage.

Widespread ca. 1910-1865 Ma retrogression followed and is evidenced particularly in the TMA by late monazite growth in biotite gneiss, charnockite, pelitic mylonite, and some granite. Retrograde muscovite and chlorite occurs along fractures and pseudomorphs garnet, and muscovite/sericite surrounds patches of retrograded sillimanite in mylonitic pelite (4245b). Similar muscovite replacement of K-feldspar and garnet replacement by chlorite and biotite at low grade is observed by Grover et al.

(1997) in TMZ paragneisses. As well, ca. 1904-1907 Ma monazite and zircon from Thubun Lakes high-grade metasediments are interpreted by Bostock and van Breemen (1994) as growth during later granitic intrusion coinciding with retrograde metamorphism. Post-1860 Ma monazite growth in several rock types within the TMA supports intermittent reactivation or fluid ingress into an area of weakness throughout the Paleoproterozoic and into the Mesoproterozoic. Similar late-stage mineralogical regression during ca. 1900-1800 Ma overprinting, recorded by Ar-Ar and K-Ar data, is observed in both the TMZ shear zones and BH domain (Plint and Ross, 1993; Burwash et al., 1962; Plint and McDonough, 1995).

In summary, the comparisons made above indicate many petrological and geochronological similarities between pre- and post-2.0 Ga relationships shared between rocks of the RGD (and TMA), TMZ, and western Rae Province. The only ages present in the RGD but not represented in the TMZ or the Churchill craton are the ca. 2014 Ma metamorphic and ca. 2020 to 2000 Ma magmatic ages. Some of these ages have been reported in the Thelon and may yet be discovered in the Churchill craton. Implications of these similarities for tectonic models proposed for the formation and assembly of western Laurentia are considered in the next section.

IMPLICATIONS FOR PALEOPROTEROZOIC TECTONICS IN WESTERN LAURENTIA

The pre- and post-2.0 Ga history of the BH and adjacent domains can broadly be assessed in terms of two groups of models. The first set of models proposes that a large portion of western Laurentia amalgamated along its western margin between 2.0 to 1.9 Ga, by the accretion of separate, and perhaps unrelated crustal blocks via consumption of bounding tracts of oceanic crust (Ross and Eaton, 2002; Ross et al., 1991; Ross, 1990, 2002; Thériault and Ross, 1991; Thériault, 1992; Hoffman, 1987, 1988, 1989). In these models, the BH domain originally occupied a position outboard of Laurentia's western margin, along with many other proposed domains. These domains were subsequently accreted to the Laurentian margin in a manner similar to the tectonic assembly of disparate crustal fragments occurring in the present-day southwestern Pacific (Ross, 2002). A second group of models proposes that western Laurentia represents a single large block assembled either in the Archean or earlier in the Paleoproterozoic (e.g. prior to ca. 2.3 Ga) (Bostock and van Breemen, 1994; Burwash et al., 2000a; De et al., 2000; Chacko et al., 2000). In the second set of models, the BH domain and other earlier assembled blocks were reworked to various degrees between 2.0 to 1.9 Ga in a plate interior setting, similar to present-day orogenesis occurring in the Tibetan Plateau, Tian Shan Mountains and other parts of central Asia (Chacko et al., 2000; De et al., 2000). The former set of models implies distinct pre-2.0 Ga histories for the different basement domains followed by complementary post-2.0 Ga histories determined by their subducting or overriding plate position during 2.0-1.9 Ga subduction and collision. In contrast, the latter set of models predicts many similarities in both the pre- and post-2.0 Ga history of basement domains in that all of these domains have been part of a single block of crust largely coherent since at least 2.3 Ga. The data for the RGD reported in the present study provides important new information with which to evaluate these models.

Pre-2.0 Ga History

A general comparison of the pre-2.0 Ga history of the various domains can be made by considering magmatic and/or metamorphic events occurring in one or more of

these domains at >2.5 Ga, ca. 2.4-2.25 Ga, ca. 2.2-2.1 Ga, ca. 2.09-2.05 Ga and ca. 2.02-1.99 Ga (Fig. 39 and Appendix A). Archean U-Pb zircon ages characteristic of the Rae Province and some gneisses of the Taltson basement complex (McNicoll et al., 2000) have not yet been reported from the BH domain although Nd isotopic data indicate that the BH domain largely represents reworked Archean crust (2.51-2.82 Ga T_{DM}) (Villeneuve et al., 1993; Thériault and Ross, 1991). Alternatively, chondritic model ages of the same Nd isotopic data suggest reworked Proterozoic, rather than Archean, crust. A significant number of ca. 2.4-2.25 Ga U-Pb zircon crystallization ages have been reported for the BH domain, the Taltson basement complex and the western Rae craton (Ross et al., 1991; Villeneuve et al., 1993; McNicoll et al., 2000; Bostock et al., 1991; Bostock and Loveridge, 1988; van Breemen et al., 1992; van Breemen and Bostock, 1994). Similarly, ca. 2.2-2.1 Ga zircon ages are present in the Chinchaga and BH domains, pelitic gneisses of the Rutledge River basin, granitic gneisses of the Taltson basement complex, and western Rae Province (Ross et al., 1991; Villeneuve et al., 1993; Bostock and van Breemen, 1994; McNicoll et al., 2000; McDonough and McNicoll. 1997). Granulite-grade metamorphism at ca. 2.09-2.05 Ga in the Rutledge River basin (Bostock and van Breemen, 1994) overlaps with a ca. 2065 Ma monazite date obtained in the present study. The latter data may represent the age of an early phase of metamorphism in the RGD or the age of a detrital grain sourced from rocks similar to those of the Rutledge River basin.

The many parallels that exist in the pre-2.0 Ga histories of the BH domain, the TMZ and the western Rae Province are more consistent with the second rather than with the first group of tectonic models proposed for western Laurentia. However, several workers have suggested a modified version of the first model that may explain some of these parallels. In the modified model, the BH domain represents a block of Rae Province crust that was rifted off the craton margin at ca. 2.4-2.3 Ga (Figure 41a) and then re-amalgamated with the craton through subduction processes between 2.0 and 1.9 Ga. (Ross and Eaton, 2002; Thériault, 1992, 1994; McNicoll et al., 2000). This model can account for the similarities in the Archean and ca. 2.4-2.25 Ga histories of the various basement domains, but additional tectonothermal events must be invoked to explain the synchronicity of events in the different blocks between ca. 2.3 and 2.0 Ga. In Figure 41b

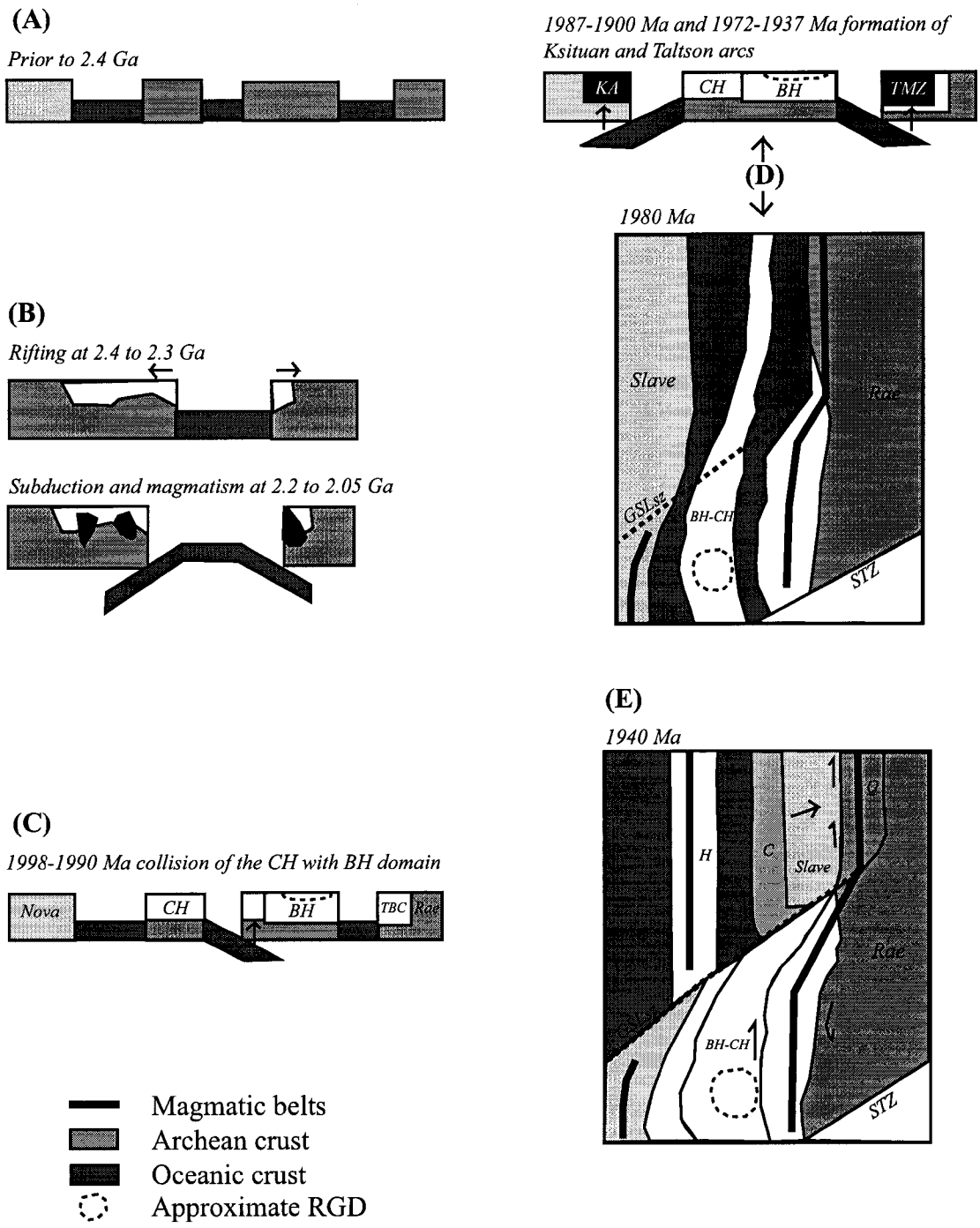

Figure 41. Basic sketches of proposed tectonic models for assembly of western Laurentia. A-E modified from Ross and Eaton (2002) and Ross (2002). F-G modified from Chacko et al. (2000). Location of the RGD placed schematically for reference. Q - Queen Maud uplift, STZ - Snowbird Tectonic Zone, C - Coronation group, H - Hottah arc, TTZ - Thelon Tectonic Zone.

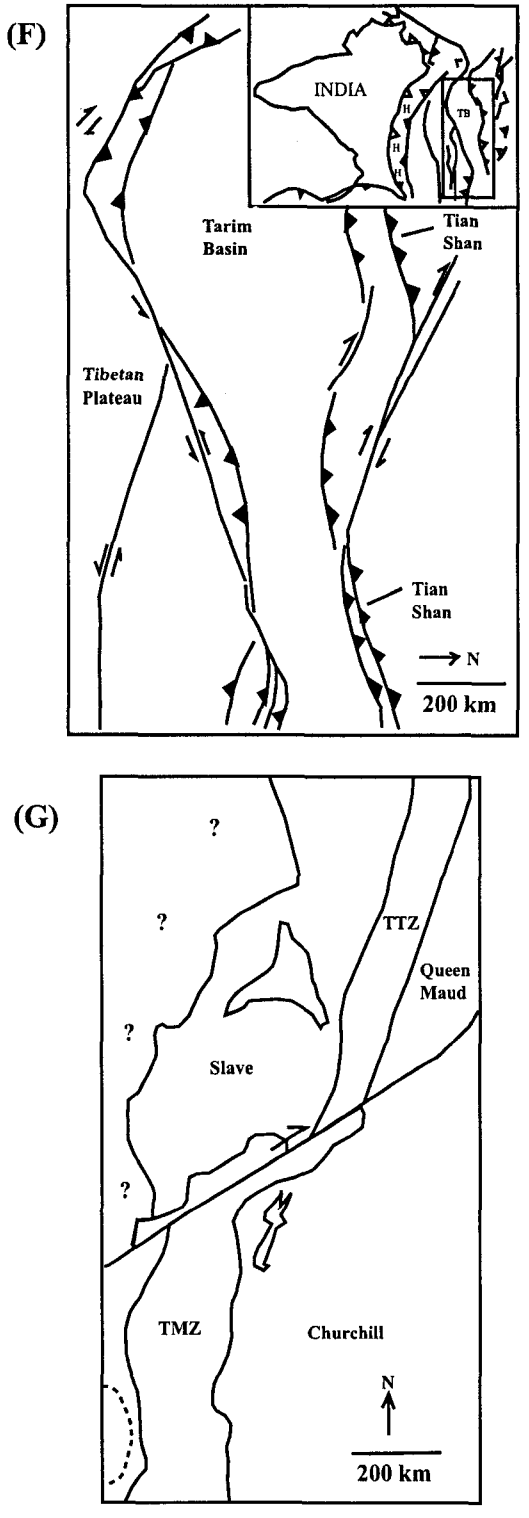

Figure 41. Continued ...

for example, Ross and Eaton (2002) suggest that rifting at 2.3 Ga was followed by 2.2-2.05 Ga subduction of opposing oceanic slabs beneath the BH domain and western Rae Province in order to generate magmatic rocks in both crustal blocks during this time interval. If some of the ca. 2.43-2.25 Ga detrital zircons present in the metasedimentary rocks of the Rutledge River basin were derived from the BH domain as suggested by Bostock and van Breemen (1994), then this rifted block of crust must have remained near to the Rae Province and permitted transport of detrital material across the putative ocean basin that separated the two blocks. Granulite-grade metamorphism at ca. 2.09-2.05 Ga in the Rutledge River basin and possible 2065 Ma metamorphism in the RGD would have to be a product of subduction-related magmatism occurring simultaneously in both blocks. Although the proposed model is possible, no evidence has yet been reported of subduction-related magmatic activity in either block during this time period.

Figure 41c also outlines Ross and Eaton's (2002) proposal for the tectonic setting of western Laurentia at ca. 2.0 Ga. These authors suggest that the BH and Chinchaga domains initially collided by east-dipping subduction of oceanic crust beneath the BH domain to form a single, composite block of crust. The presence of ca. 1998-1990 Ma granitic rocks within the western portion of the BH domain is used to substantiate this argument. The present study documents ca. 2020-1990 Ma felsic magmatism and high-grade metamorphism in the RGD, which is located in the central and eastern part of the BH domain. The model proposed by Ross and Eaton (2002) could accommodate these new findings provided that subduction beneath the BH domain began at or before ca. 2020 Ma and that the subducting plate extended further beneath the BH domain to the east. Partial melting of the lower crust to form charnockitic and granitic magmas in the RGD would then be the result of subduction-related processes. High-grade metamorphism in the middle crust would, in turn, be facilitated by the intrusion of these magmas.

It should be emphasized that the model proposed by Ross and Eaton (2002) is based on the assumption that magmatic belts invariably form by subduction or collision processes at convergent plate margins. This same assumption underlies Hoffman's (1988) model for the assembly of tectonic domains north of the Great Slave Lake shear zone. Neither of these studies provides petrologic or geochemical data on granitoids to

validate this assumption. Importantly, charnockitic and granitic magmas can also be produced in other tectonic settings. For example, ca. 2020-1990 Ma felsic magmatism in the BH domain could have formed in an extensional tectonic setting (e.g. Kilpatrick and Ellis, 1992). An extensional setting would also be conducive to the formation of small hinterland basins such as the Waugh basin (McDonough and McNicoll, 1997), which were metamorphosed during later compressional orogenesis. Alternatively, such magmatism could be the result of crustal thickening associated with compression in a plate interior rather than a plate margin setting (e.g. Kilpatrick and Ellis, 1992; Driver et al., 2000; Chacko et al., 2000). The crustal thickness of the Buffalo Head domain (Bouzidi et al., 2002) could suggest the latter example, yet the above tectonic settings are described only to point out that magmatic belts can be generated in other settings. More geochemical and isotopic data for magmatic rocks of the RGD and other BH domain rocks are needed in order to evaluate which of these tectonic models is most appropriate.

Post-2.0 Ga History

The post-2.0 Ga history of western Laurentia is characterized by ca. 1.98-1.92 Ga magmatism and high-grade metamorphism in the TMZ, ca. 1960-1910 Ma metamorphism and deformation in the BH domain, and post-1910 Ma late-stage retrogression recorded throughout BH domain, TMZ and western Rae crust. Ross and Eaton (2002) propose outward-dipping subduction zones flank the BH-CH composite domain between ca. 1.99 and 1.94 Ga (Figure 41d, e). In their model, west-dipping subduction of oceanic crust generated ca. 1987-1900 Ma magmatism beneath the Nova domain, and resulted in the formation of the Ksituan magmatic arc. Likewise, east-dipping subduction of oceanic crust triggered ca. 1972-1937 Ma magmatism beneath the Rae Province and formed many of the granitic rocks of the TMZ. Closure of the ocean basins on either side of the BH-CH domain is proposed to have accreted the various basement domains of northern Alberta onto the Rae Province (Figure 41e). Widespread ca. 1.98-1.92 Ga magmatism and ca. 1938-1919 Ma granulite- to amphibolite-grade metamorphism in metasedimentary rocks of the TMZ and the supposed absence of this metamorphic and magmatic activity in the BH domain led to the proposal that these two domains represent the overriding and subducting plates, respectively, during ocean basin

closure and domain collision (Ross et al., 1991, Theriault and Ross, 1991; Ross and Eaton, 2002).

In contrast to these models of subduction and accretion, Chacko et al. (2000) and De et al. (2000) argue that the various basement domains of western Laurentia have been a coherent crustal block since at least 2.3 Ga (Figure 41g). The recognition in the present study of upper amphibolite to possibly granulite-grade metamorphism and deformation in the RGD at ca. 1960-1910 Ma, coeval with metamorphism and deformation in the TMZ, provides a critical distinction between these two groups of models. Specifically, this finding strongly suggests a connection between the BH domain, the TMZ, and likely the western Rae Province. Metamorphism during this time interval in all of these domains appears more characteristic of a single, largely coherent entity that was reactivated over a broad area than of separate and unrelated blocks brought together by subduction of oceanic crust.

Multiple rock types in the RGD, particularly those associated with the N-S trending TMA, record ca. 1910-1865 Ma monazite growth. This episode of monazite growth is likely related to late-stage fluid influx and accompanying retrogression of high-grade assemblages. Other examples of late-stage, intermittent reactivation are given by Burwash et al. (2000b), which report three, N-S trending, low $\delta^{18}O$ samples within the TMA. Such ^{18}O depletion of rocks is generally associated with surface fluid-rock interaction along faults but a lack of publicly available seismic data prevents direct correlation of the low $\delta^{18}O$ with basement faulting. The presence of late-stage monazite growth could suggest that the RGD, or specifically the low density gravity anomaly of the TMA, marks an area of weakness in the Precambrian crust susceptible to intermittent reactivation and the influx of retrogressing fluids. In this regard, it is interesting to note that the location of the N-S trending TMA within the RGD also seems to coincide with some locations of kimberlite pipes recently discovered within the Buffalo Head Hills field (e.g. Eccles et al., 2003; Carlson et al., 1998). This suggests that this same zone of weakness may have been utilized by the kimberlite magmas to access the surface.

Summary

Implications to the understanding of the ca. 2.0 Ga tectonics of western Laurentia are extensive. Results of the present study characterize the RGD as an area of high-grade mid-crustal rocks that have experienced multiple episodes of magmatism, metamorphism, partial melting, and deformation. Importantly, many of the tectonothermal events recorded by the rocks of the RGD and the BH domain are also recorded by rocks of the TMZ and the western Rae Province. This resembles the effects of crustal shortening and thickening in a broad hinterland plateau, similar to the proposed features of the Queen Maud uplift and present-day features in the Tibetan plateau (e.g. Figure 40f, g) (Hoffman, 1987, 1988; Wei et al., 2001; Li et al., 2003). Crustal reactivation over a broad area of northern Alberta revisits earlier proposals of the dynamically reworked Athabasca Polymetamorphic terrane (otherwise known as BH domain) of Burwash and Krupicka (1969, 1970) and Burwash et al. (2000a). These workers long ago recognized the similarity between these buried basement rocks of north-central Alberta and the exposed shield rocks of northeastern Alberta and Churchill Province.

CONCLUSIONS

Detailed petrological and geochronological investigation of basement core samples greatly aids in the study of buried polymetamorphic terranes. EM and TIMS dating of RGD drill core samples provided the micron-scale ability to document rock types and the magmatic and metamorphic history over a narrow ~200 Myr Paleoproterozoic window. Pressure, temperature and age data obtained in this study lead to the following conclusions:

(1) The RGD was metamorphosed to granulite-grade conditions of at least 740-800°C and 6.2-7.0 kbars similar to P-T conditions recorded by some TMZ metasediments.

(2) A ca. 2065 Ma monazite age in a pelitic migmatite sample may represent the age of a detrital grain or an early phase of metamorphism.

(3) High-grade metamorphism occurred at ca. 2014 Ma, coeval with a previously reported metamorphic U-Pb zircon age from the BH domain.

(4) A separate ca. 1989 Ma high-grade metamorphism accompanied by partial melting may be recorded in the leucosome of a pelitic migmatitic sample. Alternatively, these data may reflect the inaccuracy of the EM dating technique that yielded this age estimate although this is not particularly indicated from other well-constrained samples.

(5) An episode of felsic magmatism is recorded in ca. 2020 Ma charnockite and ca. 2010-2000 Ma granite. Charnockitic magmatism likely reached temperatures greater than 900°C.

(6) Metasedimentary rocks spatially associated with the TMA record ca. 1960-1910 Ma upper amphibolite- or possibly granulite-facies metamorphism, which parallels high-grade metamorphism and deformation recorded in magmatic and metasedimentary rocks of the TMZ.

(7) Mesoperthite-bearing pelitic gneiss records a minimum metamorphic temperature of 905°C, similar to the P-T conditions of some TMZ lithologies.

(8) Retrograde mineral assemblages and late-stage monazite growth between ca. 1910-1865 Ma and younger than 1800 Ma could be associated with intermittent

deformation and retrogressing fluids in an area of weakness coincident with and possibly marked by the TMA.

(9) The similarities in the pre- and post-2.0 Ga histories of the Buffalo Head domain, the TMZ and western Rae Province are consistent with periodic reactivation of a single, largely coherent block of crust rather than assembly of separate blocks of crust by subduction and accretion between 2.0 to 1.9 Ga.

FUTURE WORK

With the advancing spatial resolution of isotopic probe techniques, such as laser ablation and ion microprobe, numerous *in-situ* studies could be conducted to evaluate further the accuracy of ages given by chemical and whole-grain isotopic methods. For instance:

- Analysis of metamorphic rim and oscillatory-zoned cores from detrital zircons of metasediments to determine an age of the protolith source rock and subsequent metamorphic events.
- Analysis of metamorphic zircon rims from felsic magmatic rocks in this study to compare with the age(s) of high-grade metamorphism.
- Target specific monazite crystals in the melanosome of pelitic migmatite (861510) to further resolve if the age(s) of high-grade metamorphism are linked to the timing of growth of various metamorphic minerals.

Further study could include:

- TIMS analysis of monazite from pelitic gneisses, migmatite, and Bt granite to refine the age(s) of metamorphism recorded by EM data.
- Chemical age dating of zircon (e.g. Geisler and Schleicher, 2000), such as from zircon in charnockite to correlate age with specific domains within the crystal. In this case, chemical ages could be used similarly as monazite but to determine if the 'blurred' internal structure involved lead movement.
- Geochemical and isotopic study of charnockites, TMA granites, and Ksituan arc magmatic rocks similar to that carried out by Chacko et al. (2000) and De et al. (2000) for rocks of the TMZ.
- Further EM age determinations of monazite from the CH and Ksituan domains and other parts of the BH domain.
- In the absence of widespread aluminosilicate assemblages, monazite-garnet thermometry on the basis of yttrium content (e.g. Pyle et al., 2001) could be explored and simultaneously measured during EM monazite age studies.

- Charnockite is noted by Berman and Bostock (1997) as present only as minor remnants throughout the TMZ batholiths. Further examination of such remnants could provide a missing link to charnockite present in the RGD.

LITERATURE CITED

Ahrens, L.H., Cherry, R.D. and Erlank, A.J. 1967. Observations on the Th-U relationship in zircons from granitic rocks and from kimberlites. Geochimica et Cosmochimica Acta, **31**: 2379-2387.

Alberta Basemap 1997. Northwest Quarter Provincial Basemap 1:500,000. Alberta Environmental Protection, Resource Data Division: Sheet 3.

Alling, H. L. 1938. Plutonic perthites. Journal of Geology, **46**: 142-165.

Asami, M., Suzuki, K., and Grew, E.S. 2002. Chemical Th-U-total Pb dating by electron microprobe analysis of monazite, xenotime and zircon from the Archean Napier Complex, East Antarctica: evidence for ultra-high-temperature metamorphism at 2400 Ma. Precambrian Research, **114**: 249-275.

Baadsgaard, H. and Godfrey, J.D. 1967. Geochronology of the Canadian Shield in northeastern Alberta I. Andrew Lake Area. Canadian Journal of Earth Sciences, **4**: 541-563.

Baadsgaard, H. and Godfrey, J.D. 1972. Geochronology of the Canadian Shield in northeastern Alberta II. Charles-Andrew-Colin Lakes Area. Canadian Journal of Earth Sciences, **9**: 563-881.

Berman, R.G. 1991. Thermobarometry using multi-equilibrium calculations: a new technique, with petrological applications. Canadian Mineralogist, **29**: 833-855.

Berman, R.G. and Aranovich, L.Ya. 1996. Optimized standard state and solution properties of minerals I. Model calibration for olivine, orthopyroxene, cordierite, garnet, and ilmenite in the system Fe-O-MgO-CaO-Al_2O_3-TiO_2-SiO_2. Contributions to Mineralogy and Petrology, **126**: 1-24.

Berman, R. G. and Bostock, H. H. 1997. Metamorphism in the Northern Taltson Magmatic Zone, Northwest Territories. Canadian Mineralogist, **35**: 1069-1091.

Bickford, M.E., Van Schmus, W.R., Collerson, K.D., and Macdonald, R. 1987. U-Pb Zircon Geochronology Project: new results and interpretations. *In* Summary of Investigations 1987, Saskatchewan Geological Survey; Saskatchewan Energy and Mines, Miscellaneous Report 87-4: 76-79.

Bickford, M.E., Collerson, K.D., and Lewry, J.F. 1994. Crustal history of the Rae and Hearne Provinces, southwestern Canadian Shield, Saskatchewan: constraints from geochronologic and isotopic data. Precambrian Research, **68**: 1-21.

Bohlen, S. R. and Essene, E. J. 1977. Feldspar and oxide thermometry of granulites in the Adirondack Highlands. Contributions to Mineralogy and Petrology, **62**: 153-169.

Bostock, H.H. 1981. A granitic diapir of batholithic dimensions at the west margin of the Churchill Province. *In* Current Research, Part B, Geological Survey of Canada, Paper 81-1B: 73-82.

Bostock, H.H. 1987. Geology of the south half of the Taltson Lake map area, District of Mackenzie. *In* Current Research, Part A, Geological Survey of Canada, Paper 87-1A: 443-450.

Bostock, H. H. and Loveridge, W. D. 1988. Geochronology of the Taltson magmatic zone and its eastern cratonic margin, District of Mackenzie. *In* Radiogenic Age and Isotopic Studies. Report 2: Geological Survey of Canada Paper 88-2: 59-65.

Bostock, H. H., van Breemen, O., and Loveridge, W. D. 1987. Proterozoic geochronology in the Taltson Magmatic Zone, N. W. T. *In* Radiogenic Age and Isotopic Studies: Report 1, Geological Survey of Canada, Paper 87-2: 73-80.

Bostock, H.H., van Breemen, O., and Loveridge, W.D. 1991. Further geochronology of plutonic rocks in northern Taltson Magmatic Zone, District of Mackenzie, N.W.T. *In* Radiogenic Age and Isotopic Studies: Report 4; Geological Survey of Canada, Paper 90-2: 67-78.

Bostock, H. H. and van Breemen, O. 1994. Ages of detrital and metamorphic zircons and monazites from a pre-Taltson magmatic zone basin at the western margin of Rae Province. Canadian Journal of Earth Sciences, **31**: 1353-1364.

Bouzidi, Y., Schmitt, D.R., Burwash, R.A., and Kanasewich, E.R. 2002. Depth migration of deep seismic reflection profiles: crustal thickness variations in Alberta. Canadian Journal of Earth Sciences, **39**: 331-350.

Bowring, S.A., Van Schmus, W.R., and Hoffman, P.F. 1984. U-Pb zircon ages from Athapuscow aulacogen, East Arm of Great Slave Lake, N.W.T., Canada. Canadian Journal of Earth Sciences, **21**: 1315-1324.

Bowring, S. A. and Podosek, F. A. 1989. Nd isotopic evidence from Wopmay Orogen for 2.0-2.4 Ga crust in western North America. Earth and Planetary Science Letters, **94**: 217-230.

Bowring, S.A., and Grotzinger, J.P. 1989. Implications of new U-Pb dating and stratigraphic correlations for current tectonic models for Wopmay orogen and Thelon tectonic zone. Program with Abstracts - Geological Association of Canada - Mineralogical Association of Canada; Canadian Geophysical Union, Joint Annual meeting, **14**: A74.

Bowring, S.A. and Grotzinger, J.P. 1992. Implications of new chronostratigraphy for tectonic evolution of Wopmay Orogen, Northwest Canadian Shield. American Journal of Science, **292**: 1-20.

Burwash, R.A. 1957. Reconnaissance of subsurface Precambrian of Alberta. Bulletin of the American Association of Petroleum Geologists, **41**: 70-103.

Burwash, R. A. 1978. Metamorphism of the Athabasca mobile belt a subsurface extension of the Churchill Province. *In* Metamorphism in the Canadian Shield, Geological Survey of Canada, Paper 78-10: 123-127.

Burwash, R.A. 1988. Petrology of the Precambrian Basement of Alberta. Report for Dept. of Energy, Mines & Resources, Canada, Final Report, Contract No. 23294-7-0621/01-SG: unpublished.

Burwash, R. A., Baadsgaard, H., and Peterman, Z.E. 1962. Precambrian K-Ar dates from the Western Canada Sedimentary Basin. Journal of Geophysical Research, **67**: 1617-1625.

Burwash, R.A. and Cumming, G.L. 1976. Uranium and thorium in the Precambrian basement of western Canada. I. Abundance and distribution. Canadian Journal of Earth Sciences, **13**: 284-293.

Burwash, R.A., Chacko, T., Muehlenbachs, K. and Bouzidi, Y. 2000b. Oxygen isotope systematics of the Precambrian basement of Alberta: implications for Paleoproterozoic and Phanerozoic tectonics in northwestern Alberta. Canadian Journal of Earth Sciences, **40**: 1611-1628.

Burwash, R. A. and Krupicka, J. 1969. Cratonic reactivation in the Precambrian basement of western Canada; [Part] I, Deformation and chemistry. Canadian Journal of Earth Sciences, **6**: 1381-1396.

Burwash, R. A. and Krupicka, J. 1970. Cratonic reactivation in the Precambrian basement of western Canada; [Part] II, Metasomatism and isostasy. Canadian Journal of Earth Sciences, **7**: 1275-1294.

Burwash, R.A., Krupicka, J. and Culbert, R.R. 1973. Cratonic Reactivation in the Precambrian Basement of Western Canada. III. Crustal Evolution. Canadian Journal of Earth Sciences, **10**: 283-291.

Burwash, R. A., Krupicka, J., Basu, A. R., and Wagner, P. A.. 1985. Resetting of Nd and Sr whole-rock isochrons from polymetamorphic granulites, northeastern Alberta. Canadian Journal of Earth Sciences, **22**: 992-1000.

Burwash, R. A., Krupicka, J., and Wijbrans, J. R. 2000a. Metamorphic evolution of the Precambrian basement of Alberta. Canadian Mineralogist, **38**: 423-434.

Burwash, R. A. and Power, M. A 1990. Trout Mountain Anomaly, Northern Alberta: its role in the northwest foreland of the Trans-Hudson Orogen. *In* The Early Proterozoic Trans-Hudson Orogen of North America. *Edited by* Lewry, J. F. and Stauffer, M. R..

Geological Association of Canada, Special Paper 37: 301-311.

Burwash, R.A. and Muehlenbachs, K. 1997. Tectonic setting of eastern Alberta basement granites inferred from Pearce trace element discrimination diagrams. Alberta Lithoprobe Report, 59: 35-49

Carlson, S.M., Hillier, W.D., Hood, C.T., Pryde, R.P., and Skelton, D.N. 1998. The Buffalo Hills Kimberlite Province, north-central Alberta, Canada. *In* Seventh International Kimberlite Conference - extended Abstracts, South Africa: 138-140.

Carstens, H. 1967. Exsolution in ternary feldspars, I. On the formation of antiperthites. Contributions to Mineralogy and Petrology, **14**: 27-35.

Catlos, E.J., Gilley, L.D. and Harrison, T.M. 2002. Interpretation of monazite ages obtained via in situ analysis. Chemical Geology, **188**: 193-215.

Chacko, T. 1997. Ultra-high temperature metamorphism at Pelican Rapids, Taltson magmatic zone, NE Alberta: possible implications for early Proterozoic collisional orogens. Geological Association of Canada – Mineralogical Association of Canada Annual Meeting Abstracts, **22**: 24.

Chacko, T., Creaser, R. A., and Poon, D. 1994. Spinel + quartz granites and associated metasedimentary enclaves from the Taltson magmatic zone, Alberta, Canada: a view into the root zone of a high-temperature, S-type granitic batholith. Mineralogical Magazine, **58a**: 161-162.

Chacko, T., De, S. K., Creaser, R. A., and Muehlenbachs, K. 2000. Tectonic setting of the Taltson magmatic zone at 1.9 to 2.0 Ga: a granite-based perspective. Canadian Journal of Earth Sciences, **37**: 1597-1609.

Cherniak, D.J. and Watson, E.B. 2000. Pb diffusion in zircon. Chemical Geology, **172**: 5-24.

Cherniak, D.J., Watson, E.B., Harrison, T.M., and Grove, M. 2000. Pb diffusion in monazite: a progress report on a combined RBS/SIMS study. Eos Transactions Abstracts, American Geophysical Union, 81: S25.

Cherniak, D.J., Watson, E.B., Grove, M., and Harrison, T.M. 2004. Pb diffusion in monazite: a combined RBS/SIMS study. Geochimica et Cosmochimica Acta, **68**: 829-840.

Cocherie, A., Legendre, O., Peucat, J.J., Kouamelan, A.N. 1998. Geochronology of polygenetic monazites constrained by in situ electron microprobe Th-U-total lead determination: implications for lead behavior in monazite. Geochimica et Cosmochimica Acta, **62**: 2475-2497.

Cocherie, A. and Albarede, F. 2001. An improved U-Th-Pb age calculation for electron microprobe dating of monazite. Geochimica et Cosmochimica Acta, **65**: 4509-4522.

Copeland, P., Parrish, R.R., and Harrison, T.M. 1988. Identification of inherited radiogenic Pb in monazite and its implications for U-Pb systematics. Nature, **333**: 760-763.

Creaser, R. A. and Chacko, T. 1995. Hercynite-bearing granites and associated metasedimentary enclaves from Pelican Rapids, NE Alberta; a natural example of high-temperature pelite melting. Program with Abstracts - Geological Association of Canada; Mineralogical Association of Canada; Canadian Geophysical Union, Joint Annual meeting, **20**: 21.

Crocker, C.H., Collerson, K.D., Lewry, J.F., and Bickford, M.E. 1993. Sm-Nd, U-Pb, and Rb-Sr geochronology and lithostructural relationships in the southwestern Rae Province: constraints on crustal assembly in the western Canadian shield. Precambrian Research, **61**: 27-50.

Crowley, J.L. and Ghent, E.D. 1999. An electron microprobe study of the U-Th-Pb systematics of metamorphosed monazite: the role of Pb diffusion versus overgrowth and recrystallization. Chemical geology, **157**: 285-302.

Dahl, P.S., Foland, K.A., Frei, R., Hamilton, M.A., Jercinovic, M.J., Stern, R.A., Terry, M.P., and Williams, M.L. 2001. Aqueous fluids promoting radiogenic Pb and Ar loss from minerals: evidence from disparate ages in the Black Hills. Eos Transactions Abstracts, American Geophysical Union, **82**: S275.

Davis, D.W. 1982. Optimum linear regression and error estimation applied to U-Pb data. Canadian Journal of Earth Sciences, **19**: 2141-2149.

Day, H. W. and Brown, V. M. 1980. Evolution of perthite composition and microstructure during progressive metamorphism of hypersolvus granite, Rhode Island, USA. Contributions to Mineralogy and Petrology, **72**: 353-365.

De, S.K., Chacko, T., Creaser, R.A. and Muehlenbachs, K. 2000. Geochemical and Nd-Pb-O isotope systematics of granites from the Taltson Magmatic Zone, NE Alberta; implications for early Proterozoic tectonics in western Laurentia. Precambrian Research, **102**: 221-249.

Deer, W.A., Howie, R.A. and Zussman, J. 1992. An introduction to the rock-forming minerals. Prentice Hall, Ontario: 696p.

Dobmeier, C. and Simmat, R. 2002. Post-Grenvillean transpression in the Chilka Lake area, Eastern Ghats Belt - implications for the geological evolution of peninsular India. Precambrian Research, **113**: 243-268.

Dodson, M.H. 1973. Closure temperature in cooling geochronological and petrological systems. Contributions to Mineralogy and Petrology, **40**: 259-274.

Driver, L.A., Creaser, R.A., Chacko, T., and Erdmer, P. 2000. Petrogenesis of the Cretaceous Cassiar batholith, Yukon-British Columbia, Canada: Implications for magmatism in the North American Cordilleran Interior. Geological Society of America Bulletin, **112**: 1119-1133.

Eccles, D.R., Heaman, L.M., Luth, R.W., and Creaser, R.A. 2003. Petrogenetic considerations for the Late Cretaceous Northern Alberta Kimberlite Province. *In* Eighth International Kimberlite Conference - extended Abstracts, Vancouver, B.C., Canada.

Elkins, L. T. and Grove, T. L. 1990. Ternary feldspar experiments and thermodynamic models. American Mineralogist, **75**: 544-559.

Farquhar, J., Chacko, T. and Ellis, D.J. 1996. Preservation of oxygen isotope compositions in granulites from Northwestern Canada and Enderby Land, Antarctica: implications for high-temperature isotopic thermometry. Contributions to Mineralogy and Petrology, **125**: 213-224.

Finger, F. and Helmy, H.M. 1998. Composition and total-Pb model ages of monazite from high-grade paragneisses in the Abu Swayel area, southern Eastern Desert, Egypt. Mineralogy and Petrology, **62**: 269-289.

Foster, G., Gibson, H.D., Parrish, R., Horstwood, M., Fraser, J., and Tindle, A. 2002. Textural, chemical and isotopic insights into the nature and behavior of metamorphic monazite. Chemical Geology, **191**: 183-207.

Fuhrman, M. L. and Lindsley, D. H. 1988. Ternary-feldspar modeling and thermometry. American Mineralogist, **73**: 201-215.

Geisler, T. and Schleicher, H. 2000. Improved U-Th-total Pb dating of zircons by electron microprobe using a simple new background modeling procedure and Ca as a chemical criterion of fluid-induced U-Th-Pb discordance in zircon. Chemical Geology, **163**: 269-285.

Godfrey, J. D. and Langenberg, C. W. 1978. Metamorphism in the Canadian Shield of northeastern Alberta. *In* Metamorphism in the Canadian Shield. Geological Survey of Canada, Paper 78-10: 129-138.

Goff, S.P., Godfrey, J.D., and Holland, J.G. 1986. Petrology and geochemistry of the Canadian Shield of northeastern Alberta. Alberta Research Council, Bulletin No. 51: 60p.

Griffin, W. L. 1969. Replacement antiperthites in gneisses of the Babbitt-Embarrass area, Minnesota, U.S.A. Lithos, **2**: 171-186.

Grotzinger, J.P. and McCormick, D.S. 1988. Flexure of the early Proterozoic lithosphere and the evolution of Kilohigok basin (1.9 Ga), northwest Canadian shield. *In* New Perspectives in Basin Analysis. *Edited by* Kleinspehn, K. and C. Paola, C. Heidelberg: Springer-Verlag, pp. 406-430.

Grover, T.W., McDonough, M.R., and McNicoll, V.J. 1993. Preliminary report of the metamorphic geology of Taltson magmatic zone, Canadian Shield, northeastern Alberta. *In* Current Research, Part C, Geological Survey of Canada, Paper 93-1C: 233-238.

Grover, T.W., Pattison, D.R.M., McDonough, M.R., and McNicoll V.J. 1997. Tectonometamorphic evolution of the southern Taltson magmatic zone and associated shear zones, northeastern Alberta. Canadian Mineralogist, **35**: 1051-1067.

Hanchar, J.M. and Miller, C.F. 1993. Zircon zonation patterns as revealed by cathodoluminescence and backscattered electron images: Implications for interpretation of complex crustal histories. Chemical Geology, **110**: 1-13.

Hanmer, S. 1988. Great Slave Lake Shear Zone, Canadian Shield: reconstructed vertical profile of a crustal-scale fault zone. Tectonophysics, **149**: 245-264.

Hanmer, S., Bowring, S., van Breemen, O., and Parrish, R. 1992. Great Slave Lake shear zone, NW Canada: mylonitic record of Early Proterozoic continental convergence, collision and indentation. Journal of Structural Geology, **14**: 757-773.

Hanmer, S., Parrish, R., Williams, M., and Kopf, C. 1994. Striding-Athabasca mylonite zone: complex Archean deep-crustal deformation in the East Athabasca mylonite triangle, northern Saskatchewan. Canadian Journal of Earth Sciences, **31**: 1287-1300.

Hanmer, S., Williams, M., and Kopf, C. 1995a. Striding-Athabasca mylonite zone: implications for the Archean and Early Proterozoic tectonics of the western Canadian Shield. Canadian Journal of Earth Sciences, **32**: 178-196.

Hanmer, S., Williams, M., and Kopf, C. 1995b. Modest movements, spectacular fabrics in an intracontinental deep-crustal strike-slip fault: Striding-Athabasca mylonite zone, NW Canadian Shield. Journal of Structural Geology, **17**: 493-507.

Harrison, T.M., Catlos, E.J. and Montel, J-M. 2002. U-Th-Pb Dating of Phosphate Minerals. *In* Phosphates: Geochemical, Geobiological and Materials Importance. *Edited by* Kohn, M.J., Rakovan, J., and Hughes, J.M. Reviews in Mineralogy and Geochemistry, **48**: 523-558.

Hawkins, D.P. and Bowring, S.A. 1997. U-Pb systematics of monazite and xenotime: case studies from the Paleoproterozoic of the Grand Canyon, Arizona. Contributions to Mineralogy and Petrology, **127**: 87-103.

Heaman, L. and Parrish, R. 1991. U-Pb geochronology of accessory minerals. *In* Applications of radiogenic isotope systems to problems in geology. *Edited by* Heaman, L. and Ludden, J.N.. Mineralogical Association of Canada Short Course Handbook, **19**: 59-102.

Heaman, L.M. and LeCheminant, A.N. 2000. Anomalous U-Pb systematics in mantle-derived baddelyite xenocrysts from Île-Bizard: evidence for high temperature radon diffusion? Chemical Geology, **172**: 77-93.

Heaman, L.M., Erdmer, P., and Owen, J.V. 2002a. U-Pb geochronologic constraints on the crustal evolution of the Long Range Inlier, Newfoundland. Canadian Journal of Earth Sciences, **39**: 845-865.

Heaman, L.M., Creaser, R.A. and Cookenboo, H.O. 2002b. Extreme enrichment of high field strength elements in Jericho eclogite xenoliths: a cryptic record of Paleoproterozoic subduction, partial melting, and metasomatism beneath the Slave craton, Canada. Geology, **30**: 507-510.

Hecht, L. and Cuney, M. 2000. Hydrothermal alteration of monazite in the Precambrian crystalline basement of the Athabasca Basin (Saskatchewan, Canada): implications for the formation of unconformity-related uranium deposits. Mineralium Deposita, **35**: 791-795.

Henderson, J.B. and van Breemen, O. 1992. U-Pb zircon ages from an Archean orthogneiss and a Proterozoic metasedimentary gneiss of the Thelon Tectonic Zone, District of Mackenzie, Northwest Territories. *In* Radiogenic Age and Isotopic Studies: Report 5, Geological Survey of Canada, Paper 91-2: 25-33.

Hoffman, P. F. 1987. Continental transform tectonics: Great Slave Lake shear zone (ca. 1.9 Ga), northwest Canada. Geology, **15**: 785-788.

Hoffman, P. F. 1988. United Plates of America, the birth of a craton: Early Proterozoic assembly and growth of Laurentia. Annual Review of Earth and Planetary Sciences, **16**: 543-603.

Hoffman, P. F. 1989. Precambrian geology and tectonic history of North America. *In* Vol. A, The Geology of North America - An overview, Geological Society of America: 447-512.

Hoskin, P.W.O. and Black, L.P. 2000. Metamorphic zircon formation by solid-state recrystallization of protolith igneous zircon. Journal of Metamorphic Geology, **18**: 423-439.

Hubbard, F.H. 1965. Antiperthite and mantled feldspar textures in charnockite (enderbite) from S.W. Nigeria. American Mineralogist, **50**: 2040-2051.

Hulbert, L. 1988. Investigation of mafic and ultramafic rocks for nickel-copper and platinum group elements in northern Saskatchewan: preliminary findings. *In* Summary of Investigation 1988, Saskatchewan Geological Survey; Saskatchewan Energy and Mines, Miscellaneous Report 88-4: 152-154.

Jaffey, A.H., Flynn, K.F., Glendenin, L.E., Bentley, W.C., and Essling, A.M. 1971. Precision measurement of half-lives and specific activities of ^{235}U and ^{238}U. Physical Review C, **4**: 1889-1906.

Kilpatrick, J.A. and Ellis, D.J. 1992. C-type magmas: igneous charnockites and their extrusive equivalents. Transactions of the Royal Society of Edinburgh: Earth Sciences, **83**: 155-164.

Klein, C. and Hurlbut, Jr., C. S. 1993. Manual of mineralogy. John Wiley & Sons, Inc. Toronto: 681p.

Kohn, M.J. and Spear, F.S. 1991. Error propagation for barometers: 2. Application to rocks. American Mineralogist, **76**: 138-147.

Koster, F. and Baadsgaard, H. 1970. On the geology and geochronology of northwestern Saskatchewan. I. Tazin lake region. Canadian Journal of Earth Sciences, **7**: 919-930.

Krogh, T.E. 1982. Improved accuracy of U-Pb zircon ages by the creation of more concordant systems using an air abrasion technique. Geochimica et Cosmochimica Acta, **46**: 637-649.

Kroll, H., Evangelakakis, C., and Voll, G. 1993. Two-feldspar geothermometry: a review and revision for slowly cooled rocks. Contributions to Mineralogy and Petrology, **114**: 510-518.

Langenberg, C.W. 1983. Polyphase deformation in the Canadian Shield of northeastern Alberta. Alberta Research Council, Bulletin No. 45: 33p.

Langenberg, C.W. and Nielsen, P.A. 1982. Polyphase metamorphism in the Canadian Shield of Northeastern Alberta. Alberta Research Council, Bulletin No. 42: 80p.

Lee, J.K.W., Williams, I.S., and Ellis, D.J. 1997. Pb, U and Th diffusion in natural zircon. Nature, **390**: 159-162.

LeMaitre, R.W., Streckeisen, A., Zanettin, B., LeBas, M.J., Bonin, B., Bateman, P., Bellieni, G., Dudek, A., Efremova, S., Keller, J., Lameyre, J., Sabine, P.A., Schmid, R., Sørensen, H., and Woolley, A.R. 2002. Igneous Rocks, A classification and Glossary of Terms. Recommendation of the International Union of Geological

Sciences Subcommission on the Systematics of Igneous Rocks, Cambridge University Press, U.K.: p. 20.

Lewry, J.F. and Sibbald, T.I.I. 1977. Variation in lithology and tectonometamorphic relationships in the Precambrian basement of northern Saskatchewan. Canadian Journal of Earth Sciences, **14**: 1453-1467.

Lewry, J.F. and Sibbald, T.I.I. 1980. Thermotectonic evolution of the Churchill Province in northern Saskatchewan. Tectonophysics, **68**: 45-82.

Li, S., Unsworth, M., Booker, J., Wei, W., Tan, H., and Jones, A. 2003. Partial melt or aqueous fluid in the mid-crust of Southern Tibet? Constraints from INDEPTH magnetotelluric data. Geophysical Journal International, **153**: 289-304.

Lindsley, D.H. and Nekvasil, H. 1989. A ternary feldspar model for all reasons. Eos, **70**: 506.

Ludwig, K.R. 2001. Isoplot/Ex re. 2.49. Berkeley Geochronology Center Special Publication No. 1a: 55p.

Mathieu, R., Zetterström, L., Cuney, M., Gauthier-Lafaye, F., and Hidaka, H. 2001. Alteration of monazite and zircon and lead migration as geochemical tracers of fluid paleocirculations around the Oklo-Okélobondo and Bangombé natural nuclear reaction zones (Franceville basin, Gabon). Chemical Geology, **171**: 147-171.

Mattinson, J.M., Graubard, C.M., Parkinson, D.L., and McClelland, W.C. 1996. U-Pb reverse discordance in zircons: the role of fine-scale oscillatory zoning and sub-micron transport of Pb. Geophysical Monograph, **95**: 355-370.

McDonough, M. R., Grover, T. W., McNicoll, V. J., and Lindsay, D. D. 1993. Preliminary report of the geology of the southern Taltson magmatic zone, northeastern Alberta. *In* Current Research, Part c; Geological Survey of Canada, Paper 93-1C: 221-232.

McDonough, M.R., McNicoll, V.J., and Thériault, R.J. 1995a. Taltson basement complex: Basement to a Paleoproterozoic continental collisional and magmatic orogen. Program with Abstracts, Geological Association of Canada; Mineralogical Association of Canada; Canadian Geophysical Union, Joint Annual meeting, 20: 68.

McDonough, M.R., McNicoll, V.J., Schetselaar, E.M. 1995b. Age and kinematics of crustal shortening and escape in a two sided oblique slip collisional and magmatic orogen, Paleoproterozoic Taltson Magmatic Zone, northeastern Alberta. *In* Alberta Basement Transects Workshop, Lithoprobe Report, 47. *Edited by* Ross, G.M. Lithoprobe Secretariat, University of British Columbia: 264-309.

McDonough, M.R. and McNicoll, V.J. 1997. U-Pb age constraints on the timing of deposition of the Waugh Lake and Burntwood (Athabasca) groups, southern Taltson magmatic zone, northeastern Alberta. *In* Radiogenic Age and Isotope Studies: Report 10; Geological Survey of Canada, Current Research 1997-F: 101-111.

McDonough, M.R., McNicoll, V.J., Schetselaar, E.M., and Grover, T.W. 2000. Geochronological and kinematic constraints on crustal shortening and escape in a two-sided oblique-slip collisional and magmatic orogen, Paleoproterozoic Taltson magmatic zone, northeastern Alberta. Canadian Journal of Earth Sciences, **37**: 1549-1573.

McDonough, M.R., Plint, H.E., McNicoll, V.J., and Grover, T.W. 1994. $^{40}Ar/^{39}Ar$ and K-Ar age constraints on shear zone evolution, southern Taltson magmatic zone, northeastern Alberta. *In* Alberta Basement Transects Workshop, Lithoprobe Report, 37. *Edited by* Ross, G.M. Lithoprobe Secretariat, University of British Columbia: 254-265.

McNicoll, V.J., McDonough, M.R., and Grover, T.W. 1994. U-Pb geochronological studies in the Southern Taltson Magmatic Zone, Northeastern Alberta. *In* Alberta Basement Transects Workshop, Lithoprobe Report, 37. *Edited by* Ross, G.M. Lithoprobe Secretariat, University of British Columbia: 270-273.

McNicoll, V.J., Thériault, R.J. and McDonough, M.R. 2000. Taltson basement gneissic rocks: U-Pb and Nd isotopic constraints on the basement to the Paleoproterozoic Taltson magmatic zone, northeastern Alberta. Canadian Journal of Earth Sciences, **38**: 1575-1596.

Mezger, K. and Krogstad, E.J. 1997. Interpretation of discordant U-Pb zircon ages: an evaluation. Journal of Metamorphic Geology, **15**: 127-140.

Mezger, J.E., Chacko, T., and Erdmer, P. 2001. Metamorphism at a late Mesozoic accretionaly margin: a study from the Coast Belt of the North American Cordillera. Journal of Metamorphic Geology, **19**: 121-137.

Montel, J-M., Foret, S., Veschambre, M., Nicollet, C., and Provost, A. 1996. Electron microprobe dating of monazite. Chemical Geology, **131**: 37-53.

Montel, J-M., Kornprobst, J. and Vielzeuf, D. 2000. Preservation of old U-Th-Pb ages in shielded monazite: example from the Beni Bousera Hercynian kinzigites (Morocco). Journal of Metamorphic Geology, **18**: 335-342.

Nielsen, P. A., Langenberg, C. W., Baadsgaard, H., and Godfrey, J. D. 1981. Precambrian metamorphic conditions and crustal evolution, northeastern Alberta, Canada. Precambrian Research, **16**: 171-193.

Overstreet, W.C. 1967. The geologic occurrence of monazite. Geological Survey Professional Paper 530, U.S. Department of the Interior: 333p.

Parrish, R.R. 1990. U-Pb dating of monazite and its application to geological problems. Canadian Journal of Earth Sciences, **27**: 1431-1450.

Pattison, D.R.M., Chacko, T., Farquhar, J., and McFarlane, C.R.M. 2003. Temperatures of granulite-facies metamorphism: constraints from experimental phase equilibria and thermobarometry corrected for retrograde exchange. Journal of Petrology, **44**: 867-900.

Pidgeon, R.T., O'Neil, J.R., and Silver, L.T. 1966. Uranium and lead isotopic stability in a metamict zircon under experimental hydrothermal conditions. Science, **154**: 1538-1540.

Plint, H. E. and McDonough, M.R. 1995. $^{40}Ar/^{39}Ar$ and K-Ar age constraints on shear zone evolution, southern Taltson magmatic zone, northeastern Alberta. Canadian Journal of Earth Sciences, **32**: 281-291.

Plint, H. E. and Ross, G. M. 1993. $^{40}Ar/^{39}Ar$ geochronology of selected crystalline basement samples from the Alberta Basin: the timing of Proterozoic assembly of the subsurface of western Canada. *In* Radiogenic Age and Isotopic Studies: Report 7; Geological Survey of Canada, Paper 93-2: 71-82.

Poitrasson, F., Chenery, S. and Bland, D.J. 1996. Contrasted monazite hydrothermal alteration mechanisms and their geochemical implications. Earth and Planetary Science Letters, **145**: 79-96.

Pyle, J.M., Spear, F.S., Rudnick, R.L., and McDonough, W.F. 2001. Monazite-xenotime-garnet equilibrium in metapelites and a new monazite-garnet thermometer. Journal of Petrology, **42**: 2083-2107.

Raase, P. 1998. Feldspar thermometry; a valuable tool for deciphering the thermal history of granulite-facies rocks, as illustrated with metapelites from Sri Lanka. Canadian Mineralogist, **36**: 67-86.

Raase, P. 2000. Orientation of exsolution lamellae and rods, and optimal phase-boundaries in antiperthite from pelitic granulites, Sri Lanka. Canadian Mineralogist, **38**: 695-705.

Ranger, I. 2000. Two-feldspar geothermometry applied to the Red Earth Granulite Domain in Alberta, Canada. unpublished undergraduate Honor's Thesis, University of Alberta: 46p.

Ross, G. M. 1990. Deep crust and basement structure of the Peace River Arch region: constraints on mechanisms of formation. Bulletin of Canadian Petroleum Geology,

38A: 25-35.

Ross, G.M. 2002. Evolution of Precambrian continental lithosphere in Western Canada: results from Lithoprobe studies in Alberta and beyond. Canadian Journal of Earth Science, **39**: 413-437.

Ross, G.M. and Eaton, D.W. 1999. Basement reactivation in the Alberta Basin: observational constraints and mechanical rationale. Bulletin of Canadian Petroleum Geology, **47**: 391-411.

Ross, G.M. and Eaton, D.W. 2002. Proterozoic tectonic accretion and growth of western Laurentia: results from Lithoprobe studies in northern Alberta. Canadian Journal of Earth Sciences, **39**: 313-329.

Ross, G. M., Parrish, R.R., Villeneuve, M.E., and Bowring, S.A. 1991. Geophysics and geochronology of the crystalline basement of the Alberta Basin, western Canada. Canadian Journal of Earth Sciences, **28**: 512-522.

Ross, G.M., Villeneuve, M.E., Thériault, R. and Eaton, D.W. 2000. Precambrian basement of the Alberta Basin: From drill core to Moho. Canadian Society of Exploration Geophysicists Conference Abstract.

Schärer, U. 1984. The effect of initial ^{230}Th disequilibrium on young U-Pb ages: the Makalu case, Himalaya. Earth and Planetary Science Letters, **67**: 191-204.

Scherrer, N.C., Engi, M., Gnos, E., Jakob, V., and Liechti, A. 2000. Monazite analysis; from sample preparation to microprobe age dating and REE quantification. Schweizerische Mineralogische und Petrographische Mitteilungen, **80**: 93-105.

Schmitz, M.D. and Bowring, S.A. 2003. Ultrahigh-temperature metamorphism in the lower crust during Neoarchean Ventersdorp rifting and magmatism, Kaapvaal Craton, southern Africa. Geological Society of America Bulletin, **115**: 533-548.

Scott, V.D. and Love, G. 1983. Quantitative Electron-Probe Microanalysis. John Wiley & Sons, Ontario: 134-142.

Seck, H. A. 1971. Der Einfluß des Drucks auf die Zusammensetzung koexistierender Alkalifeldspäte und Plagioklase im System $NaAlSi_3O_8$-$KAlSi_3O_8$-$CaAl_2Si_2O_8$-H_2O. Contributions to Mineralogy and Petrology, **31**: 67-86.

Sen, S. K. 1959. Potassium content of natural plagioclases and the origin of antiperthites. Journal of Geology, **67**: 479-495.

Sharpton, V.L. 1987. Horizontal gravity gradient: an aid to the definition of crustal structure in North America. Geophysical Research Letters, **14**: 808-811.

Shillibeer, H.A. and Burwash, R.A. 1956. Some potassium-argon ages for western Canada. Science, **123**: 938-939.

Smith, J.V. and Brown, W.L. 1988. Feldspar minerals: crystal structures, physical, chemical, and microtextural properties. Springer-Verlag, New York, 1: 828p.

Smith, H.A. and Giletti, B.J. 1997. Lead diffusion in monazite. Geochimica et Cosmochimica Acta, **61**: 1047-1055.

Snoeyenbos, D.R., Williams, M.L. and Hanmer, S. 1995. Archean high-pressure metamorphism in the western Canadian Shield. European Journal of Mineralogy, **7**: 1251-1272.

Spear, F.S. 1995. Metamorphic phase equilibria and pressure-temperature-time paths. Mineralogical Society of America Monograph, Washington, D.C.: 799p.

Spear, F.S. and Florence, F.P. 1992. Thermobarometry in granulites: pitfalls and new approaches. Precambrian Research, **55**: 209-241.

Spear, F.S. and Pyle, J.M. 2002. Apatite, monazite, and xenotime in metamorphic rocks. *In* Phosphates: Geochemical, Geobiological and Materials Importance. *Edited by* Kohn, M.J., Rakovan, J., and Hughes, J.M. Reviews in Mineralogy and Geochemistry, **48**: 293-335.

Spear, F.S. and Selverstone, J. 1983. Quantitative P-T paths from zoned minerals: theory and tectonic applications. Contributions to Mineralogy and Petrology, **83**: 348-357.

Stacey, J.S. and Kramers, J.D. 1975. Approximation of terrestrial lead isotope evolution by a two-stage model. Earth and Planetary Science Letters, **26**: 207-221.

Suzuki, K. and Adachi, M. 1991. Precambrian provenance and Silurian metamorphism of the Tsubonosawa paragneiss in the South Kitakami terrane, Northeast Japan, revealed by the chemical Th-U-total Pb isochron ages of monazite, zircon and xenotime. Geochemical Journal, **25**: 357-376.

Suzuki, K., Adachi, M. and Tanaka, T. 1991. Middle Precambrian provenance of Jurassic sandstone in the Mino Terrane, central Japan: Th-U-total Pb evidence from an electron microprobe monazite study. Sedimentary Geology, **75**: 141-147.

Suzuki, K., Adachi, M. and Kajizuka, I. 1994. Electron microprobe observations of Pb diffusion in metamorphosed detrital monazites. Earth and Planetary Science Letters, **128**: 391-405.

Teufel, S. and Heinrich, W. 1997. Partial resetting of the U-Pb isotope system in monazite through hydrothermal experiments: an SEM and U-Pb isotope study. Chemical Geology, **137**: 273-281.

Thériault, R. J. 1992. Nd isotopic evolution of the Taltson Magmatic Zone, Northwest Territories, Canada: insights into early Proterozoic accretion along the western margin of the Churchill Province. Journal of Geology, **100**: 465-475.

Thériault, R.J. 1994. Nd Isotopic evidence for Protopaleozoic pre-Taltson Magmatic Zone (1.99-1.90 Ga) rifting of the western Churchill Province. *In* Alberta Basement Transects Workshop, Lithoprobe Report, 37. *Edited by* Ross, G.M. Lithoprobe Secretariat, University of British Columbia: 267-269.

Thériault, R. J. and Ross, G. M. 1991. Nd isotopic evidence for crustal recycling in the ca. 2.0 Ga subsurface of western Canada. Canadian Journal of Earth Sciences, **28**: 1140-1147.

Thompson, A.B. 1988. Heat, fluids, and melting in the granulite facies. *In* NATO ASI Series, Series C. *Edited by* Vielzeuf, D. and Vidal, P. Mathematical and Physical Sciences, **311**: 37-57.

Tremblay, L.P., Loveridge, W.D., and Sullivan, R.W. 1981. U-Pb ages of zircons from the Foot Bay gneiss and the Donaldson Lake gneiss, Beaverlodge Area, Northern Saskatchewan. *In* Current Research, Part C, Geological Survey of Canada, Paper 81-1C: 123-126.

van Breemen, O. and Aspler, L.B. 1994. Detrital zircon ages from Nonacho Basin, western Rae Province, Northwest Territories. *In* Radiogenic Age and Isotope Studies: Report 8; Geological Survey of Canada, Current Research1994-F: 49-59.

van Breemen, O. and Bostock, H.H. 1994. Age of emplacement of Thoa metagabbro, western margin of Rae Province, Northwest Territories: initiation of rifting prior to Taltson magmatism? *In* Radiogenic Age and Isotope Studies: Report 8; Geological Survey of Canada, Current Research 1994-F: 61-68.

van Breemen, O., Bostock, H.H., and Loveridge, W.D. 1992. Geochronology of granites along the margin of the northern Taltson Magmatic Zone and western Rae Province, Northwest Territories. *In* Radiogenic Age and Isotopic Studies: Report 5; Geological Survey of Canada, Paper 91-2: 17-24.

van Breemen, O. and Hanmer, S. 1986. Zircon morphology and U-Pb geochronology in active shear zones: studies on syntectonic intrusions along the northwest boundary of the Central Metasedimentary Belt, Grenville Province, Ontario. *In* Current Research, Part B, Geological Survey of Canada, Paper 86-1B: 775-784.

van Breemen, O., Henderson, J.B., Loveridge, W.D., and Thompson, P.H. 1987. U-Pb zircon and monazite geochronology and zircon morphology of granulites and granite from the Thelon Tectonic Zone, Healey Lake and Artillery Lake map areas, N.W.T. *In* Current Research, Part A, Geological Survey of Canada, Paper 87-1A: 783-801.

Van Schmus, W.R., Persons, S.S., Macdonald, R., and Sibbald, T.I.I. 1986. Preliminary Results from U-Pb Zircon Geochronology of the Uranium City Region. *In* Summary of Investigation 1986, Saskatchewan Geological Survey; Saskatchewan Energy and Mines, Miscellaneous Report 86-4: 108-111.

Villeneuve, M.E., Ross, G.M., Thériault, R.J., Miles, W., Parrish, R.R., and Broome, J. 1993. Tectonic Subdivision and U-Pb Geochronology of the Crystalline Basement of the Alberta Basin, Western Canada. Geological Survey of Canada, Bulletin 447: 1-86.

Voll, G., Evangelakakis, C., and Kroll, H. 1994. Revised two-feldspar geothermometry applied to Sri Lankan feldspars. Precambrian Research, **66**: 351-377.

Walcott, R. I. and Boyd, J. B. 1971. The gravity field of northern Alberta, and part of Northwest Territories and Saskatchewan. Department of Energy, Mines and Resources (Canada), Earth Physics Branch, Gravity Map Series, Nos: 103-111.

Waters, D.J. 1991. Hercynite-quartz granulites: phase relations, and implications for crustal processes. European Journal of Mineralogy, **3**: 367-386.

Watt, G.R. 1995. High-thorium monazite-(Ce) formed during disequilibrium melting of metapelites under granulite-facies conditions. Mineralogical Magazine, **59**: 735-743.

Wei, W., Unsworth, M., Jones, A., Booker, J., Tan, H., Nelson, D., Chen, L., Li, S., Solon, K., Bedrosian, P., Jin, S., Deng, M., Ledo, J., Kay, D., Roberts, B. 2001. Detection of widespread fluids in the Tibetan crust by magnetotelluric studies. Science, **292**: 716-718.

Wen, S. and Nekvasil, H. 1994. SOLVCALC: An interactive graphics program package for calculating the ternary feldspar solvus and for two-feldspar geothermometry. Computers & Geosciences, **20**: 1025-1040.

White, R.W., Powell, R. and Holland, T.J.B. 2001. Calculation of partial melting equilibria in the system Na_2O-CaO-K_2O-FeO-MgO-Al_2O_3-SiO_2-H_2O (NCKFMASH). Journal of Metamorphic Geology, **19**: 139-153.

Yund, R. A. and Ackermand, D. 1979. Development of perthite microstructures in the Storm King Granite, N.Y. Contributions to Mineralogy and Petrology, **70**: 273-280.

Yund, R.A., Ackermand, D. and Seifert, F. 1980. Microstructures in the alkali feldspars from the granulite complex of Finnish Lapland. Neues Jahrbuch Mineralogie Abhandlung, **3**: 109-117.

Zhu, X. K. and O'Nions, R. K. 1999. Zonation of monazite in metamorphic rocks and its implications for high temperature thermochronology: a case study from the Lewisian terrain. Earth and Planetary Science Letters, **171**: 209-220.

Appendix A. Available U-Pb, Rb-Sr, Sm-Nd and select (>1700 Ma) K-Ar and Ar-Ar age data of tectonic domains of western Laurentia. Age determination methods and references included within table. K-Ar and Ar-Ar age data are original and not recalculated unless indicated.

Identifier	Location	Rock Type	Technique	Age (Ma)	Sm-Nd ε_{Nd}	T_{DM} (Ga)	Comments	Source	Ref. #
Rocks of the Buried Precambrian Shield									
Red Earth Granulite Domain (RGD)									
PREVIOUS RESEARCH									
86023a	2-27-81-9w5	leucocratic monzonite	Sm-Nd		-6.1	2.91	at 2020 Ma	P. Cavell; Burwash pers comm	
86028a	16-30-81-9w5	two pyroxene granulite	Sm-Nd		-4.8	2.72	at 2020 Ma	P. Cavell; Burwash pers comm	
86028b	16-30-81-9w5	leucocratic quartz diorite	Sm-Nd		-4.1	2.65	at 2020 Ma	P. Cavell; Burwash pers comm	
86052b	15-12-82-10w5	Hypersthene-Bt-Plag-Microcline granulite	Sm-Nd		-5.1	2.62	at 2020 Ma	P. Cavell; Burwash pers comm	
	same as above	*rock type same as above*	Sm-Nd errorchron	1817±175	-7.8±2.2 (@1817 Ma)		*all above samples*	P. Cavell; Burwash pers comm	
	same as above	*rock type same as above*	whole rock Rb-Sr	1832±5			*same as above; split fraction from Sm-Nd*	P. Cavell; Burwash pers comm; Burwash and Muehlenbachs (1997)	
Kaituan Magmatic Arc (KMA)									
GC et al. Farmton	14-27-080-11W6	granite	U-Pb zircon	1900±1			MSWD=0.08, upper intercept	Ross et al. (1991)	1
Phillips Ksituan	07-36-077-9W6	Qtz monzonite	U-Pb zircon	1986±11	-1.8	2.62	Bt-Hbl granite	Ross et al. (1991), Villeneuve et al. (1993)	2
			U-Pb titanite	1890±2			$^{207}Pb/^{206}Pb$ age	Villeneuve et al. (1993)	
			U-Pb titanite	1884±2			$^{207}Pb/^{206}Pb$ age	Villeneuve et al. (1993)	
Honolulu Belloy	06-26-079-3W6	monzonite	U-Pb zircon	1987±3	-2.1	2.63	granitic gneiss, MSWD=5.0, upper intercept	Ross et al. (1991), Villeneuve et al. (1993)	3
Chinchaga Magnetic Low (CH)									
S.R. Banff Caribou Mtn. #1	06-23-112-19W5	granite porphyry	U-Pb zircon	2088 +23/-21	-0.4	2.46	MSWD=2.55, upper intercept	Ross et al. (1991), Villeneuve et al. (1993)	4
Chevron et al. Sheldon	16-35-074-24W5	monzonite gneiss	U-Pb zircon	2159 +11/-10	-1.8	2.68		Ross et al. (1991), Villeneuve et al. (1993)	5
Pan Am A-1 Bald Mtn	11-13-068-5W6	granitic	U-Pb zircon	2175±2			MSWD=0.19, upper intercept	Ross et al. (1991)	6
Two Creek 6-11	06-11-063-16W5	granitic gneiss	U-Pb zircon	2186 +68/-51	0.6	2.57	MSWD=386, upper intercept	Ross et al. (1991), Villeneuve et al. (1993)	7
Cal. Stan. Gulf Kaybob	05-35-062-18W5	metagabbro	Ar-Ar	1934±12		2.99	Hbl	Plint and Ross (1993)	
		amphibolite	K-Ar	2210				Ross (1990) from Burwash et al. (1962)	
	54°24'N 116°36'W	Hbl gabbro	K-Ar	2110±5%			Hbl; index no. 32	Burwash et al. (1962)	
Buffalo Head Terrane (BH)									
Canhunter et al. Golden	06-24-086-15W5	Qtz monzonite	U-Pb zircon	1990 +13/-12	-6.3	2.81	granitic gneiss	Ross et al. (1991), Villeneuve et al. (1993)	8
Chevron Hunt Creek	02-17-091-6W5	granodiorite	U-Pb zircon	1991 +225/-45	-4.3	2.83	Bt-Hbl granite, opx-bearing	Ross et al. (1991), Villeneuve et al. (1993)	9
Fina Keg River	10-27-102-21W5	monzonite gneiss	U-Pb zircon	1993 +10/-5	-2.3	2.54	MSWD=34, upper intercept	Ross et al. (1991), Villeneuve et al. (1993)	
			U-Pb zircon	1996±1			text indicates 3 fractions only gives more consistent age, MSWD=0.2	Villeneuve et al. (1993)	10
			U-Pb titanite	1979±7			$^{207}Pb/^{206}Pb$ age	Villeneuve et al. (1993)	
			U-Pb titanite	1983±7			$^{207}Pb/^{206}Pb$ age	Villeneuve et al. (1993)	
Imperial Virginia Hills	06-36-063-12W5	Hbl monzonite	U-Pb zircon	1998 +5/-4	-3.2	2.69		Ross et al. (1991), Villeneuve et al. (1993)	11
			U-Pb titanite	1985±10			drawn upper intercept	Villeneuve et al. (1993)	
		pegmatite cross-cutting metasediment	Ar-Ar	1882±12			muscovite	Plint and Ross (1993)	
Arco Chevron Lafond	02-23-094-10W5	granite porphyry	U-Pb zircon	2014 +7/-6			MSWD=12.8, upper intercept	Ross et al. (1991)	12
Imperial Pelican Hills	06-10-077-25W4	Grt granulite (Qtz+Fspar+Grt+Bt+Crd+Sil	U-Pb zircon	2017 +2/-1	-6	2.74	MSWD=0.29, upper intercept	Ross et al. (1991), Villeneuve et al. (1993)	13
			U-Pb monazite	2035±1			$^{207}Pb/^{206}Pb$ age	Villeneuve et al. (1993)	
			U-Pb monazite	2055±1			$^{207}Pb/^{206}Pb$ age	Villeneuve et al. (1993)	
			U-Pb monazite	2152±1			$^{207}Pb/^{206}Pb$ age	Villeneuve et al. (1993)	
Dome et al. Peavine	16-09-075-20W5	Bt leucogranite	U-Pb zircon	2072±6	-0.4	2.51	MSWD=36, upper intercept	Ross et al. (1991), Villeneuve et al. (1993)	14
			U-Pb titanite	1980±7			$^{207}Pb/^{206}Pb$ age	Villeneuve et al. (1993)	
			U-Pb titanite	1991±8			$^{207}Pb/^{206}Pb$ age	Villeneuve et al. (1993)	
Chevron Irving Cadotte	13-19-087-21W5	monzonite gneiss	U-Pb zircon	2165 +5/-4	-1.1	2.67	MSWD=6.13, upper intercept	Ross et al. (1991)	15
			U-Pb titanite	1954±6			$^{207}Pb/^{206}Pb$ age	Villeneuve et al. (1993)	
Fina IOE Buffalo Creek	10-23-087-22W4	Bt-Grt granitic gneiss	U-Pb zircon	2203 +197/-78	-6.2	2.62	MSWD=108, upper intercept, inconclusive 1.95-2.3 Ga	Ross et al. (1991), Villeneuve et al. (1993)	16
Clear Hills 14-10	14-10-088-2W6	felsic metavolcanic	U-Pb zircon	2257 +25/-21	0.2	2.67	MSWD=114, upper intercept	Ross et al. (1991), Villeneuve et al. (1993)	17
CDCOG et al. Helen	01-08-088-24W5	granitic gneiss	U-Pb zircon	2280±3			One $^{207}Pb/^{206}Pb$ age of near concordant analysis, large data scatter	Ross et al. (1991)	18
IOE Sylvia	10-08-073-5W5	Qtz monzonite	U-Pb zircon	2317 +27/-15	-1	2.65	Bt-Hbl granite, MSWD=279, upper intercept	Ross et al. (1991), Villeneuve et al. (1993)	19
			U-Pb titanite	1915±10			titanite closure estimate	Villeneuve et al. (1993)	
			U-Pb titanite	1917±6			$^{207}Pb/^{206}Pb$ age	Villeneuve et al. (1993)	
			U-Pb titanite	1920±8			$^{207}Pb/^{206}Pb$ age	Villeneuve et al. (1993)	
Imperial Joussard	11-11-073-13W5	Bt-Cpx diorite	U-Pb zircon	2324±1	-1.3	2.82	MSWD=3.48, upper intercept	Ross et al. (1991), Villeneuve et al. (1993)	20
HB East Virginia Hills	05-31-065-6W5	Qtz diorite	U-Pb zircon	1.95-2.33	-3.4	2.75	inconclusive 1.9-2.4 Ga	Ross et al. (1991), Villeneuve et al. (1993)	
	54°41'N 114°55'W	Hbl-Bt gneiss	K-Ar	1740±5%			Biotite; index no. 33	Burwash et al. (1962)	
Imperial Kimiwan			U-Pb titanite	2056±5			(UA2208)	Burwash et al. (2000a) (L. Heaman)	
Chevron Irving Helen	16-20-087-23W5					3.75		Villeneuve et al. (1993)	
Imp Loon Lake	08-22-086-09W5	Bt adamellite gneiss	K-Ar	1730±120				Burwash 1957	
	56°27'N 115°19'W	Grt-Bt gneiss	K-Ar	1800±5%			Biotite; index no. 27	Burwash et al. (1962)	
Bear Biltmore	07-11-087-17W4	calc-alakli granite	K-Ar	1770±120 1600±110				Burwash 1957	
	56°31'N 112°35'W	Pegmatitic Bt granite	K-Ar	1720±5%			Biotite; index no. 28	Burwash et al. (1962)	
B.A. Jackpine Creek 6-20	56°44'N 117°00'W	Bt schist	K-Ar	1770±5%			Biotite; index no. 25	Burwash et al. (1962)	
Stanolind East Peace River No. 1	56°17'N 116°35'W	Hbl-Qtz diorite	K-Ar	2030±5%			Hbl; index no. 29	Burwash et al. (1962)	
Imperial Lalby #1	55°50'N 117°17'W	Hbl-Bt gneiss	K-Ar	1890±5%			Biotite; index no. 30	Burwash et al. (1962)	
Shell Imperial Springburn #2	55°59'N 116°35'W	Bt-Qtz monzonite	K-Ar	1880±5%			Biotite; index no. 31	Burwash et al. (1962)	

Identifier	Location	Rock Type	Technique	Age (Ma)	Sm-Nd ε_{Nd}	T_{DM} (Ga)	Comments	Source	Ref. #
Hosanna terrane									
Mobil et al. Pembina	11-27-049-8W5	Bt tonalite	U-Pb zircon	2322±8			MSWD=50, upper intercept	Ross et al. (1991)	
Thorsby Magnetic Low									
Imperial Clyde #1	09-29-059-24W4	Qtz diorite	U-Pb zircon	2380±20	0.9	2.79	$^{207}Pb/^{206}Pb$ age, <55pg Pb	Ross et al. (1991), Villeneuve et al. (1993)	
			Ar-Ar	2102±13			Hbl	Plint and Ross (1993)	
Imp. Bailey Selburn Riverdale	01-27-060-26W4	pegmatitic granite	U-Pb zircon	1915±23			MSWD=146, upper intercept	Ross et al. (1991)	
Home CPOG Brightbank	10-05-052-2W5	Qtz diorite	U-Pb zircon	2294 +67/-45			MSWD=1257, upper intercept	Ross et al. (1991)	
Rimbey Magnetic Arc									
Esso AEC 85 Fish. Ck	07-11-067-6W4	granite	U-Pb zircon	1831±6			MSWD=0.10, upper intercept	Ross et al. (1991)	
			U-Pb monazite	1815±3			$^{207}Pb/^{206}Pb$ age	Ross et al. (1991)	
Mobil Pan Am Heart Lake	04-03-069-10W4	Bt monzogranite	U-Pb zircon	1798 +29/-28	-17.9	4.03	leucogranite, MSWD=35, upper intercept	Ross et al. (1991), Villeneuve et al. (1993)	
			U-Pb monazite	inconclusive			inconclusive	Villeneuve et al. (1993)	
Imperial Leduc #530	08-17-050-26W4	Bt leucogranite	U-Pb monazite	1856±3	-1.4	2.36	MSWD=4.0, upper intercept	Ross et al. (1991), Villeneuve et al. (1993)	
			U-Pb zircon	inconclusive			inconclusive	Villeneuve et al. (1993)	
Can. Seaboard Ernestina Lake	54°11'N 110°28'W	Bt-Qtz diorite	K-Ar	1730±5%			Biotite; Index no. 36	Burwash et al. (1962)	
Lacombe domain									
Imperial Ardrossan	08-17-053-21W4	Bt-Musc-Grt leucogranite		ca. 1790-2096, inconclusive				Villeneuve et al. (1993)	
	53°35'N 113°04'W		K-Ar	1740±5%			Muscovite; Index no. 35	Burwash et al. (1962)	
Nova Domain									
Imperial Rainbow Lake 16-18	16-18-107-6W6	mafic Bt gneiss	U-Pb zircon	2808 +30/-27	5.6		MSWD=640, upper intercept	Ross et al. (1991), Villeneuve et al. (1993)	
	58°18'N 118°59'W		K-Ar	1760±5%			Biotite; Index no. 23	Burwash et al. (1962)	
Mobil Nova	15-34-109-4W6	Metarhyolite	Ar-Ar	1722±11	-2	2.48	Musc	Plint and Ross (1993), Villeneuve et al. (1993)	
			U-Pb zircon	1990±6			MSWD=23, upper intercept	Ross et al. (1991)	
Imperial Black Creek 10-27	58°29'N 119°25'W	Bt-Qtz diorite	K-Ar	1710±5%			Biotite; Index no. 22	Burwash et al. (1962)	
Imperial Rat Lake No. 1	59°46'N 117°08'W	Chloritized Hbl gneiss	K-Ar	1700±5%			Hbl; Index no. 20	Burwash et al. (1962)	
Imperial Sikanni Chief #1	58°05'N 121°54'W	Bt-Qtz diorite	K-Ar	1740±5%			Biotite; Index no. 21	Burwash et al. (1962)	
Kiskatinaw Low									
Home Pembina Farminton	06-18-080-15W6	granite	U-Pb zircon	1903±2			MSWD=0.29, upper intercept	Villeneuve et al. (1993)	
			U-Pb titanite	1900±13			$^{207}Pb/^{206}Pb$ age	Villeneuve et al. (1993)	
			U-Pb titanite	1900±5			$^{207}Pb/^{206}Pb$ age	Villeneuve et al. (1993)	
Pac. Imperial Parkland	06-29-081-15W6	granitic gneiss	U-Pb zircon	1983±6			MSWd=19, upper intercept	Villeneuve et al. (1993)	
Taltson-Thelon Orogen									
Outboard TNZ									
Cal. Std. Mikkwa	12-23-098-21W4	Bt-Hbl granite	U-Pb zircon	1937 +61/-45	-5.3	2.57	1935-2000 Ma	Ross et al. (1991), Villeneuve et al. (1993)	21
ROC Watchusk Lake	07-08-083-3W4	granite	U-Pb monazite	1949±2	-9.7		monzogranite, $^{207}Pb/^{206}Pb$ minimum crystallization age	Ross et al. (1991), Villeneuve et al. (1993)	22
Imperial Wolverine	07-24-076-18W4	syenogranite	U-Pb monazite	1968±1	-5	2.66	$^{207}Pb/^{206}Pb$ minimum crystallization age	Ross et al. (1991), Villeneuve et al. (1993)	23
			U-Pb zircon	1.95-2.357, inconclusive				Villeneuve et al. (1993)	
Merrill Arab Chard	05-34-078-06W4	syenogranite	U-Pb zircon	1972±5	-3.7		MSWD=14.1, upper intercept	Ross et al. (1991), Villeneuve et al. (1993)	24
IOE Jack Lakes	08-17-120-1W5	granite porphyry	U-Pb zircon	1972 +20/-17			MSWD=174, upper intercept	Ross et al. (1991)	25
Bear Vampire #1	07-28-087-12W4	monzogranite	U-Pb zircon	ca. 2.0 Ga	-6.3			Villeneuve et al. (1993) [SAB, Washington U]	26
Late Taltson Magmatic Zone (TMZ) Granitoids									
Othikethe Falls		monzogranite	U-Pb zircon	1925.4±1.2			$^{207}Pb/^{206}Pb$ age	Bostock et al. (1991)	27
			U-Pb monazite	1926±3			crystallization age	Bostock et al. (1991)	28
southern Slave dyke MRB-MLL-15	UTM 12, 497832E, 6628396N	granite to monzogranite Bt-Grt-Crd-Spl (hercynite) bearing	U-Pb zircon	1933±3				McNicoll et al. (1994), McDonough et al. (1995b, 2000)	29
		granitoid	*Rb-Sr whole rock*	*1938±29*			MSWD=184	*Nielsen et al. (1981)*	
		pegmatites cutting Slave granitoids	Rb-Sr whole rock	2470±26			M1	Nielsen et al. (1981)	
					-4.4 to -8.6	2.6-2.9		Thériault (1992)	
Konth		syenogranite Grt+Sil+Crd+Hercynite, Hypersthene, mesoperthite	U-Pb monazite	1935 +3/-1			NW	Bostock and Loveridge (1988)	30
			U-Pb monazite	1938 +3/-1			SW	Bostock and Loveridge (1988)	31
			U-Pb monazite	1936 +2/-1			E	Bostock and Loveridge (1988)	32
					-4.6 to -5.5	2.5-2.7		Thériault (1992)	
Slave		Bt monzogranite Grt+Sil+Crd+Hercynite bearing	U-Pb monazite	1955±2			High U zircon (1200-1500 ppm), crystallization age	Bostock et al. (1987), Thériault (1992)	33
Early Taltson Magmatic Zone (TMZ) Granitoids									
Collin Lake MSB-93-148	UTM 12, 554461E, 6629170N, NTS 74M/16	Qtz diorite	U-Pb zircon	1971±4				McNicoll et al. (1994), McDonough et al. (1995b), McDonough and McNicoll (1997)	34
Deskenatlata		Bt-Hbl granodiorite	U-Pb zircon	1986.4 +2.4/-2				Bostock et al. (1987)	35
					-2.7 to -3.6	2.58-2.59		Thériault (1992)	
Thelon Tectonic Zone									
Hanbury granite		granite	U-Pb monazite	1920±4			emplacement age, high U (1000-1750 ppm)	van Breemen et al. (1987)	36
			U-Pb zircon				unable to accurately determine - Pb loss/inheritance?	van Breemen et al. (1987)	
Hypersthene metagabbro		Hypersthene metagabbro	U-Pb zircon	ca. 1958			charnockite	van Breemen et al. (1987)	39
			U-Pb zircon	ca. 1940			charnockite	van Breemen et al. (1987)	37
Mylonitic granitic granulite gneiss		mylonite	U-Pb monazite	1950±4			minimum granulite-grade metamorphic age	van Breemen et al. (1987)	38
			U-Pb zircon	ca. 1992 unabraded			mixed igneous/metamorphic ages, metamorphic upper limit	van Breemen et al. (1987)	40

Identifier	Location	Rock Type	Technique	Age (Ma)	Sm-Nd ε_{Nd}	T_{DM} (Ga)	Comments	Source	Ref. #
			U-Pb zircon	ca. 1997 abraded			mixed igneous/metamorphic ages, metamorphic upper limit	van Breemen et al. (1987)	41
tonalitic granulite gneiss		tonalitic granulite gneiss	U-Pb zircon	ca. 2200-2100 array			>2200 igneous, <2100 metamorphic (ca. 2000 Ma?)	van Breemen et al. (1987)	
Mary Francis metasedimentary gneiss MLB-88-17	63° 23.0' 106° 17.5'	metasedimentary gneiss (Bt, Qtz, rare Sil - Bt rich part has Hbl+Cpx)	U-Pb zircon	2000±10			C, E, F, A, metamorphic	Henderson and van Breemen (1992)	42
			U-Pb zircon	2214.2±1			$^{207}Pb/^{206}Pb$ age; D, core, detrital or reset	Henderson and van Breemen (1992)	
			U-Pb zircon	2178.0±1.1			$^{207}Pb/^{206}Pb$ age, I, core, detrital or reset	Henderson and van Breemen (1992)	
			U-Pb zircon	2032.4±1.1			$^{207}Pb/^{206}Pb$ age, G, core	Henderson and van Breemen (1992)	
			U-Pb zircon	2013.5±1.0			$^{207}Pb/^{206}Pb$ age, H, core	Henderson and van Breemen (1992)	
			U-Pb zircon	2009.1±1.4			$^{207}Pb/^{206}Pb$ age, C, tip	Henderson and van Breemen (1992)	
			U-Pb zircon	2005.3±1.0			$^{207}Pb/^{206}Pb$ age, E, tip	Henderson and van Breemen (1992)	
			U-Pb zircon	2004.8±1.3			$^{207}Pb/^{206}Pb$ age, K, core	Henderson and van Breemen (1992)	
			U-Pb zircon	1994.3±2.1			$^{207}Pb/^{206}Pb$ age, F, tip	Henderson and van Breemen (1992)	
			U-Pb zircon	1993.6±1.2			$^{207}Pb/^{206}Pb$ age, A, metamorphic	Henderson and van Breemen (1992)	
			U-Pb zircon	1963.6±1.4			$^{207}Pb/^{206}Pb$ age, J, core	Henderson and van Breemen (1992)	
			U-Pb zircon	1958.4±1.1			$^{207}Pb/^{206}Pb$ age, B, metamorphic	Henderson and van Breemen (1992)	
Taltson Basement Complex (TBC)									
Gneisses		granitic orthogneiss	U-Pb zircon	2287±21				McNicoll et al. (1994)	
			U-Pb monazite	1915±10			metamorphic	McNicoll et al. (1994)	
		granitic orthogneiss	U-Pb zircon	2.4-2.3 Ga				McNicoll et al. (1994)	
			U-Pb monazite	1927±2			metamorphic	McNicoll et al. (1994)	
		tonalite		3040				McDonough et al. (1995a)	
		granite		ca. 3200				McDonough et al. (1995a)	
Orthogneisses		orthogneiss		ca. 2350-2140	-1.7 to -11.3		ε_{Nd} (2.2 Ga); n=13	McDonough et al. (1995a), Thériault (1994)	
Berrigan Lake Block									
Berrigan Lake inclusion melange matrix		granitic	U-Pb zircon	2294±5			granite emplacement	Bostock et al. (1991)	43
Borrowes Lake	Northern megacrystic hinterland monzogranite	augen gneiss	U-Pb zircon	2436±12				Bostock and Loveridge (1988), Bostock et al. (1991)	
Mixed gneisses of western Rae province overlain by Nonacho Group	older mixed gneisses	Qtz diorite gneiss	U-Pb zircon	2400±10			crystallization age, U (165-2268 ppm)	van Breemen et al. (1992)	46
granitic gneisses of western Rae Province					-5.2 to -9.3	2.8-3.5		Thériault (1992)	
mixed gneisses of western Rae Province					-9.2 to -21.4	2.8-4.2		Thériault (1992)	
Andrew Lake Block									
MSB93-139	533672E, 6592615N	Bt tonalite gneiss	U-Pb zircon	3076±15	-14.3	3.73	2 most concordant points with error range, ε_{Nd} (2.2 Ga)	McNicoll et al. (2000)	
			U-Pb zircon	3014±2			$^{207}Pb/^{206}Pb$ age	McNicoll et al. (2000)	
			U-Pb zircon	2948±1			$^{207}Pb/^{206}Pb$ age	McNicoll et al. (2000)	
			U-Pb zircon	3076±5			$^{207}Pb/^{206}Pb$ age	McNicoll et al. (2000)	
			U-Pb zircon	3013±2			$^{207}Pb/^{206}Pb$ age	McNicoll et al. (2000)	
			U-Pb zircon	2955±2			$^{207}Pb/^{206}Pb$ age	McNicoll et al. (2000)	
			U-Pb zircon	3080±2			$^{207}Pb/^{206}Pb$ age	McNicoll et al. (2000)	
			U-Pb zircon	3043±1			$^{207}Pb/^{206}Pb$ age	McNicoll et al. (2000)	
			U-Pb zircon	3085±2			$^{207}Pb/^{206}Pb$ age	McNicoll et al. (2000)	
			U-Pb monazite	1917±1			$^{207}Pb/^{206}Pb$ age, metamorphic	McNicoll et al. (2000)	47
			U-Pb monazite	1917±1			$^{207}Pb/^{206}Pb$ age, metamorphic	McNicoll et al. (2000)	48
			U-Pb monazite	1928±1			$^{207}Pb/^{206}Pb$ age, metamorphic	McNicoll et al. (2000)	49
			U-Pb monazite	1930±1			$^{207}Pb/^{206}Pb$ age, metamorphic	McNicoll et al. (2000)	50
MSB94-47	529281E, 6552523N	Bt tonalite gneiss	U-Pb zircon	2562±6	-5.9	2.83	upper intercept (MSWD=5.34), age of rock, E_{Nd} (2.2 Ga)	McNicoll et al. (2000)	
			U-Pb zircon	2481±2			$^{207}Pb/^{206}Pb$ age	McNicoll et al. (2000)	
			U-Pb zircon	2532±4			$^{207}Pb/^{206}Pb$ age	McNicoll et al. (2000)	
			U-Pb zircon	2532±3			$^{207}Pb/^{206}Pb$ age	McNicoll et al. (2000)	
			U-Pb zircon	2541±2			$^{207}Pb/^{206}Pb$ age	McNicoll et al. (2000)	
			U-Pb zircon	2555±2			$^{207}Pb/^{206}Pb$ age	McNicoll et al. (2000)	
MSB93-MC10		pegmatitic granite	U-Pb zircon	2335±2			minimum age of rock	McNicoll et al. (2000)	53
			U-Pb zircon	2312±2			$^{207}Pb/^{206}Pb$ age	McNicoll et al. (2000)	
			U-Pb zircon	2328±1			$^{207}Pb/^{206}Pb$ age	McNicoll et al. (2000)	
			U-Pb zircon	2335±2			$^{207}Pb/^{206}Pb$ age	McNicoll et al. (2000)	
			U-Pb zircon	2334±2			$^{207}Pb/^{206}Pb$ age	McNicoll et al. (2000)	
MRB-TAN-67	541600E, 6645386N	banded mafic to felsic orthogneiss			-5.2	2.84	ε_{Nd} (2.2 Ga)	McNicoll et al. (2000)	
MSB-93-V21	534339E, 6578622N	banded mafic orthogneiss			-5.1	2.84	ε_{Nd} (2.2 Ga)	McNicoll et al. (2000)	
MSB-93-38	534573E, 6622880N	banded mafic to felsic orthogneiss			-5	2.86	ε_{Nd} (2.2 Ga)	McNicoll et al. (2000)	
MSB-93-112	545245E, 6626200N	migmatitic mafic to felsic orthogneiss			-6	2.98	ε_{Nd} (2.2 Ga)	McNicoll et al. (2000)	
MRB-MAN-20	549187E, 6630419N	amphibolite			-0.3	2.59	ε_{Nd} (2.2 Ga)	McNicoll et al. (2000)	
Potts Lake Block									
MSB93-114	530390E, 6665150N	Bt amphibolitic gneiss	U-Pb zircon	2295 +6/-5	-9.2	3.34	upper intercept, minimum crystallization age, E_{Nd} (2.2 Ga)	McNicoll et al. (2000)	54
			U-Pb zircon	2264±1			$^{207}Pb/^{206}Pb$ age	McNicoll et al. (2000)	
			U-Pb zircon	2301±2			$^{207}Pb/^{206}Pb$ age	McNicoll et al. (2000)	
			U-Pb zircon	2283±2			$^{207}Pb/^{206}Pb$ age	McNicoll et al. (2000)	
			U-Pb zircon	2282±2			$^{207}Pb/^{206}Pb$ age	McNicoll et al. (2000)	
			U-Pb zircon	2302±2			$^{207}Pb/^{206}Pb$ age	McNicoll et al. (2000)	
			U-Pb zircon	2249±3			$^{207}Pb/^{206}Pb$ age	McNicoll et al. (2000)	
			U-Pb zircon	2219±2			$^{207}Pb/^{206}Pb$ age	McNicoll et al. (2000)	

Identifier	Location	Rock Type	Technique	Age (Ma)	Sm-Nd ε_{Nd}	T_{DM} (Ga)	Comments	Source	Ref. #
			U-Pb zircon	2283±2			$^{207}Pb/^{206}Pb$ age	McNicoll et al. (2000)	
			U-Pb zircon	2293±2			$^{207}Pb/^{206}Pb$ age	McNicoll et al. (2000)	
MRB-VAN-47	549527E, 6631915N	banded mafic orthogneiss			-3.3	2.68	ε_{Nd} (2.2 Ga)	McNicoll et al. (2000)	
MSB-93-151	532174E, 6640165N	amphibolite			-2.5	2.78	ε_{Nd} (2.2 Ga)	McNicoll et al. (2000)	
Cornwall Lake Block									
MSB94-33	518053E, 6600357N	Hbl granite gneiss	U-Pb zircon	2393 +12/-20	-12.5	3.19	upper intercept and weighted average of $^{207}Pb/^{206}Pb$ age, E_{Nd} (2.2 Ga)	McNicoll et al. (2000)	60
			U-Pb zircon	2344±4			$^{207}Pb/^{206}Pb$ age	McNicoll et al. (2000)	
			U-Pb zircon	2387±2			$^{207}Pb/^{206}Pb$ age	McNicoll et al. (2000)	
			U-Pb zircon	2370±2			$^{207}Pb/^{206}Pb$ age	McNicoll et al. (2000)	
			U-Pb zircon	2457±2			$^{207}Pb/^{206}Pb$ age	McNicoll et al. (2000)	
			U-Pb zircon	2376±1			$^{207}Pb/^{206}Pb$ age	McNicoll et al. (2000)	
			U-Pb zircon	2382±1			$^{207}Pb/^{206}Pb$ age	McNicoll et al. (2000)	
			U-Pb zircon	2584±1			$^{207}Pb/^{208}Pb$ age	McNicoll et al. (2000)	
			U-Pb zircon	2377±2			$^{207}Pb/^{208}Pb$ age	McNicoll et al. (2000)	
			U-Pb monazite	1925±3			$^{207}Pb/^{206}Pb$ age	McNicoll et al. (2000)	55
			U-Pb monazite	1935±2			$^{207}Pb/^{206}Pb$ age	McNicoll et al. (2000)	56
			U-Pb monazite	1936±1			$^{207}Pb/^{206}Pb$ age	McNicoll et al. (2000)	57
			U-Pb monazite	1936±1			$^{207}Pb/^{206}Pb$ age	McNicoll et al. (2000)	58
MSB93-101	526985E, 6599885N	Hbl-Bt syenogranite gneiss	U-Pb zircon	2138±2	-1.8	2.72	upper intercept, age of rock, ε Nd (2.2 Ga)	McNicoll et al. (2000)	59
			U-Pb titanite	ca. 1920			titanite closure after metamorphism	McNicoll et al. (2000)	
			U-Pb zircon	2138±1			$^{207}Pb/^{206}Pb$ age	McNicoll et al. (2000)	
			U-Pb zircon	2130±1			$^{207}Pb/^{206}Pb$ age	McNicoll et al. (2000)	
			U-Pb zircon	2133±1			$^{207}Pb/^{206}Pb$ age	McNicoll et al. (2000)	
			U-Pb zircon	2129±1			$^{207}Pb/^{208}Pb$ age	McNicoll et al. (2000)	
			U-Pb zircon	2139±11			$^{207}Pb/^{208}Pb$ age	McNicoll et al. (2000)	
			U-Pb titanite	1917±6			$^{207}Pb/^{208}Pb$ age	McNicoll et al. (2000)	
			U-Pb titanite	1919±23			$^{207}Pb/^{208}Pb$ age	McNicoll et al. (2000)	
MSB-93-100	526731E, 6599922N	migmatitic mafic to felsic orthogneiss			-11.3	3.21	ε_{Nd} (2.2 Ga)	McNicoll et al. (2000)	
MSB-MCH-5	525806E, 66335028N	banded mafic to felsic orthogneiss			-5	2.73	ε_{Nd} (2.2 Ga)	McNicoll et al. (2000)	
MSB-MCH-14	524988E, 6641091N	amphibolite			3.9		ε_{Nd} (2.2 Ga)	McNicoll et al. (2000)	
Dore Lake Block									
MSB94-95		Hbl-Bt syenogranite gneiss	U-Pb zircon	2330±3			age of rock, weighted average	McNicoll et al. (2000)	61
			U-Pb zircon	2300±1			$^{207}Pb/^{206}Pb$ age	McNicoll et al. (2000)	
			U-Pb zircon	2330±2			$^{207}Pb/^{206}Pb$ age	McNicoll et al. (2000)	
			U-Pb zircon	2325±4			$^{207}Pb/^{206}Pb$ age	McNicoll et al. (2000)	
			U-Pb zircon	2297±2			$^{207}Pb/^{206}Pb$ age	McNicoll et al. (2000)	
			U-Pb zircon	2332±2			$^{207}Pb/^{206}Pb$ age	McNicoll et al. (2000)	
			U-Pb zircon	2329±3			$^{207}Pb/^{206}Pb$ age	McNicoll et al. (2000)	
MSB-93-118 *	526319E, 6575709N	migmatitic granodiorite gneiss			-4.2	2.9	ε_{Nd} (2.2 Ga)	McNicoll et al. (2000)	
MSB-93-129	524491E, 6577144N	Qtz diorite gneiss			-1.6	2.75	ε_{Nd} (2.2 Ga)	McNicoll et al. (2000)	
MSB-93-141	525603E, 6587332N	amphibolite			-4.3		ε_{Nd} (2.2 Ga)	McNicoll et al. (2000)	
Separated by Charles Lake shear zone									
Mercredi Lake Block									
MSB-93-116	516122E, 6629512N	Bt-Hbl granodiorite gneiss	U-Pb zircon	2382±5	-5.7	2.84	upper intercept, MSWD=0.25, crystallization age, E_{Nd} (2.2 Ga)	McNicoll et al. (2000)	65
			U-Pb zircon	2315±3			$^{207}Pb/^{206}Pb$ age	McNicoll et al. (2000)	
			U-Pb zircon	1904±9			$^{207}Pb/^{206}Pb$ age	McNicoll et al. (2000)	
			U-Pb zircon	2313±25			$^{207}Pb/^{206}Pb$ age	McNicoll et al. (2000)	
			U-Pb zircon	1913±5			$^{207}Pb/^{206}Pb$ age, metamorphic	McNicoll et al. (2000)	62
			U-Pb zircon	2142±11			$^{207}Pb/^{206}Pb$ age	McNicoll et al. (2000)	
			U-Pb zircon	2374±2			$^{207}Pb/^{206}Pb$ age	McNicoll et al. (2000)	
			U-Pb zircon	2168±6			$^{207}Pb/^{206}Pb$ age	McNicoll et al. (2000)	
			U-Pb zircon	1914±4			$^{207}Pb/^{206}Pb$ age, metamorphic	McNicoll et al. (2000)	63
			U-Pb zircon	1961±2			$^{207}Pb/^{208}Pb$ age	McNicoll et al. (2000)	
			U-Pb zircon	1917±3			$^{207}Pb/^{206}Pb$ age, metamorphic	McNicoll et al. (2000)	64
MRB-MMC-7	493524E, 6622611N	banded mafic orthogneiss			-4.7	2.82	ε_{Nd} (2.2 Ga)	McNicoll et al. (2000)	
MRB-MMC-5	515524E, 6641615N	banded granitic gneiss			-1.7	2.82	ε_{Nd} (2.2 Ga)	McNicoll et al. (2000)	
MRB-MMC-3	514468E, 6641574N	banded granitic gneiss			-12.3	3.09	ε_{Nd} (2.2 Ga)	McNicoll et al. (2000)	
Leland Lakes Block									
MSB93-2	493524E, 6622611N	mylonitic Bt-Hbl granite gneiss	U-Pb zircon	3186 +17/-13	-9.9	3.29	upper intercept, MSWD=9.4, age of rock, E_{Nd} (2.2 Ga)	McNicoll et al. (2000)	
			U-Pb zircon	3207±1			$^{207}Pb/^{206}Pb$ age	McNicoll et al. (2000)	
			U-Pb zircon	3154±4			$^{207}Pb/^{206}Pb$ age	McNicoll et al. (2000)	
			U-Pb zircon	3140±1			$^{207}Pb/^{206}Pb$ age	McNicoll et al. (2000)	
			U-Pb zircon	2930±2			$^{207}Pb/^{208}Pb$ age	McNicoll et al. (2000)	
			U-Pb zircon	3118±1			$^{207}Pb/^{208}Pb$ age	McNicoll et al. (2000)	
			U-Pb zircon	3146±1			$^{207}Pb/^{208}Pb$ age	McNicoll et al. (2000)	
			U-Pb monazite	1917±3			$^{207}Pb/^{208}Pb$ age	McNicoll et al. (2000)	66
			U-Pb monazite	1925±1			$^{207}Pb/^{208}Pb$ age	McNicoll et al. (2000)	67
			U-Pb monazite	1930±2			$^{207}Pb/^{206}Pb$ age	McNicoll et al. (2000)	68
TLL-1B	494351E, 6623526N	banded granitic gneiss			-8.6	3.36	ε_{Nd} (2.2 Ga)	McNicoll et al. (2000)	
MSB-MLL-35	*500187E, 6640601N*	*amphibolite*			-0.9		ε_{Nd} (2.2 Ga)	McNicoll et al. (2000)	
MSB-MLL-42	500027E, 6639063N	amphibolite			0.7		ε_{Nd} (2.2 Ga)	McNicoll et al. (2000)	
MSB-93-R1	497042E, 6629326N	amphibolite			-2.2		ε_{Nd} (2.2 Ga)	McNicoll et al. (2000)	
Timing of Shear Zone Deformation									
Andrew Lake Shear Zone									
Andrew Lake MRB-MAN-27	east shore	Bt-Hbl granodiorite	U-Pb zircon	1962 +16/-10			MSWD=2.5	McDonough et al. (1995a, b, 2000)	74
			U-Pb titanite	1853-1860			discordant, 3 mulit-grain fractions, cooling?	McDonough et al. (1995b, 2000)	

Identifier	Location	Rock Type	Technique	Age (Ma)	Sm-Nd ε_{Nd}	T_{DM} (Ga)	Comments	Source	Ref. #
MRB-TAN-70	Swinnerton window	granodiorite	U-Pb zircon	1959±3			upper intercept age, MSWD=0.34, regression excluding A and B, crystallization age	McDonough et al. (1995b, 2000)	73
			U-Pb zircon	2094±1			$^{207}Pb/^{206}Pb$ age, A	McDonough et al. (2000)	
			U-Pb zircon	1968±2			$^{207}Pb/^{206}Pb$ age, B	McDonough et al. (2000)	
			U-Pb zircon	1950±1			$^{207}Pb/^{206}Pb$ age	McDonough et al. (2000)	
			U-Pb zircon	1932±1			$^{207}Pb/^{206}Pb$ age	McDonough et al. (2000)	
			U-Pb zircon	1946±2			$^{207}Pb/^{206}Pb$ age	McDonough et al. (2000)	
			U-Pb zircon	1930±1			$^{207}Pb/^{206}Pb$ age	McDonough et al. (2000)	
			U-Pb zircon	1959±3			$^{207}Pb/^{206}Pb$ age	McDonough et al. (2000)	
			U-Pb monazite	1924±1			$^{207}Pb/^{206}Pb$ age, metamorphic or cooling	McDonough et al. (2000)	69
			U-Pb monazite	1931±1			$^{207}Pb/^{206}Pb$ age, metamorphic or cooling	McDonough et al. (2000)	70
			U-Pb monazite	1933±1			$^{207}Pb/^{206}Pb$ age, metamorphic or cooling	McDonough et al. (2000)	71
			U-Pb monazite	1934±1			$^{207}Pb/^{206}Pb$ age, metamorphic or cooling	McDonough et al. (2000)	72
		granite-granodiorite	U-Pb whole rock	ca. 1900				Baadsgaard and Godfrey (1972)	
		Qtz monzonite, (porphyroblastic) Qtz monzonite gneiss	Rb-Sr	1690-1800 1730-1860 1880-2060 2090-2240			Kfs	Baadsgaard and Godfrey (1967)	
			U-Pb zircon and allanite	1900 2100 1900-2250 2020-2300				Baadsgaard and Godfrey (1967)	
44-1		Bt schist; phyllite; pegmatite	U-Pb uraninite	1900±50				Baadsgaard and Godfrey (1967)	
			K-Ar	1740-1930			Bt, Musc, Hbl	Baadsgaard and Godfrey (1967)	
			K-Ar	1852±40			Hbl; Mean K-Ar ages for Baadsgaard and Godfrey (1967)	Plint and McDonough (1995)	
			K-Ar	1792±40			Musc; Mean K-Ar ages for Baadsgaard and Godfrey (1967)	Plint and McDonough (1995)	
			K-Ar	1772±40			Bt; Mean K-Ar ages for Baadsgaard and Godfrey (1967)	Plint and McDonough (1995)	
	59°57'N 110°04'W	Coarse-grained pegmatite	K-Ar	1830±5%			Biotite; Index no. 1	Burwash et al. (1962)	
	59°57'N 110°03'W	Porphyroblastic Bt granite	K-Ar	1740±5%			Biotite; Index no. 2	Burwash et al. (1962)	
TBC	Hanging wall ALSZ	Hbl amphibolite	Ar-Ar	1904±12				McDonough et al. (1994), Plint and McDonough (1995)	
MAN-20									
MAN-27	Footwall ALSZ	Hbl granodiorite	Ar-Ar	1899±12				McDonough et al. (1994), Plint and McDonough (1995)	
Colin Lake MRB-TAN-61	UTM 12, 551561E, 6645193N	Musc granite	U-Pb zircon and monazite	1921-1923			age of granite	McDonough et al. (2000)	
			U-Pb zircon	1947±2			$^{207}Pb/^{206}Pb$ age, highly discordant, high U (2916 ppm)	McDonough et al. (2000)	
			U-Pb zircon	1923±2			$^{207}Pb/^{206}Pb$ age, least discordant, high U (1086 ppm)	McDonough et al. (2000)	78
			U-Pb zircon	1867±2			$^{207}Pb/^{206}Pb$ age, highly discordant, high U (2067 ppm)	McDonough et al. (2000)	
			U-Pb monazite	1932±1			$^{207}Pb/^{206}Pb$ age; xenocrystic?	McDonough et al. (2000)	
			U-Pb monazite	1913±1			$^{207}Pb/^{206}Pb$ age, growth during cooling	McDonough et al. (2000)	75
			U-Pb monazite	1917±1			$^{207}Pb/^{206}Pb$ age, growth during cooling	McDonough et al. (2000)	76
			U-Pb monazite	1922±1			$^{207}Pb/^{206}Pb$ age	McDonough et al. (2000)	77
Charles Lake Shear Zone									
Wylie Lake MSB-93-107	UTM 12, 530910E, 6571187N	Bt-Hbl granodiorite gneiss	U-Pb zircon	1963 +6/-4			crystallization age, upper intercept, MSWD=0.04, 3 fractions	McDonough et al. (1995b, 2000)	79
			U-Pb zircon	1963±3			$^{207}Pb/^{206}Pb$ age	McDonough et al. (2000)	
			U-Pb zircon	1918±8			$^{207}Pb/^{206}Pb$ age, not regressed	McDonough et al. (2000)	
			U-Pb zircon	1963±3			$^{207}Pb/^{206}Pb$ age	McDonough et al. (2000)	
			U-Pb zircon	1962±13			$^{207}Pb/^{206}Pb$ age	McDonough et al. (2000)	
Arch Lake MSB-94-31	UTM 12, 520971E, 6637322N	granite-syenogranite gneiss	Concordant zircon, monazite, upper intercept	1938±3			Hercynite-Grt-bearing, low Th/U ratios, max estimate for granulite-grade deformation	McDonough et al. (2000)	80
			U-Pb zircon	1940±1			upper intercept, MSWD=25.4	McDonough et al. (2000)	
			U-Pb zircon	1938±5			$^{207}Pb/^{206}Pb$ age	McDonough et al. (2000)	
			U-Pb zircon	1935±1			$^{207}Pb/^{206}Pb$ age	McDonough et al. (2000)	
			U-Pb zircon	1926±1			$^{207}Pb/^{206}Pb$ age, high U (3514 ppm)	McDonough et al. (2000)	
			U-Pb zircon	1909±1			$^{207}Pb/^{206}Pb$ age	McDonough et al. (2000)	
			U-Pb zircon	1930±4			$^{207}Pb/^{206}Pb$ age, high U (2271 ppm)	McDonough et al. (2000)	
			U-Pb zircon	1938±1			$^{207}Pb/^{206}Pb$ age, high U (1875 ppm)	McDonough et al. (2000)	
			U-Pb monazite	1931±1			$^{207}Pb/^{206}Pb$ age	McDonough et al. (2000)	
			U-Pb monazite	1938±1			$^{207}Pb/^{206}Pb$ age	McDonough et al. (2000)	
			U-Pb monazite	1934±1			$^{207}Pb/^{206}Pb$ age	McDonough et al. (2000)	
Charles Lake MRB-VCH-28	UTM 12, 527015E, 6637166N, intrudes Potts Lake block	Bt granite	U-Pb monazite	1933			best minimum estimate	McNicoll et al. (1994), McDonough et al. (2000)	82
			U-Pb monazite	1919			$^{207}Pb/^{206}Pb$ age, age of middle amphibolite-faces metamorphism and deformation (?)	McNicoll et al. (1994), McDonough et al. (2000)	81
			U-Pb zircon	1933±3			$^{207}Pb/^{206}Pb$ age	McDonough et al. (2000)	
			U-Pb zircon	2055±2			$^{207}Pb/^{206}Pb$ age	McDonough et al. (2000)	
			U-Pb zircon	1838±2			$^{207}Pb/^{206}Pb$ age	McDonough et al. (2000)	

Identifier	Location	Rock Type	Technique	Age (Ma)	Sm-Nd ε_{Nd}	T_{DM} (Ga)	Comments	Source	Ref. #
			U-Pb zircon	1905±2			$^{207}Pb/^{206}Pb$ age, high U (1200 ppm)	McDonough et al. (2000)	
			U-Pb zircon	1860±6			$^{207}Pb/^{204}Pb$ age	McDonough et al. (2000)	
			U-Pb monazite	1934±1			$^{207}Pb/^{206}Pb$ age	McDonough et al. (2000)	
			U-Pb monazite	1934±1			$^{207}Pb/^{206}Pb$ age	McDonough et al. (2000)	
			U-Pb monazite	1933±1			$^{207}Pb/^{206}Pb$ age	McDonough et al. (2000)	
			U-Pb monazite	1918±1			$^{207}Pb/^{206}Pb$ age	McDonough et al. (2000)	
			Ar-Ar	1856±12				McDonough et al. (1994), Plint and McDonough (1995)	
MCH-38		Bt granite	Ar-Ar	1799±11				McDonough et al. (1994), Plint and McDonough (1995)	
Chipewyan 94-55	MSB- UTM 12, 498660E, 6536125N	granite	U-Pb zircon	1925 +5/-3			upper intercept, age of rock	McDonough et al. (1995b, 2000)	83
			U-Pb zircon	1899±3			$^{207}Pb/^{206}Pb$ age	McDonough et al. (2000)	
			U-Pb zircon	1924±2			$^{207}Pb/^{206}Pb$ age	McDonough et al. (2000)	
			U-Pb zircon	1915±1			$^{207}Pb/^{206}Pb$ age	McDonough et al. (2000)	
			U-Pb zircon	1925±2			$^{207}Pb/^{206}Pb$ age	McDonough et al. (2000)	
			U-Pb zircon	1925±3			$^{207}Pb/^{206}Pb$ age	McDonough et al. (2000)	
Leland Lakes Shear Zone									
Western Slave granite dyke MRB-MLL-15		S- type granite - monzogranite with Bt-Hercynite-Grt-Crd and restite	U-Pb zircon	1934±2			weighted $^{207}Pb/^{206}Pb$ average of A and D, estimate of age of rock	McDonough et al. (2000)	84
			U-Pb zircon	1934±2			$^{207}Pb/^{206}Pb$ age, A, high U (1587 ppm)	McDonough et al. (2000)	
			U-Pb zircon	2247±3			$^{207}Pb/^{206}Pb$ age	McDonough et al. (2000)	
			U-Pb zircon	1705±1			$^{207}Pb/^{206}Pb$ age, high U (1317 ppm)	McDonough et al. (2000)	
			U-Pb zircon	1935±8			$^{207}Pb/^{206}Pb$ age, D	McDonough et al. (2000)	
			U-Pb zircon	1639±7			$^{207}Pb/^{206}Pb$ age, high U (1016 ppm)	McDonough et al. (2000)	
			U-Pb zircon	2175±1			$^{207}Pb/^{206}Pb$ age	McDonough et al. (2000)	
			U-Pb zircon	2101±1			$^{207}Pb/^{206}Pb$ age	McDonough et al. (2000)	
			U-Pb zircon	1637±3			$^{207}Pb/^{206}Pb$ age, high U (1758 ppm)	McDonough et al. (2000)	
Colin-Andrew-Charles Lake area									
			K-Ar	1772±40			recalculated mean Bt age	McDonough et al. (1994)	
			K-Ar	1792±40			recalculated mean Musc age	McDonough et al. (1994)	
			K-Ar	1820-1940 (ca. 1880)			hornblende	Baadsgaard and Godfrey (1972)	
			K-Ar	1852±40			recalculated mean Hbl age	McDonough et al. (1994)	
			K-Ar	1790±40			mean Bt and Musc age	Baadsgaard and Godfrey (1972)	
		granite and gneisses	whole rock Rb-Sr	1760±60			mean age; apatite	Baadsgaard and Godfrey (1972)	
			U-Pb monazite, allanite, uraninite	ca. 1880				Baadsgaard and Godfrey (1972)	
		Bt and leucocratic granite	whole rock Rb-Sr	ca. 1893				Baadsgaard and Godfrey (1972)	
Metasedimentary Rocks (including Rutledge River basin)									
Rutledge Lake									
Rutledge Lake Moose complex) 477C, #1942	(Mama 87BK- UTM 12, 515120E, 6831990N	metapelite	U-Pb zircon	2601.8±1.8			$^{207}Pb/^{206}Pb$ age, detrital	Bostock and van Breemen (1994)	
			U-Pb zircon	2576.4±2.6			$^{207}Pb/^{206}Pb$ age, detrital	Bostock and van Breemen (1994)	
			U-Pb zircon	2381.9±1.7			$^{207}Pb/^{206}Pb$ age, detrital	Bostock and van Breemen (1994)	85
			U-Pb zircon	2307.2±3.2			$^{207}Pb/^{206}Pb$ age, detrital	Bostock and van Breemen (1994)	86
			U-Pb zircon	2305.8±1.0			$^{207}Pb/^{206}Pb$ age, detrital	Bostock and van Breemen (1994)	87
			U-Pb zircon	2251.2±1.1			$^{207}Pb/^{206}Pb$ age, detrital	Bostock and van Breemen (1994)	88
			U-Pb zircon	2165.8±1.2			$^{207}Pb/^{206}Pb$ age, detrital	Bostock and van Breemen (1994)	89
			U-Pb zircon	2152.5±1.1			$^{207}Pb/^{206}Pb$ age, detrital	Bostock and van Breemen (1994)	90
			U-Pb zircon	2110.1±3.0			$^{207}Pb/^{206}Pb$ age, detrital	Bostock and van Breemen (1994)	91
			U-Pb zircon	2089.4±1.5			$^{207}Pb/^{206}Pb$ age, detrital	Bostock and van Breemen (1994)	92
			U-Pb zircon	2077.5±1.0			$^{207}Pb/^{206}Pb$ age, metamorphic	Bostock and van Breemen (1994)	93
			U-Pb zircon	2074.8±1.0			$^{207}Pb/^{206}Pb$ age, metamorphic	Bostock and van Breemen (1994)	94
			U-Pb monazite	2079.6±1.0			$^{207}Pb/^{206}Pb$ age, metamorphic or cooling	Bostock and van Breemen (1994)	95
			U-Pb monazite	2063.3±1.3			$^{207}Pb/^{206}Pb$ age, metamorphic or cooling	Bostock and van Breemen (1994)	96
			U-Pb monazite	2056.0±1.2			$^{207}Pb/^{206}Pb$ age, metamorphic or cooling	Bostock and van Breemen (1994)	97
Thubun Lakes									
Thubun lakes 89BK-9X, #2349	UTM 12, 446190E, 6824270N	pelitic gneiss	U-Pb zircon	2153.4±1.3			$^{207}Pb/^{206}Pb$ age, detrital	Bostock and van Breemen (1994)	98
			U-Pb zircon	2152.8±2.3			$^{207}Pb/^{206}Pb$ age, detrital	Bostock and van Breemen (1994)	99
			U-Pb zircon	2141.8±2.3			$^{207}Pb/^{206}Pb$ age, detrital	Bostock and van Breemen (1994)	100
			U-Pb zircon	2092.8±1.4			$^{207}Pb/^{206}Pb$ age, detrital	Bostock and van Breemen (1994)	101
			U-Pb zircon	2077.7±1.1			$^{207}Pb/^{206}Pb$ age, detrital	Bostock and van Breemen (1994)	102
			U-Pb zircon	2044.4±1.5			$^{207}Pb/^{206}Pb$ age, detrital	Bostock and van Breemen (1994)	103
			U-Pb zircon	1904.7±1.2			$^{207}Pb/^{206}Pb$ age, metamorphic, high U (2252 ppm)	Bostock and van Breemen (1994)	104
			U-Pb monazite	1906.9±1.1			$^{207}Pb/^{206}Pb$ age, metamorphic	Bostock and van Breemen (1994)	105

Identifier	Location	Rock Type	Technique	Age (Ma)	Sm-Nd ε_{Nd}	T_{DM} (Ga)	Comments	Source	Ref. #
			U-Pb monazite	1904.4±1.0			$^{207}Pb/^{206}Pb$ age, metamorphic	Bostock and van Breemen (1994)	106
Tsu Lake									
Tsu Lake 89BK-1X, #1944	UTM 12, 451800E, 6737750N	quartzite	U-Pb zircon	2678.4±3.0			$^{207}Pb/^{206}Pb$ age	Bostock and van Breemen (1994)	
			U-Pb zircon	2431.3±1.8			$^{207}Pb/^{206}Pb$ age, detrital	Bostock and van Breemen (1994)	
			U-Pb zircon	2422.3±4.8			$^{207}Pb/^{206}Pb$ age, detrital	Bostock and van Breemen (1994)	
			U-Pb zircon	2397.7±1.3			$^{207}Pb/^{206}Pb$ age, detrital	Bostock and van Breemen (1994)	107
			U-Pb zircon	2374.9±1.7			$^{207}Pb/^{206}Pb$ age, detrital	Bostock and van Breemen (1994)	108
			U-Pb zircon	2290.9±3.2			$^{207}Pb/^{206}Pb$ age, detrital	Bostock and van Breemen (1994)	109
			U-Pb zircon	2142.7±2.4			$^{207}Pb/^{206}Pb$ age, metamorphic	Bostock and van Breemen (1994)	110
			U-Pb zircon	2132.9±3.1			$^{207}Pb/^{206}Pb$ age, metamorphic	Bostock and van Breemen (1994)	111
			U-Pb zircon	2074.0±3.7			$^{207}Pb/^{206}Pb$ age, high U (1359 ppm), metamorphic	Bostock and van Breemen (1994)	112
			U-Pb zircon	2059.8±2.3			$^{207}Pb/^{206}Pb$ age, metamorphic	Bostock and van Breemen (1994)	113
Pelitic Gneisses near Leland and Charles Lake shear zones									
Myers Lake MSB-93-15		pelitic gneiss		1923-1926			cooling ages	McDonough et al. (2000)	
			U-Pb monazite	1925±1			$^{207}Pb/^{206}Pb$ age, metamorphic	McDonough et al. (2000)	114
			U-Pb monazite	1926±1			$^{207}Pb/^{206}Pb$ age, metamorphic	McDonough et al. (2000)	115
			U-Pb monazite	1923±1			$^{207}Pb/^{206}Pb$ age, metamorphic	McDonough et al. (2000)	116
			U-Pb monazite	1924±1			$^{207}Pb/^{206}Pb$ age, metamorphic	McDonough et al. (2000)	117
eastern Charles Lake MSB-MCH-41		pelitic gneiss	U-Pb monazite	1919±1			$^{207}Pb/^{206}Pb$ age, metamorphic	McDonough et al. (2000)	118
			U-Pb monazite	1919±1			$^{207}Pb/^{206}Pb$ age, metamorphic	McDonough et al. (2000)	119
			U-Pb monazite	1925±1			$^{207}Pb/^{206}Pb$ age, metamorphic	McDonough et al. (2000)	120
MCH-41	between Charles Lake and Bayonet Lake shear zones	Musc pelitic gneiss (Grt-Sil-Bt-Qtz-Kfs)	Ar-Ar	1803±11				McDonough et al. (1994), Plint and McDonough (1995)	
pelitic paragneiss		pelitic paragneiss			-0.7 to -2.8		ε_{Nd} (2.2 Ga)	Thériault (1994)	
amphibolite enclaves		amphibolite enclaves			+3.9 to -4.3		ε_{Nd} (2.2 Ga)	Thériault (1994)	
Slave and Konth xenoliths		engulfed metasediments'			-4.1 to -6	2.6-2.8		Thériault (1992)	
Mountain Rapids Granulite									
		6 mafic and 1 felsic granulites	Sm-Nd isochron	2436±44	-2.55±0.98		T_{CHUR}	Burwash et al. (1985)	
UA 887		felsic granulite	TNd Chur	2.66 ±<=0.2% 2.74±<=0.2%				Burwash et al. (1985)	
		6 mafic granulties	TNd Chur	2.78 to 14.42±<=0.2%				Burwash et al. (1985)	
		mafic granulites	whole rock Rb-Sr	1898±5				Burwash et al. (1985)	
Snowbird Tectonic Zone (STZ)									
	Upper Deck, East Athabasca mylonite triangle			ca. 3.2-2.6 Ga				c.f. Snoeyenbos et al. (1995)	
Great Slave Lake Shear Zone (GSLsz)									
Laloche batholith (?)		megacrystic Bt granitoid	U-Pb zircon	1.98 Ga			protolith, U-rich zircon	Hanmer (1988) cited (Bowring, pers comm 1987)	
Wall rock	McDonald Lake	Two mica leucogranite	U-Pb zircon	ca. 2.55 Ga				Hanmer et al. (1992)	
Migmatitic wall rock		Grt leucogranite	U-Pb zircon	ca. 1.96 Ga			upper intercept	Hanmer et al. (1992)	
Northeast segment		mylonite	U-Pb zircon	ca. 1.976 Ga			Bt megacrystic granite protolith	Hanmer et al. (1992)	
		biotite megacrystic granite	U-Pb zircon	ca. 1.978 Ga				Hanmer et al. (1992)	
Southwest segment		megacrystic granite protolith to granulite facies belt	U-Pb zircon	ca. 1.98 Ga			$^{207}Pb/^{206}Pb$ model age	Hanmer et al. (1992)	
		megacrystic granite protolith to lower amphibolite facies belt	U-Pb zircon	ca. 1.924 Ga			upper intercept	Hanmer et al. (1992)	
		granite protomylonite	U-Pb zircon	2.05±0.065 Ga			poor upper intercept	Hanmer et al. (1992)	
	Second Lake and Falls Lake	granite	U-Pb zircon	ca. 1.92 Ga			upper intercept	Hanmer et al. (1992)	
		leucogranite	U-Pb zircon	ca. 1.89 Ga				Hanmer et al. (1992)	

Western Rae Province (WRP)

Granitoids living and intruding western Rae margin hinterland gneisses									
Benna Thy	along margin	monzogranite	U-Pb monazite	1906 +3/-1			$^{207}Pb/^{206}Pb$ crystallization age U ppm (116 - 1253)	Bostock and Loveridge (1988)	139
Gagnon granite	northern megacrystic granite (north)		U-Pb zircon and sphene	1960-1920				van Breemen et al. (1992)	
	northern megacrystic granite (south)	megacrystic monzogranite	U-Pb zircon and monazite	1940±8			high U zircons (1140-2810 ppm)	van Breemen et al. (1992)	141
	northern equigranular granite	equigranular Bt granite	U-Pb zircon and monazite	1882 +7/-6			igneous crystallization age, high U zircon (2140-5470 ppm)	van Breemen et al. (1992)	
Thekulthili		syenogranite	U-Pb zircon	1813±5				Bostock et al. (1991)	
Natael 83BK-437A, #662	UTM 12; 554760E, 6716000N	granite	U-Pb monazite	1934±2			crystallization age, intruding Hill Island sediments	Bostock and van Breemen (1994)	140
Thoa metagabbro	mafic remnant within Berrigan Lake Block	gabbro		2340±7			remnant mafic rock, emplacement age	van Breemen and Bostock (1994)	44
	intruding mixed gneiss of Berrigan Lake block	syenogranite	U-Pb zircon	2394±2				van Breemen et al. (1992)	45
Berrigan anorthosite within Berrigan lake complex?		anorthosite	U-Pb zircon	1956±3			igneous crystallization age	Bostock et al. (1991)	142
Yatsore Lake augen gneiss	intruding Andrew Lake block	augen gneiss	U-Pb zircon	2270±4			intrudes Andrew lake block, primary granite crystallization	Bostock et al. (1991)	51
pre-Benna Thy granite country rock'	Eastern equigranular hinterland monzogranite, intruding Andrew Lake block	monzogranite	U-Pb zircon	2334 +22/-18			intrudes Andrew lake block	Bostock and Loveridge (1988), Bostock et al. (1991)	52

Identifier	Location	Rock Type	Technique	Age (Ma)	Sm-Nd ε_{Nd}	T_{DM} (Ga)	Comments	Source	Ref. #
Basins along the western Slave margin									
Hill Island Lake									
87BK-360X, #1943	UTM 12, 560840E, 6711220N	greywacke	U-Pb zircon	2168.3±5.5			$^{207}Pb/^{206}Pb$ age, detrital zircon	Bostock and van Breemen (1994)	121
			U-Pb zircon	2167.4±5.9			$^{207}Pb/^{206}Pb$ age, detrital zircon	Bostock and van Breemen (1994)	122
			U-Pb zircon	2133.8±8.0			$^{207}Pb/^{206}Pb$ age, detrital zircon	Bostock and van Breemen (1994)	123
			U-Pb zircon	1917.5±2.7			brown zircon, $^{207}Pb/^{206}Pb$ age	Bostock and van Breemen (1994)	124
			U-Pb zircon	1917.7±3.4			brown zircon, $^{207}Pb/^{206}Pb$ age	Bostock and van Breemen (1994)	125
			U-Pb zircon	1903.2±3.6			brown zircon, $^{207}Pb/^{206}Pb$ age, high U (1097 ppm)	Bostock and van Breemen (1994)	126
			U-Pb zircon	1871.3±2.2			brown zircon, $^{207}Pb/^{206}Pb$ age, high U (2218 ppm)	Bostock and van Breemen (1994)	127
			U-Pb zircon	1863.2±1.9			brown zircon, $^{207}Pb/^{206}Pb$ age	Bostock and van Breemen (1994)	128
			U-Pb zircon	1818.0±1.4			brown zircon, $^{207}Pb/^{206}Pb$ age, high U (3638 ppm)	Bostock and van Breemen (1994)	129
Waugh Group									
MRB-MAN-14	UTM 12, 554502E, 6630797N, MTS 74M/16	pebbly feldspathic wacke	U-Pb zircon	2.02-1.97 Ga			timing of Waugh basin deposition	McNicoll et al. (1994)	
			U-Pb zircon	2006±15			$^{207}Pb/^{206}Pb$ age, detrital zircon	McDonough and McNicoll (1997)	130
			U-Pb zircon	2096±2			$^{207}Pb/^{206}Pb$ age, detrital zircon	McDonough and McNicoll (1997)	131
			U-Pb zircon	2114±6			$^{207}Pb/^{206}Pb$ age, detrital zircon	McDonough and McNicoll (1997)	132
			U-Pb zircon	2161±5			$^{207}Pb/^{206}Pb$ age, detrital zircon	McDonough and McNicoll (1997)	133
			U-Pb zircon	2247±6			$^{207}Pb/^{206}Pb$ age, detrital zircon	McDonough and McNicoll (1997)	134
			U-Pb zircon	2251±5			$^{207}Pb/^{206}Pb$ age, detrital zircon	McDonough and McNicoll (1997)	135
			U-Pb zircon	2315±4			$^{207}Pb/^{206}Pb$ age, detrital zircon	McDonough and McNicoll (1997)	136
			U-Pb zircon	2318±4			$^{207}Pb/^{206}Pb$ age, detrital zircon	McDonough and McNicoll (1997)	137
			U-Pb zircon	2321±15			$^{207}Pb/^{206}Pb$ age, detrital zircon	McDonough and McNicoll (1997)	138
			U-Pb zircon	2738±41			$^{207}Pb/^{206}Pb$ age, detrital zircon	McDonough and McNicoll (1997)	
Burntwood / Athabasca Group									
MSB-95-45	Lake Athabasca	Qtz pebble sandstone	U-Pb zircon	1919±2			$^{207}Pb/^{206}Pb$ age, detrital zircon	McDonough and McNicoll (1997)	
			U-Pb zircon	1941±2			$^{207}Pb/^{206}Pb$ age, detrital zircon	McDonough and McNicoll (1997)	
			U-Pb zircon	2123±51			$^{207}Pb/^{206}Pb$ age, detrital zircon	McDonough and McNicoll (1997)	
			U-Pb zircon	2204±2			$^{207}Pb/^{206}Pb$ age, detrital zircon	McDonough and McNicoll (1997)	
			U-Pb zircon	2256±2			$^{207}Pb/^{206}Pb$ age, detrital zircon	McDonough and McNicoll (1997)	
			U-Pb zircon	2270±2			$^{207}Pb/^{206}Pb$ age, detrital zircon	McDonough and McNicoll (1997)	
			U-Pb zircon	2304±2			$^{207}Pb/^{206}Pb$ age, detrital zircon	McDonough and McNicoll (1997)	
			U-Pb zircon	2310±10			$^{207}Pb/^{206}Pb$ age, detrital zircon	McDonough and McNicoll (1997)	
			U-Pb zircon	2504±1			$^{207}Pb/^{206}Pb$ age, detrital zircon	McDonough and McNicoll (1997)	
Nonacho Group - upperintercept and $^{207}Pb/^{206}Pb$ model age									
			U-Pb zircon	ca. 3300-3050, 2480-2310, 2130-2060 Ma			summary, detrital zircon, w. Rae provenance	van Breemen and Aspler (1994)	
	Upper Tronka Chua Formation		U-Pb zircon	2395±2			$^{207}Pb/^{206}Pb$ age, detrital zircon	van Breemen and Aspler (1994)	
	Upper Tronka Chua Formation		U-Pb zircon	2386±1			$^{207}Pb/^{206}Pb$ age, detrital zircon	van Breemen and Aspler (1994)	
	Upper Tronka Chua Formation		U-Pb zircon	2379±3			$^{207}Pb/^{206}Pb$ age, detrital zircon	van Breemen and Aspler (1994)	
	Upper Tronka Chua Formation		U-Pb zircon	2349±2			$^{207}Pb/^{206}Pb$ age, detrital zircon	van Breemen and Aspler (1994)	
	Upper Tronka Chua Formation		U-Pb zircon	2325±2			$^{207}Pb/^{206}Pb$ age, detrital zircon	van Breemen and Aspler (1994)	
	Upper Tronka Chua Formation		U-Pb zircon	2310±1			$^{207}Pb/^{206}Pb$ age, detrital zircon	van Breemen and Aspler (1994)	
	Upper Tronka Chua Formation		U-Pb zircon	1995±4			$^{207}Pb/^{206}Pb$ age, detrital zircon	van Breemen and Aspler (1994)	
	Newshethdezza Formation		U-Pb zircon	3246±3			$^{207}Pb/^{206}Pb$ age, detrital zircon	van Breemen and Aspler (1994)	
	Newshethdezza Formation		U-Pb zircon	3229±2			$^{207}Pb/^{206}Pb$ age, detrital zircon	van Breemen and Aspler (1994)	
	Newshethdezza Formation		U-Pb zircon	2819±2			$^{207}Pb/^{206}Pb$ age, detrital zircon	van Breemen and Aspler (1994)	
	Newshethdezza Formation		U-Pb zircon	2479±10			$^{207}Pb/^{206}Pb$ age, detrital zircon	van Breemen and Aspler (1994)	
	Newshethdezza Formation		U-Pb zircon	2453±3			$^{207}Pb/^{206}Pb$ age, detrital zircon	van Breemen and Aspler (1994)	
	Taltson Formation		U-Pb zircon	3070±1			$^{207}Pb/^{206}Pb$ age, detrital zircon	van Breemen and Aspler (1994)	
	Taltson Formation		U-Pb zircon	3059±2			$^{207}Pb/^{206}Pb$ age, detrital zircon	van Breemen and Aspler (1994)	
	Taltson Formation		U-Pb zircon	2395±3			$^{207}Pb/^{206}Pb$ age, detrital zircon	van Breemen and Aspler (1994)	
	Taltson Formation		U-Pb zircon	2378±3			$^{207}Pb/^{206}Pb$ age, detrital zircon	van Breemen and Aspler (1994)	
	Taltson Formation		U-Pb zircon	2102±2			$^{207}Pb/^{206}Pb$ age, detrital zircon	van Breemen and Aspler (1994)	
	Taltson Formation		U-Pb zircon	2018±3			$^{207}Pb/^{206}Pb$ age, detrital zircon	van Breemen and Aspler (1994)	
	Upper Tronka Chua Formation		U-Pb zircon	2411±3			detrital zircon, upper intercept age	van Breemen and Aspler (1994)	

Identifier	Location	Rock Type	Technique	Age (Ma)	Sm-Nd ε_{Nd}	T_{DM} (Ga)	Comments	Source	Ref. #
	Upper Tronka Chua Formation		U-Pb zircon	2392±2			detrital zircon, upper intercept age	van Breemen and Aspler (1994)	
	Upper Tronka Chua Formation		U-Pb zircon	2607±4			detrital zircon, upper intercept age	van Breemen and Aspler (1994)	
	Upper Tronka Chua Formation		U-Pb zircon	2369±2			detrital zircon, upper intercept age	van Breemen and Aspler (1994)	
	Upper Tronka Chua Formation		U-Pb zircon	2334±3			detrital zircon, upper intercept age	van Breemen and Aspler (1994)	
	Upper Tronka Chua Formation		*U-Pb zircon*	*2342±2*			*detrital zircon, upper* intercept age	*van Breemen and Aspler (1994)*	
	Upper Tronka Chua Formation		U-Pb zircon	2175±8			detrital zircon, upper intercept age	van Breemen and Aspler (1994)	
	Newshethdezza Formation		U-Pb zircon	3293±3			detrital zircon, upper intercept age	van Breemen and Aspler (1994)	
	Newshethdezza Formation		U-Pb zircon	3242±5			detrital zircon, upper intercept age	van Breemen and Aspler (1994)	
	Newshethdezza Formation		U-Pb zircon	2848±2			detrital zircon, upper intercept age	van Breemen and Aspler (1994)	
	Newshethdezza Formation		U-Pb zircon	2481±12			detrital zircon, upper intercept age	van Breemen and Aspler (1994)	
	Newshethdezza Formation		U-Pb zircon	2491±3			detrital zircon, upper intercept age	van Breemen and Aspler (1994)	
	Taltson Formation		U-Pb zircon	3160±2			detrital zircon, upper intercept age	van Breemen and Aspler (1994)	
	Taltson Formation		U-Pb zircon	3257±3			detrital zircon, upper intercept age	van Breemen and Aspler (1994)	
	Taltson Formation		U-Pb zircon	2405±5			detrital zircon, upper intercept age	van Breemen and Aspler (1994)	
	Taltson Formation		U-Pb zircon	2380±4			detrital zircon, upper intercept age	van Breemen and Aspler (1994)	
	Taltson Formation		U-Pb zircon	2131±3			detrital zircon, upper intercept age	van Breemen and Aspler (1994)	
	Taltson Formation		U-Pb zircon	2059±5			detrital zircon, upper intercept age	van Breemen and Aspler (1994)	
Western Granulite Domain and Adjacent Domains									
Western Granulite Domain / Clearwater Anorthosite Complex									
		anorthosite	Sm-Nd isochron	2480±30				Hulbert (1988)	
HUD-85-9	central Careen lake	augen gneiss	U-Pb zircon	1934±1			$^{207}Pb/^{206}Pb$ age, metamorphic	Bickford et al. (1994)	
			U-Pb zircon	1939±13			$^{207}Pb/^{206}Pb$ age, metamorphic	Bickford et al. (1994)	
			U-Pb zircon	1931±16			$^{207}Pb/^{206}Pb$ age, metamorphic	Bickford et al. (1994)	
			U-Pb zircon	1932±2			$^{207}Pb/^{206}Pb$ age, metamorphic	Bickford et al. (1994)	
HUD-85-8	east Fournier Lake	tonalitic gneiss	U-Pb zircon	2006±34	-25	2.843	metamorphic, upper intercept	Bickford et al. (1994)	
HUD-85-10	west Careen lake	Hbl-Bt gneiss	U-Pb zircon	2234±1			$^{207}Pb/^{206}Pb$ age, metamorphic	Bickford et al. (1994)	
			U-Pb zircon	2263±1			$^{207}Pb/^{206}Pb$ age, metamorphic	Bickford et al. (1994)	
			U-Pb zircon	2170±2			$^{207}Pb/^{206}Pb$ age, metamorphic	Bickford et al. (1994)	
			U-Pb zircon	2074±1			$^{207}Pb/^{206}Pb$ age, metamorphic	Bickford et al. (1994)	
			U-Pb zircon	1925±1			$^{207}Pb/^{206}Pb$ age, metamorphic	Bickford et al. (1994)	
CC-88-59	Careen Lake	agmatitic anorthosite	U-Pb zircon	~2900 2300-2200 2100-1900 1800			summary	Crocker et al. (1993)	
			U-Pb zircon	2317			SHRIMP; metamorphic	Crocker et al. (1993)	
			U-Pb zircon	2309			SHRIMP; metamorphic	Crocker et al. (1993)	
			U-Pb zircon	2250			SHRIMP; metamorphic	Crocker et al. (1993)	
			U-Pb zircon	2181			SHRIMP; metamorphic	Crocker et al. (1993)	
			U-Pb zircon	2176			SHRIMP; metamorphic	Crocker et al. (1993)	
			U-Pb zircon	2074			SHRIMP; metamorphic	Crocker et al. (1993)	
			U-Pb zircon	2061			SHRIMP; metamorphic	Crocker et al. (1993)	
			U-Pb zircon	1987			SHRIMP; metamorphic	Crocker et al. (1993)	
			U-Pb zircon	1928			SHRIMP; metamorphic	Crocker et al. (1993)	
			U-Pb zircon	1787			SHRIMP; metamorphic	Crocker et al. (1993)	
Tazin Lake									
HUD84-304		granitic gneiss	U-Pb zircon	2639±16			arkosic metasediment protolith	Van Schmus et al. (1986)	
HUD84-302		granodioritic xenoliths	U-Pb zircon	2596±10				Van Schmus et al. (1986)	
HUD84-303		granodioritic xenoliths	U-Pb zircon	2605±10				Van Schmus et al. (1986)	
HUD84-301		granitic gneiss	U-Pb zircon	2595±7				Van Schmus et al. (1986)	
Tazin Lake region		granodiorite-diorite	K-Ar	2370±40			Mean Bt and amphibole age	Koster and Baadsgaard (1970)	
Nolan Lake									
HUD84-305		granodiorite	U-Pb zircon	2581±4				Van Schmus et al. (1986)	
Beaverlodge Area, northern Saskatchewan									
HUD84-307		Macintosh Granite	U-Pb zircon	2356±14				Van Schmus et al. (1986)	
HUD84-315		Gunnar Mine granite	U-Pb zircon	2181±5				Van Schmus et al. (1986)	
HUD84-31		Box Mine Granite	U-Pb zircon	1994±37			high U zircon (1000-3000 ppm), Au-bearing	Van Schmus et al. (1986)	143
HUD84-322		Athona Mine granite	U-Pb zircon	2327±17				Van Schmus et al. (1986)	
HUD84-319		Elliot Bay granite	U-Pb zircon	3014±10				Van Schmus et al. (1986)	
HUD84-325		Lodge Bay granite	U-Pb zircon	3072±41				Van Schmus et al. (1986)	
		Foot Bay gneiss	U-Pb zircon	2513 +36/-22				Tremblay et al. (1981)	
		Donaldson Lake gneiss	U-Pb zircon	2179±12				Tremblay et al. (1981)	
Churchill Platform									
HUD-85-1	Keewatin Zone	Junction granite	U-Pb zircon	1820±19			inherited Archeann cores?, anatexis	Bickford et al. (1987)	
HUD-85-5	Dipper Lake, Mudjatik Domain, Cree Lake zone	charnockite	U-Pb zircon	ca. 2000			metamorphic (Hearne)	Bickford et al. (1987)	
HUD-85-6	Dipper Lake, Mudjatik Domain, Cree Lake zone	upper amphibolite facies gneiss'	U-Pb zircon	1889-2003			metamorphic (Hearne)	Bickford et al. (1987)	
Fontaine Lake, Saskatchewan	59°45'N 106°25'W	Pegmatite	K-Ar	1740±5%			Musc; Index no. 3	Burwash et al. (1962)	
Stony Rapids, Sask	59°21'N 105°41'W	Porphyritic Bt granite	K-Ar	1720±5%			Bt; Index no. 4	Burwash et al. (1962)	
Stony Rapids, Sask	59°29'N 105°36'W	Px-Hbl granulite cobble	K-Ar	2350±5%			Hbl; Index no. 5	Burwash et al. (1962)	
Cree Lake, Sask	57o26'N 106o54'W	Diabase dike	K-Ar	1230±5%			Hornblende; Index no. 6	Burwash et al. (1962)	
Wopmay Orogen									
Great Bear Magmatic Arc (2.0-1.8 Ga) (GBMA)									
Mobil et al. Pert	*11-15-123-1W6*	*tonalite*	*U-Pb zircon*	*1.75-1.95, inconclusive*				*Ross et al. (1991)*	
TH84-62		McLaren Pluton	U-Pb zircon	1870	-0.19			Bowring and Podosek (1989) [Age c.f Bowring 1985 unpubl. Thesis]	
TH84-32			U-Pb zircon	1870	-1.35			Bowring and Podosek (1989) [Age c.f Bowring 1985 unpubl. Thesis]	

Identifier	Location	Rock Type	Technique	Age (Ma)	Sm-Nd ε_{Nd}	T_{DM} (Ga)	Comments	Source	Ref. #
TH84-1			U-Pb zircon	1870	-0.23			Bowring and Podosek (1989) [Age c.f Bowring 1985 unpubl. Thesis]	
TH84-10			U-Pb zircon	1870	-0.78			Bowring and Podosek (1989) [Age c.f Bowring 1985 unpubl. Thesis]	
F84-6		xenolith	U-Pb zircon	1870	-0.83			Bowring and Podosek (1989) [Age c.f Bowring 1985 unpubl. Thesis]	
TH84-23		Spence Pluton	U-Pb zircon	1865	-1.41			Bowring and Podosek (1989) [Age c.f Bowring 1985 unpubl. Thesis]	
TH84-35		Sloan rhyodacite	U-Pb zircon	1870	-1.63			Bowring and Podosek (1989) [Age c.f Bowring 1985 unpubl. Thesis]	
H-80-15		Balachey Pluton	U-Pb zircon	1870	-0.1			Bowring and Podosek (1989) [Age c.f Bowring 1985 unpubl. Thesis]	
HWA-86-G-57		Handley-Page Pluton	U-Pb zircon	1870	-1.13			Bowring and Podosek (1989) [Age c.f Bowring 1985 unpubl. Thesis]	
H-80-59		Calder Pluton	U-Pb zircon	1875	-1.4			Bowring and Podosek (1989) [Age c.f Bowring 1985 unpubl. Thesis]	
H-77-50		Echo Bay Andesite	U-Pb zircon	1870	-1.35			Bowring and Podosek (1989) [Age c.f Bowring 1985 unpubl. Thesis]	
H-80-85		Animal Andesite	U-Pb zircon	1870	0.09			Bowring and Podosek (1989) [Age c.f Bowring 1985 unpubl. Thesis]	
H-80-112		Camsell River Andesite	U-Pb zircon	1870	-0.01			Bowring and Podosek (1989) [Age c.f Bowring 1985 unpubl. Thesis]	
L255		Bishop Granite	U-Pb zircon	1865	-8.59			Bowring and Podosek (1989) [Age c.f Bowring 1985 unpubl. Thesis]	
L268			U-Pb zircon	1865	-5.93			Bowring and Podosek (1989) [Age c.f Bowring 1985 unpubl. Thesis]	
Hottah Terrane (2.0-2.4 Ga) (HT)									
Imperial Black Creek	10-27-109-9W6	tonalite	U-Pb zircon	1870 +12/-11	-0.6	2.32		Ross et al. (1991), Villeneuve et al. (1993)	
BA West Rainbow	06-33-110-10W6	granodiorite	U-Pb zircon	1845 +61/-58			MSWD=1291, upper intercept	Ross et al. (1991)	
Imperial Amber	13-11-116-8W6	gneiss	U-Pb zircon	1.75-1.95 Ga, inconclusive				Villeneuve et al. (1993)	
Mobil et al. Bark Bistcho	14-16-121-7W6	syenogranite	U-Pb zircon	1924 +25/-24			MSWD=23, upper intercept	Ross et al. (1991)	
HZr-84-1		Hottah granite	U-Pb zircon	1920	-1.67			Bowring and Podosek (1989) [Age c.f Bowring 1985 unpubl. Thesis]	
HWA-83A-54			U-Pb zircon	1920	0.25			Bowring and Podosek (1989) [Age c.f Bowring 1985 unpubl. Thesis]	
HWAR-84-272		Bloom basalt	U-Pb zircon	1900	2.81			Bowring and Podosek (1989) [Age c.f Bowring 1985 unpubl. Thesis]	
Fort Simpson High (1.85 Ga) (FSH)									
Imperial Sikanni Chief		*Bt monzogranite*	*U-Pb zircon*	*1846±3*	*1.3*	*2.14*		*Villeneuve et al. (1993)*	
	B-092-D/094-I-04		U-Pb zircon	1845±1				Ross (1990)	
Imperial Island River		Bt granodiorite	U-Pb zircon	1844 +5/-3	-2.1	2.45		Villeneuve et al. (1993)	
Kilohigok Basin									
				1900				c.f. Grotzinger and McCormick (1988)	
		volcanic ash bed	U-Pb zircon	ca. 1970				Bowring and Grotzinger (1989)	
Hackett Fm		volcanic ash bed	U-Pb zircon	1969±1				Bowring and Grotzinger (1992)	
Rifle/Beechey Fm		volcanic ash bed	U-Pb zircon	1963±6				Bowring and Grotzinger (1992)	
Athapuscow aulacogen									
Hearne Channel granite	62°3.2'N 112°45.6'W		U-Pb zircon	2175±5				Bowring et al. (1984)	
Thor Lake syenite	62°6'N 112°35'W		U-Pb zircon	2094±10				Bowring et al. (1984)	
Wilson Island group	61°48.5'N 112°53.0'W	felsite	U-Pb zircon	1928±11				Bowring et al. (1984)	
Butte Island Intrusive Suite	61°40.9'N 113°19.3'W	granite	U-Pb zircon	1895±5				Bowring et al. (1984)	
Compton laccoliths-Stark Lake	62°30.9'N 110°0.0'W		U-Pb zircon	1895±8 1872±8 1867±22				Bowring et al. (1984)	
Compton laccoliths-Christie Bay	62°24.1'N 110°59.3'W		U-Pb zircon	1861±17				Bowring et al. (1984)	
Calderian Supergroup (Hepburn Intrusive Suite)									
L200D		Spider Pluton	U-Pb zircon	1885	-1.07			Bowring and Podosek (1989) [Age c.f Bowring 1985 unpubl. Thesis]	
L99-81		McIntosh Pluton	U-Pb zircon	1885	-1.84			Bowring and Podosek (1989) [Age c.f Bowring 1985 unpubl. Thesis]	
VS 79 121		Van's Rock Pluton	U-Pb zircon	1883	-1.28			Bowring and Podosek (1989) [Age c.f Bowring 1985 unpubl. Thesis]	
Akaitcho Group									
Turetok F467 80	HY	rhyolite	U-Pb zircon	1900	0.31			Bowring and Podosek (1989) [Age c.f Bowring 1985 unpubl. Thesis]	
HY F28 80		basalt	U-Pb zircon	1900	2.26			Bowring and Podosek (1989) [Age c.f Bowring 1985 unpubl. Thesis]	

Appendix B. Available pressure-temperature determinations from western Laurentia.

Identifier	Location	Met. Facies	Mineral Assemblage	Lithology	Technique	P (kbar)	T(°C)	Comments	Source
Red Earth Granulite Domain (RGD)									
4061-2 (4016)	06-10-077-25W4	granulite	Grt-Pl-Perthite	Grt-Pl-microcline gneiss	Reintegrated Fspar T	7 (estimate)	850		Burwash et al. (2000a)
86058-2	05-26-084-05W5	granulite	Bt-Grt-Pl-Perthite	Bt-Grt-Pl-Kfs paragneiss	Reintegrated Fspar T	7 (estimate)	850		Burwash et al. (2000a)
86060-2	04-16-084-08W5	granulite	Bt-Grt-Perthite-Pl	Bt-Grt-Kfs-Pl paragneiss	Reintegrated Fspar T	7 (estimate)	800		Burwash et al. (2000a)
86062-2	10-28-084-08W5	granulite	Bt-Grt-Perthite-Pl	Bt-Grt-Kfs-Pl gneiss	Reintegrated Fspar T	7 (estimate)	800		Burwash et al. (2000a)
194a-3	04-03-100-07W5	granulite	Crd-Sil-Grt-Pl-Perthite	Crd-Dil-Grt-Pl-Kfs paragneiss	Reintegrated Fspar T	7 (estimate)	850		Burwash et al. (2000a)
Northeastern Alberta									
		mod P granulite	Crd-Grt-Sil-Qtz with matrix Bt-Qtz-Plag-Kfs (perthite)		Grt-Bt T; Cord-Grt P-T	5.0±0.7	740±30	Aphebian M2.1, XH2O < 0.4	Nielsen et al. (1981), Langenberg and Nielsen (1982)
		low P granulite	Crd-Grt-Microcline-Plag-Bt-Sil		Grt-Bt T; Cord-Grt P-T	3.0±0.3	550±55	Aphebian M2.2, XH2O > 0.4	Nielsen et al. (1981), Langenberg and Nielsen (1982)
		greenschist	retrograde Musc-Chl-Bt-Ept			unknown	unknown	Aphebian M2.3	Nielsen et al. (1981)
Pelican Rapids									
		granulite	(hercynite) Spl–Qtz–Crd–Grt±Sil±Plag	granite and metasedimentary enclaves	GASP; Grt-Crd-Sil-Qtz-Spl Equilibration	6-8	900-1000		Chacko (1997)
					Qtz-Grt O isotope thermometry		920-1000		Farquhar et al. (1996)
					Reintegrated Fspar T		975-1000		Chacko (1997)
		granulite	Grt-Crd-Spl-Plag	migmatitic textures, qtz-rich leucosomes	Multi-equilibrium thermobarometry	5-7	830-940		Chacko et al. (1994)
Mountain Rapids									
	on Slave River	granulite	granite (Sil-Crd-Grt)	mafic granulite xenolitha	Crd-Gar P	5.5±0.7			Burwash et al. (1985)
Taltson Magmatic Zone (TMZ)									
TBC					Grt-Crd Fe-Mg exchange,				
MSB93-T2A		granulite	Spl+Qtz+Bt+Grt+Crd+Kfs+Sil	metapelitic gneiss	GASP, Grt-Crd P	7.2	880	Bt not used	Grover et al. (1997)
VAN53B			Grt+Bt+Crd+Kfs+Sil+Qtz			6.9	780	Bt not used	Grover et al. (1997)
TCH51B			Grt+Bt+Crd+Kfs+Sil+Qtz with Spl inclusions in Grt and Crd			6	810	Bt not used	Grover et al. (1997)
MSB93-T11A			Spl+Qtz+Bt+Grt+Crd+Kfs+Sil			6.5	730	Bt not used	Grover et al. (1997)
JG568			Grt+Bt+Crd+Kfs+Sil+Qtz with Spl inclusions in Grt and Crd			5.8	770	Bt not used	Grover et al. (1997)
JG568			Grt+Bt+Crd+Kfs+Sil+Qtz with Spl inclusions in Grt and Crd			6.4	840	Bt not used	Grover et al. (1997)
Arch Lake					Grt-Crd Fe-Mg exchange ± Grt-				
TLL-8		granulite	Spl+Qtz+Grt+Crd+Kfs+Sil	metapelitic gneiss	Bt T, GASP, Grt-Crd P	6.6	870		Grover et al. (1997)
MLL-5						6.5	870		Grover et al. (1997)
Chipewyan			Grt+Bt+Crd+Kfs+Sil+Qtz with Spl		Grt-Crd Fe-Mg exchange,				
MSB93-T52		granulite	inclusions in Grt and Crd	metapelitic gneiss	GASP, Grt-Crd P	6.3	830	Bt not used	Grover et al. (1997)
Eastern Slave			Grt+Bt+Crd+Kfs+Sil+Qtz with Spl		Grt-Crd Fe-Mg exchange ± Grt-				
JG449		granulite	inclusions in Grt and Crd	metapelitic gneiss	Bt T, GASP, Grt-Crd P	6.2	810		Grover et al. (1997)
Western Slave					Grt-Crd Fe-Mg exchange ± Grt-				
MSB93-18		granulite	Spl+Qtz+Grt+Crd+Kfs+Sil	metapelitic gneiss	Bt T, GASP, Grt-Crd P	6.3	820		Grover et al. (1997)
MSB93-T54D						7.1	880		Grover et al. (1997)
JG654			Spl+Qtz+Bt+Grt+Crd+Kfs+Sil			2.9	610	No Crd, Bt used	Grover et al. (1997)
106b, 146b, 187c, 205a, 223b, 258a, 310a, 317a, 353a, 40a, 505b, 59a,b, 718a, 96b	NorthernTMZ	granulite	Grt-Opx-Pl-Qtz	Slave, Konth and Rae Province paragneiss and granite		6.7	930	recalculated from Berman and Bostock (1997)	Pattison et al. (2003)
Great Slave Lake Shear Zone (GSLSZ)									
L-047	Belt 1	granulite	Grt-Sil-Bt-Pl-Qtz±Crd	metasediment	Grt-Bt T; GASP P	8.2	839		Hanmer (1988)
S-619	Belt 2					7.4	895		Hanmer (1988)
S-619	Belt 2					7.3	882		Hanmer (1988)
S-672	Belt 2					7.8	885		Hanmer (1988)
S-576	Belt 3					3.8	652		Hanmer (1988)
S-576	Belt 3					4.5	707		Hanmer (1988)
Snowbird Tectonic Zone (STZ)									
DS9322	Upper Deck, East Athabasca mylonite triangle	granulite	Grt-Cpx-corundum	garnet clinopyroxenite	Grt-Cpx	15	950		Snoeyenbos et al. (1995)
DS9318, M2498, M2315, M2506, R77	Upper Deck, East Athabasca mylonite triangle	granulite	Mesoperthite	felsic gneiss (+/- opx, cm), Grt quartzite	Reintegrated Fspar T	15 (estimate)	1000-1100	with kyanite	Snoeyenbos et al. (1995)

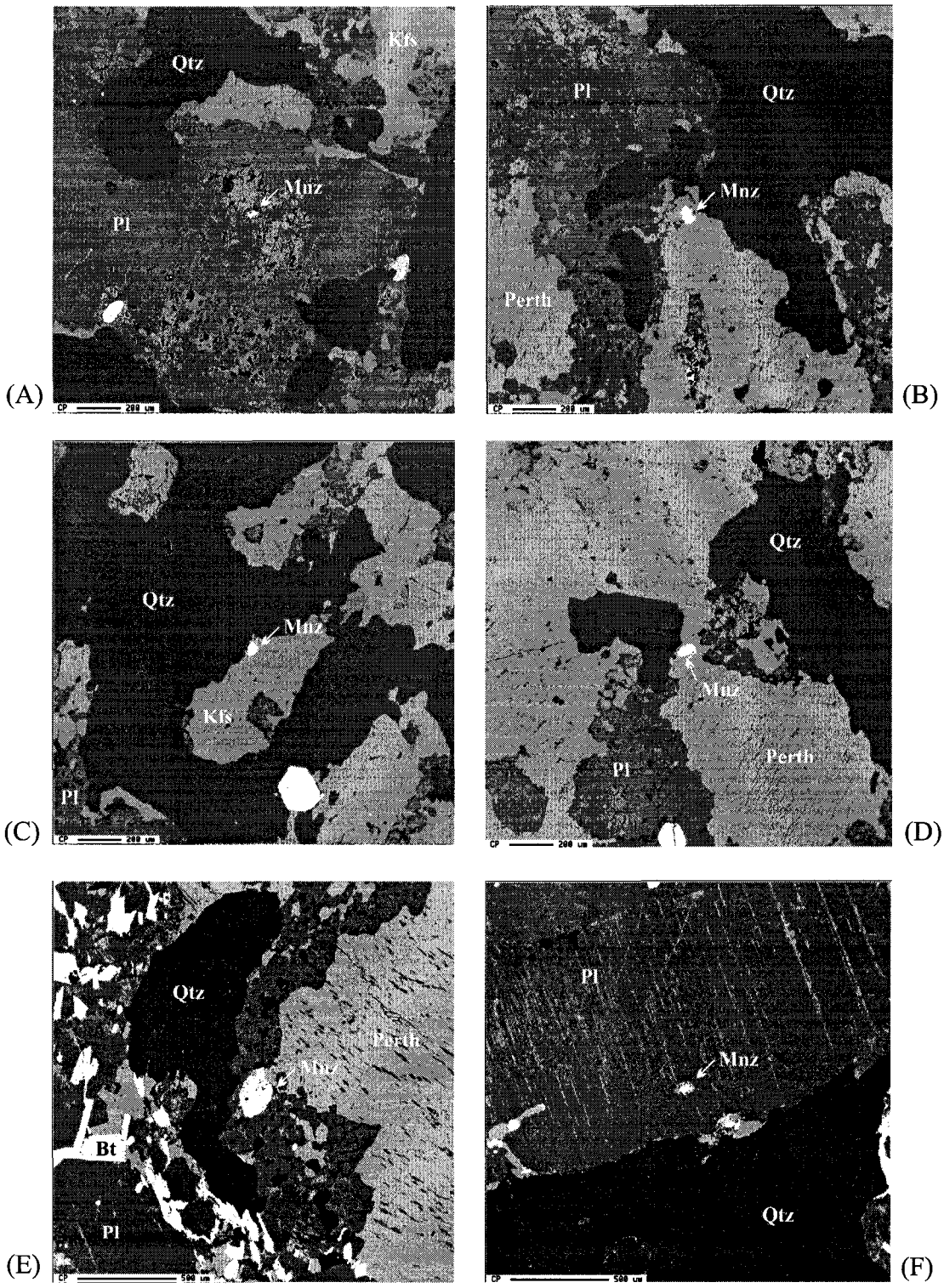

Appendix C. BSE composition maps of monazite (center) within thin section: (A) 4240-mon1, (B) 4240-mon2, (C) 4240-mon4, (D), 4240-mon5, (E) 860970-mon1, and (F) 860970-mon2.

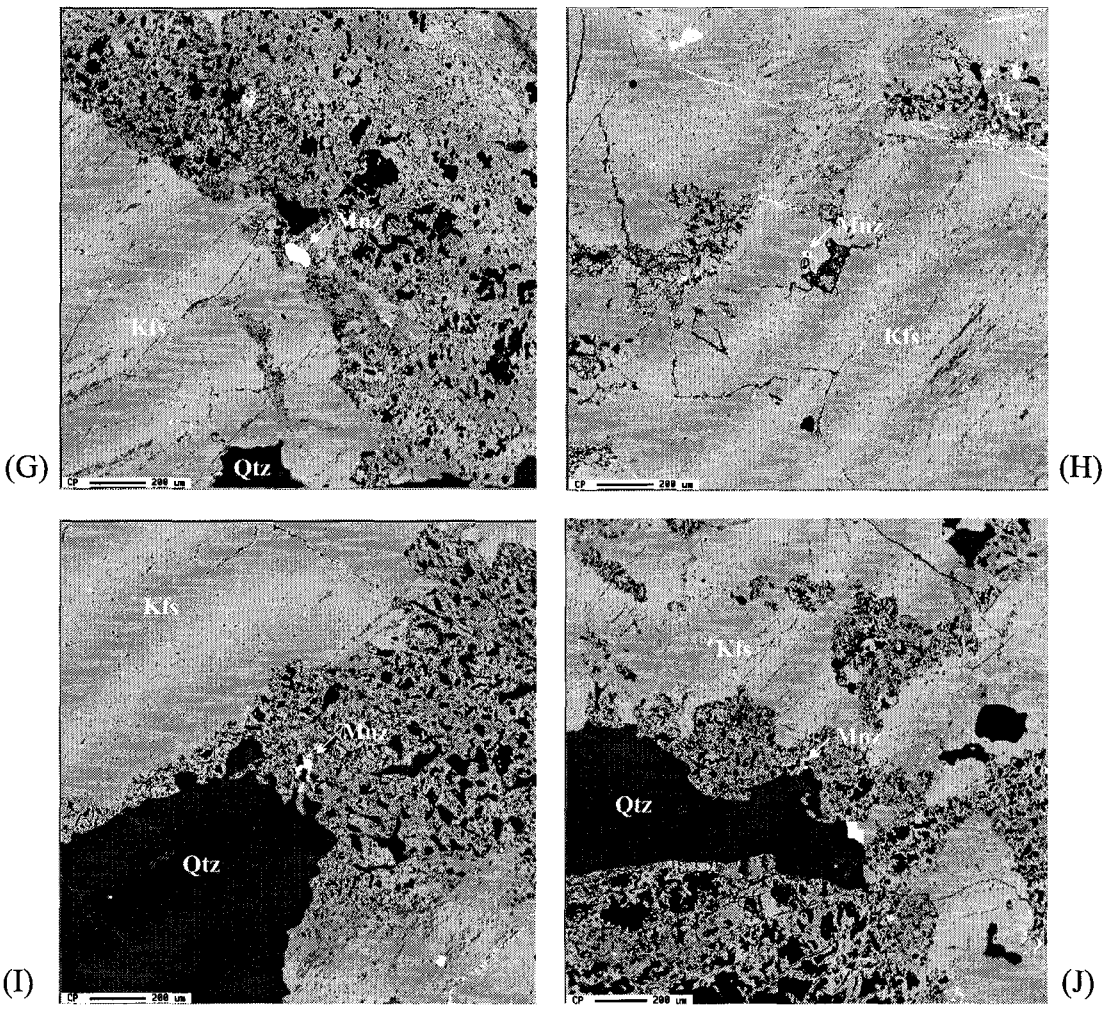

Appendix C. BSE composition maps of monazite (center) within thin section: (G) 860140-mon1, (H) 860140-mon2, (I) 860140-mon3, and (J) 860140-mon4.

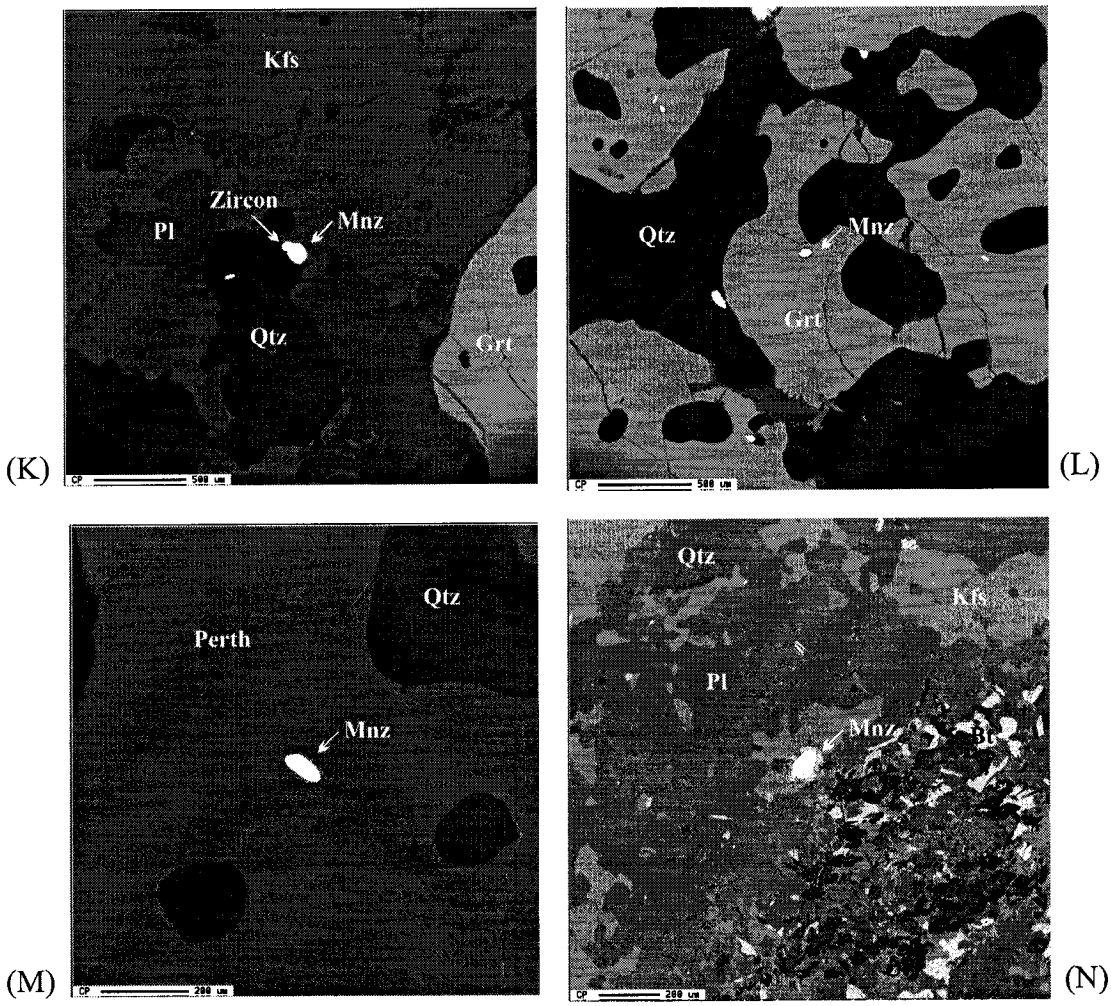

Appendix C. BSE composition maps of monazite (center) within thin section: (K) 861510-mon4, (K) 861510-mon8, (M) 861510-mon12, and (N) 861380-mon2.

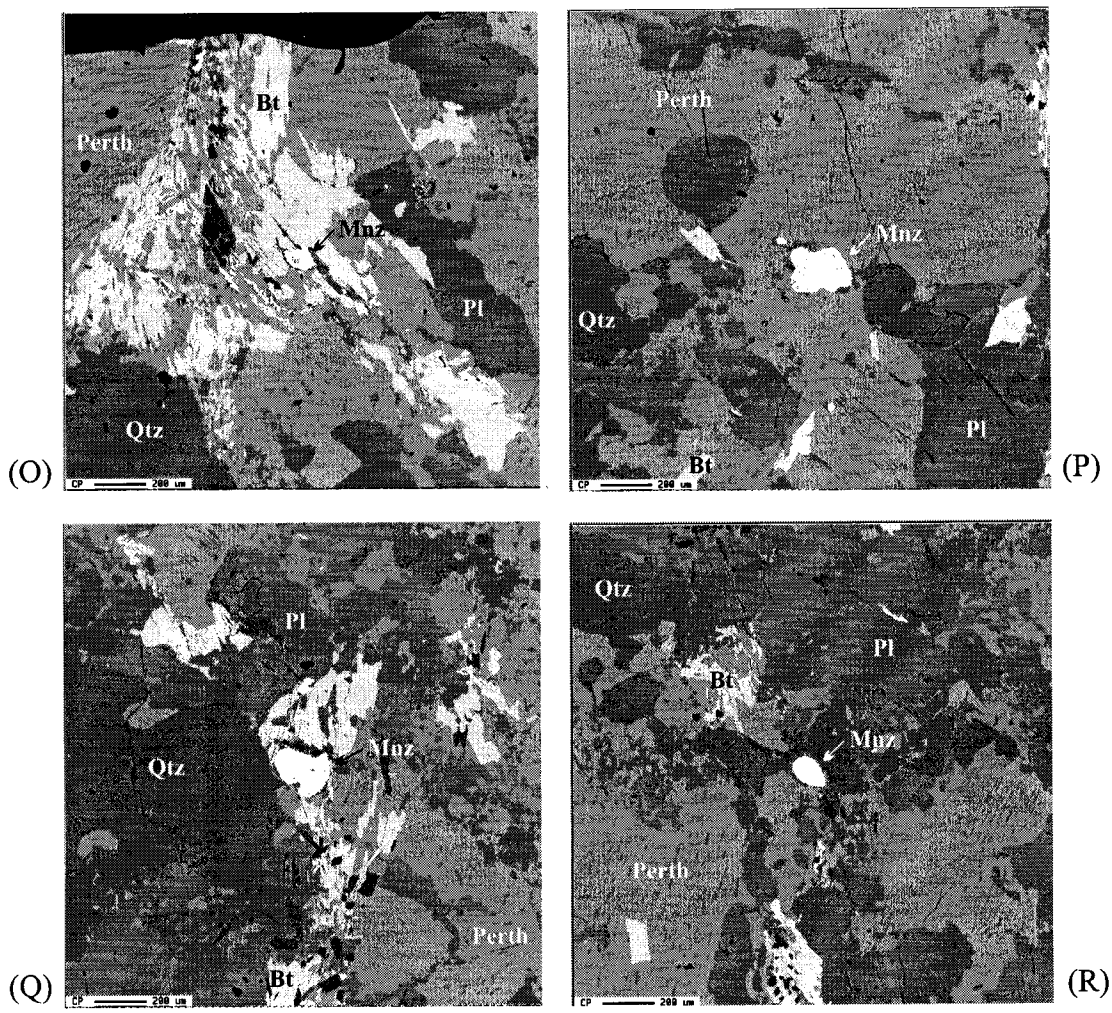

Appendix C. BSE composition maps of monazite (center) within thin section: (O) 861420-mon22, (P) 861420-mon18 (Q) 861420-mon24, and (R) 861420-mon28.

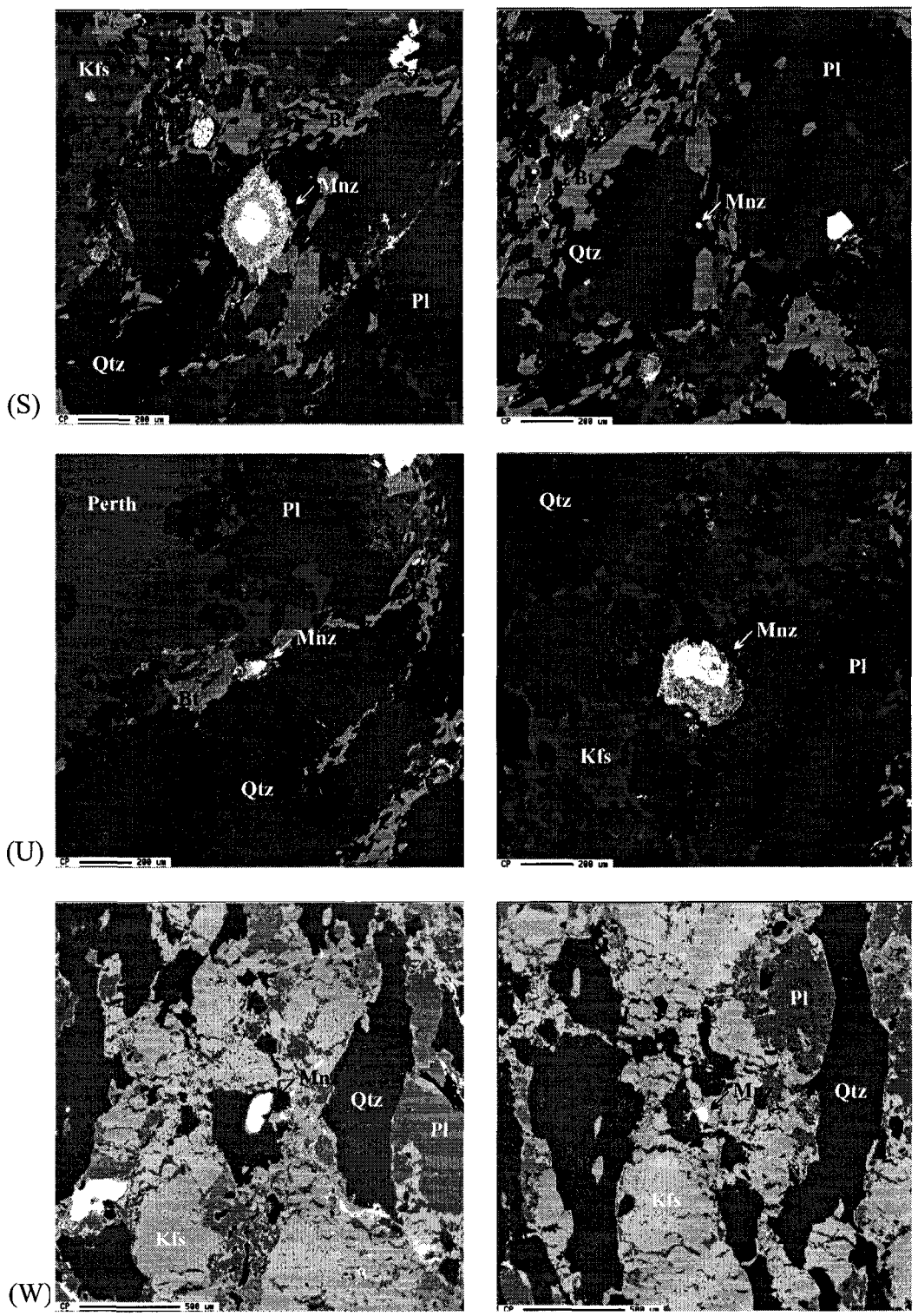

Appendix C. BSE composition maps of monazite (center) within thin section: (S) 860781-mon1, (T) 860781-mon3, (U) 860781-mon5, (V), 860781-mon6, (W) 860880-mon1, and (X) 860880-mon2.

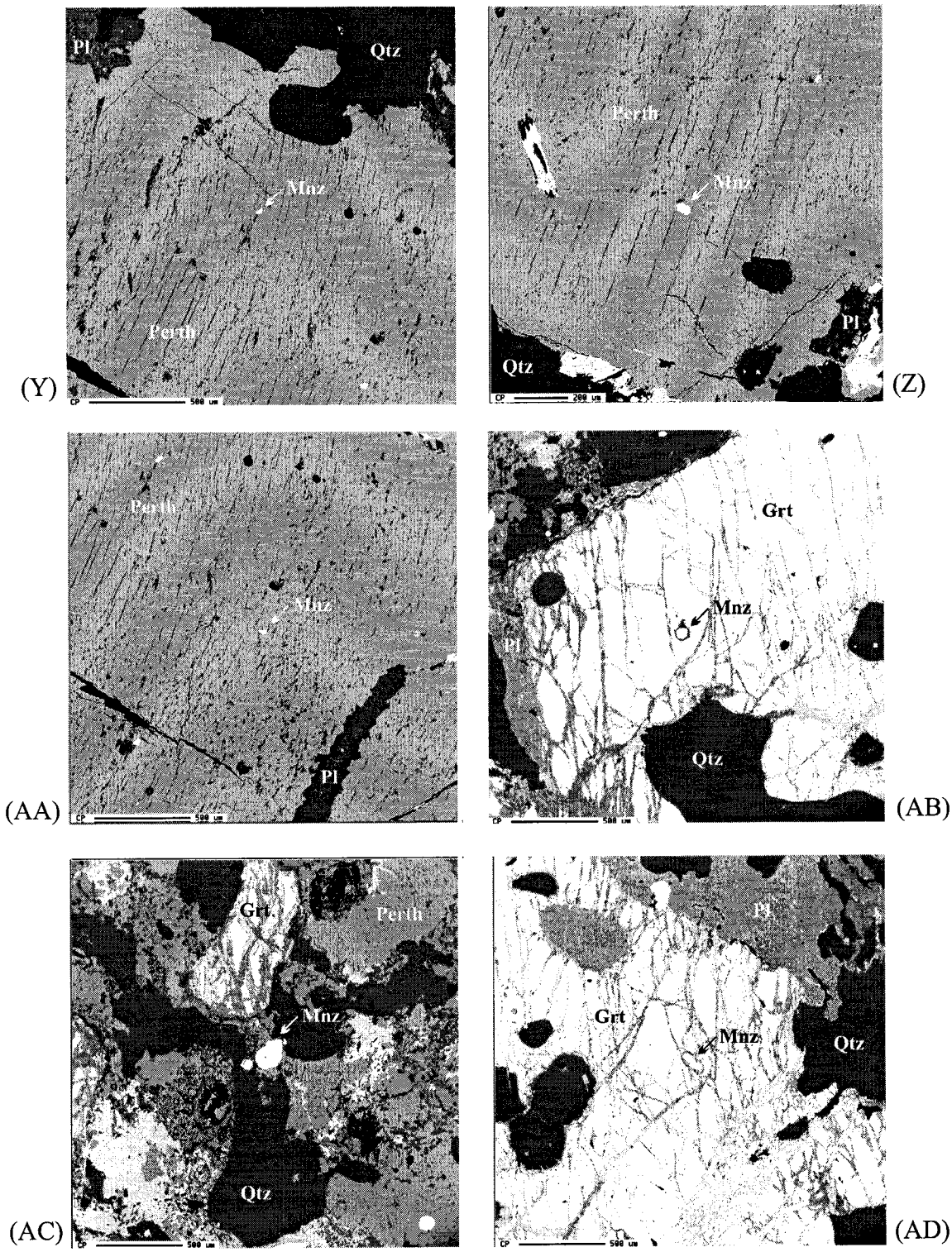

Appendix C. BSE composition maps of monazite (center) within thin section: (Y) 861790-mon1, (Z) 861790-mon2, (AA) 861790-mon5, (AB) 4245b-mon1, (AC) 4245b-mon5 and (AD) 4245b-mon 9.

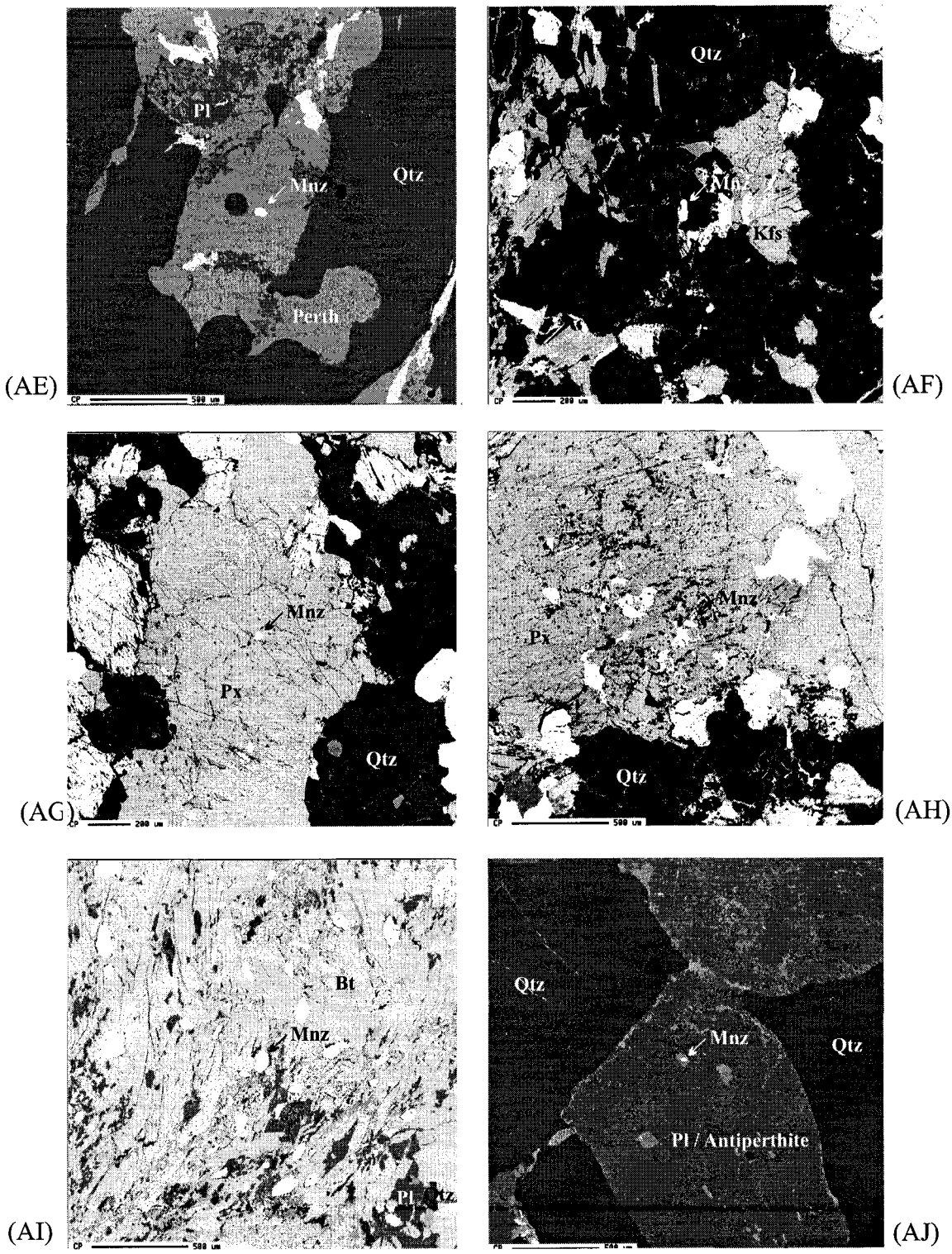

Appendix C. BSE composition maps of monazite (center) within thin section: (AE) 861740-mon1, (AF), 860220-mon4, (AG) 860220-mon13, (AH) 860220-mon24, (AI) 860770-mon3 and (AJ) 860380-mon1.

(AK)

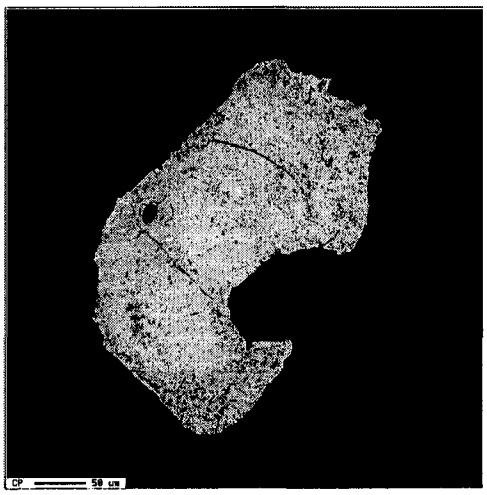

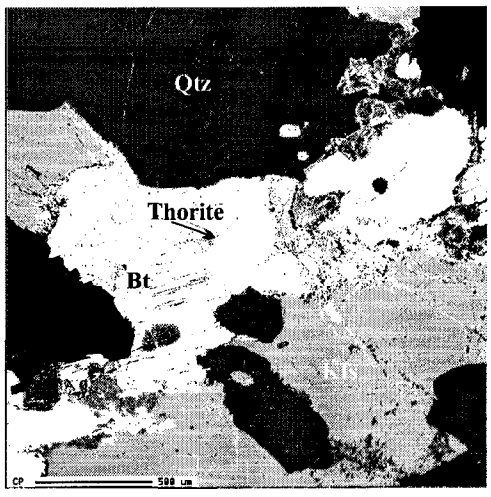

(AL)

(AM)

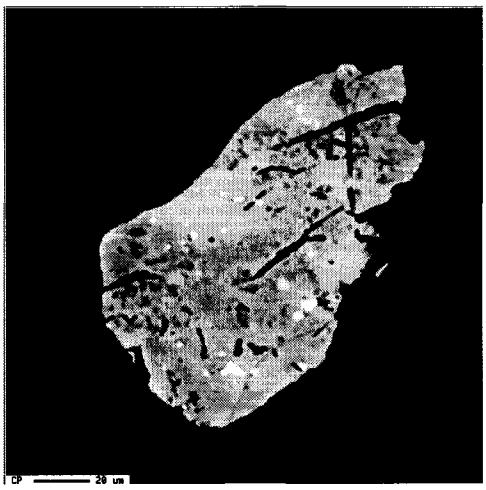

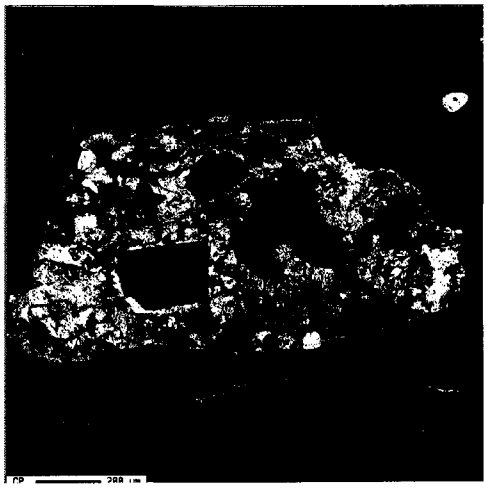

(AN)

(AO)

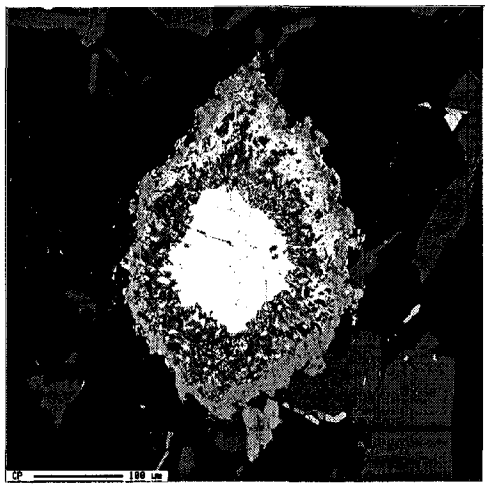

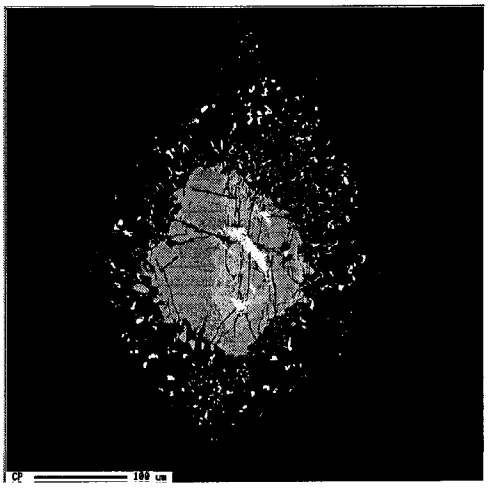

(AP)

Appendix C. BSE composition maps of Thorium-silicate grains; (AK) 861710 and (AL) grain located within center of thin section, (AM) and (AN) 4249 Th-silicate and Ca-REE porphyroblast, respectively, and (AO) and (AP) BSE image contrasted to show alteration surrounding 860781-mon1.

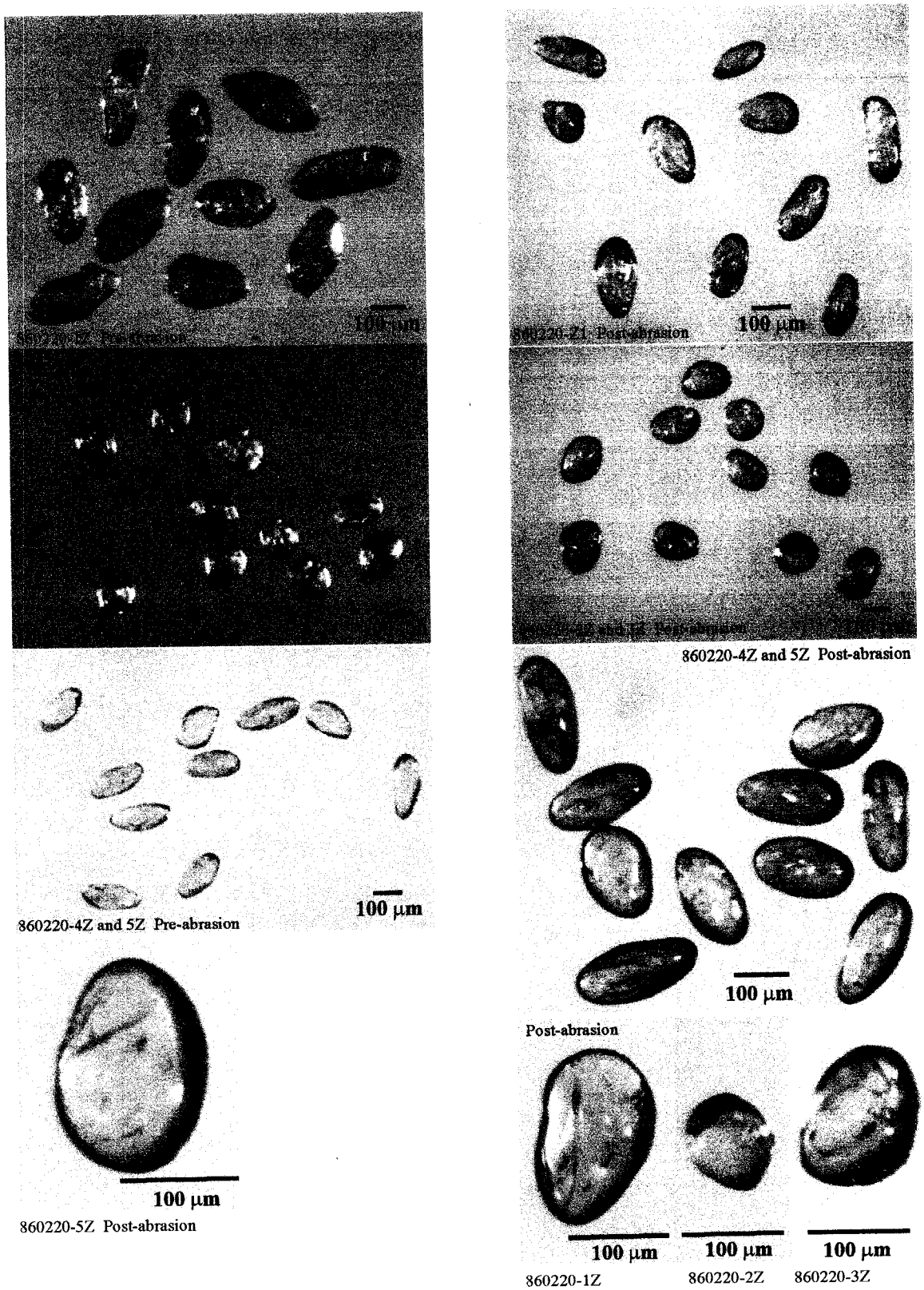

Appendix D. Single zircon fractions, before and after abrasion, from Bt-Cpx charnockite (860220).

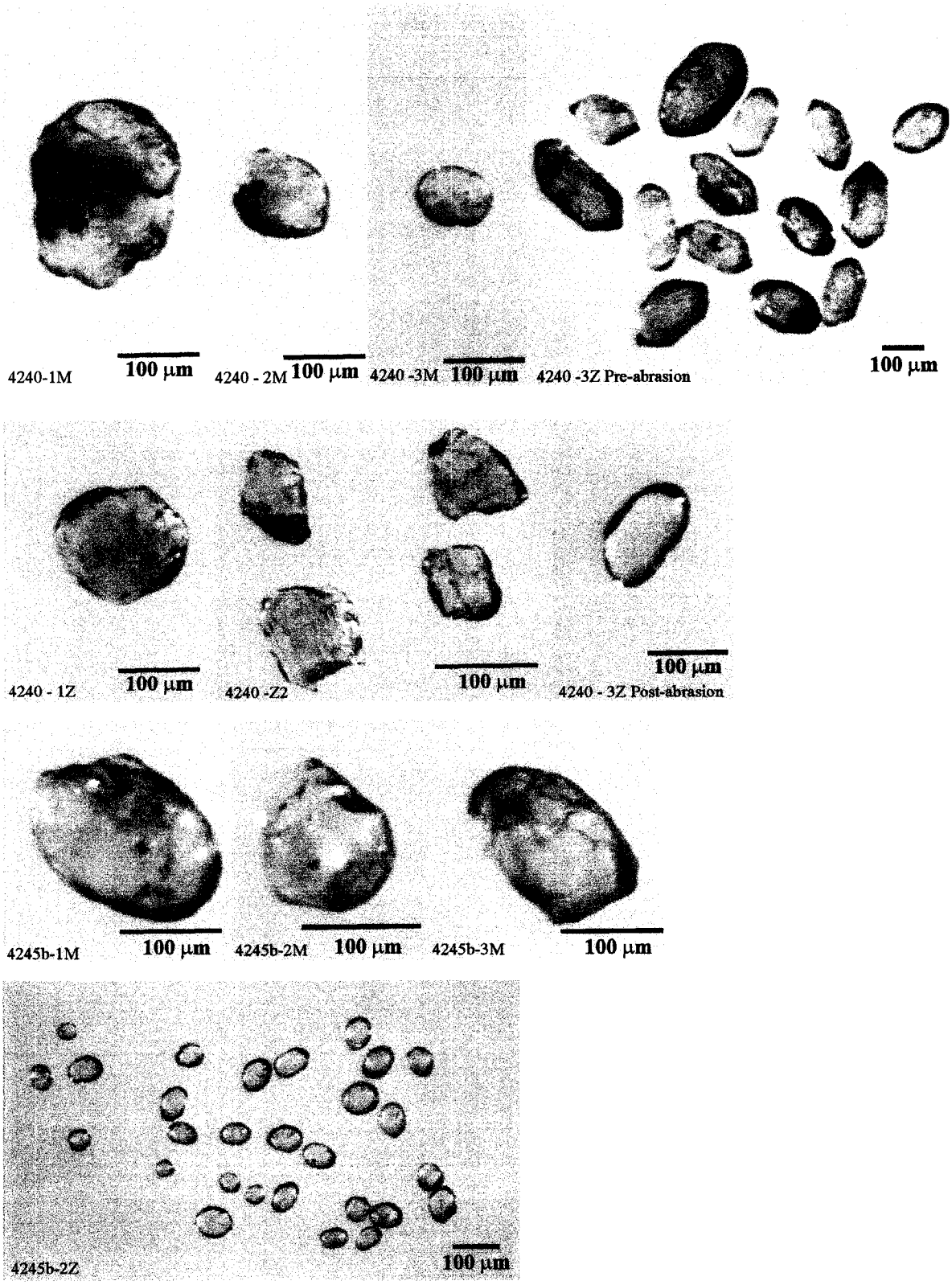

Appendix D. Monazite (M) and zircon (Z) fractions from a Bt granite (4240) and Sil-Grt pelitic mylonite (4245b).

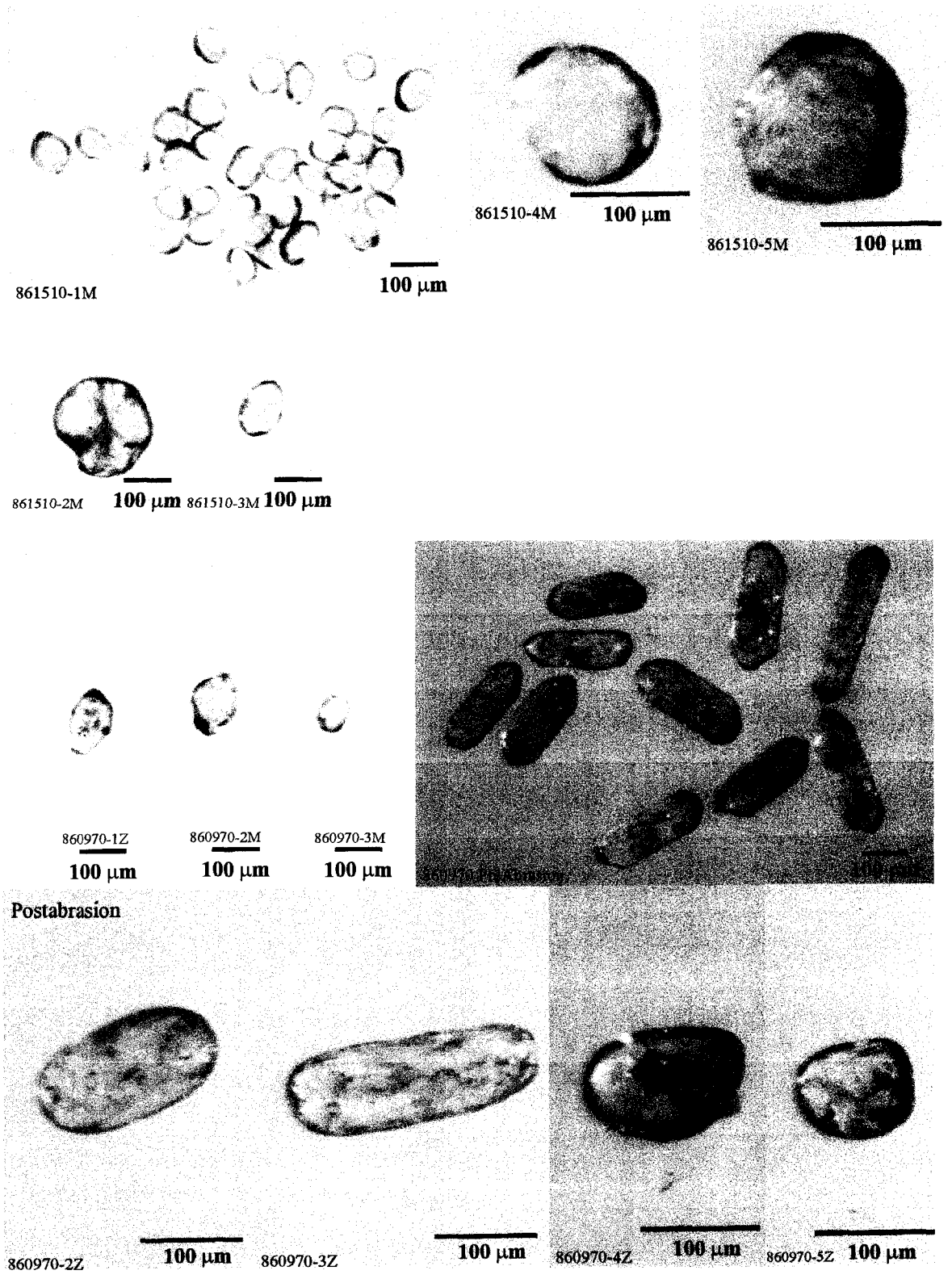

Appendix D. Monazite (M) and zircon (Z) fractions from a Spl-Crd-Sil-Grt pelitic migmatite (861510) and Bt granite (860970).

Appendix E. Samples numbers used in this study with reference numbers of the University of Alberta Basement Core Collection

B.R.P. #	University of Alberta Ref. #
Granitoid	
64 (M34)	M34
100 (4035)	M4035
860140	M12363
860550	M12405
860970	M12445
123 (4240)	M4240
861810	M12519
Pelitic Gneiss	
861510	M12490
861590	M12497
110 (B54-9)	M12573
82 (4419)	M4419
861380	M12476
861420	M12481
127 (3226)	M3226
128 (4239)	M4239
861100	M12454
Gneiss	
133 (4248)	M4248
860600	M12409
860670	M12416
860781	M12428
860790	M12429
860880	M12436
861150	M12457
861450	M12485
861520	M12491
861630	M12501
861740	M12511
861750	M12512
861790	M12517
108 (4007k)	M4007k
861800	M12518
Mylonite	
126 (4245b)	M4245b
Charnockite	
860220	M12371
860700	M12419
860770	M12426
860870	M12435
860070	M12356
860200	M12369
860380	M12390
860530	M12403
860570	M12406
860640	M12413
860930	M12440
861280	M12467
861360	M12476
860830	M12433